Quantum Logic Spectroscopy of Atomic and Molecular Ions

Von der QUEST-Leibniz-Forschungsschule
der Gottfried Wilhelm Leibniz Universität Hannover

zur Erlangung des Grades

Doktor der Naturwissenschaften
Dr. rer. nat.

genehmigte Dissertation

von

Dipl.-Phys. Yong Wan
geboren am 2. Oktober 1983 in Wuhan, Hubei

2014

Referent: Prof. Dr. Piet O. Schmidt
Korreferent: Prof. Dr. Christian Ospelkaus
Tag der Promotion: 23. Juli 2014

Abstract

Laser spectroscopy is a versatile tool to investigate the internal structure of atoms, molecules and nuclei. High precision spectroscopy requires laser cooling to reduce Doppler broadening and Doppler shifts. Sympathetic cooling extends these advantages to species which do not have an appropriate transition for laser cooling and allows precision spectroscopy of previously inaccessible species using the quantum logic technique. The original implementation of quantum logic spectroscopy relies on the long lifetime of the excited spectroscopy state to realize a transfer sequence. Precision spectroscopy of transitions with a short-lived excited state is typically performed using laser induced fluorescence or laser absorption spectroscopy. Neither of these methods has reached the fundamental quantum projection noise limit and are rather limited by photon shot noise.

For these situations, we develop the technique of photon recoil spectroscopy as an extension of quantum logic spectroscopy to broad transitions. The common motion of a sideband-cooled two-ion crystal is excited by photon recoil during photon absorption on the spectroscopically investigated ion. This motional excitation is transferred to an internal state excitation on the co-trapped ion of a different species and detected with high efficiency. We demonstrate the technique on the $^2S_{1/2} \leftrightarrow {}^2P_{1/2}$ transition of the $^{40}Ca^+$ ion and resolve the line center to 1/300 of its observed linewidth. The simplicity and versatility of the technique promises applications to other previously inaccessible species.

A variation of the technique is proposed for rotational state preparation of molecular ions. A moving optical lattice is employed to exert a state-dependent force on the molecule. This would allow the detection of the rotational state of the molecular ion and therefore enable precision spectroscopy of specific rovibrational transitions in the molecule.

keywords: sideband cooling, photon recoil spectroscopy, quantum logic technique

Zusammenfassung

Laserspektroskopie ist ein vielseitiges Instrument zur Untersuchung der internen Struktur von Atomen, Molekülen und Atomkernen. Hochpräzise Spektroskopie erfordert Laserkühlung um Dopplerverbreiterung und Dopplerverschiebungen zu reduzieren. Coulomb-Kühlung erweitert diese Vorteile auf Spezies, die keinen passenden Übergang zur Laserkühlung aufweisen und ermöglicht Präzisionsspektroskopie von bisher unzugänglichen Spezies mit Hilfe der Quantenlogik-Technik. Die erste Realisierung der Quantenlogik-Spektroskopie erfordert jedoch eine lange Lebensdauer des angeregten Spektroskopie-Zustandes um die Anregung auf ein in der selben Falle gefangenes Logik-Ion zu übertragen. Präzisionsspektroskopie von Übergängen mit einem kurzlebigen angeregten Zustand wird in der Regel mittels Laserinduzierten Fluoreszenz oder Absorptionsspektroskopie durchgeführt. Keine der beiden Methoden erreicht das fundamentale Limit des Quantenprojektionsrauschens, sondern sind durch das Photonenschrotrauschen-limitiert.

Für diese Situationen entwickelten wir die Photon-Rückstoß-Spektroskopie als eine Erweiterung der Quantenlogik-Spektroskopie zu breiten Übergängen. Die gemeinsame Bewegung eines Seitenband-gekühlten Zwei-Ion-Kristalls wird durch Photonenrückstöße während der Absorption des spektroskopierten Ions angeregt. Diese Anregung des Bewegungszustandes wird in eine Anregung des internen Zustandes des mitgefangenen Ions einer anderen Spezies umgewandelt und mit hoher Effizienz detektiert. Wir demonstrieren die Technik auf dem $^2S_{1/2} \leftrightarrow {}^2P_{1/2}$ Übergang des $^{40}Ca^+$ Ions und lösen die Übergansfrequenz bis auf 1/300 ihrer beobachteten Linienbreite auf. Die Einfachheit und Vielseitigkeit der Technik ermöglicht Spektroskopie vieler anderer zuvor unzugänglicher Spezies.

Eine Variation der Technik wird zur Preäparation eines spezifischen Rotationszustandes von molekularen Ionen vorgeschlagen. Ein sich bewegendes optisches Gitter wird verwendet, um eine zustandsabhängige Kraft auf das Molekül auszuüben. Dies würde die Detektion des Rotationszustandes des molekularen Ions und daher die Präzisionsspektroskopie bestimmter Rotationsschwingungsübergänge im Molekül ermöglichen.

Schlagworte: Seitenbandkühlung, Photon-Rückstoß-Sepktroskopie, Quantenlogik-Technik

Contents

List of Figures

LIST OF FIGURES

List of Tables

Chapter 1

Introduction

Spectroscopy has played an important role in the investigation of the internal structure of atoms, molecules, and nuclei. In atomic physics, precision spectroscopy of hydrogen atoms permits the unique confrontation of experiment and theory (Hänsch, 2006). Precision spectroscopy of molecules allows one to infer an improved value of the proton-to-electron mass ratio (Koelemeij et al., 2007b) and some molecules such as H_3^+ are of great importance for astrophysics and interstellar chemistry (Geballe et al., 2006). The nuclear structure is revealed by isotope-shift measurements (Nörtershäuser et al., 1998a; Batteiger et al., 2009; Lee et al., 2013) or precision spectroscopy of exotic species like muonic hydrogen (Antognini et al., 2013).

Since the first demonstration of laser cooling (Wineland et al., 1978; Neuhauser et al., 1978), trapped ions became the ideal system for precision spectroscopy. Reduced Doppler broadening and shifts allow high-resolution investigation of optical transitions revealing the natural linewidths (Drullinger et al., 1980) and promise application as potential ultimate laser frequency standard (Dehmelt, 1982). This inspired physicists working on neutral atoms to use the technique of laser cooling to decelerate an atomic beam (Phillips et al., 1982) and cool a cloud of atoms to the Doppler cooling limit (Chu et al., 1985). The development of new cooling techniques allows cooling the atoms to below the Doppler cooling limit using Sisyphus cooling (Lett et al., 1988; Dalibard et al., 1989) and below the recoil limit using velocity-selective coherent population trapping (Aspect et al., 1988) or Raman cooling (Kasevich et al., 1992). This led to the creation of a new state

of matter, the "Bose-Einstein condensate" (Anderson et al., 1995). For trapped ions, the technique of resolved sideband cooling (SBC) allows physicists to bring a singly trapped charged particle to the absolute ground state of the confining potential (Diedrich et al., 1989; Monroe et al., 1995b). Later on, this technique has also been implemented to cool the collective motion of a two-ion crystal (King et al., 1998; Rohde et al., 2001). Besides conventional SBC, a new cooling technique using electromagnetically induced transparency (EIT) (Harris et al., 1990; Boller et al., 1991; Field et al., 1991; Fleischhauer et al., 2005) promises simultaneous cooling of multiple modes (Morigi et al., 2000; Roos et al., 2000; Schmidt-Kaler et al., 2001; Lin et al., 2013a). Other cooling schemes such as Stark-shift cooling (Retzker et al., 2007) allowing low final temperatures and superfast laser cooling (Machnes et al., 2010) allowing fast cooling rates have recently been proposed.

The ability to sideband cool a single ion or an ion crystal opens the door to a whole new world by exploiting the quantum nature of the ion's motion in the trap. Shortly after Monroe et al. (1995b) realized the SBC of a singly trapped ion along all three directions, experiments which demonstrated the generation of non-classical states of motion (Meekhof et al., 1996a) including the creation of a Schrödinger cat state (Monroe et al., 1996) and the implementation of the CNOT gate (Monroe et al., 1995a) confirmed the "intrinsic appeal" of placing a bound particle in its ground state of motion (Wineland, 2013).

These advantages of laser cooling were limited to species that possess suitable cooling transitions. The technique of sympathetic cooling (Larson et al., 1986) removes this limitation and allows the implementation of quantum logic spectroscopy (Schmidt et al., 2005). The first demonstration using a $^{9}Be^{+}$ ion as the logic ion enabled the spectroscopy of a narrow transition in the inaccessible $^{27}Al^{+}$ ion. Later on, quantum logic spectroscopy of the clock transition of the $^{27}Al^{+}$ ion achieved an unprecedented inaccuracy up to 8.6×10^{-18} (Rosenband et al., 2007; Rosenband et al., 2008; Chou et al., 2010). This implementation of the quantum logic technique on the two-ion crystal of $^{9}Be^{+}$ and $^{27}Al^{+}$ ions requires a long lifetime of the excited spectroscopy state to implement the internal state transfer sequence between the spectroscopy ion $^{27}Al^{+}$ and the logic ion $^{9}Be^{+}$.

There are many interesting transitions where the excited states have submicrosecond lifetimes. Spectroscopy of such broad transitions is typically im-

plemented by detecting scattered photons in laser induced fluorescence (LIF) (Drullinger et al., 1980; Herrmann et al., 2009; Batteiger et al., 2009) or absorbed photons in laser absorption spectroscopy (LAS) (Wineland et al., 1987a). The signal-to-noise ratio (SNR) of these techniques is limited by the small photon collection efficiency and the small atom-light-coupling efficiency, respectively. This poses a challenge, especially for transitions where only a limited number of photons can be scattered. These include transitions in metal ions of the transition elements, molecular ions and highly charged ions, which are important for answering fundamental questions in many fields of physics.

Through a comparison between astrophysical and laboratory spectroscopy data of metal ions, tests for a possible variation of the fine structure constant α over cosmological time length scales can be performed (Savedoff, 1956; Dzuba et al., 1999). Such a comparison relies on the existence and the accuracy of the laboratory data, so that precision laboratory data on the transition frequencies and isotopic shifts of such ions (e.g. Si^+, Ti^+, Fe^+, Ni^+) are desirable (Berengut et al., 2011b; Murphy et al., 2014). A similar comparison can be performed for the rotational and vibrational transitions in molecules (Murphy et al., 2008). The frequencies of those transitions depend on the proton-to-electron mass ratio $\mu = m_\mathrm{p}/m_\mathrm{e}$ (Dunham, 1932) and therefore allow for a test of its possible variation (Thompson, 1975). Highly charged ions provide an ideal playground for precision tests of quantum electrodynamics (QED) in strong fields (Epp et al., 2007; Nörtershäuser, 2011; Blau, 2012).

The subject of this thesis is the extension of the original quantum logic technique to broad transitions for a variety of ionic systems which do not meet the prerequisites of direct laser cooling. In comparison to conventional spectroscopy methods like LIF and LAS, the common motion of the two-ion crystal is employed to transfer the spectroscopic information. Clark et al. (2010) have demonstrated this idea on a Doppler cooled two-ion crystal using sympathetic heating spectroscopy and were able to detect the heating generated by observing a reduction of fluorescence of less than 1500 scattered photons from the co-trapped cooling ion. By applying short spectroscopy pulses synchronous with the ions' motion in the trap, Lin et al. (2013b) were able to detect the seeded motion from around 150 absorbed photons after a motional amplification scheme. The ultimate sensitivity

has been achieved using an interferometric sequence on a Schrödinger cat state of motion, demonstrating the detection of the photon recoil from a single photon (Hempel et al., 2013). These works paved the way for applying the quantum logic technique to broad transitions in atomic ions, and demonstrated the applicability of the technique to spectroscopy of these transitions. We demonstrate in this thesis for the first time precision spectroscopy of broad transitions in atomic ions using the quantum logic technique.

Compared to the atomic systems molecules have a much richer level structure. This limits the techniques of laser cooling currently to a small number of species, which have diagonal Franck-Condon factors (Shuman et al., 2010). Sympathetic cooling with a co-trapped laser cooled atomic ion has been demonstrated to bring the translational degrees of freedom of the molecular ion to a temperature below 100 mK (Bowe et al., 1999; Mølhave et al., 2000), but leaves the molecules in a thermal equilibrium distributed over different rovibrational states via coupling to the blackbody radiation (BBR) at room temperature. Before precision spectroscopy of rovibrational transitions in single molecular ions can be performed, it is necessary to prepare these ions in a pure quantum mechanical state. For this purpose, several approaches have been pursued. Staanum et al. (2010) and Schneider et al. (2010a) have demonstrated BBR-assisted rotational cooling using optical pumping on dipole-allowed transitions. A fractional population of 36.7% and 78% in the rotational ground state have been achieved on $^{24}MgH^+$ and HD^+, respectively. On apolar molecules, state-selective threshold photoionization has been employed to produce N_2^+ ions in selected rotational states (Tong et al., 2010). In another approach using He buffer-gas cooling, both the internal and external degrees of freedom of molecular ions are cooled (Gerlich, 1995; Kreckel et al., 2005; Trippel et al., 2006). A combination of the two techniques allows cooling the rotational degrees of freedom to a temperature of 7.5 K (Hansen et al., 2014). We propose here the preparation of a single molecular ion in a pure quantum mechanical state by detecting a selected rotational state of the molecular ion on the co-trapped atomic ion using the quantum logic technique. A successful detection reveals the ion's rotational state and allows precision spectroscopy of specific rovibrational transitions in the molecular ion as the next step.

The thesis is structured as follows. We introduce the basic theory for ion-laser interaction in Chapter 2. In Chapter 3, the principle of ion traps and the current experimental setup are discussed. The basic properties of the logic ion $^{25}Mg^+$ along with the available experimental tools are discussed and the measurement principles using a single ion are introduced. In Chapter 4, an optimized SBC scheme is developed. We demonstrate the scheme on a singly trapped $^{25}Mg^+$ ion and on a two-ion crystal of $^{25}Mg^+$ and $^{24}MgH^+$. Starting with ions in the motional ground state, coherent states of motion are generated using electric modulations at the axial trap frequency in Chapter 5. In an inverse approach, these coherent states are used as signal to determine the axial trap frequency. In Chapter 6 we extend the quantum logic technique to broad transitions of atomic ions. A new spectroscopy scheme, photon recoil spectroscopy (PRS), is developed and an absolute frequency measurement on the $^2S_{1/2} \leftrightarrow {}^2P_{1/2}$ transition of the $^{40}Ca^+$ ion is performed. A possible implementation of the quantum logic technique for rotational state preparation of molecular ions is discussed in Chapter 7. A summary and outlook of the project is provided in Chapter 8. Several appendices providing more details of the experimental and theoretical considerations are listed at the end of the main text.

Chapter 2

Theory

In this chapter, the interaction of a trapped ion with monochromatic light is discussed. In Sec. 2.1, we introduce the Hamiltonians describing the interaction of a laser with a trapped particle in a semi-classical treatment and discuss the coupling strength in Sec. 2.2. The reader is referred to (Cohen-Tannoudji et al., 1992; Wineland et al., 1998; Leibfried et al., 2003b; Foot, 2005) for further details.

2.1 Ion-Laser interaction

Consider an ion as a two-level system with transition frequency ω_0 between the ground $|\mathrm{g}\rangle$ and the excited state $|\mathrm{e}\rangle$ confined in a one-dimensional harmonic potential with the trap frequency ω_T. The total Hamiltonian describing the interaction of the ion with a monochromatic light source with frequency ω_L can be written as (Leibfried et al., 2003b, p. 290)

$$\hat{H} = \hat{H}^{(m)} + \hat{H}^{(a)} + \hat{H}^{(i)}, \tag{2.1}$$

where $\hat{H}^{(m)}$, $\hat{H}^{(a)}$ and $\hat{H}^{(i)}$ correspond to the Hamiltonians for the ion's motion in the trap, for the electronic states, and for the atom-light-interaction, respectively.

These three terms take the form

$$\hat{H}^{(m)} = \hbar\omega_{\mathrm{T}}(\hat{a}^\dagger\hat{a} + \frac{1}{2}) \tag{2.2}$$

$$\hat{H}^{(a)} = \frac{\hbar\omega_0}{2}\hat{\sigma}_z \tag{2.3}$$

$$\hat{H}^{(i)} = \frac{\hbar\Omega_0}{2}\hat{\sigma}_+ \exp\left[i\eta(\hat{a} + \hat{a}^\dagger)\right] e^{-i\omega_{\mathrm{L}}t} + \mathrm{h.c.}\,, \tag{2.4}$$

where $\hat{\sigma}_z = |\mathrm{e}\rangle\langle\mathrm{e}| - |\mathrm{g}\rangle\langle\mathrm{g}|$ is a Pauli-matrix, $\hat{\sigma}_+ = |\mathrm{e}\rangle\langle\mathrm{g}|$ is the spin-flip operator, $\hat{a}$ is the annihilation operator of the motion and Ω_0 is the Rabi frequency of the laser. The Lamb-Dicke parameter η

$$\eta \coloneqq kz_0 = 2\pi\frac{z_0}{\lambda}\,, \tag{2.5}$$

gives the ratio of the spatial extent z_0 of the atomic wave packet in the ground state of the harmonic potential, where k is the wave number of the laser. The total Hamiltonian $\hat{H}$ can be transformed into different frames according to

$$\hat{H}^{(R)} = \hat{U}^\dagger\hat{H}\hat{U} - i\hbar\cdot\frac{\partial\hat{U}^\dagger}{\partial t}\hat{U} \tag{2.6}$$

with $\hat{U} = \exp\left[-i/\hbar\cdot\hat{H}_0^{(R)}\right]$ as the unitary operator for the transformation and $\hat{H}_0^{(R)}$ is the Hamiltonian in the reference frame.

In the rotating frame with respect to the atom and the trap (Leibfried et al., 2003b, p. 291), the total Hamiltonian becomes

$$\hat{H}^{(AT)}(t) = \frac{\hbar\Omega_0}{2}\hat{\sigma}_+ \exp\left[i\eta\left(\hat{a}e^{-i\omega_{\mathrm{T}}t} + \hat{a}^\dagger e^{+i\omega_{\mathrm{T}}t}\right)\right] e^{-i\delta t} + \mathrm{h.c.}\,, \tag{2.7}$$

where $\delta = \omega_{\mathrm{L}} - \omega_0$ is the detuning of the laser from the atomic transition frequency. In the Lamb-Dicke approximation to 1^{st} order, the Hamiltonian takes the form

$$\hat{H}^{(AT)}(t) \approx \frac{\hbar\Omega_0}{2}\hat{\sigma}_+ \left[1 + i\eta\left(\hat{a}e^{-i\omega_{\mathrm{T}}t} + \hat{a}^\dagger e^{+i\omega_{\mathrm{T}}t}\right)\right] e^{-i\delta t} + \mathrm{h.c.}\,, \tag{2.8}$$

which shows three resonances for $\delta = 0, \pm\omega_{\mathrm{T}}$:

- **Carrier transition** With $\delta = 0$, the Hamiltonian simplifies after the rotating wave approximation (RWA) to

$$\hat{H}_{\mathrm{carr}} = \frac{\hbar\Omega_0}{2}\hat{\sigma}_+ + \mathrm{h.c.}\,, \tag{2.9}$$

which couples the two states $|\mathrm{g}, n\rangle$ with $|\mathrm{e}, n\rangle$. In a carrier transition, the motional number is not changed and the effective Rabi frequency between the two states is given in the Lamb-Dicke approximation to 1st order by $\Omega_{n,n} = \Omega_0$.

- **1st blue sideband** With $\delta = \omega_\mathrm{T}$, the Hamiltonian

$$\hat{H}_\mathrm{bsb} = i\frac{\hbar\Omega_0}{2}\eta\hat{\sigma}_+\hat{a}^\dagger + \mathrm{h.c.}\,, \tag{2.10}$$

drives a transition $|\mathrm{g}, n\rangle \leftrightarrow |\mathrm{e}, n+1\rangle$ on the 1st blue sideband (BSB). Simultaneous to absorption of a photon, the motional quantum number is increased by one. The effective Rabi frequency for a transition between $|\mathrm{g}, n\rangle$ and $|\mathrm{e}, n+1\rangle$ is given by $\Omega_{n+1,n} = \eta\Omega_0\sqrt{n+1}$ and is reduced compared to the carrier transition by a factor of $\eta\sqrt{n+1}$.

- **1st red sideband** With $\delta = -\omega_\mathrm{T}$, the Hamiltonian

$$\hat{H}_\mathrm{rsb} = i\frac{\hbar\Omega_0}{2}\eta\hat{\sigma}_+\hat{a} + \mathrm{h.c.}\,, \tag{2.11}$$

becomes equivalent to the Jaynes-Cummings Hamiltonian (Jaynes et al., 1963) and drives a 1st red sideband (RSB) transition $|\mathrm{g}, n\rangle \leftrightarrow |\mathrm{e}, n-1\rangle$. In such a transition, one quantum of motion is removed as the ion goes to the excited state. The effective Rabi frequency between the two states is given by $\Omega_{n-1,n} = \eta\Omega_0\sqrt{n}$, which vanishes for the motional ground state $|\mathrm{g}, n=0\rangle$.

In the rotating frame with respect to the laser, the total Hamiltonian

$$\hat{H}^{(L)} = \hat{H}^{(m)} - \frac{\hbar\delta}{2}\hat{\sigma}_z + \left\{\frac{\hbar\Omega_0}{2}\hat{\sigma}_+ \exp\left[i\eta\left(\hat{a}+\hat{a}^\dagger\right)\right] + \mathrm{h.c.}\right\} \tag{2.12}$$

becomes independent of time, and is therefore useful for numerical simulations. In the Lamb-Dicke approximation to 1st order, the Hamiltonian in Eq. (2.12) can be further simplified to

$$\hat{H}^{(LD)} = \hat{H}^{(m)} - \frac{\hbar\delta}{2}\hat{\sigma}_z + \left\{\frac{\hbar\Omega_0}{2}\hat{\sigma}_+ \left[1 + i\eta\left(\hat{a}+\hat{a}^\dagger\right)\right] + \mathrm{h.c.}\right\}. \tag{2.13}$$

Without the presence of the laser, the system evolves under the Hamiltonian

$$\hat{H}_0 = \hat{H}^{(m)} - \frac{\hbar\delta}{2}\hat{\sigma}_z\,. \tag{2.14}$$

The Hamiltonians in Eqs. (2.13) and (2.14) are used in Sec. 6.3.5.1 for the numerical simulation of photon recoil spectroscopy.

2.2 Effective Rabi frequencies

Besides the carrier and first order sideband transitions, the interaction Hamiltonian also gives rise to a coupling between two arbitrary motional states $|\mathrm{g}, n\rangle$ and $|\mathrm{e}, n'\rangle$. The effective Rabi frequency between the two states can be calculated according to (Cahill et al., 1969; Wineland et al., 1979)

$$\begin{aligned}\Omega_{n',n} &= \Omega_0 \left|\langle n'| \exp[i\eta(a + a^\dagger)] |n\rangle\right| \\ &= \Omega_0 \exp\left[\frac{-\eta^2}{2}\right] \sqrt{\frac{n_<!}{n_>!}} \eta^{|n'-n|} L_{n_>}^{|n'-n|}(\eta^2)\end{aligned} \tag{2.15}$$

with $n_<$ ($n_>$) as the lesser (greater) of n' and n and L_n^α as the generalized Laguerre polynomial. Fig. 2.1 shows the effective Rabi frequencies as a function of the motional quantum number n for the first three RSBs. With a Lamb-Dicke parameter of $\eta = 0.3$, the effective Rabi frequencies of the 1st RSB shows a zero crossing at around $n = 40$. The effect prohibits SBC using only 1st order RSB and will be discussed in detail in Chapter 4.

For an ion string with L ions, there are altogether $3L$ motional modes and we choose one of the $3L$ modes as the logic mode k for transferring the information. The effective Rabi frequency for driving a transition between the two states $|\downarrow, n_k, \{n_{p\neq k}\}\rangle$ and $|\uparrow, n'_k, \{n_{p\neq k}\}\rangle$ on the jth ion equals

$$\Omega^j_{n'_k,n_k}(\{n_{p\neq k}\}) = \Omega^j_{n'_k,n_k} \prod_{p\neq k} S_p\,, \tag{2.16}$$

where $\Omega^j_{n'_k,n_k} = \Omega_0 \left|\langle n'_k| \exp[i\eta^j_k(a_k + a_k^\dagger)] |n_k\rangle\right|$ is the Rabi frequency for a transition between $|\downarrow, n_k\rangle$ and $|\uparrow, n'_k\rangle$ under the influence of the effective Lamb-Dicke parameter η^j_k of the jth ion on the kth mode, as if the other $3L - 1$ modes were not present and

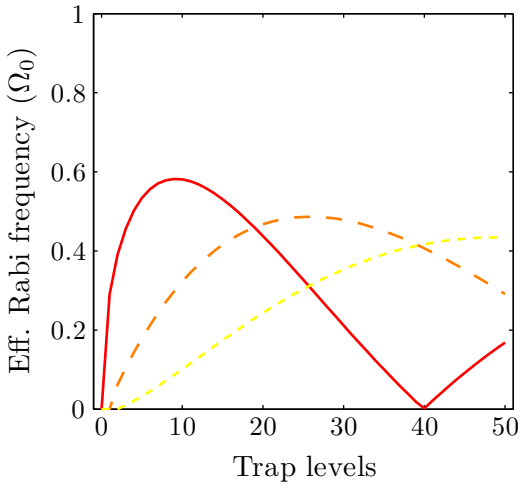

Figure 2.1: **Effective Rabi frequencies.** Effective Rabi frequencies as a function of the trap levels calculated with $\eta = 0.30$. The effective Rabi frequencies for different RSB orders have zero crossings at different trap levels. *solid/dashed/dotted*: $1^{\text{st}}/2^{\text{nd}}/3^{\text{rd}}$ order RSB.

$$\begin{aligned} S_p = & \left| \langle n_p | \exp[i\eta_p^j (a_p + a_p^\dagger)] \, | n_p \rangle \right| \\ = & \exp\left[-\frac{(\eta_p^j)^2}{2} \right] L_{n_p}^0 \left[(\eta_p^j)^2 \right] , \end{aligned} \tag{2.17}$$

is the Debye-Waller factor for each companion mode (Wineland et al., 1998). Eq. (2.16) shows that the effective Rabi frequency for driving a transition in the ion string does not only depend on the motional quantum number n_k of the logic mode, but also on the motional quantum numbers $\{n_{p\neq k}\}$ of the companion modes, although no state change occurs for them. The Debye-Waller factor is only present if the companion modes have a non-vanishing Lamb-Dicke parameter, or in other words if the k-vector of the laser has a non-vanishing component along the direction of the companion modes. Consider a two ion crystal undergoing a transition driven by a laser aligned, e.g. along the axial direction. The exact Rabi frequency of the transition between $|\downarrow, n_{\text{ip}}, n_{\text{op}}, \{n_r\}\rangle$ and $|\downarrow, n'_{\text{ip}}, n_{\text{op}}, \{n_r\}\rangle$ with altered quantum number $n_{\text{ip}} \to n'_{\text{ip}}$ for the in-phase mode along the axial direction does not depend on the quantum numbers $\{n_r\}$ of the radial modes, but indeed on the exact quantum state n_{op} of the out-of-phase mode. We discuss the influence of the Debye-Waller factors on SBC further in Chapter 4.

Chapter 3

Experimental setup

In this chapter, a description of the basic experimental setup is provided. In Sec. 3.1, we discuss the principle of ion traps. For more details about ion traps and the design of the trap used in the experiment, the reader is referred to Paul, 1990; Ghosh, 1995; Major, 2005; Berkeland et al., 1998; Hemmerling, 2011. In Sec. 3.2, we introduce the level scheme and the laser systems for the magnesium ion. With these laser systems, coherent manipulation of the internal and external degrees of freedom of $^{25}Mg^{+}$ ions can be performed. We introduce different experimental methods, which allow us to extract the state information of the system. For a detailed description of the experimental setup, the reader is referred to Hemmerling et al., 2011; Hemmerling et al., 2012; Hemmerling, 2011; An der Lan, 2008; Nigg, 2009.

3.1 Ion trap

The ions are confined using a linear Paul trap. A schematic of a linear Paul trap is shown in Fig. 3.1. The two endcaps are supplied with a DC voltage U. Two of the radial electrodes are supplied with a voltage oscillating at radio frequency (RF) $V(t) = V_0 \cos(\Omega_{\mathrm{rf}} t)$, while the other two are connected to the electric ground as depicted in Fig. 3.1b. The total electric potential generated by the DC and RF electrodes is given by (Berkeland et al., 1998)

$$\Phi(x, y, z, t) = \frac{\kappa U}{z_0^2}\left[z^2 - \frac{x^2 + y^2}{2}\right] + \frac{V_0}{2}\left[1 + \frac{x^2 - y^2}{r_0^2}\right]\cos(\Omega_{\mathrm{rf}} t)\,, \tag{3.1}$$

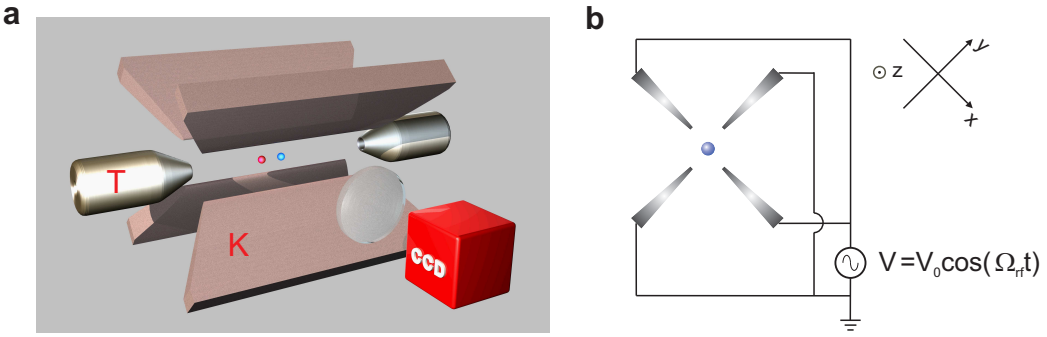

Figure 3.1: **Linear Paul trap.** (**a**) The four radial electrodes (*blades* K) and the two axial electrodes (*endcaps* T) produce a three-dimensional pseudo-potential confining the ion/ions in the center region of the trap. (**b**) One pair of opposing radial electrodes are supplied with a voltage at high frequency RF, while the other pair is grounded. The coordinate system in the figure serves only as a demonstration of the spatial dependence of the electric potential/field generated by the trap electrodes and differs from the coordinate system used in the other parts of the thesis.

where κ is a geometric factor, z_0 is the distance from the trap center to the endcap and r_0 is the distance from the trap axis to the RF electrodes. The electric field from the trap electrodes reads

$$\boldsymbol{E} = -\nabla\Phi = \frac{\kappa U}{z_0^2}\begin{pmatrix} x \\ y \\ -2z \end{pmatrix} + \frac{V_0}{r_0^2}\begin{pmatrix} -x \\ y \\ 0 \end{pmatrix}\cos(\Omega_{\mathrm{rf}}t)\,. \tag{3.2}$$

The motion of an ion with charge $q = e$ and mass m under the influence of the electric field is given by (Ghosh, 1995)

$$\ddot{u}_i + \frac{\Omega_{\mathrm{rf}}^2}{4}\left[a_i + 2q_i\cos(\Omega_{\mathrm{rf}}t)\right]u_i = 0 \tag{3.3}$$

where $\boldsymbol{u} = \begin{pmatrix} u_x & u_y & u_z \end{pmatrix}^{\mathsf{T}}$ denotes the ion's position. The stability parameters a_i, q_i of the trap are given by

$$a_x = a_y = -\frac{1}{2}a_z = -\frac{4e\kappa U}{mz_0^2\Omega_{\mathrm{rf}}^2}\,, \tag{3.4}$$

$$q_x = -q_y = \frac{2eV_0}{mr_0^2\Omega_{\mathrm{rf}}^2}\,,\quad q_z = 0\,. \tag{3.5}$$

After a variable transformation $\nu = \Omega_{\mathrm{rf}} t/2$, Eq. (3.3) takes the form of a Mathieu equation

$$\frac{\mathrm{d}^2 u_i}{\mathrm{d}\nu^2} + [a_i + 2q_i \cos(2\nu)]\, u_i = 0\,. \tag{3.6}$$

The ion remains in the trap if Eq. (3.6) has bound solutions for all three directions. In the parameter regime $|a_i| \ll 1$, $|q_i| \ll 1$, Eq. (3.3) has a stable solution (Berkeland et al., 1998; Major, 2005), which takes the approximate form

$$u_i(t) \approx u_{1i} \cos(\omega_i t + \phi_i) \left[1 + \frac{q_i}{2} \cos(\Omega_{\mathrm{rf}} t)\right] \tag{3.7}$$

with the amplitude u_{1i} and the phase ϕ_i determined by the initial conditions and the frequency ω_i given by

$$\omega_i = \frac{\Omega_{\mathrm{rf}}}{2} \sqrt{a_i + \frac{q_i^2}{2}}\,. \tag{3.8}$$

The ion's motion in the trap along a certain direction i consists of a harmonic oscillation at the frequency ω_i, called secular motion, and a fast oscillation at the trap drive frequency Ω_{rf}, called micromotion. The amplitude of the micromotion is much smaller than the amplitude of the secular motion ($|q_i| \ll 1$). Neglecting micromotion, the motion of the ion is identical to the motion of the particle in the pseudo-potential (Dehmelt, 1968; Major, 2005)

$$\Psi(x, y, z) = \frac{m}{2} \left(\omega_x^2 x^2 + \omega_y^2 y^2 + \omega_z^2 z^2\right)\,. \tag{3.9}$$

In the presence of an additional static electric field $\boldsymbol{E}_{\mathrm{dc}}$, the ion will be moved out of the field-free regime and oscillates around the new equilibrium position

$$u_{0i} = \frac{e\boldsymbol{E}_{\mathrm{dc}} \cdot \hat{\boldsymbol{e}}_i}{m\omega_i^2} \tag{3.10}$$

with $\hat{\boldsymbol{e}}_i$ as the unit vector along the dierection $i = x, y, z$. The motion of the ion in the trap is described in this case by (Berkeland et al., 1998)

$$u_i(i) \approx [u_{0i} + u_{1i} \cos(\omega_i t + \phi_i)] \left[1 + \frac{q_i}{2} \cos(\Omega_{\mathrm{rf}} t)\right]\,. \tag{3.11}$$

This additional term proportional to u_{0i} corresponds to a change of the equilibrium position and a fast oscillation at the trap drive frequency Ω_{rf}. Since this part of the micromotion can be avoided by applying additional compensation voltages, it is called "excess micromotion", while the residual micromotion even at the field-free position as in Eq. (3.7) is called "intrinsic micromotion".

3.2 Magnesium system

3.2.1 Laser system and beam configuration

In all the experiments presented in this thesis, we use $^{25}Mg^{+}$ ions as the logic ion species, over which we have full control in terms of internal and external degrees of freedom. A simplified level scheme for the $^{25}Mg^{+}$ ion is shown in Fig. 3.2. The electronic ground state $^2S_{1/2}$ has a hyperfine splitting of 1.789 GHz (Itano et al., 1981). We choose the two electronic states

$$\begin{aligned} |^2S_{1/2}, F = 2, m_F = 2\rangle &\equiv |\uparrow\rangle \\ |^2S_{1/2}, F = 3, m_F = 3\rangle &\equiv |\downarrow\rangle \end{aligned} \tag{3.12}$$

as the qubit states, on which information of interest is stored. A frequency-quadrupled fiber laser system[1] with a typical output power of 60 mW UV light at 280 nm is employed to perform cooling, coherent manipulation and state detection. In order to fulfill all these requirements, the fiber laser itself is ~ 9.2 GHz detuned from the $^2S_{1/2} \leftrightarrow {}^2P_{3/2}$ transition and an electro-optical modulator (EOM) generates sidebands at ± 9.2 GHz via phase modulation on the green light at 560 nm (Hemmerling et al., 2011). By switching the EOM, we switch the fiber laser between the resonant and off-resonant configuration. The resonant part corresponding to the 1st order sideband of the EOM is used for Doppler cooling and state detection on the $|\downarrow\rangle \leftrightarrow |^2P_{3/2}, F = 4, m_F = 4\rangle$ transition. The off-resonant light is split into two beams with their frequencies shifted apart by ~ 1.789 GHz using acousto-optical modulators (AOMs). These two beams, called σ-Raman and π-Raman beam, are used to drive Raman transitions between the qubit states.

A schematic of all the laser beams and their orientation with respect to the vacuum chamber is shown in Fig. 3.3. In the experiment, a bias magnetic field B of $\sim 5.8 \times 10^{-4}$ T is applied to lift the degeneracy of the Zeeman sub-levels. The direction of the magnetic field, which defines the quantization axis for the ions, is tilted by 45° with respect to the trap axis (z-axis in Fig. 3.3). The Doppler cooling beam and the σ-Raman beam are circularly polarized and aligned along

[1] Koheras Boostik^{TM} System Y10/Menlosystem

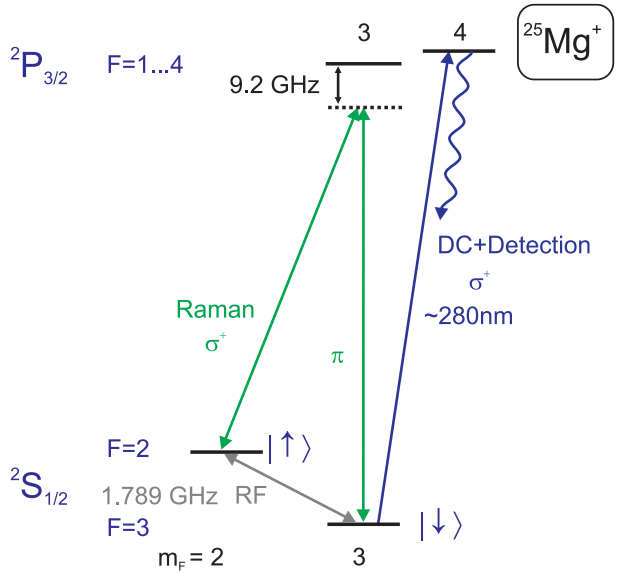

Figure 3.2: **Level structure of Magnesium ion.** The two hyperfine states $|\uparrow\rangle$ and $|\downarrow\rangle$ of $^{25}Mg^+$ ion separated by 1.789 GHz are used as qubit states to store the information of interest. These two states can be coherently manipulated through RF and Raman spectroscopy, and are distinguished using the electron shelving technique.

the direction of the magnetic field to drive a σ^+-transition on the $^{25}Mg^+$ ion. The linearly polarized π-beam is aligned perpendicular to the magnetic field B with the electric field vector of the laser co-linear with the magnetic field B to drive a π-transition. The photoionization laser for magnesium ions is aligned along the axial direction of the trap.

In the following chapters, extensions of this base setup to meet the requirement of each experiment are described in detail. In Chapter 4, a second frequency-quadrupled fiber laser ($^2P_{1/2}$ laser in Fig. 3.3) is employed to implement quasi-continuous sideband cooling (SBC) on $^{25}Mg^+$ ions. In Chapter 6, a spectroscopy laser at 397 nm and a repump laser at 866 nm (spectroscopy and repump laser in Fig. 3.3) are used for photon recoil spectroscopy (PRS). In Chapter 7, a pair of counter-propagating beams (lattice laser in Fig. 3.3) is used to generate a moving optical lattice for the state preparation of molecular ions.

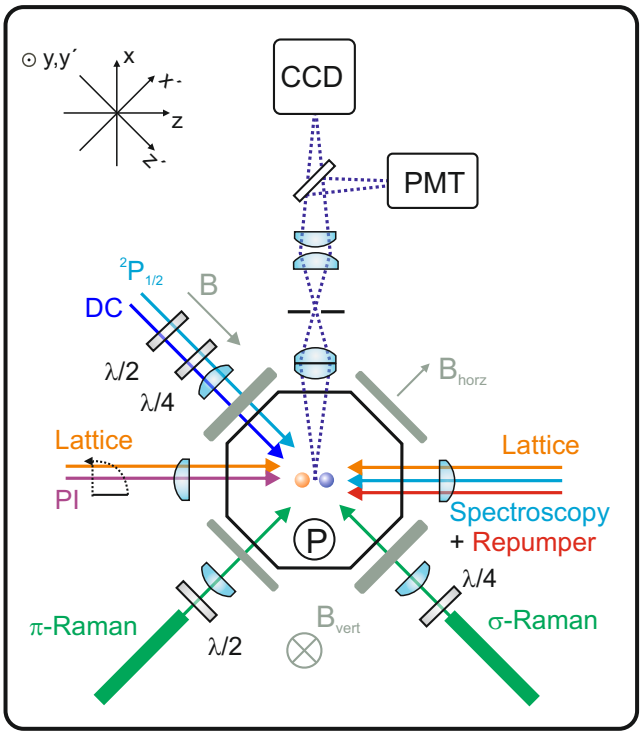

Figure 3.3: **Top view of the experimental setup.** The quantization axis (z'-axis) for the ions is defined by the direction of the magnetic field B, which is tilted by 45° from the trap axis (z-axis). The Doppler cooling beam (DC) and the σ-Raman beam are co-linear with the magnetic field and circularly polarized, while the π-Raman beam is perpendicular to the magnetic field with linear polarization in the plane of the figure. The photoionization laser beam (PI) enters the chamber along the axial direction. The $^2P_{1/2}$ laser for quasi-continuous sideband cooling enters through the same path as the Doppler cooling laser. The spectroscopy and repump lasers for photon recoil spectroscopy and a pair of counter-propagating beams (lattice laser) for state preparation of molecular ions enter the chamber from the axial direction. The figure is reproduced based on Hemmerling, 2011.

3.2.2 Measurement principle

In the experiment presented in this thesis, a single $^{25}Mg^+$ ion or an ion crystal consisting of a $^{25}Mg^+$ ion as logic ion and a second spectroscopy ion is trapped in the linear Paul trap. A typical experimental cycle consisting of state preparation, state interrogation, state manipulation and state detection is illustrated in

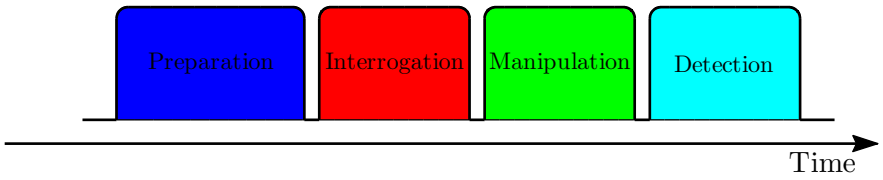

Figure 3.4: **Typical experimental sequence.** A typical experimental sequence consists of periods of state preparation, state interrogation, state manipulation and state detection.

Fig. 3.4. During the state preparation, the ion or the two-ion crystal is initialized to a specific state ρ_{init}, typically using different cooling techniques combined with optical pumping. This target state can be a mixed state, a pure quantum mechanical state, a superposition, or an entangled state. In the interrogation period, a series of operations are applied to the ions and the state of the ions is changed. The effect of these operations must be verified experimentally. These changes include a change in motional energy, a change of internal states or a reduced coherence between the internal states. In order to detect these changes, the quantum states of the $^{25}Mg^{+}$ ion are manipulated using some well-characterized operations based on the detailed theory of the ion-laser interaction was described in Sec. 2.1.

- **Radio frequency transitions** The two qubit states $|\uparrow\rangle$ and $|\downarrow\rangle$ can be coupled using a RF radiation at 1.789 GHz, which drives a magnetic dipole transition between the two states. Hyperfine qubits can exhibits long coherence time (Langer et al., 2005) and can be driven with a high fidelity (Brown et al., 2011). The former property allows investigation of the loss of coherence between the two internal states induced during the interrogation period (Clos et al., 2014), while the latter can be used to improve the fidelity of state detection of hyperfine qubits (Hemmerling et al., 2012). The long wavelength of RF radiation leads to small Lamb-Dicke parameters, so that only carrier transition can be driven with free propagating RF radiation, while strong magnetic field gradients generated in the near field of microwave current allows sideband transitions (Ospelkaus et al., 2011).

- **Raman transitions** A coherent transition between the two qubit states can also be achieved by driving two-photon stimulated Raman transition. As a result of non-zero Lamb-Dicke parameter, a Raman transition can change not only the internal state but also the external state of the ions. A carrier transition induces only a spin-flip between the $|\downarrow\rangle$ and $|\uparrow\rangle$ states, while a blue (red) sideband transition increases (decreases) the motional quantum number of the ions, as the ion goes to the excited state $|\downarrow\rangle \rightarrow |\uparrow\rangle$. In the resolved sideband regime, the type of transition can be chosen by the frequency difference of the two Raman lasers from the two qubit resonance frequency. The transition strength depends on the type of the transition and the exact quantum number of the motional states (Wineland et al., 1998). These state-dependent excitation strengths allow determination of the population (Meekhof et al., 1996a) of and the coherence (Leibfried et al., 1996) between motional levels.

- **Stimulated Raman adiabatic passage (STIRAP)** The motional state dependence of the coupling strength of Raman transitions can be avoided using the technique of stimulated Raman adiabatic passage (STIRAP). A state-independent transfer is achieved by adiabatically sweeping the frequency of the laser (Wunderlich et al., 2007) or ramping the power of the lasers (Sørensen et al., 2006) during the transfer pulse. A spin-flip between the $|\downarrow\rangle$ and $|\uparrow\rangle$ state independent of the motional levels has been implemented on the $^{25}Mg^{+}$ ion using the latter method. Tuning the Raman lasers to the 1^{st} red sideband e.g. allows transferring all the population in the motional excited state from $|\downarrow\rangle$ to $|\uparrow\rangle$ without affecting the population in the $|\downarrow, n = 0\rangle$ state (Gebert, 2015). This provides an efficient method to detect the depletion of the motional ground state induced by excitation during the interrogation period.

The task of the state manipulation period is to transfer the signal from the reference onto the two qubit states. A final internal state discrimination is performed via the electron shelving technique. Resonant laser pulses coupling the $|\downarrow\rangle$ state to the $\left|^2P_{3/2}, F = 4, m_F = 4\right\rangle$ state result in a high scattering rate for the $|\downarrow\rangle$ state and a low scattering rate for the $|\uparrow\rangle$ state. From the number of photons collected

on the photomultiplier tube (PMT) as shown in Fig. 3.3, the internal state of the ion can be determined. An improved fidelity for the internal state discrimination of hyperfine qubits can be achieved using the π-detection technique (Hemmerling et al., 2012). We can assign a result to a single experiment depending on the internal state of the $^{25}Mg^{+}$ ion

$$\begin{aligned} |\downarrow\rangle &\rightarrow 0 \\ |\uparrow\rangle &\rightarrow 1\,, \end{aligned} \tag{3.13}$$

typically also indicating if the operations during the interrogation period have changed the initial state or not. The quantum mechanical probability for the $^{25}Mg^{+}$ ion to be in the $|\uparrow\rangle$ state is extracted by repeating the experiment N_{cycles} times.

Chapter 4

Quasi-continuous sideband cooling

In this chapter, we introduce quasi-continuous sideband cooling (SBC), which we developed for efficient sideband cooling of a single $^{25}Mg^+$ ion and sympathetic cooling of the molecular ion $^{24}MgH^+$. We review the previous SBC techniques and discuss the challenges of SBC of an ion crystal in Sec. 4.1. In Sec. 4.2, we introduce quasi-continuous SBC for a single $^{25}Mg^+$ ion and extend the scheme to a two-ion crystal consisting of $^{25}Mg^+$ and $^{24}MgH^+$ in Sec. 4.3. In Sec. 4.4, we demonstrate the applicability of the technique at low trap frequencies. In the last section, we discuss possible applications of the technique. The results of this chapter ahve been summarized in Wan et al., 2015.

4.1 Introduction

Coherent control of quantum systems has been a dream pursued in a wide range of fields in physics and chemistry. The ability to control internal and external degrees of freedom of quantum systems promises application such as quantum computation (Monroe et al., 1995a; Leibfried et al., 2003a), quantum metrology (Schmidt et al., 2005; Rosenband et al., 2008) and ultracold chemistry (Willitsch et al., 2008a; Willitsch et al., 2008b; Staanum et al., 2008). The control over the internal degrees of freedom of the atomic species is often accomplished by optical pumping followed by coherent laser pulses from a narrow linewidth laser, while the external degrees of freedom are typically controlled with various laser cooling techniques. One possibility is the so-called *resolved sideband cooling*,

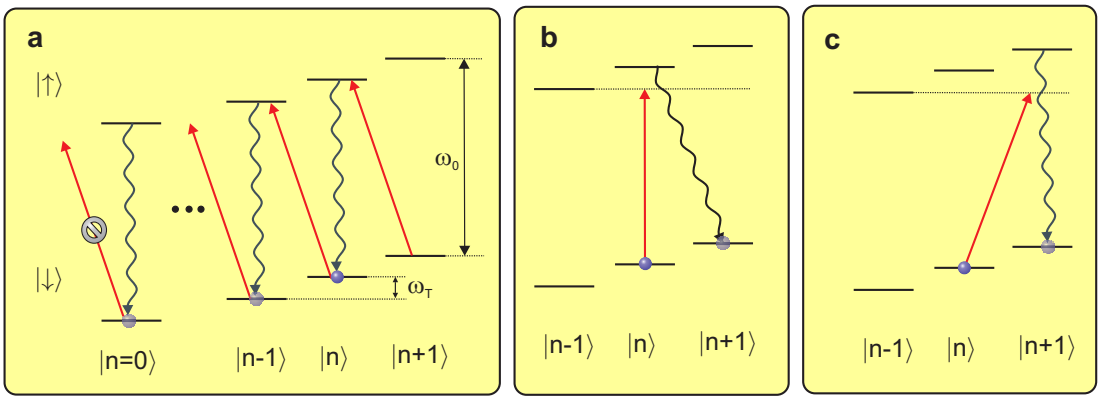

Figure 4.1: **Principle of resolved sideband cooling.** (**a**) Resolved SBC requires the linewidth of the transition to be smaller than the trap frequency, so that individual transitions (carrier, red sideband (RSB), blue sideband (BSB)) can be selectively driven. With the cooling laser tuned to the RSB, one quantum of motion is removed from the system simultaneous to each absorption event. In the Lamb-Dicke regime, the decay back to the $|\downarrow\rangle$ state happens dominantly on the carrier transition. The two-level system can be pumped down to the motional ground state, which is a dark state for the cooling laser. (**b-c**) The achievable $\bar{n}$ is limited by off-resonant excitation on the carrier followed by a decay on the BSB (b) and off-resonant excitation on the BSB followed by a decay on the carrier transition (c).

which has been demonstrated in various systems from single trapped ions in Paul traps (Diedrich et al., 1989; Monroe et al., 1995b; Roos, 2000; Eschner et al., 2003) to neutral atoms in optical lattices (Hamann et al., 1998; Vuletić et al., 1998) or optical tweezers (Thompson et al., 2013) and micromechanical oscillators (Schliesser et al., 2008; Park et al., 2009).

The principle of SBC is illustrated in Fig. 4.1. Consider a two-level system confined in a one-dimensional harmonic potential. The separation ω_0 of the two internal states is much larger than the spacing ω_T between the eigenstates of the harmonic oscillator. The joint system consists of a set of motional levels on top of each internal state. At the beginning of the SBC sequence, the ion is assumed to be located in a certain trap level $|n\rangle$. For the technique of SBC to be applicable, the linewidth of the transition Γ used for cooling must be smaller than

the trap frequency ω_T ($\Gamma \ll \omega_T$) so that the individual sidebands are *resolved*. In this case, carrier, RSB and BSB transitions can be selectively driven. With the cooling laser tuned to the RSB transition, one quantum of motion is removed from the system simultaneous to each absorption event (Fig. 4.1a). In the case that the trap frequency is much larger than the recoil frequency so that the strong confinement from the trap prevents recoil heating during the spontaneous emission process (*Lamb-Dicke regime*), the two-level system decays back to the $|\downarrow\rangle$ state pre-dominantly on the carrier transition (Morigi et al., 1999), which provides the necessary dissipation for cooling. In this way, the two-level system can be pumped down to the motional ground state, which is a dark state for the cooling laser. Off-resonant excitation on the carrier followed by a decay on the BSB and off-resonant excitation on the BSB followed by a decay on the carrier transition (Fig. 4.1b and c) limit the achievable $\bar{n}$ with the technique to

$$\bar{n} \approx \left(\frac{\Gamma}{2\omega_T}\right)^2 \left[\left(\frac{\widetilde{\eta}}{\eta}\right)^2 + \frac{1}{4}\right] \tag{4.1}$$

with η and $\widetilde{\eta}$ as the Lamb-Dicke parameters during absorption and spontaneous emission, respectively (Wineland et al., 1987b; Schulz et al., 2008). A small final $\bar{n}$ can be achieved by choosing transitions with narrow linewidths (Roos, 2000) or by making use of Raman transitions (Diedrich et al., 1989). Using the technique of SBC, final ground state populations ranging down to 99.9% have been demonstrated with trapped ions (Roos, 2000).

Besides the final temperature, the total duration of SBC is a crucial parameter describing the performance of the cooling. Here we distinguish two cases: *continuous* and *pulsed* SBC.

Continuous SBC Under continuous SBC, one understands that the spontaneous decay process happens simultaneously with the RSB excitation so that more than one photon is absorbed on the cooling transition within one pulse and therefore multiple phonons are removed from the system within one pulse. For the simplest case where only one long pulse is applied, the total duration of SBC is identical with the time spent on the RSB excitation. The total time scale for

cooling is determined solely by the cooling rate W, which fulfils the equation

$$\frac{\mathrm{d}}{\mathrm{d}t}\bar{n}(t) = -W\bar{n} + A_+, \tag{4.2}$$

and can be expressed in the low intensity case ($\Omega_0 \ll \Gamma$) as

$$W = \eta^2(A_- - A_+) \approx \frac{\eta^2\Omega_0^2}{\Gamma} \tag{4.3}$$

with A_+ and A_- denoting the transition rates upwards and downwards on the motional ladder and Ω_0 as the carrier Rabi frequency between two electronic states (Stenholm, 1986; Cirac et al., 1992).

This method allows for simple implementation, since a single cooling pulse assures sideband cooling independent of the initial motional state of the ion. The Rabi frequency and the decay rate between the two states $|\downarrow\rangle$ and $|\uparrow\rangle$ have an influence on the total cooling time.

In systems where the transition linewidth Γ is too small to allow a large cooling rate, the excited electronic state can be quenched to the ground state. This establishes an effecitve Γ_{eff} which can be tuned to optimize cooling speed and final $\bar{n}$ (Roos et al., 1999; Diedrich et al., 1989; Marzoli et al., 1994).

Pulsed SBC In case of pulsed SBC, the experimental sequence consists of a series of interleaved pulses for RSB excitation and dissipation, where the latter is typically realized by a repumping pulse followed by spontaneous emission. The cooling laser drives Rabi oscillations between $|\downarrow\rangle$ and $|\uparrow\rangle$. At most one photon is absorbed from the cooling laser during a single pulse. The total duration of SBC is the sum of the time spent on the RSB excitation and the time for repumping. Typically a sequence as demonstrated in Hemmerling et al., 2011 is used to achieve the maximal cooling speed. The pulse duration t of the SBC pulses is adjusted for each state $|\downarrow, n\rangle$ to ensure a complete spin-flip

$$\Omega_{n-1,n}t = \pi\,, \tag{4.4}$$

where $\Omega_{n-1,n}$ is the effective Rabi frequency between the two states $|\downarrow, n\rangle$ and $|\uparrow, n-1\rangle$. This ideal situation can in principle be implemented for SBC of a single ion, where only one mode along the direction under consideration is present and

the effective Rabi frequency can be calculated according to Eq. (2.15). Assuming that each RSB pulse transfers the population completely, the cooling rate for the target state $|\downarrow, n\rangle$ equals

$$W_{\text{eff}}(n) = \frac{\Delta n}{\Delta t} \cdot \frac{1}{n} \approx \frac{\sqrt{n}\eta\Omega_0}{\pi} \cdot \frac{1}{n}, \tag{4.5}$$

where Δn is the number of quanta removed during the RSB excitation, $\Delta t = \pi/\Omega_{n-1,n}$ is the duration of the π-pulse and the Lamb-Dicke approximation is used in the second step.

For an ion string with L ions, the effective Rabi frequency for driving a transition between two states $|\downarrow, n_k, \{n_{p\neq k}\}\rangle$ and $|\uparrow, n'_k, \{n_{p\neq k}\}\rangle$ depends not only on the quantum number n_k and n'_k, but also the quantum number of the companion modes $\{n_{p\neq k}\}$ (see Debye-Waller factor in Sec. 2.2). This additional factor for the effective Rabi frequency in the case of multiple ions makes the prediction of the exact pulse length for the state $|\downarrow, n_k\rangle$ impossible without the knowledge of the quantum numbers of the companion modes.

Furthermore, the effective Rabi frequency for any order RSB $\Omega^j_{n'_k,n_k}$ shows zero crossings at certain trap levels (Fig. 2.1). A cooling sequence with only 1$^{\text{st}}$ order RSB can not transfer the population in the trap levels beyond the zero crossing down to the ground state (Hemmerling et al., 2011), and therefore higher order sidebands with a zero crossing at a higher trap level are necessary.

In the following sections, we implement a quasi-continuous SBC, in which we combine the advantages of continuous and pulsed SBC by introducing a conditional decay channel. We demonstrate this on a single trapped $^{25}Mg^+$ ion and on a two-ion crystal of $^{25}Mg^+/^{24}MgH^+$. We show that our approach enables fast SBC with high stability against variations in experimental parameters like Rabi frequency or pulse lengths.

4.2 SBC of a single ion

4.2.1 Cooling scheme and laser configuration

Based on the scheme developed in Monroe et al., 1995b, a pulsed SBC scheme using a single laser system for cooling $^{25}Mg^+$ in a weak magnetic field (Hem-

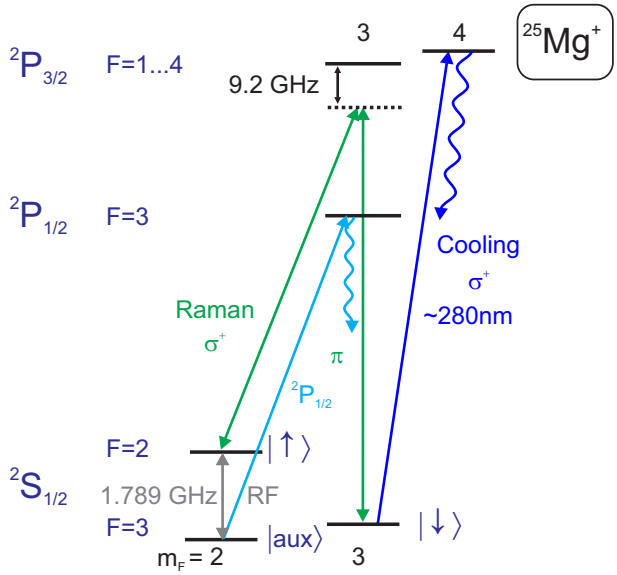

Figure 4.2: **Relevant level structure for SBC of a $^{25}Mg^+$ ion.** In addition to the Doppler cooling laser and the Raman lasers coupling the $^2S_{1/2} \leftrightarrow {}^2P_{3/2}$ transition, a second fiber laser system is employed for repumping the $|^2S_{1/2}, F = 3, m_F = 2\rangle$ state via the the $^2S_{1/2} \leftrightarrow {}^2P_{1/2}$ transition.

merling et al., 2011) was demonstrated. We trap a single $^{25}Mg^+$ ion in a linear Paul trap with an axial and radial trap frequency of 2.21 MHz and $\sim$ 5 MHz. The relevant levels for SBC of a single $^{25}Mg^+$ ion are shown in Fig. 4.2. A single frequency-quadrupled fiber laser ($^2P_{3/2}$ laser in the following) provides laser beams for Doppler cooling, coherent control and state detection on the $^{25}Mg^+$ ion as described in Sec. 3.2.1 and Hemmerling et al., 2011. This scheme however requires the precise knowledge of the Rabi frequency of the Raman lasers to be able to predict the correct pulse length to implement a π-pulse on the RSB transition. After each RSB pulse, multiple repump pulses are necessary to bring the population in the $|\uparrow\rangle$ state back to the $|\downarrow\rangle$ state. The ion can decay to the $|\text{aux}\rangle$ state during the repump process, so that additional radio frequency (RF) coupling $|\text{aux}\rangle$ and $|\uparrow\rangle$ is necessary to bring the population in $|\text{aux}\rangle$ back to the $|\downarrow\rangle$ state. The cooling speed is mainly limited by the weak RF coupling used for repumping. We extend the scheme by employing a second fiber laser[1]

[1]Koheras BoostiK^{TM} System Y10/Menlosystem

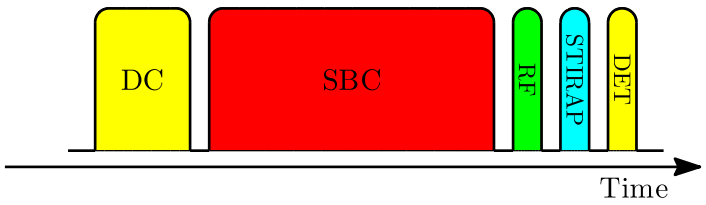

Figure 4.3: **Full experimental sequence.** Full experimental sequence consisting of Doppler cooling, sideband band cooling, RF π-pulse, STIRAP pulse and detection pulse.

system as a repumper to speed up the SBC sequence. This second fiber laser with maximal output power of 1 W at 1121 nm is frequency quadrupled and provides an optical power of 16 mW at 280 nm, which is far more than necessary in the experiment. The experimental sequence (see Fig. 4.3) starts with Doppler cooling on the $|^2\mathrm{S}_{1/2}, F = 3, m_F = 3\rangle \equiv |\downarrow\rangle \leftrightarrow \left|^2\mathrm{P}_{3/2}, F = 4, m_F = 4\right\rangle$ transition for 400 μs followed by the SBC sequence. After Doppler cooling, a $\bar{n}$ of around 16(5) is achieved (Hemmerling, 2011). A pair of Raman lasers provided by the $^2\mathrm{P}_{3/2}$ laser is employed for SBC with an effective Lamb-Dicke parameter of 0.3 (Hemmerling et al., 2011). During the SBC cycle, we first apply a series of 2^{nd} order RSB pulses followed by a series of 1^{st} order RSB pulses. After each SBC pulse a short optical repumping pulse with the Raman σ-laser tuned to resonance by switching on the electro-optical modulator (EOM) and the $^2\mathrm{P}_{1/2}$ laser are applied to clear out the population left in $|^2\mathrm{S}_{1/2}, F = 3, m_F = 2\rangle \equiv |\mathrm{aux}\rangle$ and $|^2\mathrm{S}_{1/2}, F = 2, m_F = 2\rangle \equiv |\uparrow\rangle$. In contrast to the pulsed SBC scheme described in Hemmerling et al., 2011, we apply simultaneously with the Raman SBC pulses the RF coupling the $|\mathrm{aux}\rangle$ and $|\uparrow\rangle$ state and the optical repumper with the $^2\mathrm{P}_{1/2}$ laser tuned to be resonant with the $|\mathrm{aux}\rangle \leftrightarrow \left|^2\mathrm{P}_{1/2}, F = 3, m_F = +3\right\rangle$ transition. The RF and the optical repumper together open up an additional decay channel for the $|\uparrow\rangle$ state with a controllable decay rate. After SBC, the population in the excited motional states is probed by driving a RF π-pulse between $|\uparrow\rangle$ and $|\downarrow\rangle$ followed by a stimulated Raman adiabatic passage (STIRAP) pulse on the 1^{st} BSB (Gebert et al., 2014b). These combined detection pulses are used instead of a simple STIRAP pulse on the RSB because of technical limitations. After the SBC, the population in the motional ground state $\rho_{n=0}$ and the excited motional

states $\rho_{n>0}$ go through the path

$$\rho_{n=0} : |\downarrow, n=0\rangle \xrightarrow[\pi-\text{pulse}]{\text{RF}} |\uparrow, n=0\rangle \xrightarrow[\text{BSB}]{\text{STIRAP}} |\uparrow, n=0\rangle$$
$$\rho_{n>0} : |\downarrow, n>0\rangle \xrightarrow[\pi-\text{pulse}]{\text{RF}} |\uparrow, n>0\rangle \xrightarrow[\text{BSB}]{\text{STIRAP}} |\downarrow, n-1\rangle \ ,$$

respectively.

As an alternative SBC scheme, we keep the RF repumper and the $^2\mathrm{P}_{1/2}$ laser on during the Raman cooling cycle, but tune the $^2\mathrm{P}_{1/2}$ laser to be resonant with the $|\uparrow\rangle \leftrightarrow \left|^2\mathrm{P}_{1/2}, F=3, m_F=+3\right\rangle$ transition. However, this scheme fails especially in the case of long SBC pulses, where off-resonant excitation from the Raman lasers leads to decay into other Zeeman sub-levels of the $F=3$ hyperfine states and therefore induces loss of population from the cooling cycle.

4.2.2 SBC sequence

In the following we describe a parametrized SBC pulse sequence that allows us to optimize the time spent on various parts of the sequence.

The sequence for SBC of a single $^{25}\mathrm{Mg}^+$ ion is illustrated in Fig. 4.4. Depending on the pulse length of the 1st and 2nd order RSB pulses $t_{\mathrm{R1}}/t_{\mathrm{R2}}$, we apply N_{R2} 2nd order and N_{R1} 1st order RSB pulses

$$N_{\mathrm{R2}} = \left\lfloor \frac{\alpha T_{\mathrm{c}}}{t_{\mathrm{R2}}} \right\rfloor \tag{4.6}$$
$$N_{\mathrm{R1}} = \left\lfloor \frac{(1-\alpha) T_{\mathrm{c}}}{t_{\mathrm{R1}}} \right\rfloor \tag{4.7}$$

with the sign $\lfloor x \rfloor = \max\{n \in \mathbb{Z}, n \leq x\}$ denoting the floor function and α as the time scaling factor, which divides the total cooling time[1] T_{c} into parts for the 2nd and 1st order RSB. Short RSB pulses for compensating the remaining time (with pulse length of $\alpha T_{\mathrm{c}} - N_{\mathrm{R2}} t_{\mathrm{R2}}$ and $(1-\alpha)T_{\mathrm{c}} - N_{\mathrm{R1}} t_{\mathrm{R1}}$ respectively) are added at the end of each RSB pulse group. After each RSB pulse a repumping pulse with duration $t_{\mathrm{r}} = 3\,\mu\mathrm{s}$ is applied. In the experiment the actual elapsed time between two SBC pulses equals $t'_{\mathrm{r}} = 5\ \mu\mathrm{s}$ caused by delays from the control electronics. The total duration spent on the SBC cycle is then expressed as

$$T_{\mathrm{total}} = T_{\mathrm{c}} + N_{\mathrm{r}} \cdot t'_{\mathrm{r}}. \tag{4.8}$$

[1] Time spent on driving Raman RSB pulses

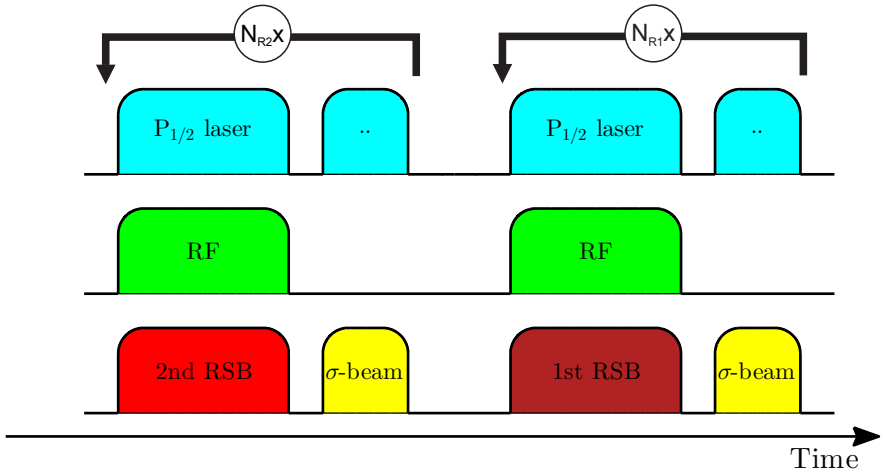

Figure 4.4: **Sequence for SBC.** Sequence for SBC on a single $^{25}Mg^{+}$ at an axial trap frequency of 2.21 MHz.

with

$$N_\mathrm{r} = \left\lceil \frac{\alpha T_\mathrm{c}}{t_\mathrm{R2}} \right\rceil + \left\lceil \frac{(1-\alpha) T_\mathrm{c}}{t_\mathrm{R1}} \right\rceil \tag{4.9}$$

as the total number of repumping pulses and $\lceil x \rceil = \min\{n \in \mathbb{Z}, n \geq x\}$ as the ceiling function.

To optimize SBC with respect to cooling time, we probe the population in the motional ground state with the STIRAP sideband pulse for different SBC times T_c. Assuming a constant cooling rate W during the SBC cycle, the mean occupation of the motional states decays exponentially (Stenholm, 1985) as

$$\bar{n}(t) = \bar{n}_\mathrm{f}(1 - e^{-Wt}) + \bar{n}_\mathrm{i} e^{-Wt} \tag{4.10}$$

where $\bar{n}_\mathrm{i}$ and $\bar{n}_\mathrm{f}$ is the initial and final mean occupation and W as the cooling rate. Assuming a thermal distribution with mean occupation of $\bar{n}(t)$ after SBC for a duration t, the population in the motional ground state can be expressed as

$$\begin{aligned} P_0(t) &= \frac{1}{1 + \bar{n}_\mathrm{f}(1 - e^{-Wt}) + \bar{n}_\mathrm{i} e^{-Wt}} \\ &= \frac{1}{1 + \bar{n}_\mathrm{f} + (\bar{n}_\mathrm{i} - \bar{n}_\mathrm{f}) e^{-t/T_0}} \,. \end{aligned} \tag{4.11}$$

A complete set of experimental data[1] is fitted with this model function to determine the time constant $T_0 = 1/W$ for SBC as in Fig. 4.5d, where $\bar{n}_\mathrm{i}$ and $\bar{n}_\mathrm{f}$ are common parameters. We investigate the dependence of the cooling time constant T_0 as a function of different experimental parameters in the following section.

4.2.3 Optimization of experimental parameters

Using the procedure described in Sec. 4.2.2, we optimize the experimental parameters such as pulse length of the RSB pulses, the time scaling factor α and the optical power of the $^2\mathrm{P}_{1/2}$ laser with and without this laser and RF applied during the SBC pulses. A numerical simulation based on the optical Bloch equation is provided in Appendix C.

Pulse length of RSB pulses Here we vary the pulse length of the 1^{st} and 2^{nd} order RSB pulses. For each parameter set, a scan of the SBC time T_c is performed, which allows us to derive the corresponding cooling time constant. In Fig. 4.5a and 4.5b, the experimentally determined cooling time constant T_0 is plotted against the pulse lengths used in the corresponding sequence. The optimal pulse length for the RSB pulses lies around $10\,\mu$s, which gives the smallest T_0. The optimal pulse length corresponds to the mean π-time of the dominating RSB pulse for each trap level n weighted by the thermal occupation of the initial states. The fact that a constnat *pi*-time is sufficient for efficient cooling is a consequence of the relatively small variation of the Rabi frequencies of the dominating RSB pulse in the relevant range of motional levels as can be seen from Fig. 2.1.

For short pulses SBC is limited by the reduced transfer efficiency due to the mismatch of the pulse length to the π-time. More precisely, the mean excitation rate decreases for short SBC pulses as illustrated in Fig. 4.5. Additionally the acousto-optical modulators (AOMs) become less efficient because of their limited switching speed. This is considered in the numerical simulation (Appendix C) by reducing the length of every individual pulse by $1\,\mu$s. As the duration of each single pulses gets longer, the additional decay channel induced by the RF and the

[1] One set of experimental data consist of a certain number of scans with only one parameter changed in different scans, e.g. pulse length of RSB pulses, time scaling factor α, etc.

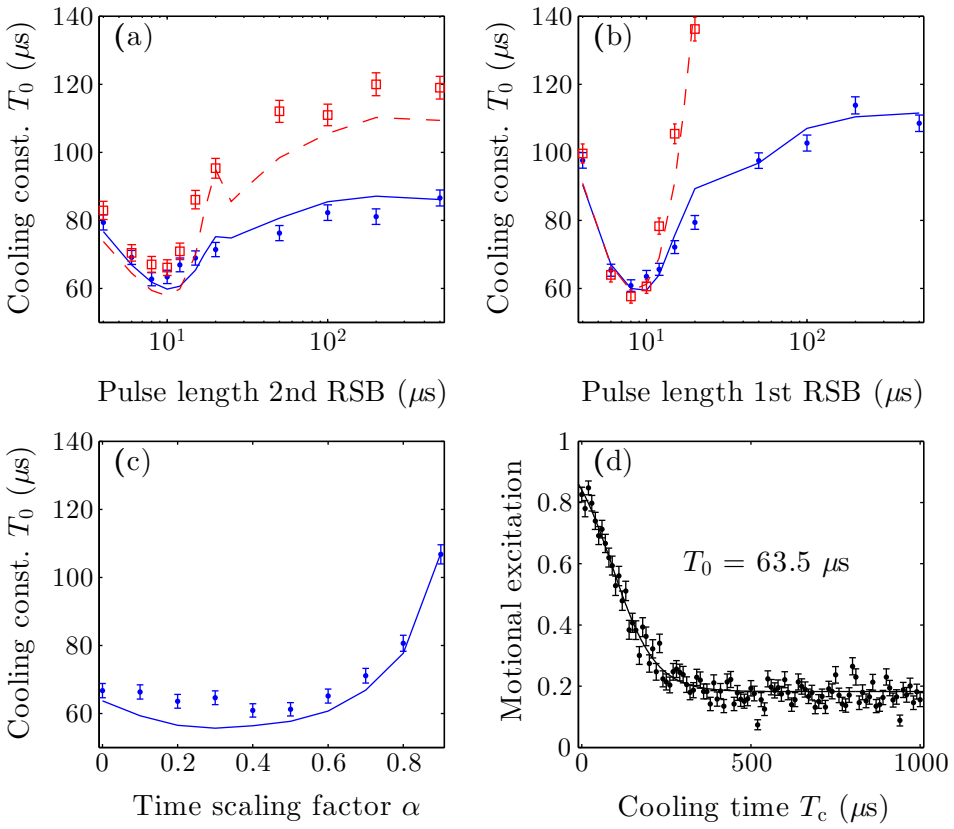

Figure 4.5: **Dependence of the cooling time constants on experimental parameters.** (**a**): The cooling time constants are examined as a function of the pulse lengths of the 2[nd] order RSB pulses with $t_{R1} = 8\,\mu$s and $\alpha = 0.5$. (**b**): The cooling time constant as a function of the pulse length of the 1[st] order RSB with $t_{R2} = 10\,\mu$s and $\alpha = 0.5$. (**c**) The cooling time constant as a function of the time scaling factor with $t_{R2} = 10\,\mu$s and $t_{R1} = 10\,\mu$s. *blue point/red square*: Experimentally determined cooling constants with the $^2P_{1/2}$ laser and RF repumper on/off during the Raman cooling period. The $^2P_{1/2}$ and RF repumper together induces a decay rate of $42\,\text{ms}^{-1}$ from the $|\uparrow\rangle$ state to the $|\downarrow\rangle$ state. *blue solid line/red dashed line*: Simulation curves with the $^2P_{1/2}$ laser and RF repumper on/off during RSB pulses. (**d**): Residual motional excitation as a function of the total cooling time T_c. The line is the fit to tht experimental data, which gives the cooling constant T_0.

optical repumper allows scattering of more than one photon within one pulse so that the scheme becomes quasi-continuous SBC.

Time scaling factor. The time scaling factor α in Eq. (4.9) scales the SBC time T_c into the time spent on the 2^{nd} RSB $T_{R1} = \alpha T_c$ and on the 1^{st} RSB $T_{R2} = (1-\alpha)T_c$. Because of the dependence of the Rabi frequency on the motional quantum number as in Fig. 2.1, the 2^{nd} RSB pulses are more efficient to cool the population in the high trap levels at the starting stage of the SBC cycle. For the low trap levels, the 1^{st} RSB pulses become more efficient, so that an α that is too large also reduces the SBC efficiency (Fig. 4.5c).

4.2.4 Effect of repumping during Raman SBC

As mentioned in the previous section, repumping via the RF and the $^2P_{1/2}$ laser during the SBC cycle enables SBC even for long Raman pulse lengths. When these repumpers are switched off during the Raman SBC cycle, the current scheme turns back into the pulsed SBC scheme. In this case, the cooling constant depends strongly on the pulse length of the RSB pulses as indicated by the red points and dashed lines in Fig. 4.5a and 4.5b, since the pulse lengths need to be optimized to achieve an optimum cooling rate. Simultaneous application of the RF and optical repumper with the Raman SBC pulses opens up a new decay channel for the population in the $|\uparrow\rangle$ state with adjustable decay rate. In the experiment, this decay rate is adjusted to about $42\,\mathrm{ms}^{-1}$ or a decay constant of about $24\,\mu\mathrm{s}$ to achieve the highest cooling rate. The effect of the repumpers is negligible and the scheme becomes equivalent to pulsed SBC. For the long RSB pulses, the ion in the $|\uparrow\rangle$ state can decay through the new channel back to the $|\downarrow\rangle$ state. The ion can cycle between the $|\downarrow\rangle$ and the $|\uparrow\rangle$ state and therefore more than one phonon can be removed within a single SBC pulse. The scheme thus becomes equivalent to continuous SBC. This makes the scheme insensitive to the exact pulse length of the RSB pulses and thus provides high stability against intensity/pointing fluctuation of the Raman lasers.

4.2.5 Cooling results

The final $\bar{n}$ after SBC is extracted from the red and blue sideband excitation. Assuming that the ion stays in a thermal distribution after SBC, the ratio of excitations on 1st red and blue sideband fulfills the following relation (Turchette et al., 2000b)

$$Q := \frac{\rho^{\mathrm{rsb}}(t)}{\rho^{\mathrm{bsb}}(t)} = \frac{\bar{n}}{1+\bar{n}} \tag{4.12}$$

with $\rho^{\mathrm{rsb}}(t)$ and $\rho^{\mathrm{bsb}}(t)$ as the excitation on the 1st red and blue sideband at time t. With the SBC sequence described in Sec. 4.2.2, we achieve

$$\bar{n} = \frac{\rho^{\mathrm{rsb}}}{\rho^{\mathrm{bsb}} - \rho^{\mathrm{rsb}}} \approx 0.01(2) \tag{4.13}$$

as shown in Fig. 4.6a-c after a cooling time of $T_{\mathrm{c}} = 500\,\mu\mathrm{s}$, where we subtracted the background from the off-resonant excitation of the Raman lasers to derive the final $\bar{n}$. The final $\bar{n}$ specified here is limited by the detection uncertainty. Although the calculated $\bar{n}$ reaches a level on the order of 0.01, the uncertainty of the detection error, especially on the RSB, leads to an error on the same order of magnitude for the final $\bar{n}$. In our case, a quantum-projection noise limited detection error (Itano et al., 1993) of around 0.02 is expected, which propagates to an uncertainty of the final $\bar{n}$ on the order of 0.02. Fig. 4.6d-e show stimulated Raman Rabi oscillations on the carrier, RSB and BSB transitions. The decay of the Rabi oscillations is dominated by off-resonant coupling of the two Raman lasers with the $^2\mathrm{P}_{3/2}$ states. This off-resonant excitation rate for an ion initialized in the $|\downarrow\rangle$ ($|\uparrow\rangle$) state has been determined by measuring the depumping rate to the $|\uparrow\rangle$ ($|\downarrow\rangle$) state induced by Raman lasers detuned between the carrier and 1st BSB. These measurements have verified qualitatively that the off-resonant excitations from the $|\downarrow\rangle$ and $|\uparrow\rangle$ states set a boundary for the highest achievable contrast of the Rabi oscillation (*dashed orange* and *dashed black lines* in Fig. 4.6). A larger detuning of the lasers from the $^2\mathrm{P}_{3/2}$ state will improve the contrast of the Raman Rabi oscillations.

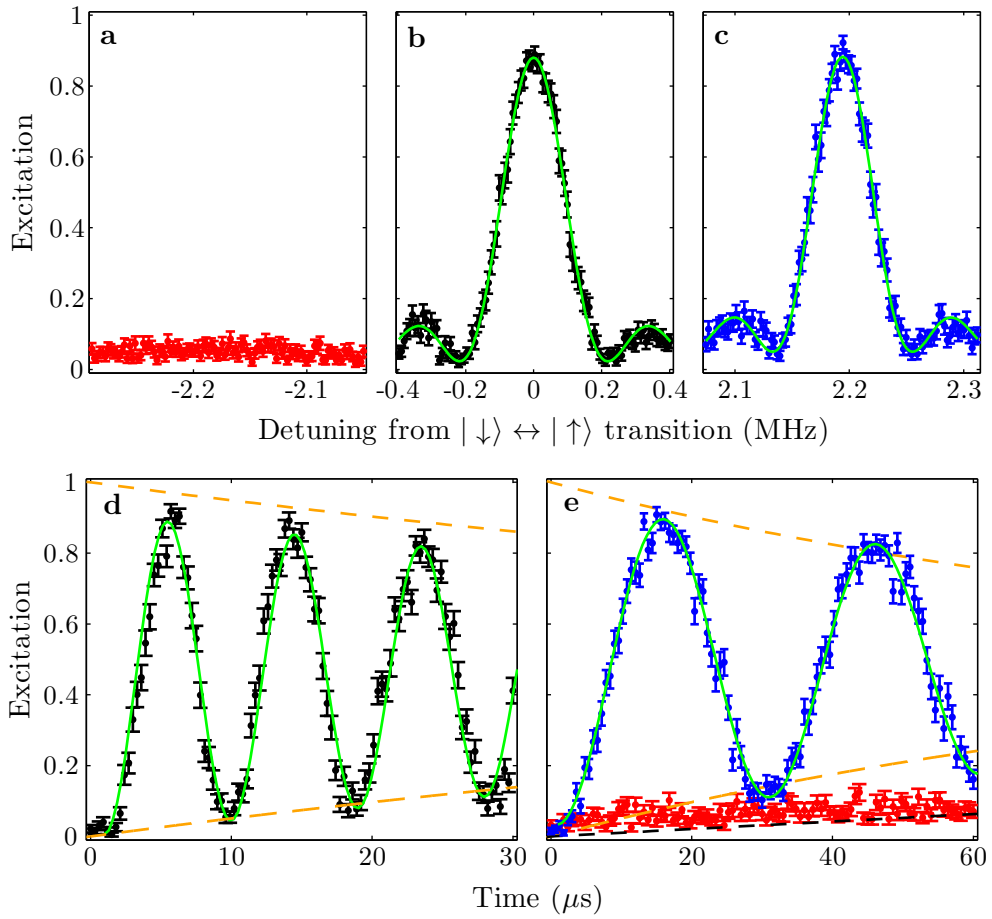

Figure 4.6: **Sideband cooling of a single magnesium ion.** (**a-c**) Frequency scans of Raman transitions over 1st RSB (*red*), carrier (*black*) and 1st BSB (*blue*) transitions after SBC of a single $^{25}Mg^{+}$. (**d**) Raman Rabi flop on carrier (**e**) Raman Rabi flops on blue and red sideband after SBC performed on a single $^{25}Mg^{+}$ ion. The *dashed orange line* indicates the boundary set by off-resonant excitation from the dark state and the *dashed black line* indicates the boundary set by off-resonant excitation from the bright state.

4.3 SBC of a two-ion crystal

The SBC scheme is also demonstrated for a two-ion crystal of $^{25}Mg^{+}$ and $^{24}MgH^{+}$. Here we use the same laser configuration as in Sec. 4.2.1, but with a modified pulse sequence. In contrast to cooling a single $^{25}Mg^{+}$, we need to cool the in-

phase (ip) and the out-of-phase (op) modes along the axial direction with trap frequencies $\omega_{\mathrm{T}}^{\mathrm{ip}} = 2\pi \times 2.21\,\mathrm{MHz}$ and $\omega_{\mathrm{T}}^{\mathrm{op}} = 2\pi \times 3.85\,\mathrm{MHz}$. The two Raman lasers give effective Lamb-Dicke parameters of $\eta_{\mathrm{ip}} = 0.21$ and $\eta_{\mathrm{op}} = 0.16$ on the $^{25}\mathrm{Mg}^{+}$ ion. With these Lamb-Dicke parameters, the effective Rabi frequencies show no zero-crossings over the range of trap levels with significant population after Doppler cooling and therefore no higher order RSB pulses are necessary. An interleaved pulse sequence for SBC employing only 1st order RSB on the ip and the op mode is used as shown in Fig. 4.7. Depending on the time scaling factor α, which in this case scales the total SBC time T_{c} into time spent for RSB on the ip mode $(1-\alpha)T_{\mathrm{c}}$ and time for RSB on the op mode αT_{c}, we apply

$$N_{\mathrm{ip}} = \left\lfloor \frac{(1-\alpha)T_{\mathrm{c}}}{t_{\mathrm{ip}}} \right\rfloor \tag{4.14}$$

$$N_{\mathrm{op}} = \left\lfloor \frac{\alpha T_{\mathrm{c}}}{t_{\mathrm{op}}} \right\rfloor \tag{4.15}$$

full pulses on the ip and the op mode, respectively. Here t_{ip}, t_{op} are the pulse lengths of the RSB pulses on the ip and the op mode. In the case $N_{\mathrm{ip}} > N_{\mathrm{op}}$ ($N_{\mathrm{ip}} < N_{\mathrm{op}}$) we start the SBC cycle with $N_{\mathrm{res}} = |N_{\mathrm{ip}} - N_{\mathrm{op}}|$ pulses on the ip (op) mode, followed by N_{op} (N_{ip}) pulses on the ip and the op mode in an interleaved fashion. At the end of the SBC sequence, short pulses are applied to compensate the residual time. After every single SBC pulse, a repumping pulse with the Raman σ-laser and $^{2}\mathrm{P}_{1/2}$ laser is applied to clear out the $|\uparrow\rangle$ and $|\mathrm{aux}\rangle$ states. Similar optimization processes as for a single $^{25}\mathrm{Mg}^{+}$ are performed to reduce the total duration of the SBC cycle.

Pulse length of 1st RSB on ip/op mode. The pulse length of the RSB pulse on the ip (op) mode is optimized by setting the frequency of the STIRAP pulse to be resonant with the 1st BSB of the ip (op) mode. This way we separate with the STIRAP pulse the population in the motional ground state and the higher motional states $n_{\mathrm{ip}} > 0$ ($n_{\mathrm{op}} > 0$). The best cooling performance with respect to cooling speed is observed with a pulse length of 15 μs (20 μs) for the RSB on the ip (op) mode as shown in Fig. 4.8a. With a π-time of $T_{\pi}^{(\mathrm{ip})} \approx 21\,\mu\mathrm{s}$ and $T_{\pi}^{(\mathrm{op})} \approx 26.5\,\mu\mathrm{s}$ for the 1st RSB on the $n = 1$ state, the Rabi frequency

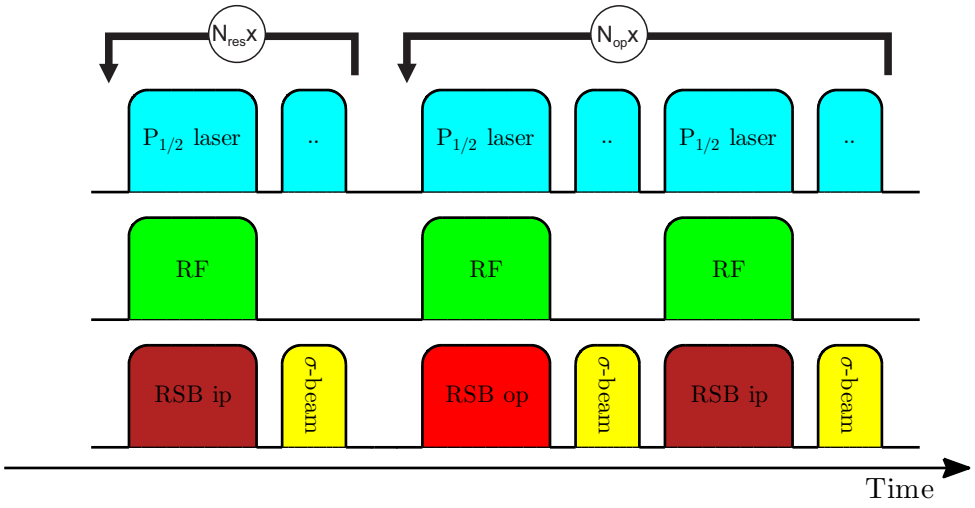

Figure 4.7: **Sequence for SBC on a two-ion crystal.** Sequence for SBC on a crystal of $^{25}Mg^+$ and $^{24}MgH^+$ at an axial trap frequency of $\omega_T^{ip} = 2\pi \times 2.21\,\mathrm{MHz}$ and $\omega_T^{op} = 2\pi \times 3.85\,\mathrm{MHz}$ for the in-phase and out-of-phase mode, respectively.

of the dominating RSB weighted by the thermal occupation of initial motional distribution results in a mean π-time of 14 μs and 25 μs for the ip and op mode.

Time scaling factor. The time scaling factor in SBC sequence for cooling a two-ion crystal divides the total cooling time T_c into the time spent on cooling the ip mode and the op mode. Setting the frequency of the STIRAP pulse to be resonant with the 1st BSB of the ip (op) mode, we determine the cooling constant for SBC as a function of α (Fig. 4.8b). Although an α that is too small (large) accelerates the cooling of the ip (op) mode, it demands a longer time for cooling the opposite mode. The optimal value for the time scaling factor $\alpha \approx 0.5$ is determined by the point where SBC of both the ip and op mode are achieved with the shortest total duration of the SBC cycle.

Results. The final $\bar{n}$ is determined from the red and blue sideband excitations as described in Sec. 4.2.5. After SBC on the ip and the op mode along the axial direction, we reach a $\bar{n}$ of 0.06(3) for the ip mode and 0.03(3) for the op mode.

In conclusion, the SBC scheme developed here requires a shorter total duration compared to an extension of the previously used scheme published in Hemmerling

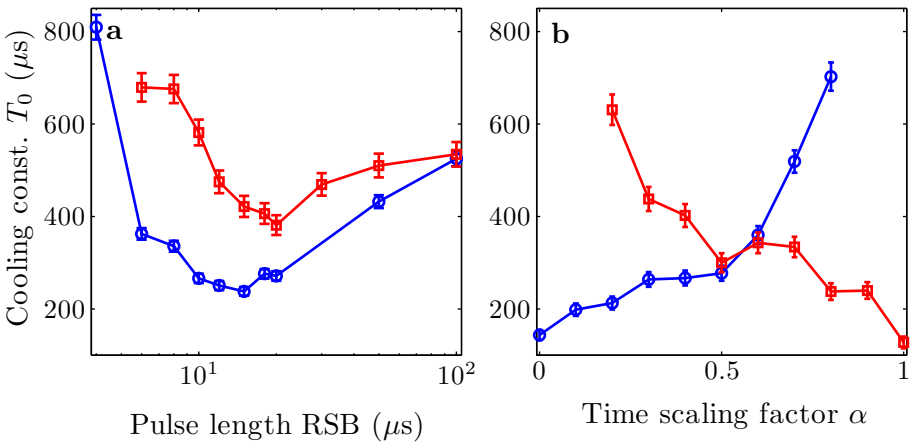

Figure 4.8: **Dependence of the cooling time constant on experimental parameters for SBC on a two-ion crystal.** (**a**) The cooling time constant as a function of the optimal pulse length of the Raman RSB pulses on ip (*blue circles*) and op (*red squares*) mode. (**b**) The cooling constant as a function of the optimal time scaling factor α.

et al., 2011 to two modes and a high stability against fluctuations of laser intensity and thus simplifies the optimization procedure in the experiment.

4.4 SBC at low trap frequency

In the last sections we demonstrated SBC at a single-$^{25}Mg^+$ axial trap frequency of 2.21 MHz. A lower axial trap frequency leads to a larger Lamb-Dicke parameter, so that a stronger coupling between the internal and external states can be achieved (Wan et al., 2014). At the same time the influence of motional heating from electric field noise (Deslauriers et al., 2006) and off-resonant excitation on the carrier and BSB transitions become more significant, and therefore efficient SBC can be challenging. We extend our SBC scheme to lower trap frequencies and develop a guideline for the more general case.

At a trap frequency of 1 MHz and a temperature of 1 mK achieved with Doppler cooling on a $^{25}Mg^+$ ion, the accumulated population in trap levels $n > 120$ amounts to less than 0.3% (Fig. 4.9a). At a trap frequency of 1 MHz, the Lamb-Dicke parameter is 0.45. The effective Rabi frequency for RSB transitions

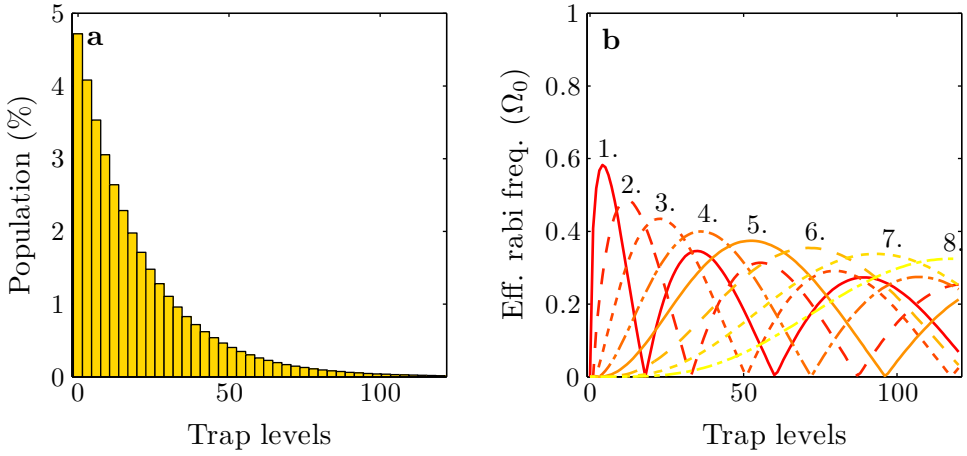

Figure 4.9: **Effective cooling rate at low trap frequency.** (**a**) Distribution over the motional levels at the trap frequency of $\omega_T = 1\,\mathrm{MHz}$ and a temperature of $T = 1\,\mathrm{mK}$ corresponding to the Doppler cooling limit of $^{25}Mg^+$ ion. Less than 0.3% of the population are in the trap levels $n > 0$. (**b**) At this trap frequency, the Lamb-Dicke parameter is $\eta = 0.45$. Effective Rabi frequencies at $\eta = 0.45$ for different RSB orders are shown as a function of the trap levels. For ions located in higher trap levels, RSB pulses of higher orders $\beta(n)$ are more efficient for cooling.

depends on the trap levels and shows several zero crossings over the range of trap levels with significant population. Employing pulses on the 2nd order sideband as in the scheme for a single $^{25}Mg^+$ is no longer sufficient. Instead, we employ a scheme which uses as many higher order sidebands as necessary. Although the relative Rabi frequencies for the higher order sidebands are lower than for the 1st or 2nd order RSB for the population in low trap levels, they become stronger than the 1st or 2nd order RSB for the population in high trap levels (Fig. 4.9b). Moreover, pulses on the higher order sidebands can be more efficient with respect to the effective cooling rate as indicated in Eq. (4.5), since each absorbed photon removes $\beta(n)$ phonons from the mode (Fig. 4.9b). For simplicity, we split the total cooling time T_c equally between all the sideband orders and apply to all of them the same pulse length as shown in Fig. 4.10. Simultaneous to each RSB pulse, the $^2P_{1/2}$ laser and the RF are switched on to introduce the weak decay channel. After each RSB pulse, a repumping pulse of the Raman σ-laser and the $^2P_{1/2}$ laser is applied.

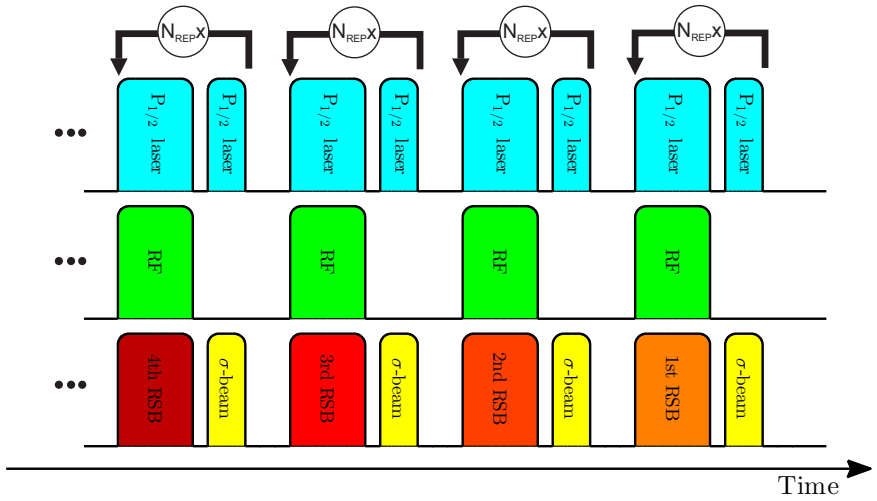

Figure 4.10: **Sequence for SBC at low trap frequency.** Sequence for SBC on a single $^{25}Mg^{+}$ at low trap frequency. Higher order sidebands are applied for efficient cooling of population in high trap levels. For simplicity, the total SBC time is split equally between all applied sideband orders and the pulse lengths of different sideband orders are chosen to be the same.

The optimal number of applied sideband orders is determined experimentally, where we measure the cooling constant as a function of the applied sideband orders (Fig. 4.11a). In the optimal sequence, we need to apply sideband pulses up to the 8th order, which confirms the prediction of Fig. 4.9b.

More generally, with known Lamb-Dicke parameter and motional distribution after Doppler cooling, a corresponding SBC strategy can be used to achieve the most efficient cooling as illustrated in Fig. 4.11b. For a selected trap level and a known Lamb-Dicke parameter, the sideband order with highest cooling rate is plotted. With a Lamb-Dicke parameter of 0.45 and significant population in trap levels up to $n = 120$, RSB pulses up to the eighth order are necessary, in agreement with the experimental findings.

4.5 Discussion

The SBC scheme developed here is not only applicable to the system with $^{25}Mg^{+}$ as logic ion, but also other hyperfine qubits such as $^{9}Be^{+}$. A variation of the

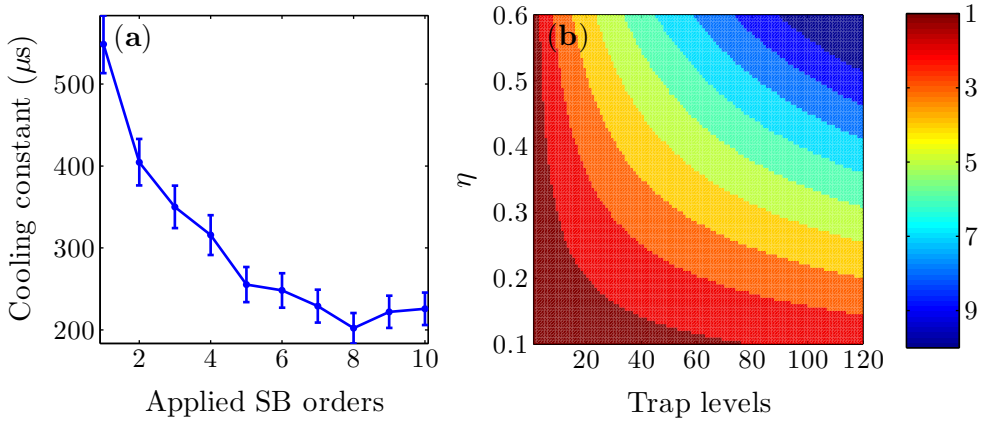

Figure 4.11: **Determination of the maximum sideband order.** (**a**) The cooling constant as a function of applied sideband orders. The optimal number for the sideband orders determined experimentally confirms the prediction shown in Fig. 4.9b. (**b**) RSB orders with highest effective cooling rate as a function of the trap level and the Lamb-Dicke parameter. With known Lamb-Dicke parameter and motional distribution a corresponding SBC sequence can be adopted.

scheme can be applied to other systems like $^{40}Ca^{+}$, $^{24}Mg^{+}$ in high magnetic field or optically trapped neutral atoms. The developed scheme is robust against variations of the Rabi frequency and therefore provides high stability against intensity and pointing fluctuations of the laser, which reduces significantly the optimization required for optimum cooling. In case of large Lamb-Dicke parameters or high initial temperature, the discussed SBC scheme with higher orders of sidebands is applicable. This is e.g. the case, when a high coupling strength between the internal and external degrees of freedom is desirable such as in photon recoil spectroscopy as described in Chapter 6 or only a limited trap frequencies are achievable as for optically trapped neutral atoms.

Chapter 5

Mass spectroscopy in the ion trap

In this chapter, we introduce a modulation technique to control the motional degrees of freedom of the ions and discuss its application to mass spectroscopy. In Sec. 5.1, we summarize different techniques for the manipulation of the ions' motion and their relation to mass spectroscopy. In Sec. 5.2, we introduce the modulation technique, which implements a displacement operator for the motion of the ions. The response of a single ion and an ion crystal to the modulation pulse is discussed. The effect of off-resonant modulation pulses is discussed in Sec. 5.3. With the basic principle and features of motional excitation described with single- and two-ion crystals initially cooled to the ground state in the previous sections, we apply the modulation technique to precise measurements of the axial trap frequencies starting either with Doppler or sideband cooled ions in Sec. 5.4 and 5.5, respectively. In the last section, we discuss possible applications of the techniques.

5.1 Introduction

Resolved sideband cooling as described in the previous chapter provides a method to prepare a single ion or an ion crystal in a fully characterized quantum mechanical state corresponding to the ground state of the system $|n = 0\rangle$. Starting from this state, one can prepare different kinds of classical and non-classical states of motion of the ions. Higher Fock states can be created by applying a sequence of π-pulses on blue sideband (BSB), red sideband (RSB) and carrier transitions

(Meekhof et al., 1996a). The fidelity of the process is limited by the accumulated transfer efficiency of all single pulses. A coherent state of motion can be created using an oscillating electric field or an oscillating optical dipole force (Meekhof et al., 1996a). We will discuss the former method in the following sections in some detail and the latter method in Sec. 7.4.3. A Schrödinger cat state has been created using a state-dependent dipole force (Monroe et al., 1996), where two motional wave packets in an internal-state superposition are displaced from the center of phase space subsequently by an oscillating optical lattice. By changing the phases of the two displacement pulses, the separation of the two wave packets can be controlled and the coherence of the two wave packets is verified. A vacuum squeezed state of motion has been demonstrated by applying an oscillating optical dipole force modulated at twice the trap frequency (Meekhof et al., 1996a). Since the generation of different motional states requires modulations at the trap frequency or twice the trap frequency, we can use these motional states as properties to infer the trap frequency.

The trap frequency itself depends on the parameters of the hardware generating the trap, like the endcap voltage, the RF power for the radial trap, the trap drive frequency and the trap geometry (Berkeland et al., 1998), but also the mass of the particles in the trap. For a two-ion crystal with mass ratio $\mu = m_\mathrm{S}/m_\mathrm{L} \geq 1$, the axial trap frequencies of the in-phase (ip) and out-of-phase (op) mode equal (Morigi et al., 2001; Wübbena et al., 2012)

$$\omega_\mathrm{T}^\gamma = \omega_\mathrm{T}^\mathrm{L}\sqrt{1+\frac{1}{\mu}\mp\sqrt{1+\frac{1}{\mu^2}-\frac{1}{\mu}}}\,, \quad \gamma = \mathrm{ip},\,\mathrm{op}\,, \tag{5.1}$$

where $\omega_\mathrm{T}^\mathrm{L}$ is the axial trap frequency for a single ion with mass m_L in the trap. The mass ratio of the two ions can be extracted from the ratio of the trap frequencies $\omega_\mathrm{T}^\gamma/\omega_\mathrm{T}^\mathrm{L}$. With the knowledge of the trap frequencies for the two different modes, no reference frequency is necessary to determine the mass ratio of the two ions. In the following sections, we describe the techniques we developed to determine the axial trap frequencies with a statistical uncertainty on the order of a few Hertz, ultimately limited by the instability.

5.2 Coherent state with uniform classical driving field

Consider a single ion initialized in the motional ground state with sideband cooling (SBC) as described in Chapter 4. A coherent state of the ion's motion can be generated with a spatially uniform classical drive field (Heinzen et al., 1990; Meekhof et al., 1996a). The uniform electric field can be produced by applying a modulation at frequency ω_{M} on the two endcaps, which are 180° out of phase with each other. This leads to a periodically modulated electric force on the ion $\boldsymbol{F} = qE\hat{\boldsymbol{z}}$, or equivalently, an additional potential $V = -qE_0 z\cos(\omega_{\mathrm{M}}t - \phi)$ along the axial direction, where q is the charge of the ion, E_0 and ϕ are the amplitude and phase of the modulation field E. The interaction Hamiltonian in the interaction picture of motion reads

$$\begin{aligned}\hat{H}_{\mathrm{int}} &= -qE_0 z_0(\hat{a}e^{-i\omega_{\mathrm{T}}t} + \hat{a}^\dagger e^{i\omega_{\mathrm{T}}t})\cos(\omega_{\mathrm{M}}t - \phi) \\ &\approx -qE_0 z_0\left[\hat{a}e^{i(\delta\omega t - \phi)} + \hat{a}^\dagger e^{-i(\delta\omega t - \phi)}\right],\end{aligned} \tag{5.2}$$

where in the second step the rotating wave approximation (RWA) is applied and $\delta\omega = \omega_{\mathrm{M}} - \omega_{\mathrm{T}}$ is the detuning of the modulation frequency from the axial trap frequency. For the resonant case $\delta\omega = 0$ the Hamiltonian becomes time-independent and the system evolves according to the propagation operator

$$\begin{aligned}\hat{U}(t) &= \exp\left[-\frac{i}{\hbar}\hat{H}_{\mathrm{int}}t\right] \\ &= \exp\left[\frac{i}{\hbar}qE_0 z_0\left(\hat{a}e^{-i\phi} + \hat{a}^\dagger e^{i\phi}\right)t\right] \\ &= \hat{D}(\Omega_{\mathrm{d}}t)\end{aligned} \tag{5.3}$$

where

$$\hat{D}(\alpha) = \exp\left(\alpha\hat{a}^\dagger - \alpha^*\hat{a}\right) \tag{5.4}$$

is the displacement operator (Glauber, 1963) and

$$\Omega_{\mathrm{d}} = i/\hbar \cdot qE_0 z_0 e^{i\phi} \tag{5.5}$$

is the displacement strength. After an excitation time t, the ion will be displaced to a coherent state

$$|\alpha\rangle = \hat{D}(\Omega_{\mathrm{d}}t)\,|0\rangle = |\Omega_{\mathrm{d}}t\rangle\,. \tag{5.6}$$

5.2.1 Coherent drive on a single Magnesium ion

Following Meekhof et al. (1996a), we verify that the generated state is indeed a coherent state by driving Rabi oscillations between the two electronic states of the ion. For this purpose, we load a single $^{25}Mg^{+}$ ion in the trap and cool the axial mode to the ground state with Doppler cooling and pulsed SBC as described in (Hemmerling et al., 2011). In this way, we initialize the ion to the

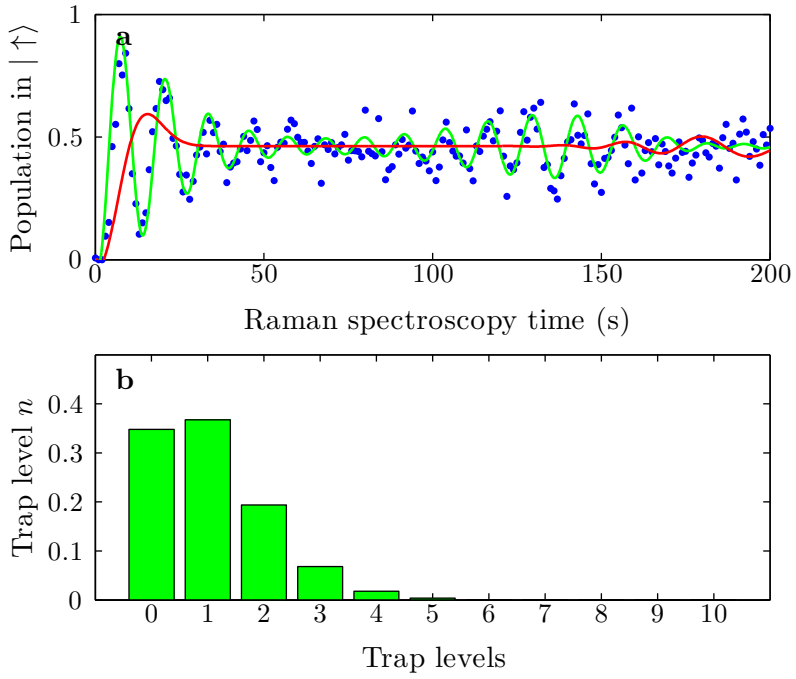

Figure 5.1: **Rabi oscillation of a coherent state.** (**a**) Rabi oscillation between the $|\uparrow\rangle$ and $|\downarrow\rangle$ states of the $^{25}Mg^{+}$ ion driven by the Raman lasers. The ion is prepared in the motional ground state using pulsed SBC. A single modulation pulse displaces the ion to a coherent state. The motional distribution after the modulation pulse is probed with Raman spectroscopy. A displacement of $\alpha = 1.03(3)$ is derived from the fit (*green line*) to the experimental data. For a coherent state with $|\alpha = 3\rangle$, the Rabi oscillation (*red line*) decays so fast, that the fitting procedure can not be applied to derive the displacement α of the corresponding state. (**b**) The motional distribution for the coherent state $|\alpha = 1.03\rangle$ in the basis of Fock states.

state $|\downarrow, n=0\rangle$. An electric modulation at a frequency around the axial trap frequency $\omega_{\mathrm{M}} \approx \omega_{\mathrm{T}}$ is applied additionally to the 2000 V on the two endcaps for a duration of $t = 5\,\mu$s and at a power level of $-25\,$dBm[1]. The motional distribution of the ion after the modulation is probed with the Raman lasers. Fig. 5.1a shows the Rabi oscillation on the carrier transition between the $|\uparrow\rangle$ and $|\downarrow\rangle$ states of the $^{25}Mg^{+}$ ion after applying the displacement. We observe collapse and revival, which is characteristic for a coherent state. The displacement of the ion is determined to be $|\alpha| = 1.03(3)$ with the corresponding distribution

$$\mathcal{P}_{\alpha}(n) = \frac{|\alpha|^{2n} e^{-|\alpha|^2}}{n!} \tag{5.7}$$

shown in Fig. 5.1b. The parameter $|\alpha|$ is extracted from a fit of the experimental data to the model function (Meekhof et al., 1996a; Meekhof et al., 1996b)

$$P_{\uparrow} = \frac{1}{2}\left[1 - \sum_{n=0} \mathcal{P}_{\alpha}(n) \cos\left(\Omega_{n,n}\tau\right) e^{-\gamma_n \tau}\right] \tag{5.8}$$

with only α as the fit parameter and τ as the probe time. The effective Rabi frequency $\Omega_{0,0}$ and the decoherence rate γ_0 for the ground state are derived from the Rabi oscillation of the Fock state $|n=0\rangle$ in an independent measurement. For higher trap levels, we calculate the effective Rabi frequencies according to Eq. (2.15). The decoherence rates γ_n describing the decay of the Rabi oscillations are set to be the same for all the trap levels, since the decoherence is, in our case, mainly caused by the off-resonant excitation of the Raman lasers as described in Sec. 4.2.5.

5.2.2 Calibration of modulation strength

The procedure described in the last section can be used to calibrate the amplitude of coherent states with small $|\alpha|$ (Turchette et al., 2000a). In case of strong modulation, where the ion is displaced to a coherent state with large $|\alpha|$, the Rabi

[1] The necessary power level to generate a certain coherent state depends on the electronic circuits before the trap and the trap geometry. The absolute power level is therefore specific for our trap, but the scaling between the applied power P, the peak modulation voltage V_0 on the endcap and the amplitude E_0 of the oscillating electric field is fixed, namely $\sqrt{P} \propto V_0 \propto E_0$.

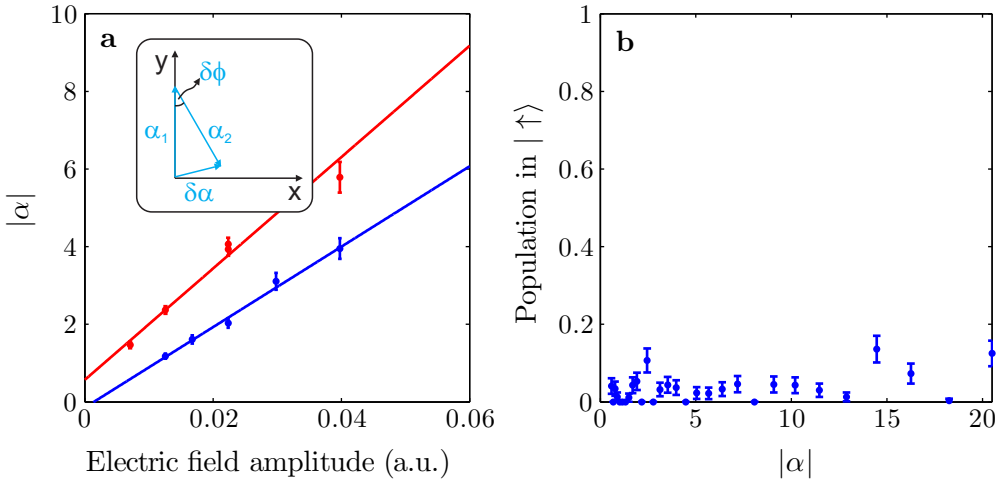

Figure 5.2: **Calibration of electric drive.** (**a**) Calibration of coherent drive for a single $^{25}Mg^+$ (*blue*) and a two-ion crystal of $^{25}Mg^+$ and $^{40}Ca^+$ (*red*). The amplitude of a single displacement $|\alpha| = |\alpha_1| = |\alpha_2|$ is calibrated using two modulation pulses with durations of $5\,\mu$s each, where the first pulse displaces the ion/ions out of the ground state by $|\alpha_1|$, while the second pulse with displacement amplitude $|\alpha_2|$ moves the ion/ions close to the origin of phase space. The amplitude of a single displacement is determined from the residual displacement and the phase difference between the two pulses. The amplitude of the modulation depends as expected on the amplitude of the oscillating electric field. (**b**) Displacement with two pulses out of phase demonstrated on a single $^{25}Mg^+$ ion. After two modulation pulses with exactly the opposite phase, the ion initialized in the motional ground state is displaced out of and afterwards back to the origin of phase space. A Raman RSB pulse after the modulation can not transfer the population from $|\downarrow\rangle$ to $|\uparrow\rangle$ state.

oscillation decays so fast that one can not extract enough information about the motional states. As shown in Fig. 5.1a, the Rabi oscillation of a coherent state with $|\alpha| = 3$ is damped completely after one oscillation period. In order to calibrate the amplitude of coherent states with large amplitudes, we apply two subsequent modulation pulses on the two endcaps with the same amplitude and duration, but different phases. The effect of the two modulation pulses is additive

up to a phase factor (Leibfried et al., 2003a; Gerry et al., 2004)

$$\begin{aligned} &\hat{D}(\alpha_2)\hat{D}(\alpha_1)\,|0\rangle \\ &= e^{i\,\mathrm{Im}(\alpha_2\alpha_1^*)}\hat{D}(\alpha_2+\alpha_1)\,|0\rangle \\ &= e^{i\,\mathrm{Im}(\alpha_2\alpha_1^*)}\,|\alpha_2+\alpha_1\rangle\,, \end{aligned} \tag{5.9}$$

and the ion is displaced to the coherent state $|\alpha_2+\alpha_1\rangle$ after the two pulses. If the two modulation pulses have exactly the opposite phase $\alpha_2 = -\alpha_1$, the ion is displaced back to the origin and a Raman RSB pulse can not cause any population transfer as depicted in Fig. 5.2b. If their phase difference $\phi_2 - \phi_1$ is slightly away from π, a residual displacement $|\delta\alpha| = |\alpha_2 + \alpha_1|$ is present. We adjust the phase difference[1] $\delta\phi := \phi_2 - \phi_1 - \pi$ of the two pulses in such a way, that the amplitude of the residual displacement $|\delta\alpha|$ equals approximately 1 and extract the residual displacement $\delta\alpha$ from the Rabi oscillation. The absolute amplitude $|\alpha| = |\alpha_1| = |\alpha_2|$ of the two displacements is derived from the residual displacement $\delta\alpha$ and the phase difference $\delta\phi$ of the two modulation pulses according to

$$|\alpha| = \frac{|\delta\alpha|/2}{\sin\left(\delta\phi/2\right)} \tag{5.10}$$

as illustrated in the inset of Fig. 5.2a. We calibrate the displacement α of a single pulse as a function of the amplitude of the modulating electric field, which shows a linear dependence as predicted in Eq. (5.5) with a slope proportional to

$$k \propto \left| q \cdot \frac{z_0 t}{\hbar} \right| . \tag{5.11}$$

5.2.3 Coherent drive on a two-ion crystal

In case of a two-ion crystal, the oscillating electric field exerts periodically modulated forces

$$\boldsymbol{F} = \begin{pmatrix} qE_0 \\ qE_0 \end{pmatrix} \cos(\omega_{\mathrm{M}} t - \phi) \tag{5.12}$$

on both ions with the jth component of the vector $\boldsymbol{F}$ indicating the force on the jth ion along the z-direction. Following the argumentation in Appendix B, in the

[1] The phase difference $\delta\phi$ is defined relative to a phase π.

normal mode picture it is equivalent to consider each mode γ as an independent harmonic oscillator with a virtual mass $m = \sum_j m_j$. We apply a force

$$\widetilde{F}_\gamma(t) = \sum_j \beta_j^\gamma F_j(t) = \left(\sum_j \beta_j^\gamma q E_0 \right) \cos\left(\omega_\mathrm{M} t - \phi\right) \tag{5.13}$$

on each of the modes γ. The transformation matrix β_j^γ converts the coordinates from the normal mode frame into the laboratory frame, while the virtual mass m depends on the normalization of β_j^γ and defines the size of the wave packet in the motional ground state $z_0^\gamma = \sqrt{\hbar/2m\omega_\mathrm{T}^\gamma}$. The effect of the force on the ip mode of the ion crystal is a displacement operator $\hat{D}(\Omega_\mathrm{d}^\mathrm{ip} t)$ with the displacement strength

$$\Omega_\mathrm{d}^\mathrm{ip} = i/\hbar \cdot \left(\sum_j \beta_j^\mathrm{ip} q E_0 \right) z_0^\mathrm{ip} e^{i\phi} \,. \tag{5.14}$$

We demonstrate the modulation technique on a two-ion crystal consisting of $^{25}\mathrm{Mg}^+$ and $^{40}\mathrm{Ca}^+$. After Doppler cooling and pulsed SBC, a short modulation pulse at around the trap frequency of the ip mode $\omega_\mathrm{M} = \omega_\mathrm{T}^\mathrm{ip}$ is applied. The displacement $|\alpha|$ is measured with Rabi oscillations as a function of the amplitude E_0 of the modulating electric field. As expected, the displacement grows linearly with the modulation strength E_0 as depicted in Fig. 5.2a. The slope is proportional to

$$k^\mathrm{ip} \propto \left| \left(\sum_j \beta_j^\mathrm{ip} q \right) \frac{z_0^\mathrm{ip} t}{\hbar} \right| . \tag{5.15}$$

The ratio of the two slopes determined from the experiments equals $k^\mathrm{ip}/k = 1.38(16)$ in agreement with the theoretical prediction of 1.29.

The displacement strength for the op mode is similarly given by

$$\Omega_\mathrm{d}^\mathrm{op} = i/\hbar \cdot \left(\sum_j \beta_j^\mathrm{op} q E_0 \right) z_0^\mathrm{op} e^{i\phi} \,. \tag{5.16}$$

Since the two ions oscillate in this case exactly out of phase but with different amplitudes, the effects of the oscillating electric field on the two ions are cancelled to some extent. Mathematically the components β_j^op of the transformation matrix have different signs. For the two-ion crystal $^{25}\mathrm{Mg}^+$ and $^{40}\mathrm{Ca}^+$ at the axial trap

frequencies of 1.92 MHz and 3.50 MHz for the ip and op mode, respectively, the displacement strength of the ip mode is by a factor of $\Omega_{\mathrm{d}}^{\mathrm{ip}}/\Omega_{\mathrm{d}}^{\mathrm{op}} \approx 3.8$ larger than the displacement strength of the op mode. The power of the modulation pulse needs to be increased by more than 10 dB to create the same magnitude of displacement.

5.3 Non-resonant modulation pulses

Consider a single ion in the trap initialized in a motional state described by the density matrix ρ_{i}. A modulation pulse with duration t at the frequency ω_{M} that differs from the axial trap frequency ω_{T} results in a time-dependent interaction Hamiltonian. We can split the total modulation duration into an infinite number of short intervals $[\tau, \tau + \mathrm{d}\tau)$ and consider the interaction Hamiltonian inside each interval as time-independent. Inside each interval, the modulation pulse leads to a displacement $\hat{D}(\mathrm{d}\alpha)$ and the total effect of the modulation pulse after repeatedly invoking Eq. (5.9) becomes (Leibfried et al., 2003a)

$$\hat{D}_{\mathrm{total}} = \hat{D}\left(\int_0^t \frac{\mathrm{d}\alpha}{\mathrm{d}\tau}\,\mathrm{d}\tau\right) e^{i\Phi}\,, \tag{5.17}$$

with

$$\Phi = \mathrm{Im}\left[\int_0^t \frac{\mathrm{d}\alpha}{\mathrm{d}\tau}\alpha^*(\tau)\,\mathrm{d}\tau\right]. \tag{5.18}$$

At a fixed modulation frequency ω_{M}, the total displacement and its amplitude simplify to

$$\alpha(\delta\omega, t) = \int_0^t \Omega_{\mathrm{d}} e^{-i\delta\omega\tau}\,\mathrm{d}\tau = \Omega_{\mathrm{d}} t \cdot \frac{i\left[\exp(-i\delta\omega t) - 1\right]}{\delta\omega t}\,, \tag{5.19}$$

$$|\alpha(\delta\omega, t)| = \left|\Omega_{\mathrm{d}} t \cdot \mathrm{sinc}\left(\frac{\delta\omega t}{2}\right)\right|, \tag{5.20}$$

where $\mathrm{sinc}(x) = \sin(x)/x$ is the sinc-function. Eq. (5.19) expresses the displacements as a function of the detuning $\delta\omega = \omega_{\mathrm{M}} - \omega_{\mathrm{T}}$ and the modulation duration t. At a non-zero detuning, Eq. (5.19) is the parametric form of a circle on the complex plane with the center at $-i\Omega_{\mathrm{d}}/\delta\omega$ and the radius $|\Omega_{\mathrm{d}}/\delta\omega|$. After a modulation duration $t_{2\pi} = 2\pi/\delta\omega$, the ion is displaced back to the origin of phase

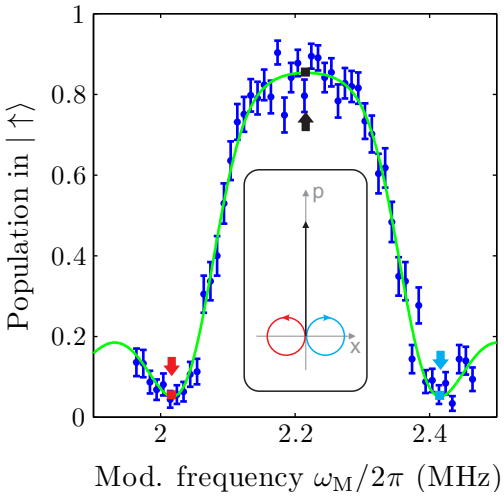

Figure 5.3: **Frequency dependent displacement.** With a single $^{25}Mg^{+}$ ion initialized in the state $|\downarrow, n = 0\rangle$, the modulation pulse with a duration of $5\,\mu$s generates a frequency dependent displacement. On resonance $\omega_M = \omega_T$, the ion is displaced to a coherent state $|\alpha \approx 2.2\rangle$. At the detunings $\delta\omega = \pm 200\,$kHz, the ion runs through a circle in phase space and returns back to the origin at the end of the modulation pulse. The motional excitation from the modulation pulse is detected with a STIRAP pulse on the RSB, which transfers the motionally excited population from the $|\downarrow\rangle$ to $|\uparrow\rangle$ state.

space. For a fixed modulation duration, the frequency dependent displacement is given by Eq. (5.20).

In Fig. 5.3, we demonstrate the frequency dependent displacement on a single $^{25}Mg^{+}$ ion. The $^{25}Mg^{+}$ ion is initialized in the state $|\downarrow, n = 0\rangle$ with Doppler cooling followed by SBC. We apply the modulation pulse for a duration of $t = 5\,\mu$s at a power level of $-20\,$dBm. On resonance, the modulation pulse displaces the ion to a coherent state $|\alpha \approx 2.2\rangle$. We detect the motional excitation with a stimulated Raman adiabatic passage (STIRAP) pulse, which transfers the excited population

$$P_{\text{exc}} = 1 - \exp\left[-|\alpha(\delta\omega, t)|^2\right] \tag{5.21}$$

from the $|\downarrow\rangle$ to $|\uparrow\rangle$ state. As we scan the modulation frequency over the axial trap frequency, the motional excitation reaches the maximum at the axial trap frequency and disappears at the detunings $|\delta\omega| = n \cdot 2\pi/t$ with n being an integer

number. For a pulse duration of 5 μs, the first excitation minima appear at the detunings $\pm$200 kHz as illustrated in Fig. 5.3. At those detunings, the ion runs through a circle in phase space and is displaced back to the origin after the duration of the modulation pulse.

A single modulation pulse together with the STIRAP detection technique provides a high resolution method to determine the axial trap frequency. The linewidth of the resonance curve is fundamentally limited by the modulation duration t. With a modulation duration of 5 μs and a modulation strength below saturation, the resonance in Fig. 5.3 has a linewidth of $\sim$ 200 kHz. Increasing the modulation duration by a factor 100 will reduce the linewidth by the same amount. At the same time, it's necessary to reduce the modulation power by 10^4, or equivalently 40 dB, to avoid saturation of the motional excitation. In fact, the sideband cooled ion together with the STIRAP detection technique is an extremely sensitive method to detect modulations/noise at the trap frequencies. We observe on the measured spectrum in Fig. 5.3 already a flat top, which corresponds to a complete depletion of the ion out of the motional ground state.

In the next section, we apply the modulation technique to Doppler-cooled ions and infer the influence of the modulation pulses directly from the fluorescence of the ion.

5.4 Laser fluorescence mass spectroscopy

One of the techniques often used to identify the mass of the ions in the trap is laser fluorescence mass spectroscopy (LFMS). The technique has first been applied in Penning traps to indirect measurements of the proton-to-electron mass ratio and the electron g_J factor of the $^9Be^+$ ion (Wineland et al., 1983) and later on in RF traps with the purpose of identification of molecular ions (Baba et al., 1996; Drewsen et al., 2004). The basic idea of the technique is to excite the ions' motion by an external oscillating field around the trap frequency. After heating the ions by such a modulation pulse, the optical transition of the ions is Doppler broadened, resulting in a reduction of the fluorescence scattering induced by a slightly red-detuned or resonant detection laser. It is worth mentioning here that, with the detection laser several linewidths red-detuned with respect to the atomic

transition, the electric modulation can also give rise to an increase in fluorescence rate (Jefferts et al., 1995).

A simple model can be established to describe the line profile of LFMS. Consider a single ion initialized in a thermal distribution ρ_{th} achieved with e.g. Doppler cooling, which can be expressed in the Glauber-Sudarshan P-representation (Gerry et al., 2004) as

$$\rho_{\mathrm{th}} = \int P_{\mathrm{th}}(\beta) \left|\beta\right\rangle \left\langle\beta\right| \mathrm{d}^2\beta \tag{5.22}$$

with

$$P_{\mathrm{th}}(\beta) = \frac{1}{\pi\bar{n}} e^{-|\beta|^2/\bar{n}}. \tag{5.23}$$

The external modulation exerted on the ion applies a displacement $\hat{D}(\alpha)$ in phase space and leads to a final density matrix

$$\begin{aligned}
\rho_{\mathrm{f}} &= \hat{D}(\alpha)\rho_{\mathrm{th}}\hat{D}^{\dagger}(\alpha) \\
&= \int P_{\mathrm{th}}(\beta)\hat{D}(\alpha) \left|\beta\right\rangle \left\langle\beta\right| \hat{D}^{\dagger}(\alpha) \, \mathrm{d}^2\beta \\
&= \int P_{\mathrm{th}}(\beta) e^{i\mathrm{Im}(\alpha\beta^*)} \left|\beta+\alpha\right\rangle \left\langle\beta+\alpha\right| e^{-i\mathrm{Im}(\alpha\beta^*)} \, \mathrm{d}^2\beta \\
&= \int P_{\mathrm{th}}(\beta-\alpha) \left|\beta\right\rangle \left\langle\beta\right| \mathrm{d}^2\beta \, .
\end{aligned} \tag{5.24}$$

The effect of the external modulation pulse is therefore displacing the whole distribution function $P_{\mathrm{th}}(\beta)$ in phase space by $\alpha = |\alpha| \exp(i\phi_\alpha)$ with ϕ_α as the phase of the displacement. The displaced thermal state described by the P-distribution $P_{\mathrm{th}}(\beta-\alpha)$ has the same momentum as the coherent state $|\alpha\rangle$

$$\langle\hat{p}\rangle = \sqrt{\frac{\hbar m\omega_{\mathrm{T}}}{2}} \cdot 2|\alpha| \cdot \sin\phi_\alpha \, . \tag{5.25}$$

In the laboratory frame, the ion oscillates in the trap at a velocity

$$\begin{aligned}
v(\tau) &= \frac{1}{m} \cdot \sqrt{\frac{\hbar m\omega_{\mathrm{T}}}{2}} \cdot 2|\alpha| \cdot \sin(\omega_{\mathrm{T}}\tau + \phi_\alpha) \\
&= v_0 \sin(\omega_{\mathrm{T}}\tau + \phi_\alpha)
\end{aligned} \tag{5.26}$$

with v_0 as the maximum velocity during the oscillation in the trap. If we probe the optical transition of the ion with resonant light after the modulation, the

transition frequency is Doppler shifted depending on the velocity of the ion and the scattering rate is modified to

$$\Gamma_{\mathrm{sc}} = \frac{\Gamma}{2} \frac{s}{1 + s + \left[2kv(\tau)/\Gamma\right]^2}\,, \tag{5.27}$$

where s is the saturation parameter and Γ the scattering rate of the probed transition. For detection pulses much longer than the oscillation period $T = 2\pi/\omega_{\mathrm{T}}$ of the ion in the trap, the detected fluorescence rate is an average over many oscillation periods during which the velocity of the ion varies according to Eq. (5.26)

$$\begin{aligned} \overline{\Gamma}_{\mathrm{sc}} &= \frac{1}{T} \int_0^T \frac{\Gamma}{2} \frac{s}{1 + s + \left[2kv(\tau)/\Gamma\right]^2} \,\mathrm{d}\tau \\ &= \frac{\Gamma}{2} \frac{s}{\sqrt{\left[1 + s^2\right]\left[1 + s^2 + \left(2kv_0/\Gamma\right)^2\right]}} \\ &= \frac{\Gamma}{2} \frac{s}{1 + s^2} \frac{1}{\sqrt{1 + \left[b\,\mathrm{sinc}(\delta\omega \mathrm{t}/2)\right]^2}}\,, \end{aligned} \tag{5.28}$$

where the coefficient b takes the form

$$b = \frac{4k}{\Gamma\sqrt{1 + s^2}} \sqrt{\frac{\hbar\omega_{\mathrm{T}}}{2m}} \cdot \Omega_{\mathrm{d}} t\,. \tag{5.29}$$

We demonstrate the technique of LFMS on a single $^{25}Mg^+$ ion. The experiment starts from a Doppler cooled ion, which has a $\bar{n}$ of about 16(5) (Hemmerling, 2011). After Doppler cooling, an electric modulation pulse with a duration t is applied on the two endcaps to excite the ion's motion. The resonant detection laser at 280 nm probes the $|{\downarrow}\rangle \leftrightarrow \left|^2\mathrm{P}_{3/2}, F = 4, m_{\mathrm{F}} = 4\right\rangle$ transition of the $^{25}Mg^+$ ion for a duration of 8 μs. As we scan the frequency of the modulation pulse over the axial trap frequency, the fluorescence rate from the probed transition shows the resonance curve depicted in Fig. 5.4. In the experiment, we apply the modulation pulse for 1000 μs at a power level of -27 dBm, which corresponds to a displacement of about $\alpha \approx 200$ at the resonance $\omega_{\mathrm{M}} = \omega_{\mathrm{T}}$, extrapolated from the calibration line (see Fig. 5.2). With such a high displacement amplitude, the ion oscillates in the trap with a maximum speed $v_0 \approx 50$ m/s and an oscillation amplitude of 4 μm. The Doppler shift at maximum speed equals 130 MHz. On

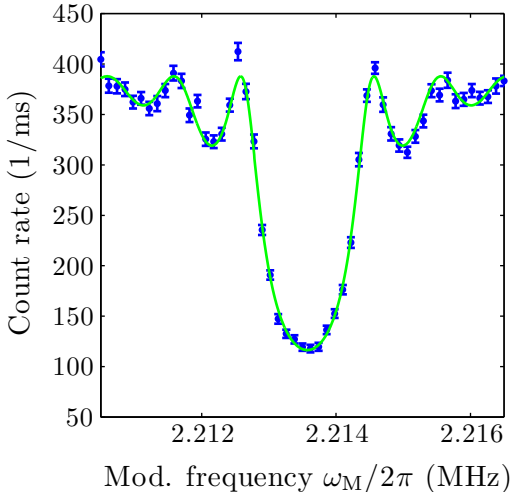

Figure 5.4: **Laser fluorescence mass spectroscopy.** After Doppler cooling, a single $^{25}Mg^+$ ion is modulated for a duration of 1000 μs at a power level of -27 dBm. After the modulation, the cycling transition of the $^{25}Mg^+$ ion is probed with a resonant laser for a duration of 8 μs (*blue points*). At the resonant modulation frequency $\omega_M = \omega_T$, the ion is excited to high motional states. The optical transition becomes Doppler broadened and the scattering rate drops. The *green line* is the fit of the theoretical model to the experimental data using Eq. (5.28).

the camera, the ion smears out along the axial direction (Drewsen et al., 2004) while the ion shows stronger fluorescence at the turning points and weaker fluorescence at the center. The experimental data is fitted with Eq. (5.28) The linewidth of the resonance is limited by the modulation duration t. With a pulse duration of 1 ms, the linewidth of the spectrum is about 1 kHz. In this way, we determine the axial trap frequency for a single $^{25}Mg^+$ in the trap from the fit with an uncertainty of 6 Hz, which only includes the statistical error. The day-to-day variations of the endcap voltage, RF power and thermal effects from the ovens, which are slightly changing the geometry of the trap electrodes, will lead to a variation of the measured value of up to 1 kHz.

In Sec. 6.4.3 and 7.5.1, we used the technique of LFMS to identify the components of the ion crystal in the trap before proceeding with quantum logic spectroscopy on the atomic and molecular ions.

5.5 Ramsey sequence

The technique of LFMS allows us to determine the axial trap frequency with a linewidth determined by the spectroscopy duration t. With a typical spectroscopy time of $t = 1\,\mathrm{ms}$, a linewidth on the order $1\,\mathrm{kHz}$ is attainable. A higher resolution can be achieved using a Ramsey sequence based on the coherent excitation of a sideband cooled ion crystal and subsequent detection using a STIRAP pulse on the 1^{st} RSB as described in Sec. 5.3. This results in a smaller linewidth of the resonance curve for the axial trap frequency, and thus a higher sensitivity compared to LFMS for the same probe time. A saturation of motional excitation, which appears by detecting the depletion of the motional ground state using a STIRAP pulse as described in Sec. 5.3, is also avoided in the Ramsey sequence.

At the beginning of the sequence, the ion is initialized to the motional ground state. The Ramsey sequence consists of a displacement pulse, a waiting period with duration T and a second displacement pulse. The first displacement pulse moves the ion out of the origin to a coherent state $|\alpha(\delta\omega, t)\rangle$ according to Eq. (5.19). The waiting time T together with the second modulation pulse imposes a displacement on the ion with a varying phase. The two displacement pulses have the same duration t and are at the same strength, so that the residual displacement equals

$$\delta\alpha = \alpha(\delta\omega, t) + \alpha(\delta\omega, t)e^{i(\phi_2 - \phi_1 - \delta\omega\, T)} \tag{5.30}$$

The ion can be displaced back to the origin of phase space under the condition

$$\phi_2 - \phi_1 - \delta\omega\, T = \pi\,, \tag{5.31}$$

which also depends on the detuning of the modulation pulses $\delta\omega$ and the waiting time T. Choosing the phase difference of the two modulation pulses to be $\phi_2 - \phi_1 = \pi$, the minimal motional excitation will appear on resonance $\delta\omega = 0$, independent of the waiting time T. The amplitude of the residual displacement simplifies to

$$|\delta\alpha| = 2\left|\Omega_{\mathrm{d}} \sin\left(\frac{\delta\omega\, T}{2}\right) \mathrm{sinc}\left(\frac{\delta\omega\, t}{2}\right) t\right|\,. \tag{5.32}$$

The pulse sequence with two displacement pulses has the advantage over a single displacement pulse, that the motional excitation can be kept small, so that a

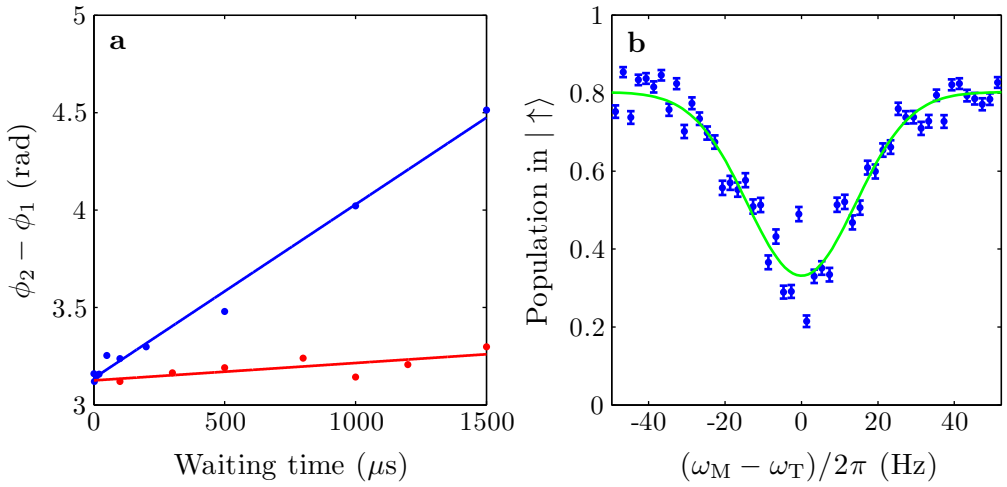

Figure 5.5: **Mass spectroscopy using Ramsey sequence.** (**a**) In a Ramsey sequence, the ion is displaced back to the motional ground state at an appropriate phase, which depends on the detuning $\delta\omega$ of the modulation pulses and the waiting time T. This compensating phase is a linear function of the waiting time T and the slope gives the detuning of the modulation pulses from the trap frequency. (**b**) Frequency scan of the coherent drive frequency ω_M around the axial trap frequency ω_T in a Ramsey sequence with a waiting time of $T = 1000\,\mu$s. The modulation pulses have a duration of $20\,\mu$s and are at a power level of $-20\,$dBm. A single modulation pulse generates on resonance a displacement $|\alpha| = 8.7$. The linewidth of the resonance curve is determined by the waiting time T and the amplitude of a single displacement $|\Omega_d t|$.

saturation of the motion as observed while detecting with a STIRAP pulse can be avoided without reducing the amplitude $|\alpha|$. The signal extracted from the STIRAP detection pulse equals

$$P_{exc} = 1 - \exp\left(-|\delta\alpha|^2\right) . \tag{5.33}$$

We demonstrate the Ramsey sequence on a single $^{25}Mg^+$ ion initialized in the electronic state $|\downarrow\rangle$ and the motional ground state $|n = 0\rangle$ with SBC. The two modulation pulses generate a residual displacement $\delta\alpha$ and we detect the motional excitation with the STIRAP pulse. With the detuning $\delta\omega$ approximately at zero, we determine the phase of minimal excitation as a function of the waiting time

as depicted in Fig. 5.5a, which show a linear dependence with an offset π as predicted in Eq. (5.31). The slope of the line gives the deviation of the modulation frequency from the axial trap frequency. After fixing the phase difference of the two modulation pulses to π, we scan the modulation frequency ω_{M} over the axial trap frequency ω_{T} with a modulation duration $t = 20\,\mu\mathrm{s}$ and a modulation strength of $-20\,\mathrm{dBm}$. A single modulation pulse induces a displacement of $|\alpha| \approx 8.7$ on resonance. The linewidth of the spectrum

$$\Delta\omega_{\mathrm{FWHM}} \approx 2\pi \times \frac{\sqrt{\ln 2}}{\pi} \cdot \frac{1}{\Omega_{\mathrm{d}} t} \cdot \frac{1}{T} \tag{5.34}$$

is in this case not only determined by the waiting period T, but also the amplitude of a single displacement $\Omega_{\mathrm{d}} t$. With a displacement of $\Omega_{\mathrm{d}} t \approx 8.7$ from the single modulation pulse and a waiting time $T = 1000\,\mu\mathrm{s}$, we achieve a linewidth on the order of 40 Hz with a corresponding statistical uncertainty of 0.6 Hz as shown in Fig. 5.5. A similar technique has been developed independently in the context of mass spectroscopy of the electron in Penning traps (Sturm et al., 2014).

5.6 Discussion

With a statistical uncertainty down to 1 Hz, the modulation techniques can be used to distinguish the components of an ion crystal. In the isotope shift measurement using photon recoil spectroscopy (Gebert et al., 2014a), a single $^{25}\mathrm{Mg}^{+}$ is trapped together with different isotopes of Ca^{+} ions. The different isotopes with mass numbers 40, 42, 44 and 48 have axial trap frequencies that differ on the order of 30 kHz and are clearly distinguishable using LFMS. A similar task appears in Sec. 7.5.1, where identification of the ion crystal consisting of $^{25}\mathrm{Mg}^{+}$ and $^{24}\mathrm{MgH}^{+}$ is necessary.

Besides the frequency difference introduced by the mass, the presence of a permanent dipole moment in the molecular ion will influence the trap frequency. A molecular ion with a permanent dipole moment $\boldsymbol{p}$ experiences in addition to the confinement from the trap and the Coulomb interaction between the ions, two additional terms:

- Coupling of the permanent dipole moment to the electric field

$$V_{\text{dipole}} = -p_z \cdot E_z(z_i) = -p_z \cdot \left(-\frac{u_0}{e} z_i\right) , \tag{5.35}$$

  where p_z is the projection of the dipole moment along the axial direction, u_0 is the spring constant of the trap, z_i as the position of the molecular ion and e is the elementary charge. This term has a linear dependence on the position z_i of the molecular ion. Therefore it only changes the equilibrium position of the ion crystal, but does not influence the trap frequency (Morigi et al., 2001).

- Ion-dipole interaction

$$V_{\text{ion-dipole}} = -\sum_{j \neq i} \frac{1}{4\pi\epsilon_0} \frac{p_z \cdot e}{|z_i - z_j|^2} , \tag{5.36}$$

  where z_j are the positions of the ions.

In our case with an axial trap frequency of $\omega_{\text{T}} = 2\pi \times 2.21\,\text{MHz}$ for a single $^{25}\text{Mg}^+$ ion, the spring constant equals $u_0 = m\omega_{\text{T}}^2 \approx 7.8 \times 10^{-12}\,\text{kg/s}^2$ and the two ions are separated by Morigi et al., 2001

$$d = \left(\frac{2e^2}{4\pi\epsilon_0 u_0}\right)^{1/3} \approx 3.9\,\mu\text{m} . \tag{5.37}$$

For $^{24}\text{MgH}^+$ in the electronic ground state with a permanent dipole moment on the order of 3 Debye (Aymar et al., 2009). In this scenario, the ion-dipole interaction is 5 orders of magnitude smaller than the ion-ion interaction. By comparing the axial trap frequency of a single $^{25}\text{Mg}^+$ with the axial trap frequency of the ion crystal $^{25}\text{Mg}^+$ and $^{24}\text{MgH}^+$, the influence of the permanent dipole moment on the axial trap frequency could be detected with the Ramsey sequence described above, which allows to determine the axial trap frequency with a relative uncertainty of $3 \cdot 10^{-7}$.

In contrast to mass ratio measurements, absolute mass measurements would require precise calibration of the trap potentials. For any of the techniques described above for precision mass ratio measurements, a detailed investigation of systematic effects beyond the scope of this thesis is required.

Chapter 6

Photon recoil spectroscopy

In this chapter, we demonstrate photon recoil spectroscopy (PRS) on the $^2S_{1/2} \leftrightarrow {}^2P_{1/2}$ transition of the $^{40}Ca^+$ ion. In Sec. 6.1, we discuss different techniques for laser spectroscopy. We introduce the technique of PRS as an extension of quantum logic spectroscopy in Sec. 6.2 and develop theoretical models explaining PRS in Sec. 6.3. We provide an illustrative picture and a full master equation simulation for the experiment. The latter allows us to estimate a systematic frequency shift inherent to the technique. The experimental setup is described in Sec. 6.4. In Sec. 6.5, the experimental results of PRS are presented and the influence of systematic effects are evaluated in Sec. 6.6. In the last section, we discuss possible applications of the technique. Parts of this chapter have been published in Wan et al. (2014).

6.1 Introduction

Laser spectroscopy is one of the most powerful tools to investigate the internal structure of atoms, molecules and nuclei. Through comparison with astrophysical data, precision laboratory data of the atomic and molecular level structure allows to probe for a possible variation of fundamental constants, like the fine structure constant α (Webb et al., 2011) or the proton-to-electron mass ratio $\beta = m_p/m_e$ (Reinhold et al., 2006; Flambaum et al., 2007; Murphy et al., 2008). Isotope shift measurements allow to determine the influence of the nuclei on the atomic transition frequencies and gives insight into the details of the nuclear structure

(Nörtershäuser et al., 1998a; Nakamura et al., 2006; Takamine et al., 2009; Lee et al., 2013; Blaum et al., 2013). Combined with the technique of laser cooling, trapped ions are the ideal candidates for precision laser spectroscopy. Laser-cooled ions stored in a field-free environment are not subject to Doppler shift and systematic shifts caused by external fields can be reduced at a minimum. Provided a narrow spectroscopy transition, the electron shelving technique promises a SNR limited by the quantum projection noise (QPN). Using such systems, optical clocks with record inaccuracies have been realized with e.g. a single trapped Hg^+ ion (Rosenband et al., 2008), $^{171}Yb^+$ (Huntemann et al., 2012) and $^{88}Sr^+$ ion (Madej et al., 2012). These realizations require that the target species has a narrow spectroscopy transition and appropriate transitions, which allow for laser cooling, state preparation and state detection. The quantum logic technique (Schmidt et al., 2005) extends laser spectroscopy to atomic and molecular species (Rosenband et al., 2008; Chou et al., 2010), to which direct laser cooling is not applicable. The spectroscopy ion is sympathetically cooled by a co-trapped logic ion, on which laser cooling, coherent manipulation, and state detection are performed.

In comparison, spectroscopy on transitions with short-lived excited states is typically implemented via detection of scattered photons in laser induced fluorescence (LIF) (Drullinger et al., 1980; Herrmann et al., 2009; Batteiger et al., 2009) or detection of absorbed photons in laser absorption spectroscopy (LAS) (Wineland et al., 1987a). Both methods cannot reach the fundamental quantum projection noise limit due to small photon collection efficiency in the former case and small atom-light-coupling efficiency in the latter case.

Instead of direct detection of scattered or absorbed photons, the ions' motional degrees of freedom can be used as the logic channel to transfer the spectroscopy signal to the logic ion. The transfer is based on the coupling of the internal and external degrees of freedom during absorption/emission of laser light. Photon recoil influences the ions' motion due to absorption or emission of photons. This effect has been used to macroscopically heat a Doppler-cooled two-ion crystal using a resonant spectroscopy laser and detect this motional heating on the logic ion via a reduction of the fluorescent rate (Clark et al., 2010). This technique, sympathetic heating spectroscopy, allows to detect the heating from less than 1500

scattered photons, which is below the typical fluorescent detection limit. Similar to a driven harmonic oscillator, the ions' motion can be efficiently excited by applying short spectroscopy pulses synchronous with the secular frequency (Drewsen et al., 2004). The seeded motion of a single Doppler-cooled ion from around 150 photons has been measured by Doppler velocimetry (Biercuk et al., 2010) after a motional amplification scheme (Lin et al., 2013b). The highest photon sensitivity has been achieved using an interferometric sequence on a Schrödinger cat state of motion (Hempel et al., 2013), where a single scattered photon was detected with a signal-to-noise ratio (SNR) of around 0.34.

In this chapter, we demonstrate a method for performing precision laser spectroscopy on broad transitions. As an extension of the quantum logic spectroscopy, *photon recoil spectroscopy* (PRS) uses a common mode of the two-ion crystal to transfer the spectroscopic information from the spectroscopy ion to the logic ion. Sympathetic cooling extends the applicability of the technique to a broad range of atomic and molecular species, while efficient state detection on the logic ion using the electron shelving technique promises a QPN limited SNR.

6.2 Principle & implementation

The principle of photon recoil spectroscopy (PRS) is illustrated in Fig. 6.1. A single spectroscopy ion is trapped together with a single logic ion in the linear Paul trap. At the beginning of the sequence, the two-ion crystal is prepared in the ground state of the axial modes using resolved sideband cooling (SBC) (Fig. 6.1a). During absorption of photons from the spectroscopy laser, the ions' motion becomes excited due to photon recoil (Fig. 6.1b). Efficient excitation of motion is achieved via synchronous application of the spectroscopy laser with the oscillation of a chosen normal mode (spectroscopy mode). This motional excitation is shared by both ions because of the strong Coulomb interaction and converted into an internal excitation of the logic ion via a stimulated Raman adiabatic passage (STIRAP) pulse on the red sideband (Fig. 6.1c). The spectroscopy signal is obtained from a detection pulse, which determines the internal state of the logic ion using the electron-shelving technique (Fig. 6.1d).

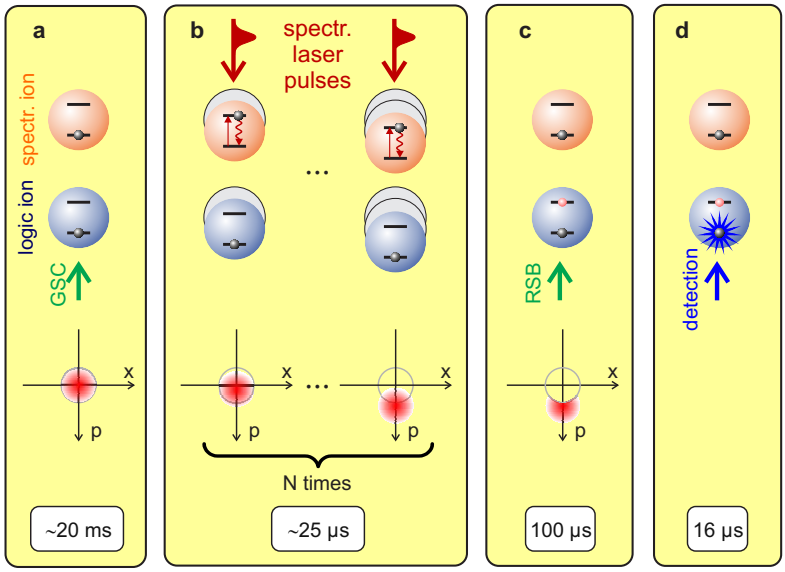

Figure 6.1: **Principle of photon recoil spectroscopy.** Photon recoil spectroscopy is performed on a single spectroscopy ion co-trapped with a laser-cooled logic ion. A single experimental cycle is split into four different periods with the typical timescales for the experimental implementation shown in the bottom part of the figure. The excitation of the internal and external degrees of freedom in each period is shown in the top part of the figure while the Wigner representation of the spectroscopy mode in phase space is depicted in the center part. (**a**) The two-ion crystal is initialized to the motional ground state via sideband cooling (SBC) on the logic ion. (**b**) Spectroscopy ion absorbs photons from the pulsed spectroscopy laser and the common motion of the two-ion crystal becomes excited due to photon recoil. Due to synchronous application of the spectroscopy laser with the oscillation of the spectroscopy mode, the motional displacements from the subsequent absorption events are additive and the motional distribution is displaced out of the origin of phase space. (**c**) The population in the excited Fock states $|n > 0\rangle$ indicated by the red moon-shaped disc are distinguishable from the population in the motional ground state $|n = 0\rangle$. They are transferred to an internal state excitation of the logic ion via a stimulated Raman adiabatic passage (STIRAP) pulse on the red sideband (RSB). (**d**) A final detection pulse determines the internal state of the logic ion using the electron shelving technique and provides the spectroscopy signal.

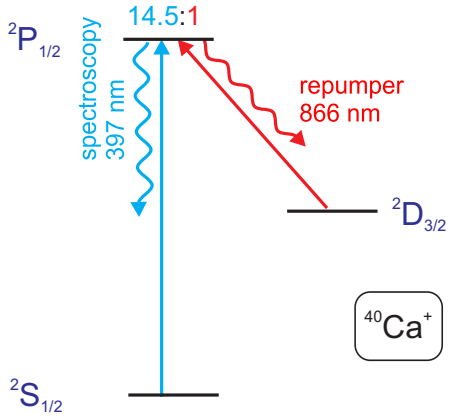

Figure 6.2: **Level scheme of the calcium ion.** Photon recoil spectroscopy is demonstrated on the $^2S_{1/2} \leftrightarrow {}^2P_{1/2}$ transition of the $^{40}Ca^+$ ion at 397 nm. The excited $^2P_{1/2}$ state after typically 7 ns decays into the $^2S_{1/2}$ and $^2D_{3/2}$ state with a branching ratio of 14.5 : 1. A repump pulse at 866 nm after each spectroscopy pulse brings the ion back to the $^2S_{1/2}$ state.

We implement photon recoil spectroscopy on a single $^{40}Ca^+$ ion (spectroscopy ion) co-trapped with a single $^{25}Mg^+$ ion (logic ion) and perform an absolute frequency measurement of the $^2S_{1/2} \leftrightarrow {}^2P_{1/2}$ transition in the $^{40}Ca^+$ ion. The relevant level scheme of the $^{25}Mg^+$ and the $^{40}Ca^+$ ion is depicted in Fig. 3.2 and Fig. 6.2, respectively. We cool the two-ion crystal with Doppler cooling followed by resolved sideband cooling along the axial direction as described in (Hemmerling et al., 2011). The in-phase (ip) and out-of-phase (op) modes with trap frequencies $\omega_T^{ip} = 2\pi \times 1.92\,\text{MHz}$ and $\omega_T^{op} = 2\pi \times 3.51\,\text{MHz}$ reach a residual mean occupation number of $\bar{n}_{ip} \approx 0.07$ and $\bar{n}_{op} \approx 0.02$, respectively. With the spectroscopy laser aligned along the axial direction, the ip and op modes have a Lamb-Dicke parameter of $\eta_S^{ip} = 0.108$ and $\eta_S^{op} = 0.051$ for the spectroscopy ion, respectively. We choose the ip mode as the spectroscopy mode because of its larger Lamb-Dicke parameter. In each experimental cycle, typically N_{pulses} spectroscopy pulses are applied. Each spectroscopy pulse has a duration of τ, corresponding to a duty cycle $d = \tau/T$ where $T = 1/\omega_T^{ip}$ is the oscillation period of the spectroscopy mode. Once the $^{40}Ca^+$ ion is excited to the $^2P_{1/2}$ state, it decays after typically 7 ns (Gosselin et al., 1988; Jin et al., 1993) into the $^2S_{1/2}$ state and the metastable $^2D_{3/2}$ state with a branching ratio of 14.5 : 1 (Ramm

et al., 2013). It is therefore necessary to apply a repump pulse after each spectroscopy pulse to clear out the population in the $^2D_{3/2}$ state. The application of the spectroscopy laser is synchronized with the oscillation of the ip mode to enhance the sensitivity to photon recoil. The motional excitation on the ip mode is converted into an internal excitation of the $^{25}Mg^+$ ion via a STIRAP pulse on the RSB, which is realized with two Raman lasers coupling $|\downarrow\rangle|n\rangle$ and $|\uparrow\rangle|n-1\rangle$ states. The STIRAP pulse with a typical duration of 100 μs transfers the population in the motional excited states $|\downarrow\rangle|n>0\rangle$ to $|\uparrow\rangle|n-1\rangle$ independent of the motional state $|n\rangle$ with more than 80% transfer efficiency, while the population in the motional ground state $|\downarrow\rangle|n=0\rangle$ is left untouched (Gebert et al., 2014b). The two internal states of the $^{25}Mg^+$ ion are distinguished by applying resonant light at 280 nm coupling the $|\downarrow\rangle$ state with the $\left|^2P_{3/2}, F=4, m_F=4\right\rangle$ state using π-detection technique (Hemmerling et al., 2012). The PRS signal corresponds to the population in the electronic excited state $|\uparrow\rangle$ of the $^{25}Mg^+$ ion.

6.3 Models

In this section, we establish theoretical models for PRS. We provide an intuitive picture for the emergence of photon recoil excitation in Sec. 6.3.1 and 6.3.2. A simplified picture based on a two-level system is valid, since in the low intensity regime the number of scattered photons in a single spectroscopy-repump-cycle is much less than 1 and the repump pulse after each spectroscopy pulse brings the $^{40}Ca^+$ ion back to the spectroscopy cycle. The photon emission statistics for a two-level and a three-level system is discussed in Sec. 6.3.3 and its influence on the photon recoil excitation is discussed in Sec. 6.3.4. In Sec. 6.3.5, full numerical simulations of two-level system and eight-level system are presented.

6.3.1 Effect of a single absorption-emission cycle

Consider an ion in the absolute ground state $|\psi_0\rangle = |g, n=0\rangle$ at time $t=0$ under the influence of a short pulse with duration τ. At time t_1 $(0 < t_1 < \tau)$ the first spontaneous emission happens. The system evolves under the effective

Hamiltonian

$$\begin{aligned}\hat{H}_{\text{eff}} &= \hat{H} - i\frac{\hbar\Gamma}{2}\hat{\sigma}_+\hat{\sigma}_- \\ &= \hat{H}^{(m)} - \frac{\hbar\delta}{2}\hat{\sigma}_z + \left[\frac{\hbar\Omega_0}{2}\hat{\sigma}_+\hat{D}(i\eta) + \text{h.c.}\right] - i\frac{\hbar\Gamma}{2}\hat{\sigma}_+\hat{\sigma}_-\end{aligned} \tag{6.1}$$

to an un-normalized state

$$\begin{aligned}\left|\psi(t_1^-)\right\rangle &= \exp\left[-\frac{i}{\hbar}\hat{H}_{\text{eff}}t_1\right]|\psi_0\rangle \\ &\approx \left(\mathbb{1} - \frac{i}{\hbar}\hat{H}_{\text{eff}}t_1\right)|\psi_0\rangle\ ,\end{aligned} \tag{6.2}$$

where the approximation in the second step is justified by the assumption of short pulses and weak excitation (less than one absorption/emission event per cycle) and t_1^- indicates the time immediately before the spontaneous emission. Within the Lamb-Dicke regime, the spontaneous emission happens predominantly on the carrier transition. The final state after the spontaneous emission reads

$$\begin{aligned}\left|\psi(t_1^+)\right\rangle &= \frac{\sqrt{\Gamma}\hat{\sigma}_-\left|\psi(t_1^-)\right\rangle}{\|\sqrt{\Gamma}\hat{\sigma}_-\left|\psi(t_1^-)\right\rangle\|} \\ &= |\text{g}, \alpha = i\eta\rangle\ ,\end{aligned} \tag{6.3}$$

where $|\text{g}, \alpha = i\eta\rangle$ denotes the ion in the electronic state $|\text{g}\rangle$ and a motional coherent state $|\alpha = i\eta\rangle$ and t_1^+ indicates the time immediately after the spontaneous emission. The effect of a single absorption event during a short pulse followed by spontaneous emission is equivalent to a displacement of the ion's motion in phase space by $i\eta$. This coherent state of motion $|\alpha = i\eta\rangle$ has the momentum

$$\begin{aligned}\langle\alpha = i\eta\,|\,\hat{p}\,|\,\alpha = i\eta\rangle &= i\sqrt{\frac{\hbar m\omega_{\text{T}}}{2}}\left\langle\alpha = i\eta\,\middle|\,(\hat{a}^\dagger - \hat{a})\,\middle|\,\alpha = i\eta\right\rangle \\ &= \sqrt{\frac{\hbar m\omega_{\text{T}}}{2}}\cdot 2\eta \\ &= \hbar k\end{aligned} \tag{6.4}$$

and the energy

$$\begin{aligned}\left\langle\alpha = i\eta\,\middle|\,\hat{H}^{(m)}\,\middle|\,\alpha = i\eta\right\rangle &= \left\langle\alpha = i\eta\,\middle|\,\hbar\omega_{\text{T}}(\hat{a}^\dagger\hat{a} + \frac{1}{2})\,\middle|\,\alpha = i\eta\right\rangle \\ &= \hbar\omega_{\text{T}}\left(\eta^2 + \frac{1}{2}\right) \\ &= \frac{\hbar^2k^2}{2m} + \frac{\hbar\omega_{\text{T}}}{2}.\end{aligned} \tag{6.5}$$

After one absorption-emission cycle (AEC), the momentum and the energy of the system is increased by the momentum of a single photon $\hbar k$ and the recoil energy $E_{\text{recoil}} = \hbar^2 k^2 / 2m$, respectively.

6.3.2 Momentum transfer on a single ion and two-ion crystal

In the following, the previous treatment of a single ion after a single AEC is extended to a two-ion crystal after multiple AECs. We discuss first the effect of multiple AECs and provide a consistent view in both the classical and quantum mechanical pictures. After that, the momentum transfer in a two-ion crystal is discussed, where only one of the two ions is excited by the laser.

In the classical picture, we consider a single ion in the trap with the spectroscopy laser aligned along the axial direction. We synchronize the application of the spectroscopy laser with the ion's motion in the trap at the frequency ω_{T}. If an absorption event happens during the spectroscopy period, the ion receives a momentum kick of $\hbar\boldsymbol{k}$ where $\hbar$ is the reduced Planck's constant and $\boldsymbol{k}$ is the wave vector of the spectroscopy laser. Assuming that the spectroscopy pulse τ is short compared to the period of the ion's oscillation in the trap ($\tau \ll 2\pi/\omega_{\text{T}}$), the momentum kicks from subsequent absorption events are additive, so that after N absorption events the ion has a total momentum of $p = N \cdot \hbar k$.

In the quantum mechanical picture, the interaction Hamiltonian describing the coupling between the laser and the ion in the rotating frame of the laser reads

$$\hat{H}_{\text{int}} = \frac{\hbar\Omega_0}{2}\hat{\sigma}_+ e^{ik\hat{z}} + \text{h.c.} \tag{6.6}$$

In case of a single ion, there is only a single mode available along the z-direction. The interaction Hamiltonian becomes

$$\hat{H}_{\text{int}} = \frac{\hbar\Omega_0}{2}\hat{\sigma}_+ \hat{D}(i\eta) + \text{h.c.} \tag{6.7}$$

In the extreme of ultrashort pulses, the effect of a single absorption event followed by a spontaneous emission is displacing the ion's motion in phase space by $i\eta$. Starting from the motional ground state, the synchronous application of the spectroscopy laser ensures that the subsequent displacements are along the same

direction in phase space. After N AECs, the ion is in the coherent motional state $|\alpha = N \cdot i\eta\rangle$ with total momentum

$$\langle \alpha = N \cdot i\eta \,|\, \hat{p} \,|\, \alpha = N \cdot i\eta \rangle = N \cdot \hbar k \tag{6.8}$$

as predicted from the classical picture.

Consider now that we have an ion string in the trap. For simplicity we limit ourselves to an ion string consisting of two ions of different species. Absorption from the spectroscopy laser can only happen on the spectroscopy ion, which receives a periodic momentum kick of $\hbar\boldsymbol{k}$. In the normal mode picture, the motional dynamics of the two ions can be described as two independent harmonic oscillators with a virtual mass m (Appendix B). Although the momentum kick is only exerted on the spectroscopy ion, this kick is effective in the normal mode picture on both modes with reduced amplitudes

$$p_\gamma = \beta_{\mathrm{S}}^{\gamma} \hbar k, \qquad \gamma = \{\mathrm{ip}, \mathrm{op}\} \tag{6.9}$$

with the transformation matrix $\boldsymbol{\beta}$ defined and normalized in Eqs. (B.5) and (B.8). The subscript S indicates that the momentum kick $\hbar k$ stems from the spectroscopy ion. The synchronization is only possible for one of the normal modes. If we synchronize the application of the spectroscopy laser with e.g. the ip mode, the momentum kicks from subsequent absorption events are additive for the ip mode, so that after N AECs, the momentum accumulated in the ip mode equals

$$p_{\mathrm{ip}} = N \cdot \beta_{\mathrm{S}}^{\mathrm{ip}} \hbar k \,, \tag{6.10}$$

while the excitation in the op mode is much less efficient than in the ip mode. In the case of an ion string the interaction Hamiltonian becomes

$$\begin{aligned} \hat{H}_{\mathrm{int}} &= \frac{\hbar\Omega_0}{2} \hat{\sigma}_+ \exp\left[ik \sum_\gamma \beta_{\mathrm{S}}^{\gamma} \hat{q}_\gamma \right] + \mathrm{h.c.} \\ &= \frac{\hbar\Omega_0}{2} \hat{\sigma}_+ \prod_\gamma \hat{D}\left(i\eta_{\mathrm{S}}^{\gamma}\right) + \mathrm{h.c.}, \end{aligned} \tag{6.11}$$

where in the first step we transform from the laboratory coordinate into the coordinate of normal modes $\hat{q}_\gamma$. η_i^γ denotes the Lamb-Dicke parameter of the i-th

ion on the mode γ and takes the form

$$\eta_i^\gamma = \beta_i^\gamma \cdot k z_0^\gamma \tag{6.12}$$

with $z_0^\gamma = \sqrt{\hbar/2m\omega_\mathrm{T}^\gamma}$ as the spatial extension of the motional ground state of the mode γ at the frequency ω_T^γ and $m = \sum_i m_i$ as the virtual mass. Starting from the motional ground state $|n=0\rangle$, a single absorption event followed by a spontaneous emission displaces the ion to $|\alpha_\mathrm{ip} = i\eta_\mathrm{S}^\mathrm{ip}, \alpha_\mathrm{op} = i\eta_\mathrm{S}^\mathrm{op}\rangle$. The synchronous application of the pulses at the ip mode frequency ensures the phase coherence of the subsequent displacements on the ip mode. After N AECs, the ion is displaced to the motional state $|\alpha_\mathrm{ip} = N \cdot i\eta_\mathrm{S}^\mathrm{ip}, \alpha_\mathrm{op}\rangle$. The momentum in the in-phase mode is accumulated to

$$\begin{aligned} p_\mathrm{ip} &= \left\langle \alpha_\mathrm{ip} = N \cdot i\eta_\mathrm{S}^\mathrm{ip} \right| \hat{p}_\mathrm{ip} \left| \alpha_\mathrm{ip} = N \cdot i\eta_\mathrm{S}^\mathrm{ip} \right\rangle \\ &= N \cdot \beta_\mathrm{S}^\mathrm{ip} \hbar k \end{aligned} \tag{6.13}$$

in agreement with the classical picture as given in Eq. (6.10). Unlike the displacements in the ip mode, the final state $|\alpha_\mathrm{op}\rangle$ depends on the exact timing of each AEC event and is therefore different for each single trajectory. Consider the displacements on the op mode as randomly distributed, the mean momentum accumulated in the op averages to 0 and the variance of the momentum scales as

$$\overline{\langle \alpha_\mathrm{op} \,|\, \hat{p}_\mathrm{op}^2 \,|\, \alpha_\mathrm{op} \rangle} \propto N\,, \tag{6.14}$$

where the overline denotes the average over different trajectories.

6.3.3 Statistics for photon scattering events

In the following, we discuss the photon emission statistics for a two and three level atom and discuss the influence of the photon distribution on the photon recoil spectroscopy signal in the next section.

6.3.3.1 Photon emission statistics for a two-level atom

Consider a two-level atom driven by a monochromatic light with a Rabi frequency Ω_0 and a detuning δ. In a time interval $[0, t]$, the probability that the atom scatters

N photons follows certain statistics $\mathcal{P}(N,t)$. For the resonant case, this statistics is sub-poissonian as demonstrated for a single trapped ion (Diedrich et al., 1987), characteristic for non-classical light. Photon anti-bunching is due to the quantum nature of scattering: after excitation of the atom, it first needs to decay before any subsequent absorption is possible (Walls et al., 1995). In the limit of weak excitation, Mandel's Q factor after long counting time

$$Q(\infty) \propto \frac{\Omega_0^2}{2} \frac{\delta^2 - \frac{3}{4}\Gamma^2}{\frac{\Omega_0^2}{2} + \delta^2 + \frac{\Gamma^2}{4}} \to 0 \tag{6.15}$$

approaches 0 (Arnoldus et al., 2012). The time between subsequent absorptions is long compared to the time scale of spontaneous emission and therefore the effect of photon anti-bunching is less dominant. In this case, photon emission statistics for a two-level system approaches a Poisson distribution.

6.3.3.2 Photon emission statistics for a three-level atom

For a three-level system in Λ-configuration as in the case of the $^{40}Ca^+$ ion, where the decay rate Γ_{SP} on the $^2P_{1/2} \to {}^2S_{1/2}$ transition is much larger than the decay rate Γ_{DP} on the $^2P_{1/2} \to {}^2D_{3/2}$ transition, the photon emission statistics under the influence of a laser resonant with the $^2S_{1/2} \leftrightarrow {}^2P_{1/2}$ transition, can be considered as follows. At a certain time t, we distinguish two cases, depending on whether a decay to the $^2D_{3/2}$ state has happened or not.

No decay to $^2D_{3/2}$ state In case there is no decay to the $^2D_{3/2}$ state at time t, the system is equivalent to a two-level system and the photon emission statistics is described by a Poisson distribution

$$\mathcal{P}^{\mathrm{S}}(N, \lambda(t)) = \frac{\lambda^N e^{-\lambda}}{N!} \tag{6.16}$$

with mean number of scattered photons $\overline{N} = \lambda(t)$. The probability distribution function is normalized to 1 according to

$$\sum_{N=0}^{\infty} \mathcal{P}^{\mathrm{S}}(N, \lambda(t)) = 1. \tag{6.17}$$

Decay to $^2D_{3/2}$ state In case that a decay to the $^2D_{3/2}$ state has already occured at time t, the photon emission statistics can be expressed analytically. We assume that N decay events occur during the time interval $[0, t]$, which indicates that $N-1$ decay events happen on the $^2P_{1/2} \rightarrow {}^2S_{1/2}$ transition and one decay event happens on the $^2P_{1/2} \rightarrow {}^2D_{3/2}$ transition. For long excitation time, where an unlimited number of photons can be scattered in a single experiment and the ion falls down to the $^2D_{3/2}$ state with a probability of 1, the statistics for emitted photons is given by the geometric distribution

$$\mathcal{P}^{\mathrm{D}}(N, \xi) = (1-\xi)^{N-1}\xi \tag{6.18}$$

with $1-\xi$ and ξ as the probability of decaying from $^2P_{1/2}$ into the $^2S_{1/2}$ state and the $^2D_{3/2}$ state, respectively. The total probability for scattering different number of photons is normalized to 1

$$\sum_{N=1}^{\infty} \mathcal{P}^{\mathrm{D}}(N, \xi) = \frac{\xi}{1-(1-\xi)} = 1. \tag{6.19}$$

The average number of scattered photon equals

$$\langle N \rangle^{\mathrm{D}} = \sum_{N=1}^{\infty} \mathcal{P}^{\mathrm{D}}(N, \xi) \cdot N = \frac{1}{\xi} \tag{6.20}$$

6.3.4 Photon recoil excitation

As described in Sec. 6.3.2 N consecutive AECs in a synchronized experimental sequence lead to a displacement of $N \cdot i\eta$ in phase space. For an ion in the coherent state $|N \cdot i\eta\rangle$, the population in the motional excited states is given by

$$P_{\mathrm{exc}}(N) = 1 - e^{-N^2\eta^2}. \tag{6.21}$$

This corresponds to the excitation where N AECs happened. Since the number of absorbed/emitted photons in a single experiment follows a certain distribution $\mathcal{P}(N, \overline{N})$ as described in Sec. 6.3.3, the PRS signal is obtained after averaging over the distribution $\mathcal{P}(N, \overline{N})$

$$S_{\mathrm{PRS}}(\overline{N}) = \sum_{N=0}^{\infty} P_{\mathrm{exc}}(N)\mathcal{P}(N, \overline{N}). \tag{6.22}$$

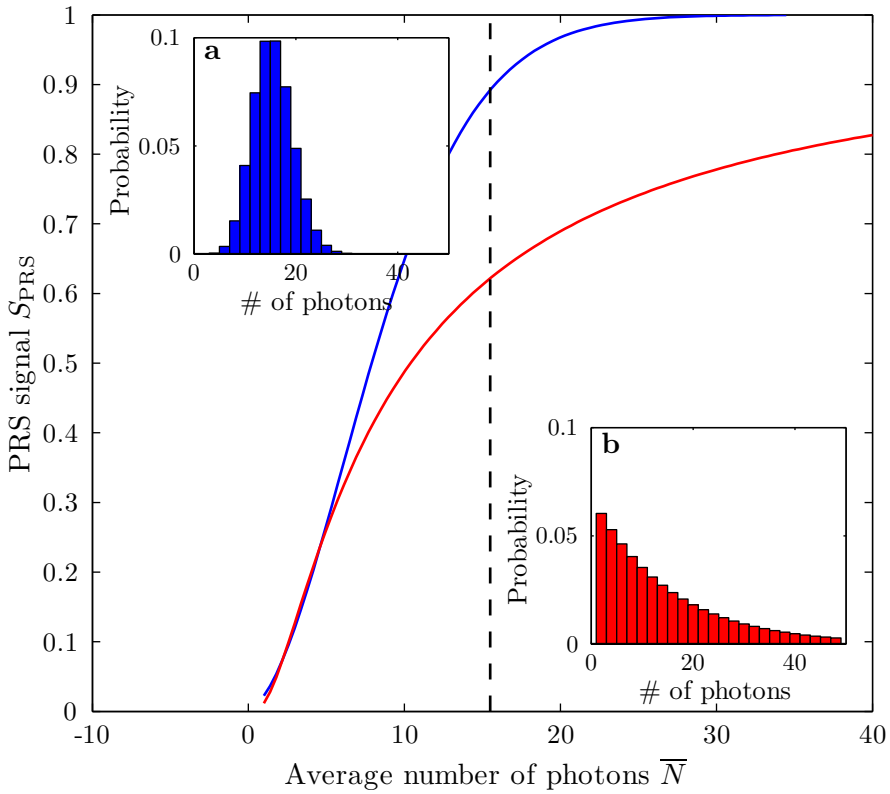

Figure 6.3: **Photon recoil excitation depending on photon distribution.** The calculated PRS signal S_{PRS} is plotted as a function of the mean number of absorbed photons $\overline{N}$ for Poisson (*blue*) and geometric (*red*) distributions. The insets show the corresponding photon distributions for $\overline{N} = 15.5$. Because of the exponential scaling with the square of the number of absorbed photons, the photon recoil excitation depends not only on the mean number of absorbed photons, but also the distribution of the absorbed photons. In the calculation, $\eta = 0.1084$ is used.

Note that the motional excitation $P_{\mathrm{exc}}(N)$ after N AECs does not depend on the number of absorbed photons in a linear way, so that the photon recoil spectroscopy signal is not simply determined by the average number of absorbed photons but rather depends on the actual photon statistics.

Consider two photon emission statistics, one Poisson distribution

$$\mathcal{P}_{\mathrm{coh}}(N, \lambda = \overline{N}) = \frac{\lambda^N e^{-\lambda}}{N!} \tag{6.23}$$

and one geometric distribution

$$\mathcal{P}_{\text{geom}}(N, p = \frac{1}{\overline{N}}) = (1-p)^{N-1}p \tag{6.24}$$

with the same average number of absorbed photons $\overline{N}$. The Poisson distribution is used to approximate the photon emission statistics for a two-level system or a three-level system with repumping, while the geometric distribution represents the photon emission statistics for a three-level system without repumping and after long excitation time. The PRS signal S_{PRS} is plotted in Fig. 6.3 as a function of the average number of absorbed photons. The exponential scaling with the square of the number of absorbed photons given in Eq. (6.21) favors the Poisson distribution. After e.g. $\overline{N} = 15.5$ AECs on average, the photon recoil excitation reaches a level of ~ 0.9 with a Poisson distribution and ~ 0.6 with a geometric distribution.

6.3.5 Master equation model

6.3.5.1 Two level system

The full dynamics of the system is modelled with a master equation in 1$^{\text{st}}$ order Lamb-Dicke approximation using the quantum optics toolbox for Matlab (Tan, 1999). We split a single spectroscopy-repump-cycle into a period of spectroscopy and a period of free evolution. During the spectroscopy pulse, the system evolves according to

$$\dot{\rho}(t) = -\frac{i}{\hbar}[\hat{H}^{(LD)}, \rho] + \frac{\Gamma}{2}\left(2\hat{\sigma}_-\rho\hat{\sigma}_+ - \hat{\sigma}_+\hat{\sigma}_-\rho - \rho\hat{\sigma}_+\hat{\sigma}_-\right), \tag{6.25}$$

where the Hamiltonian $\hat{H}^{(LD)}$ is defined in Eq. (2.13) and Γ is the linewidth of the $^2\text{S}_{1/2} \leftrightarrow {}^2\text{P}_{1/2}$ transition. During free evolution, the system evolves according to

$$\dot{\rho}(t) = -\frac{i}{\hbar}[\hat{H}_0, \rho] + \frac{\Gamma}{2}\left(2\hat{\sigma}_-\rho\hat{\sigma}_+ - \hat{\sigma}_+\hat{\sigma}_-\rho - \rho\hat{\sigma}_+\hat{\sigma}_-\right), \tag{6.26}$$

where we use the Hamiltonian in Eq. (2.14). Starting from the absolute ground state $\rho_0 = |\text{g}, 0\rangle\langle\text{g}, 0|$, the system evolves according to Eq. (6.25) for a short time τ corresponding to a duty cycle of $d = \tau/T$ with $T = 1/\omega_{\text{T}}$ as the period of the ions' oscillation in the trap. The density matrix $\tilde{\rho}_1$ at the end of the pulse is used

as the input density matrix for the free evolution according to Eq. (6.26) for a duration $T - \tau$. The procedure is iterated for N_{pulse} spectroscopy-repump-cycles and the motional excitations are extracted. The results from the density matrix simulation allow us to investigate different properties of the system.

Dependence on excitation time In Fig. 6.4a, the motional excitation is plotted as a function of the effective spectroscopy time $T_{\text{spec}} = N_{\text{pulse}} \cdot \tau$ with the laser on resonance. The motional excitation increases with the effective spectroscopy time and saturates at 1. The simulated result is fitted with

$$S_{\text{PRS}} = \sum_{N=0}^{\infty} P_{\text{exc}}(N, \eta) \mathcal{P}_{\text{coh}}(N, \Gamma_{\text{eff}} T_{\text{spec}}) \tag{6.27}$$

with the effective decay rate Γ_{eff} as the only fit parameter. The result from the density matrix simulation is in agreement with the model considering the averaging over the photon distribution described in Sec. 6.3.4 with a maximum error of less than 0.01. For a comparison, the PRS signal ignoring the averaging over the photon distribution

$$P_{\text{exc}} = 1 - \exp\left[-(\Gamma_{\text{eff}} T_{\text{spec}})^2 \eta^2\right] \tag{6.28}$$

is plotted as a red line in Fig. 6.4 with the same effective scattering rate Γ_{eff}.

Resonance line The resonance line is produced by repeating the density matrix simulation at different laser detunings. The motional excitation for the different laser detunings are extracted and plotted in Fig. 6.4b. The simulation result is fitted with the model in Eq. (6.27), where we replace the effective decay rate Γ_{eff} with a detuning-dependent expression

$$\Gamma_{\text{eff}} \to \frac{\Gamma_{\text{eff}}}{1 + (2\delta/\Gamma_0)^2} \,. \tag{6.29}$$

The effective width of the transition Γ_0 is used as the only fit parameter and the value for Γ_{eff} is taken from the fit of the excitation strength in the last paragraph. The linewidth of the transition extracted from the fit equals $\Gamma_0 \approx 26\,\text{MHz}$ and is larger than the natural linewidth ($\approx 22\,\text{MHz}$) of the investigated transition, which is caused by the Fourier broadening due to 125 ns short pulses.

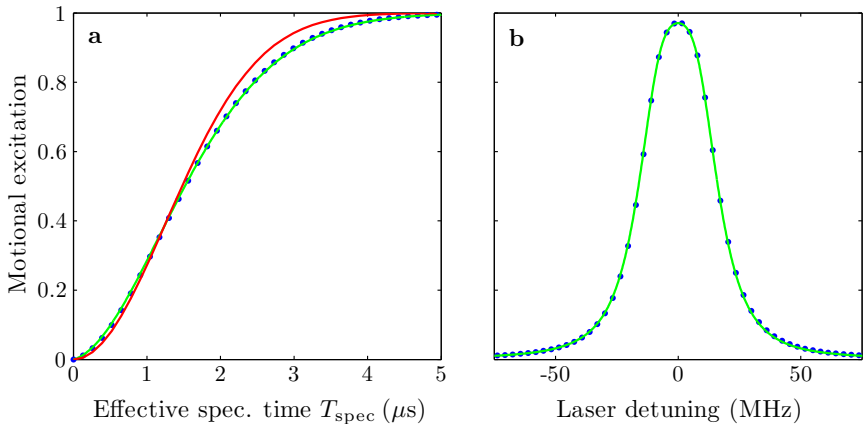

Figure 6.4: **Excitation strength and resonance line.** The dynamics of photon recoil spectroscopy is simulated using the master equation for a two level system. *blue dots*: density matrix simulation, *green line*: A fit to the result of master equation simulation using the model including the averaging over the photon distribution according to Eq. (6.27), *red line*: simple model ignoring the averaging over the photon distribution according to Eq. (6.21) using the same effective scattering rate Γ_{eff} resulted from the green line. (**a**) The motional excitation extracted from the density matrix simulation is plotted as a function of the effective spectroscopy time. The laser is on resonance with the optical transition. The excitation difference of the density matrix simulation and the model including the averaging over the photon distribution is smaller than 0.01. (**b**) The motional excitation for different detunings after an effective spectroscopy time of $4\,\mu$s are extracted from the density matrix simulation to produce the resonance curve (*blue dots*). The linewidth of the optical transition extracted from the fit (*green line*) using the model including the averaging over the photon distribution is broader than the natural linewidth of the investigated transition, which reflects the Fourier broadening of the 125 ns spectroscopy pulses. The parameters used in the simulation are the natural linewidth of the transition $\Gamma = 140 \times 10^6\,/\mathrm{s}$, the trap frequency of the ip mode $\omega_{\mathrm{T}}^{\mathrm{ip}} = 2\pi \times 1.92\,\mathrm{MHz}$, the Rabi frequency $\Omega_0 = 2\pi \times 5\,\mathrm{MHz}$ corresponding to a saturation parameter of $s = 0.1$, the Lamb-Dicke parameter of the spectroscopy on the ip mode $\eta_{\mathrm{S}}^{\mathrm{ip}} = 0.1084$ and the duty cycle $d = 0.24$.

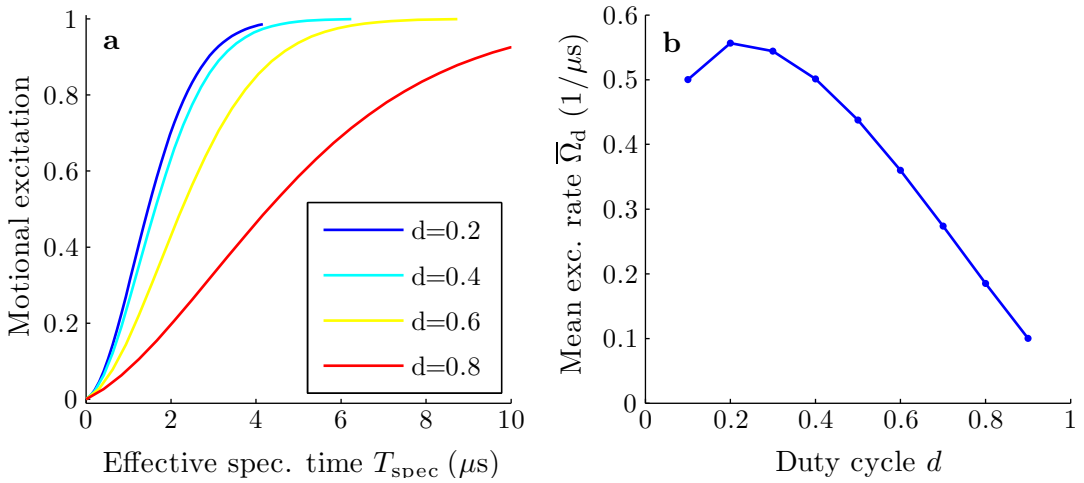

Figure 6.5: **PRS signal dependence on the duty cycle.** The density matrix simulation for photon recoil spectroscopy is performed on a two level system for different duty cycles d. (**a**) The motional excitations are plotted as a function of the effective spectroscopy time T_{spec}. For large duty cycles, the phase coherence of subsequent displacements is less ensured, which leads to a smaller excitation strength. (**b**) The mean excitation rate $\overline{\Omega}_{\mathrm{d}}$ drops for large duty cycles. But the maximum of the mean excitation rate appears at around $d = 0.2$ instead of infinitely short pulses.

Dependence on duty cycle The procedure described in the last two paragraphs is carried out for different duty cycles d. As described before, the application of synchronized short pulses ensures the phase coherence of the subsequent displacements. For large duty cycles, the subsequent displacements point along different directions in phase space, so that the excitation rate is reduced. In Fig. 6.5a, the motional excitation is plotted as a function of the effective spectroscopy time T_{spec} for four different duty cycles d. In order to describe the excitation strength for different duty cycles, we introduce a mean excitation rate $\overline{\Omega}_{\mathrm{d}}$. After an effective spectroscopy time $T_{\mathrm{spec}} = 1/\overline{\Omega}_{\mathrm{d}}$, the motional excitation reaches the level $1 - e^{-1}$. In Fig. 6.5b, the mean excitation rate is plotted as a function of the duty cycle. As expected, the mean excitation rate $\overline{\Omega}_{\mathrm{d}}$ drops for large duty cycles. The maximum shows up at around $d = 0.2$ instead of infinitely short pulses, reflecting the quantum Zeno effect (Itano et al., 1990), which starts

to play a role for short excitation pulses.

6.3.5.2 Eight level system

In order to include the effect of Zeeman broadening and repumping from the $^2D_{3/2}$ state, we perform numerical simulations using QuTip (Johansson et al., 2013) including eight relevant electronic levels depicted in Fig. 6.6.

In a multi-level atom, not only the frequency but also the polarization of the lasers influence the dynamics of the system. The spectroscopy and the repump laser enter the vacuum chamber along the axial direction (z-axis). Both lasers are linearly polarized with the electric field vector lying in the plane spanned by the k-vector of the laser and the magnetic field B. In the $x'y'z'$-coordinate system depicted in Fig. 3.3, in which the magnetic field B points along the z'-direction, the polarization vector for both lasers reads

$$\hat{\boldsymbol{\epsilon}} = \frac{1}{\sqrt{2}}\hat{\boldsymbol{x}}' - \frac{1}{\sqrt{2}}\hat{\boldsymbol{z}}' \,. \tag{6.30}$$

with $\hat{\boldsymbol{x}}'$ and $\hat{\boldsymbol{z}}'$ as the unit vectors of the x' and z'-axis, respectively. In the spherical basis

$$\hat{\boldsymbol{\epsilon}}_1 = -\frac{1}{\sqrt{2}}(\hat{\boldsymbol{x}}' + i\hat{\boldsymbol{y}}') \,, \tag{6.31a}$$

$$\hat{\boldsymbol{\epsilon}}_0 = \hat{\boldsymbol{z}}' \,, \tag{6.31b}$$

$$\hat{\boldsymbol{\epsilon}}_{-1} = \frac{1}{\sqrt{2}}(\hat{\boldsymbol{x}}' - i\hat{\boldsymbol{y}}') \,, \tag{6.31c}$$

the polarization vector $\hat{\boldsymbol{\epsilon}} = \sum_q \epsilon^q \hat{\boldsymbol{\epsilon}}_q$ has the components (Auzinsh et al., 2010)

$$\epsilon^1 = -\frac{1}{\sqrt{2}}(\epsilon_x - i\epsilon_y) = -\frac{1}{2} \,, \tag{6.32a}$$

$$\epsilon^0 = \epsilon_z = -\frac{1}{\sqrt{2}} \,, \tag{6.32b}$$

$$\epsilon^{-1} = \frac{1}{\sqrt{2}}(\epsilon_x + i\epsilon_y) = \frac{1}{2} \,. \tag{6.32c}$$

which indicates the presence of all three possible polarizations. The spectroscopy and repump laser contain equal amount of σ^+ and σ^- ($|\epsilon| = |\epsilon^{-1}|$), which is

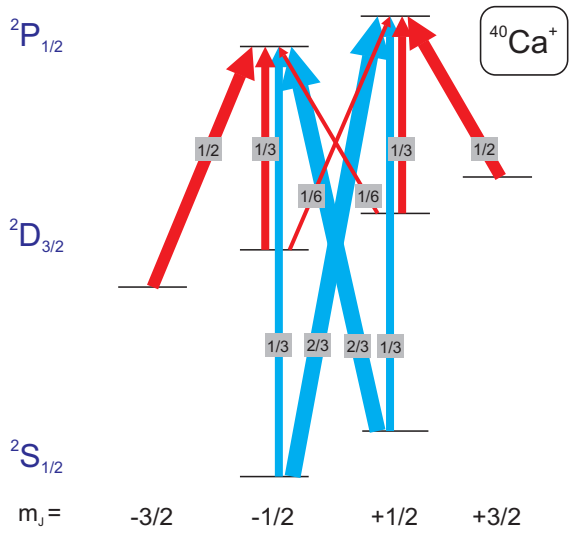

Figure 6.6: **Level scheme of Calcium ion including Zeeman sublevels.** The density matrix simulation including eight relevant electronic levels of the $^{40}Ca^+$ ion are performed using QuTip. The spectroscopy and the repump laser contain all three possible polarizations symmetrically ($|\epsilon^1|0|\epsilon^{-1}|$) and can therefore drive the transitions indicated with the blue and red arrows, respectively. The widths of the arrows and the corresponding numbers are the square of the Clebsch-Gordon coefficients $|\left\langle J_{\mathrm{S/D}}, m_J; 1, q \,\middle|\, J_{\mathrm{P}}, m_J + q\right\rangle|^2$ of the transitions $|\mathrm{S/D}, m_J\rangle \leftrightarrow |\mathrm{P}, m_J + q\rangle$.

important for a symmetric lineshape during spectroscopy. The master equation is modified to

$$\dot{\rho}(t) = -\frac{i}{\hbar}[\hat{H}_{\mathrm{sl}}, \rho] + \sum_i \frac{1}{2}\left(2\,\hat{c}_i\rho\hat{c}_i^\dagger - \hat{c}_i^\dagger\hat{c}_i\rho - \rho\hat{c}_i^\dagger\hat{c}_i\right) , \tag{6.33}$$

where the Hamiltonian $\hat{H}_{\mathrm{sl}} = \hat{H}_0 + \hat{H}_{\mathrm{int}} + \hat{H}_{\mathrm{B}}$ expressed in the rotating frame of the two lasers contains three terms:

- Hamiltonian for the unperturbed system

$$\hat{H}_0 = \hat{H}^{(m)} - \frac{\delta}{2}\left(\sum_{m_J} |\mathrm{P}, m_J\rangle\langle \mathrm{P}, m_J| - \sum_{m_J} |\mathrm{S}, m_J\rangle\langle \mathrm{S}, m_J|\right) , \tag{6.34}$$

  where $\hat{H}^{(m)}$ is the Hamiltonian describing the ion's motion in the trap (Eq. (2.2)), δ is the detuning of the spectroscopy laser, and m_J is the magnetic quantum number.

- Hamiltonian for ion-laser-interaction

$$\hat{H}_{\text{int}} = \frac{\hbar\Omega_{\text{SP}}}{2} \sum_{q=-1}^{1} \epsilon^q \hat{A}_q^{(SP)} + \text{h.c.}\,, \tag{6.35}$$

with Ω_{SP} is the Rabi frequency of the spectroscopy laser. The operators $\hat{A}_{-1}^{(SP)}$, $\hat{A}_0^{(SP)}$ and $\hat{A}_1^{(SP)}$ are the corresponding spin-flip operators

$$\hat{A}_q^{(SP)} = \sum_{m_J=-J_{\text{S}}}^{J_{\text{S}}} \langle J_{\text{S}}, m_J; 1, q \,|\, J_{\text{P}}, m_J + q\rangle \, |S, m_J\rangle \, \langle P, m_J + q| \tag{6.36}$$

for σ^-, π and σ^+ transitions, which include the Clebsch-Gordon-Coefficients $\langle J_{\text{S}}, m_J; 1, q \,|\, J_{\text{P}}, m_J + q\rangle$ of the transition.

- The term for Zeeman splitting

$$\hat{H}_{\text{B}} = \mu_{\text{B}} B g_J m_J\,, \tag{6.37}$$

where μ_{B} is the Bohr magneton, B is the amplitude of the magnetic field, and g_J is the Landé g-factor.

The spontaneous emission back to the S states and to the metastable D-states is implemented with 6 collapse operators

$$\hat{c} = \Big[\sqrt{\Gamma_{\text{SP}}}\hat{A}_{-1}^{(SP)}, \sqrt{\Gamma_{\text{SP}}}\hat{A}_0^{(SP)}, \sqrt{\Gamma_{\text{SP}}}\hat{A}_1^{(SP)}, ... \tag{6.38}$$

$$\sqrt{\Gamma_{\text{DP}}}\hat{A}_{-1}^{(DP)}, \sqrt{\Gamma_{\text{DP}}}\hat{A}_0^{(DP)}, \sqrt{\Gamma_{\text{DP}}}\hat{A}_1^{(DP)}\Big]\,, \tag{6.39}$$

where Γ_{SP} and Γ_{DP} are the linewidth of the $^2\text{S}_{1/2} \leftrightarrow {}^2\text{P}_{1/2}$ and $^2\text{D}_{3/2} \leftrightarrow {}^2\text{P}_{1/2}$ transition, respectively. In the experiment, a single spectroscopy-repump cycle is separated into a spectroscopy period with duration τ and a repump period with duration $T - \tau$ with $T = 2\pi/\omega_{\text{T}}$ as the period of the ions' oscillation in the trap. During the spectroscopy period, the system evolves from the initial state

$$\rho_0 = \frac{1}{2}\,|\text{S}, m_J = -\frac{1}{2}\rangle\,\langle \text{S}, m_J = -\frac{1}{2}| + \frac{1}{2}\,|\text{S}, J = +\frac{1}{2}\rangle\,\langle \text{S}, m_J = +\frac{1}{2}| \tag{6.40}$$

according to Eq. (6.33) to a final state $\tilde{\rho}_1$, which is used as the input density matrix for the repump period. The interaction Hamiltonian during the repump period reads

$$\hat{H}_{\text{int}} = \frac{\hbar\Omega_{\text{DP}}}{2} \sum_{q=-1}^{1} \epsilon^q \hat{A}_{\text{q}}^{(DP)} + \text{h.c.}\,, \tag{6.41}$$

where Ω_{DP} is the Rabi frequency of the repump laser. We repeat the numerical integration for N_{pulse} cycles and extract the motional excitation as the PRS signal. The results of the numerical simulation are presented together with the experimental results in Sec. 6.5.

6.4 Experimental setup

6.4.1 Laser systems

The spectroscopy light at 397 nm is provided by a frequency-doubled external cavity diode laser (ECDL)[1]. The blue light is transmitted from the laser laboratory through a 35-meter single mode fiber[2] to our setup. The frequency of the infrared light at 794 nm is referenced to a frequency comb[3]. The repetition rate and the off-resonant frequency of the comb is locked to 10 MHz from one of the hydrogen masers of PTB using standard techniques (Diddams et al., 2000). For the repumping from the $^2\mathrm{D}_{3/2}$ state via $^2\mathrm{P}_{1/2}$ back to $^2\mathrm{S}_{1/2}$, we use an ECDL[4] operating at 866 nm, which is sent through a 35-meter single mode[5] fiber from the laser laboratory to our setup.

The frequency of the spectroscopy laser is locked to the frequency comb. The schematics for the lock is shown in Fig. 6.7. The output port of the frequency comb with radiation at around $1458 - 1588$ nm is frequency-doubled with a periodically-poled Lithium Niobate (PPLN) crystal in one of the comb modules. The beat signal of the infrared part of the spectroscopy laser with the frequency-doubled comb is measured with a fast photodiode. The beat signal at around 70 MHz is mixed with a 30 MHz sine-wave from a direct digital synthesizer (DDS) board. The resulting signal at around 40 MHz is split into two parts. One of the signals (line a in Fig. 6.7) is mixed with a second DDS board at 40 MHz to DC and used as the error signal for a fast proportional-integral (PI) controller. The output of the PI controller is fed back into the laser diode

[1] Toptica TA-SHG pro
[2] OZ Optics QSMJ-3A3A-400-3/125-3-35
[3] MenloSystems FC1500
[4] Toptica DL pro
[5] Thorlabs 780HP-CUSTOM

through a CC-coupled fast current modulation port. The second signal (line b) is fed together with the 40 MHz signal from the same DDS board as for the first path into a phase frequency comparator (PFC). The output of the PFC is used to correct the laser frequency through the piezo actuator for the grating of the laser with a slow feedback bandwidth. The quality of the lock is monitored by measuring the frequency after the mixer M1 using a frequency counter[1].

6.4.2 AOM setup

The spectroscopy beam from the laser laboratory is further frequency shifted in the experimental laboratory with two additional acousto-optical modulators (AOMs) as depicted in Fig. 6.8. The first AOM[2] (AO397-1) is set up in a double-pass configuration and used for frequency scanning. It is supplied with a continuous RF-source at around 200 MHz extending over the experimental cycle with duration of typically 20 ms. The frequency shifted beam is transmitted through a single-mode polarization maintaining fiber (F397-1), which transforms the pointing variation of the beam, e.g. while scanning the frequency, into a power variation. The beam is sampled after the fiber after a polarizing beam splitter (PBS) cube and the power is stabilized through a feedback loop. The second AOM[3] (AO397-2), driven at around 413 MHz is used to generate the spectroscopy pulses. With a trap frequency ω_T on the order of 2 MHz, the synchronization condition requires spectroscopy laser pulses synchronized to the period ($2\pi/\omega_T \approx 500$ ns) of the ions' oscillation in the trap, with a pulse duration much shorter than this period. In the experiment, we use pulse durations between 50–125 ns. The short pulses are generated by switching the continuous wave from a frequency generator[4] with an RF-switch[5], which has a typical rise/fall time of 5 ns. The switching time of the AOM is limited by the sound speed of the acoustic wave and the diameter of the beam in the AOM crystal. For a beam diameter of 35 μm inside

[1] K+K Messtechnik GmbH Phasenmess-Karte K+K FXE
[2] Brimrose Corp. TEF-200-50-397
[3] Brimrose Corp. QZF-450-100-280
[4] Marconi Instruments 2024
[5] Mini-Circuits ZASWA-2-50-DR+

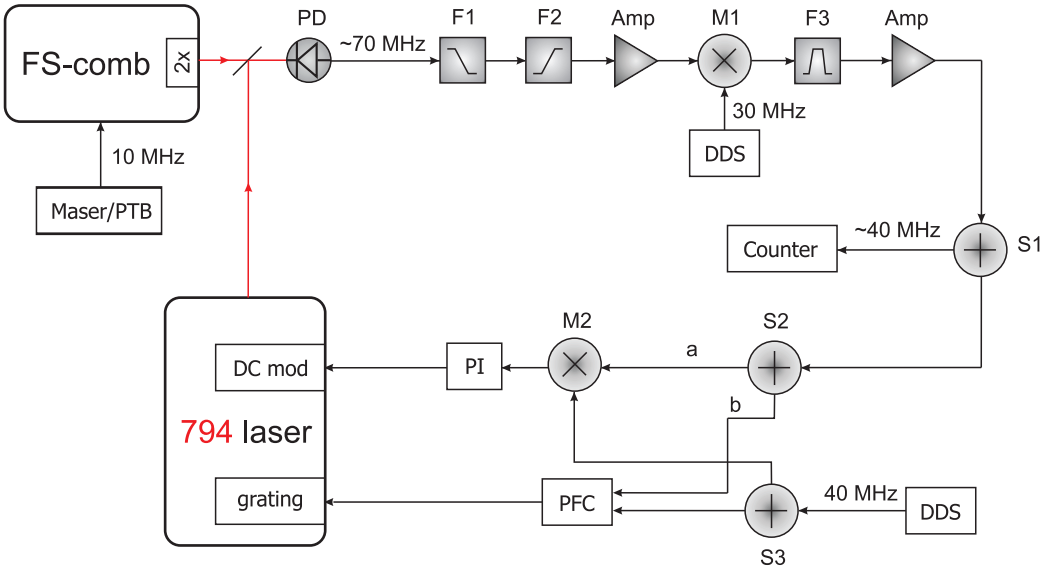

Figure 6.7: **Frequency lock for spectroscopy laser.** The beat signal of the infrared part of the spectroscopy laser at 794 nm with the frequency comb at around 70 MHz is mixed down to DC in two steps with two DDS boards at 30 MHz and 40 MHz, respectively, and appropriate filtering (F1-F3) to produce the error signal using a proportional-integral controller and a phase frequency comparator. The error signal is fed back to the DC-coupled fast current modulation of the laser diode head (path a) and the grating of the spectroscopy laser (path b). In order to monitor the quality of the lock, the signal after the mixer M1 at around 40 MHz is measured with a frequency counter. PD: photodiode. F1-F3: filters. M1-M2: mixers. S1-S3: RF splitters. Amp: apmplifier.

the AOM, the switching time is estimated to be 6 ns. A typical delay of $< 1\,\mu$s is not relevant, since it delays the entire probe sequence.

The repump laser is also frequency shifted with a double-pass AOM, which is driven with a frequency generator at 200 MHz and switched by an RF-switch. It is important to adjust the timing of the radio frequency (RF) pulses applied to the AOMs to prevent overlap of the spectroscopy and repump pulses. Both the spectroscopy and the repump laser are sent into the chamber along the axial direction. A Glan polarizer in front of the chamber ensures the desired linear polarisation for both beams.

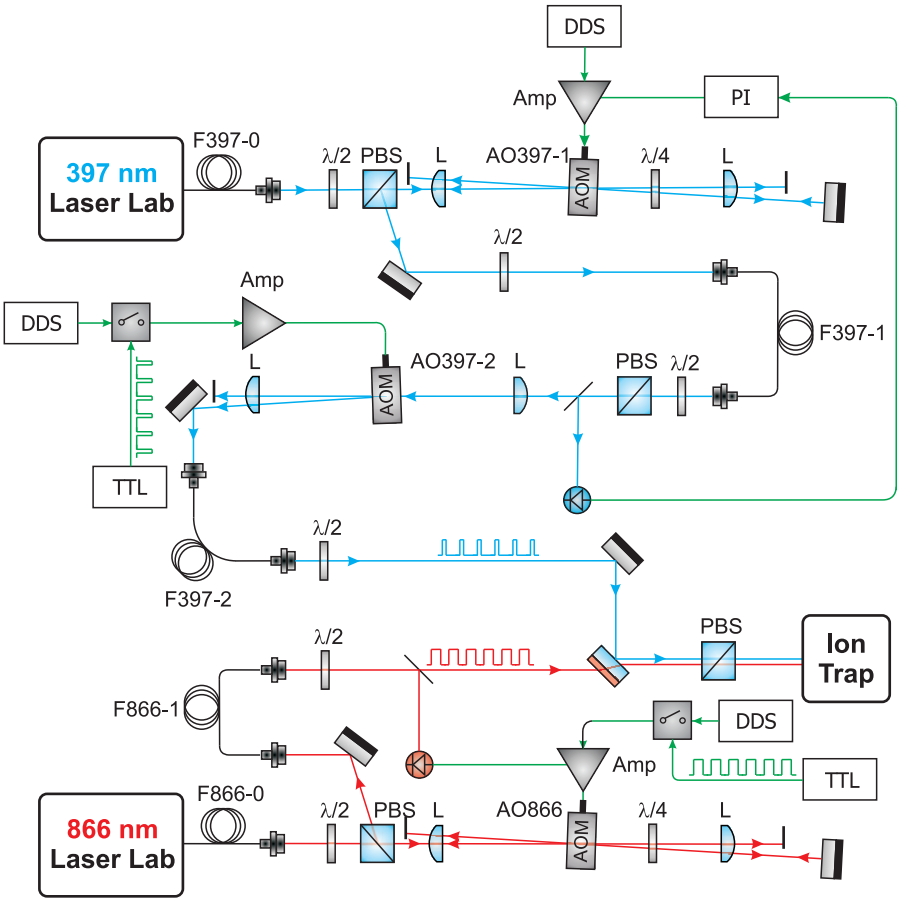

Figure 6.8: **AOM setup for spectroscopy laser and repump laser.** The short spectroscopy pulses at 397 nm are generated using two AOMs, where the first AOM (AO397-1) in a double-pass configuration is used to control the frequency and stabilize the power of the spectroscopy laser. The second AOM (AO397-2) is switched by a fast RF switcher to produce the short pulses. After each spectroscopy pulse, a repump pulse at 866 nm is applied. Both the frequency and the duration of the repump pulses are controlled using a double-pass AOM (AO866). PBS: polarizing beam splitter. L: lense. $\lambda/2$: half-wave plate. $\lambda/4$: quarter-wave plate.

6.4.3 Loading of a two-ion crystal

In order to prepare a two-ion crystal consisting of $^{25}Mg^+$ and $^{40}Ca^+$ ions, we first load a single $^{25}Mg^+$ ion into the trap. A ^{25}Mg-enriched oven is supplied

with a current of 4 A by a computer-controlled power supply[1]. Photoionization is implemented via a two-photon process with the first photon provided by a frequency-quadrupled diode laser at 285 nm and the second photon by the same laser at 285 nm or the Doppler cooling laser at 280 nm (Kjaergaard et al., 2000). The oven typically takes several minutes to heat up. In the mean time, we keep the Doppler cooling laser for magnesium ions on and monitor the photon count rate detected by the photomultiplier tube (PMT). Once a $^{25}Mg^{+}$ ion appears in the trap, the count rate rises up above a threshold ($\sim$ 200 kcounts/s), the oven power supply is switched off and a mechanical shutter blocks the photon ionization laser automatically.

For additionally loading a single $^{40}Ca^{+}$ ion into the trap, we ramp down the endcap voltage to 200 V and the RF power to $\sim$ 1.5 W, which corresponds to an axial trap frequency of 795 kHz and a radial trap frequency of $\sim$ 2.5 MHz for a single $^{25}Mg^{+}$ ion. A second computer-controlled power supply provides a current of 4.2 A for the calcium oven. The photoionization is achieved with simultaneous irradiation of two photoionization lasers at 423 nm from a frequency-doubled diode laser[2] and 375 nm from a diode laser (Lucas et al., 2004). The loading process takes on average several minutes and is mainly limited by the thermal conductivity of the oven. In contrast to the magnesium ions, which can be observed from the fluorescent light after being trapped, the $^{40}Ca^{+}$ ions are not visible with our detection setup. The presence of the second ion in the trap is indicated by a sudden change of position of the bright $^{25}Mg^{+}$ ion on the camera. As an alternative method, we monitor the fluorescence rate from the $^{25}Mg^{+}$ ion on the PMT while loading $^{40}Ca^{+}$ ions, while at the same time an electric modulation at the trap frequency of the ip mode for the target crystal ($\omega_T^{ip} \approx 2\pi \times 688$ kHz) is applied to the endcaps. This electric modulation does not change the fluorescence rate for a single $^{25}Mg^{+}$ in the trap, but will heat up the two-ion crystal via a coherent drive and therefore reduce the fluorescence rate of the $^{25}Mg^{+}$ ion. The appearance of the $^{40}Ca^{+}$ ion in the trap is indicated by a sudden reduction of the count rate down to a level lower than a preset threshold.

[1] EA Electro-Automatik EA-PS 2042-06B
[2] Toptica DL Pro

After trapping the second ion, the power supply for the Calcium oven is ramped down and a mechanical shutter blocks the photoionization laser at 423 nm.

We ramp up the endcap voltage and the RF power back to 2000 V and $\sim$ 5 W. The components in the trap are verified by measuring the trap frequencies with the modulation technique and with Raman spectroscopy. With the two-ion crystal of $^{25}Mg^{+}$ and $^{40}Ca^{+}$ in the trap, the axial trap frequencies of the ip and op modes become $\omega_T^{ip} = 2\pi \times 1.92\,\text{MHz}$ and $\omega_T^{op} = 3.50\,\text{MHz}$.

6.5 Experimental results

6.5.1 Resonance line

Using photon recoil spectroscopy, the resonance curve for the $^2S_{1/2} \leftrightarrow {}^2P_{1/2}$ transition of the $^{40}Ca^{+}$ ion is measured by scanning the frequency of the double pass AOM (AO397-1) in the range of $175 - 225\,\text{MHz}$ while the single pass AOM (AO397-2) is used for generating the pulses. The final resonance averaged over 12 scans corresponding to the curve is depicted in Fig. 6.9. In a single scan, the frequency of the AOM is tuned in a random order to one of the 50 scan points and a single experimental cycle is repeated on each scan point for 250 times. Typically 70 spectroscopy pulses are applied. The measured resonance curve has a full width at half maximum (FWHM) of $\sim$ 34 MHz, which is caused by the Fourier broadening of the 50 ns short spectroscopy pulses and the Zeeman broadening in the presence of a bias magnetic field of $5.84(1) \times 10^{-4}\,\text{T}$. Additional line broadening from the saturation effect associated with the complete depletion of the motional ground state is avoided by choosing an appropriate number of spectroscopy-repump-cycles N_{pulses}, so that the excitation on resonance corresponds to approximately 80% of the maximum excitation.

The experimental data is compared with the result of the numerical simulation of the eight level system described in Sec. 6.3.5.2. The motional excitation extracted from the numerical simulation is corrected for experimental imperfections by a reduced signal amplitude of around 0.85 and a signal offset of around 0.15 reflecting deviation of the maximum excitation from one and non-zero ex-

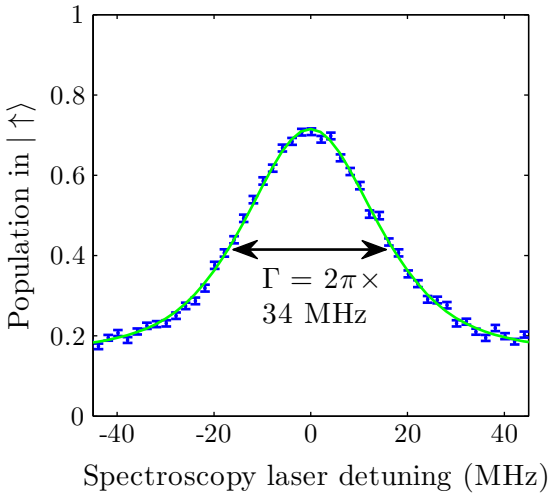

Figure 6.9: **Resonance curve.** The resonance curve for the $^2S_{1/2} \leftrightarrow {}^2P_{1/2}$ transition averaged over 12 scans (*blue dots*). The *green line* is the result of a numerical simulation of the eight level system and has been adjusted in amplitude by 0.93 and in offset by 0.15 to account for experimental imperfections.

citation at large detunings, respectively. Both effects are caused by off-resonant excitation of the Raman lasers during the 100 μs STIRAP pulse.

6.5.2 Photon sensitivity

We investigate the sensitivity of photon recoil spectroscopy using the branching ratio of an excited ion decaying into the $^2S_{1/2}$ or the $^2D_{3/2}$ state. In Fig. 6.10, the motional excitation is taken as a function of the spectroscopy-repump-cycles with the spectroscopy laser on resonance. The spectroscopy pulse has a duration of $\sim$ 125 ns corresponding to a duty cycle of $d = 0.24$ to ensure the highest excitation rate as described in 6.3.5.1. Here we distinguish two cases:

With repumper With a repumper pulse after each spectroscopy pulse, the population decayed into the $^2D_{3/2}$ state will be pumped back to the $^2S_{1/2}$ state before each new spectroscopy pulse starts. The motional excitation increases with the number of pulses and the population is depleted out of the motional ground state. The PRS signal stops increasing if all the population is in the motional

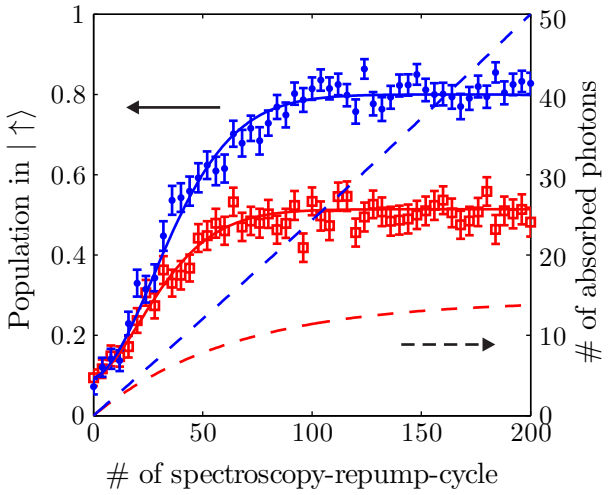

Figure 6.10: **Photon sensitivity of PRS.** The sensitivity of PRS is probed using the branching ratio for an excited ion decaying into the $^2S_{1/2}$ and $^2D_{3/2}$ state. With the spectroscopy laser tuned on resonance, the PRS signal is plotted as a function of the number of spectroscopy-repump-cycles N_{pulses}. The motional excitation increases in the presence of the repumper (*blue dots*, left axis). Without the presence of the repumper (*red squares*, left axis) the PRS signal ceases growing at a signal level of around 0.5, since the ion absorbs on average 15.5 photons before it decays to the $^2D_{3/2}$ state. The comparison with numerical simulations of the eight level system (*solid lines*) allows extracting the Rabi frequency Ω_0 of the spectroscopy laser and deriving the integrated number of absorbed photons with and without the repumper (*blue* and *red dashed line*, respectively, right axis).

excited states. This effect leads to a saturation broadening of the resonance line if too many spectroscopy pulses are used.

Without repumper In case there is no repumper pulse after each spectroscopy pulse, the metastable $^2D_{3/2}$ state becomes a dark state. The population accumulates in the $^2D_{3/2}$ state until the next initialization pulse of a new experimental cycle. An excited ion decays into the $^2S_{1/2}$ and $^2D_{3/2}$ state with a branching ratio of 14.5 : 1 (Ramm et al., 2013). After a significant spectroscopy time, the ion has absorbed $\overline{N} = 15.5$ photons on average. This number of photons will not give rise to a motional excitation of 0.94 as predicted by the simple model Eq. (6.21),

but a lower excitation level of ~ 0.5 depicted as red squares in Fig. 6.10. The lower excitation level is caused by the geometric distribution of absorbed photons in the absence of the repumper as described in Sec. 6.3.4. With the precise knowledge of the number of absorbed photons in a single experiment, this curve is used to calibrate the intensity of the spectroscopy laser. The experimental data (red squares) is compared with the result of the numerical simulation described in Sec. 6.3.5.2. Similarly, the simulation result is corrected for experimental imperfections as described in the last section. A Rabi frequency of $\Omega_0 = 2\pi \times 5.6\,\mathrm{MHz}$ for the spectroscopy laser is extracted.

From the numerical simulation, the mean number of scattered photons is calculated according to

$$\overline{N}(t) = \Gamma_{\mathrm{SP}} \int_0^t p_{\mathrm{P}}(t')\,\mathrm{d}t'\,, \tag{6.42}$$

where $p_{\mathrm{P}}(t)$ is the population in the $^2\mathrm{P}_{1/2}$ state. With the repumper switched on, the mean number of scattered photons increases linearly with the number of spectroscopy pulses (*blue dashed line* in Fig. 6.10). After absorbing 9.5(1.2) photons, a signal level of 0.5 corresponding to a SNR of 1 is achieved. Without the presence of the repumper, the mean number of scattered photons saturates at 15.5 (*red dashed line* in Fig. 6.10).

6.5.3 Two-point sampling

An absolute frequency measurement is performed on the $^2\mathrm{S}_{1/2} \leftrightarrow {}^2\mathrm{P}_{1/2}$ transition using the two-point sampling technique. The atomic excitation is probed with the spectroscopy laser at frequencies ($\nu_{\mathrm{l}} = \nu_{\mathrm{probe}} - \Delta\nu_{\mathrm{FWHM}}/2$, $\nu_{\mathrm{r}} = \nu_{\mathrm{probe}} + \Delta\nu_{\mathrm{FWHM}}/2$), where $\Delta\nu_{\mathrm{FWHM}}$ is the full width at half maximum of the spectrum. At these frequencies, the motional excitation reaches approximately a level of $p_{\mathrm{l,r}} = p(\nu_{\mathrm{l,r}}) \approx 0.5$. In every single scan the experiment is repeated at both frequencies for $N_{\mathrm{cycles}} = 5 \times 250$ times. The π-detection method with threshold at 0.5 is used for state discrimination on the $^{25}\mathrm{Mg}^+$ ion (Hemmerling et al., 2012). This method reduces the effective number of cycles to a typical value of $N'_{\mathrm{cycles}} = 1039(12)$. This leads to a quantum projection noise for the detected excitation probability of $\sigma^{(p)} = \sqrt{p(1-p)/N_{\mathrm{cycles}}} \approx 0.0155$. The excitation difference at

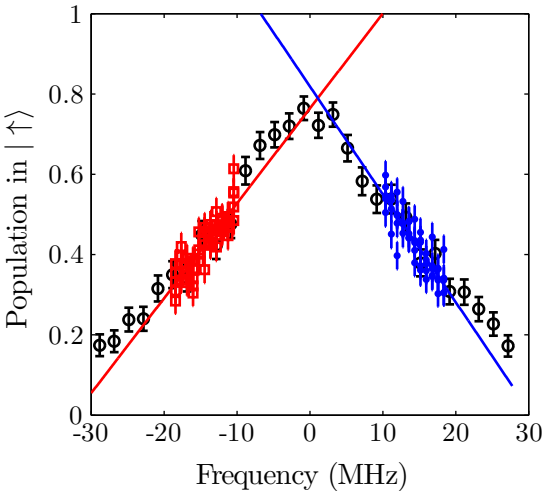

Figure 6.11: **Frequency discriminant.** The excitation probability is probed in a small frequency range at the left and right slope of the resonance line (*black circles*). From linear fits (*red and blue lines*) to these excitation probabilities (*red squares* and *blue dots*), the frequency discriminant D is derived.

the two probing frequencies $\delta p = p_\mathrm{r} - p_\mathrm{l}$ is used as an error signal to steer the probing frequency ν_probe in the following scan

$$\nu_\mathrm{probe}^{(i+1)} = \nu_\mathrm{probe}^{(i)} + k_\mathrm{P}\delta p^{(i)} + k_\mathrm{I} I^{(i)}\,, \tag{6.43}$$

where k_P and k_I are the proportional gain and the integral gain, respectively and $I^{(i)}$ is the integrated error until the ith measurement point

$$I^{(i)} = \sum_{j=1}^{i} \delta p^{(j)}\,. \tag{6.44}$$

The superscript i indicates individual scans. The uncertainty for the quantity δp rescales to $\sigma^{(\delta p)} = \sqrt{\sigma_\mathrm{l}^{(p)} + \sigma_\mathrm{r}^{(p)}} \approx 0.0220$.

The excitation difference δp is converted into an absolute frequency ν through the frequency discriminant D according to

$$\nu = \nu_\mathrm{probe} - D \cdot \delta p\,. \tag{6.45}$$

We determine the frequency discriminant experimentally for each single measurement day. The excitation probability is probed in a frequency range of about

4 MHz around ν_l and ν_r (red squares and blue dots in Fig. 6.11). Linear fits of the two sets of data give the slopes (k_1, k_2) of the resonance curve at around ν_l and ν_r, from which the frequency discriminant is derived

$$D = \frac{1}{|k_1| + |k_2|}\,. \tag{6.46}$$

The influence of the control loop on the frequency measurement is minimized by setting the parameters of the PI controller to be much smaller (typically $k_\mathrm{P} = 1\,\mathrm{MHz}$ and $k_\mathrm{I} = 0.63\,\mathrm{MHz}$) than the frequency discriminant, which is typically on the order of 20 MHz. While converting the excitation difference to frequency, the uncertainty propagates according to

$$\sigma_\nu = D|\delta p|\sqrt{\left(\frac{\sigma^{(\delta\mathrm{p})}}{\delta p}\right)^2 + \left(\frac{\sigma^\mathrm{D}}{D}\right)^2}, \tag{6.47}$$

where the first term contains the quantum projection noise and the second one the calibration error σ^D for the frequency discriminant.

6.5.4 Distribution tests

The validity of the data is checked against statistical tests using the Statistics Toolbox of Matlab. The reader is referred to textbooks for statistics e.g. Lehmann et al. (2005) for further details. The general procedure for a distribution test is as following

- Assert a null hypothesis H_0 about a population that you would like to test, e.g. H_0: the sample comes from a normal distribution with unknown mean and variance.
- Assert an alternative hypothesis H_1 which is against the null hypothesis, e.g. H_1: the sample does not come from a normal distribution.
- To conduct the hypothesis, the test statistic T based on the sample is computed. Under the null hypothesis, the distribution of the test statistic T should be known.

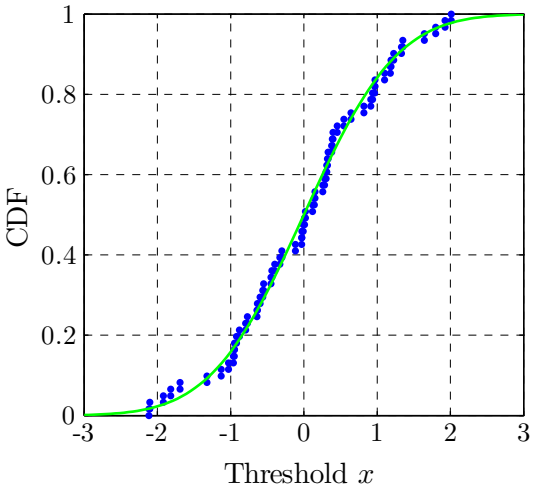

Figure 6.12: **Normality of data.** The normality of the data is tested using the Kolmogorov-Smirnov test. The empirical cumulative distribution function (CDF) $F(x)$ of the data (*blue dots*) is plotted together with the CDF $G(x)$ of the hypothesized standard normal distribution (*green line*).

- Calculate the p-value of the test, which is the probability, under the null hypothesis H_0, of obtaining a value of the test statistic as extreme or more extreme than the value computed from the sample.

- Once the p value of the test is less than a certain significance level α, the test rejects the null hypothesis. If the p value is greater than α, there is insufficient evidence to reject the null hypothesis.

6.5.4.1 One-sample tests

In the first step, we verify that the result from the two-point sampling represents a normal distribution. For this purpose, statistical tests (Kolmogorov-Smirnov test, Lillifors test, Jarque-Bera test, Shapiro-Wilk test) are performed on the data obtained on each single measurement day.

The Kolmogorov-Smirnov test is conducted to decide if the sample X comes from a standard normal distribution $\mathcal{N}(X)$. As test statistic (KS-statistic), the difference between the empirical cumulative distribution function (CDF) $F(x)$ of

the data and the CDF

$$G(x) = \int_{-\infty}^{x} \mathcal{N}(X)\,\mathrm{d}X \tag{6.48}$$

of the hypothesized distribution is evaluated

$$T^{\mathrm{KS}} = \max_{x}(|F(x) - G(x)|)\,. \tag{6.49}$$

The empirical cumulative distribution function $F(x)$ gives the probability that the sample X is smaller or equal than a threshold value x. Before conducting the Kolmogorov-Smirnov test, the results $\nu^{(i)}$ from two-point sampling are converted to

$$X^{(i)} = \frac{\nu^{(i)} - \overline{\nu}}{\sigma(\nu)}\,, \tag{6.50}$$

with $\overline{\nu}$ and $\sigma(\nu)$ as the mean and the standard deviation of the sample, respectively, so that the new sample $X^{(i)}$ has the mean value 0 and a standard deviation of 1. The empirical CDF of the sample X and the CDF of the hypothesized distribution is depicted in Fig. 6.12. The test statistic calculated for the sample in Fig. 6.12 equals $T^{\mathrm{KS}} = 0.058$, indicating a small difference between the two CDFs. The p-value gives in this case the probability that the KS-statistic calculated from a new sample Y of a standard normal distribution (null hypotheses) is greater or equal than the KS-statistic $T^{\mathrm{KS}} = 0.058$ calculated for the test sample X. With a p-value of 0.98 larger than the chosen significance level $\alpha = 0.05$, the Kolmogorov-Smirnov test does not provide enough evidence to reject the null hypotheses that the sample X comes from a standard normal distribution.

Similar procedures are applied on the data using Lilliefors test, Jarque-Bera test and Shapiro-Wilk test. All data on 7 different measurement days passed the normality tests.

6.5.4.2 Two-sample tests

In addition to the normality tests, the compatibility of measurements on different days is checked using two-sample tests (two-sample Kolmogorov-Smirnov test, two-sample t-test), which verify if those measurements arise from the same normal distribution. We perform the tests on each possible combination of two data sets from in total 7 measurement days. The numbers of rejections at a significance

Table 6.1: **Compatibility of data.** The compatibility of data sets measured on different days is checked using two-sample tests. The number of rejections for each data set compared with the other data sets are listed in the table.

data set		1	2	3	4	5	6	7
# of rejections	two-sample KS-test	2	0	1	0	2	0	1
	two-sample t-test	3	1	1	0	3	1	1

level $\alpha = 0.05$ for each data set compared with the other 6 data sets are listed in Tab. 6.1. The two-sample tests reject the compatibility of data set 1 and 5 with the other measurements. We suspect that the data was contaminated by drifts in the experimental parameters, such as STIRAP and ground-state cooling efficiency and calibration of the pulse spectrum. After excluding the data sets 1 and 5, all the other sets pass the two-sample tests.

6.5.5 Absolute frequency

6.5.5.1 Probe frequency

We derive the probe frequency of the spectroscopy laser from the beat measurement of the undoubled spectroscopy laser at 794 nm with a frequency comb (Sec. 6.4.1). Including the frequency doubling and the two AOMs, the probe frequency of the spectroscopy laser at 397 nm is given by

$$\nu_{\text{probe}} = 2 \times (n_{\text{comb}}\nu_{\text{rep}} + \nu_{\text{off}} + \nu_{\text{beat}}) + 2 \times \nu_{\text{AO397-1}} + \nu_{\text{AO397-2}}\,, \tag{6.51}$$

where $n_{\text{comb}} = 1510443$ is the comb tooth number of the frequency comb, $\nu_{\text{rep}} = 250,000,076.25\,\text{Hz}$ and $\nu_{\text{off}} = 40\,\text{MHz}$ are the repetition rate and offset frequency of the comb, respectively, $\nu_{\text{beat}} = 70\,\text{MHz}$ is the beat frequency of the infrared spectroscopy laser at 794 nm with the frequency comb, $\nu_{\text{AO397-1}}$ and $\nu_{\text{AO397-2}}$ are the frequencies of the double pass AOM (AO397-1) and the single pass AOM (AO397-2), respectively. The factor 2 in front of the parenthesis considers the frequency doubling of the spectroscopy laser from 794 nm to 397 nm.

6.5.5.2 Final frequency

From the data that passed the distribution tests, the weighted average of all the frequencies measured on a single day is computed according to

$$\overline{\nu} = \frac{\sum_i w^{(i)} \nu^{(i)}}{\sum_i w^{(i)}}; \tag{6.52}$$

with the weight given by $w^{(i)} = 1/(\sigma_\nu^{(i)})^2$. The variance of the mean equals

$$\sigma_{\overline{\nu}}^2 = \frac{1}{N} \frac{\sum_i w^{(i)} (\nu^{(i)} - \overline{\nu})^2}{\sum_i w^{(i)}} \tag{6.53}$$

with N as the number of scans on that measurement day. A weighted fit of the center frequencies from different measurement days with the weights $1/\sigma_{\overline{\nu}}^2$ as depicted in Fig. 6.13a gives a center frequency $\nu = 755,222,765,896\,\text{kHz}$ with a statistical uncertainty of 42 kHz.

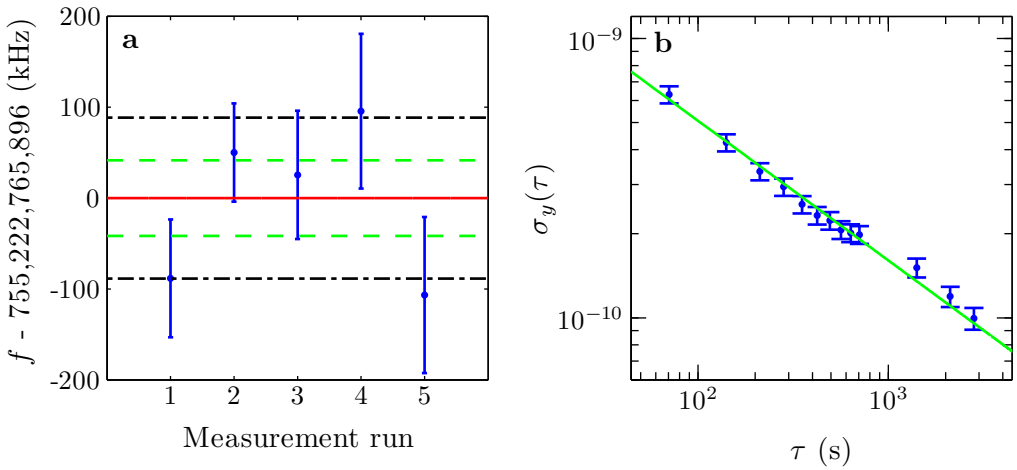

Figure 6.13: **Absolute frequency measurement.** (**a**) From the results on 5 different measurement days (*blue dots*), the absolute frequency for the $^2S_{1/2} \leftrightarrow {}^2P_{1/2}$ transition is derived (*red line*), while the *black dash-dot lines* and the *green dashed lines* give 68.3% prediction bounds for the measurement and the mean, respectively. (**b**) From the concatenated data of all the measurements, the overlapped Allan-deviation for the fractional frequency is derived (*blue dots*). This results in an inferred instability of 5.1×10^{-9} for an averaging time of 1 s.

Concatenating individual measurements $\nu^{(i)}$ performed on different days, the Allan-deviation for the fractional frequency

$$y^{(i)} = \frac{\nu^{(i)} - \nu}{\nu} \tag{6.54}$$

is derived (Fig. 6.13b). This gives an instability of 5.1×10^{-9} for an averaging time of 1 s. From the quantum projection noise limit for the excitation difference $\sigma^{(\delta p)}$ in Sec. 6.5.3, the corresponding quantum limit for the fractional frequency is derived to be

$$\sigma_{\mathrm{y}}^{\mathrm{QPN}} = \frac{D\sigma^{(\delta p)}}{\nu}\sqrt{T} = 5.8(9) \times 10^{-9}\,\sqrt{\mathrm{s}}\,, \tag{6.55}$$

with $T = 70.5\,\mathrm{s}$ as the time for repeating the experimental cycles for $N_{\mathrm{cycles}} = 1250$ times. This indicates that quantum projection noise is the limiting noise source of the measurement.

6.6 Systematic shifts

Several effects that can introduce systematic shifts are discussed in this section.

6.6.1 AC-Stark shift

In the presence of the spectroscopy laser, the atomic levels will be shifted via an AC-Stark coupling, which depends on the frequency, intensity and polarization of the laser. This shift was determined experimentally by measuring the center frequencies at three different laser intensities. While changing the power of the laser we increase the number of pulses at the same time to maintain the motional excitation. The intensity of the spectroscopy laser on the ion is extracted from the intensity calibration curve as described in Sec. 6.5.2. We performed frequency measurements at three different intensities with saturation parameters $s = (0.074, 0.13, 0.21)$, corresponding to Rabi frequencies of the spectroscopy laser $\Omega_0 = 2\pi \times (4.3, 5.6, 7.3)\,\mathrm{MHz}$. The center frequencies for different laser intensities are determined with the two point sampling technique as described in Sec. 6.5.5.2

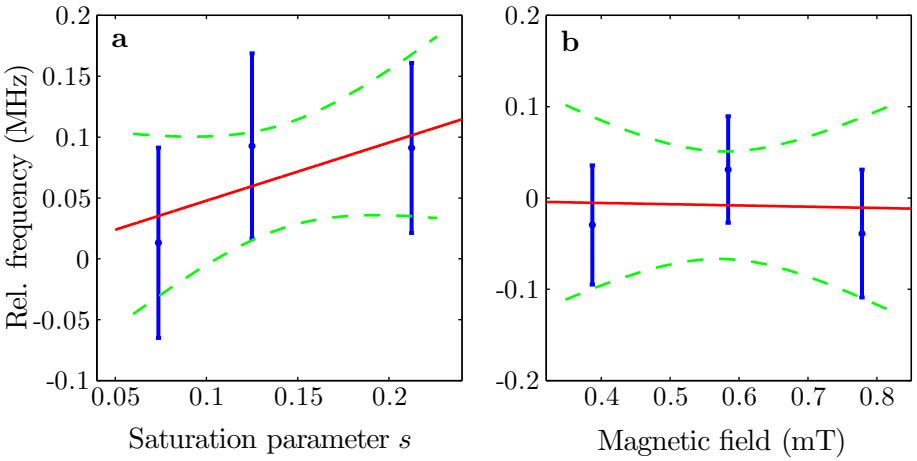

Figure 6.14: **Stark and Zeeman shifts.** (**a**) Stark shift measurement. (**b**) Zeeman shift measurement. The center frequency of the $^2S_{1/2} \leftrightarrow {}^2P_{1/2}$ transition is determined with the two point sampling technique at different laser intensities and different magnetic field strengths. A linear fit is used to extract the Stark and Zeeman shift (*red solid line*) with the corresponding errors (*green dashed line*) derived from the 68.3% prediction bound of the fit.

with corresponding error bars shown in Fig. 6.14a. A linear fit with two parameters $y = ax + b$ gives a shift of 60 kHz at the intensity level $s = 0.13$ with an uncertainty of 44 kHz corresponding to the 68.3% prediction bound of the fit.

The repump laser can cause a similar shift on the spectroscopy transition. An interleaved sequence separating the spectroscopy pulses from the repumping pulses leaves the relevant levels of the spectroscopy transition unperturbed from the AC Stark effect of the repump laser.

6.6.2 Zeeman shift

In the experiment, a weak magnetic field defining the quantization axis is used. The $^2S_{1/2}$ and $^2P_{1/2}$ states are split to several Zeeman sublevels, therefore introducing Zeeman-shifted line components. An excitation imbalance of different line components will introduce a lineshape asymmetry and therefore a shift of the observed center frequency. Such an imbalance can result from an imbalanced

σ^+/σ^- polarization of the spectroscopy and repump lasers. In the experiment, we choose the polarization of the spectroscopy and repump lasers to be linearly polarized at the entrance window, so that there are all three polarization components in these lasers with the same amount of σ^+ and σ^- light. This will cause a symmetric line-broadening, but no shift of the center frequency. A polarization distortion at the entrance window could cause imbalance of σ^+/σ^- polarized light and therefore could lead to a shift of the center frequency.

In order to determine the shift induced by the Zeeman effect, the transition frequency is measured at three different magnetic fields 0.387(2) mT, 0.584(1) mT and 0.779(3) mT with the two-point sampling technique. The center frequencies for different magnetic field strengths with corresponding error bars as shown in Fig. 6.14b. A linear fit with two parameters $y = ax + b$ gives a shift of -8 kHz at the magnetic field 0.584 mT with an uncertainty of 59 kHz given by the 68.3% prediction bound of the fit.

6.6.3 Spectroscopy laser envelope shift

The spectroscopy pulse with a duration of 125 ns is Fourier-broadened to 8 MHz. The switching AOM (AO397-2) has a limited bandwidth. The center frequency and the limited bandwidth of the AOM together define a frequency-dependent efficiency function of the AOM (response function), which depends on the alignment of the beam/AOM. For the typical application, where the AOM is driven with a continuous RF source, the response function manifests itself in a frequency-dependent variation of the efficiency. In our case, where the AOM is driven with short RF pulses, the AOM does not imprint the spectrum of the RF source directly onto the optical carrier frequency ω_L, but rather multiplies every frequency component with the response function. This effectively deforms the spectrum of the RF source and therefore shifts the center of the original spectrum. We determine this shift by measuring the beat signal of the unshifted spectroscopy laser with the 1st diffraction order of the AOM transmission as shown in Fig. 6.15. The spectrum of the beat signal has a comb structure with a spacing determined by the repetition rate of the spectroscopy pulses. Since the spontaneous emission rate of the ion is much larger than the repetition rate of the spectroscopy

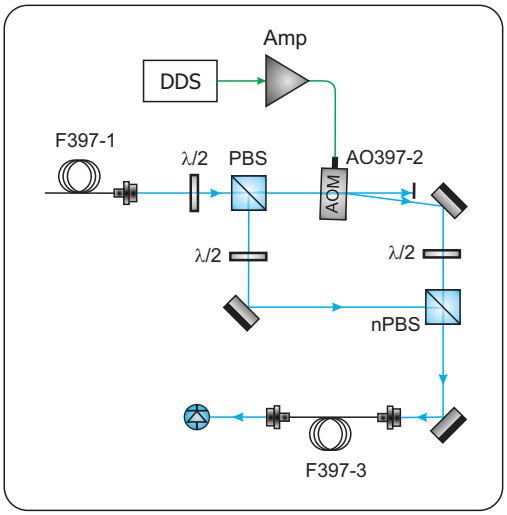

Figure 6.15: **Optical setup for envelope shift measurement.** The envelope shift of the spectroscopy laser is determined from a beat measurement of the unshifted spectroscopy laser with the 1st diffraction order of AOM transmission. The focusing lenses before and after the AOM are omitted here for clarity.

laser, the atom actually sees only a single spectroscopy pulse and the coherence between subsequent pulses does not play a role. Therefore the atomic response is rather determined by the envelope of this comb structure, corresponding to the Fourier transform of a single pulse. In order to measure the center of the envelope of the beat spectrum, we reduce the repetition rate of the spectroscopy pulse by a factor of 10 (from 1.92 MHz to 192 kHz) to reduce the spacing between the individual comb teeth without changing the spectral width of the envelope and increase the number of pulses to engage a better SNR. The envelope of the dense comb spectrum is extracted and smoothed afterwards to remove electronic noise peaks in the spectrum. This envelope function is fitted with

$$y = a \cdot \mathrm{sinc}^2 \left[\frac{\pi(f - f_0)}{\sigma} \right] + o, \tag{6.56}$$

which allows us to determine the imprinted center f_0 by deflecting through the AOM. The envelope shift

$$\Delta\nu_{\mathrm{env}} = f_0 - \nu_{\mathrm{drive}} \tag{6.57}$$

against the drive frequency ν_{drive} depends to 1st order linearly on the drive frequency as shown in Fig. 6.16b. We choose the drive frequency in such a way that

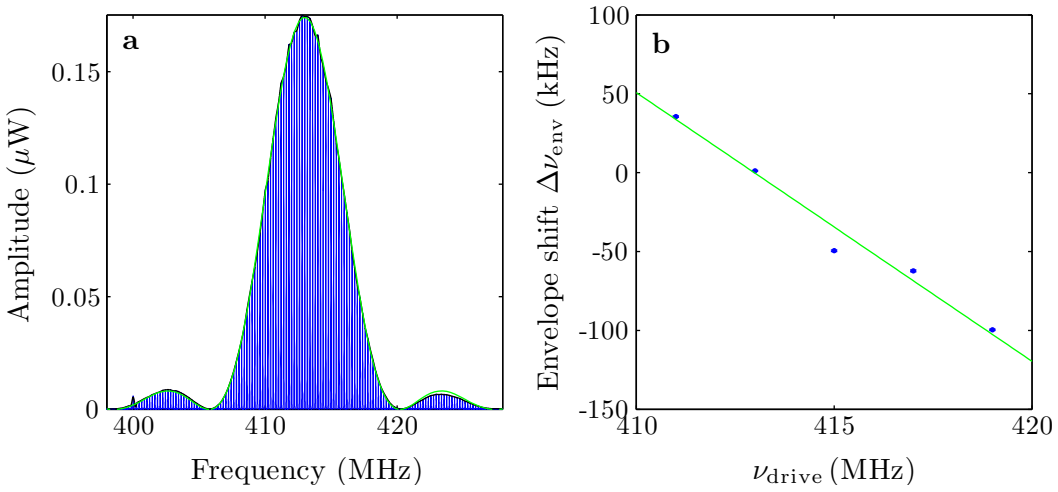

Figure 6.16: **Envelope shift.** (**a**) The periodically repeated spectroscopy pulses form a comb structure (*blue line*) with the spacing of the comb teeth determined by the repetition rate of the spectroscopy laser. The envelope of this spectrum is extracted followed by smoothing with the method of moving average (*black line*). The smoothed envelope is fitted using a squared sinc-function to determine the center of the envelope (*green line*). (**b**) The frequency-dependent response function of the AOM shifts the spectrum of the short spectroscopy pulses. These envelope shifts depend to 1st order linearly on the drive frequency of AOM.

the envelope shift is close to zero. The residual shift, which lies typically within ±50 kHz, is determined with the beat measurement on a day-to-day basis, while an uncertainty of 15 kHz for each individual measurement is derived from the standard deviation of ten subsequent beat measurements performed on a single day.

6.6.4 Photodiode calibration

The photodiode-amplifier-spectrum analyser chain used to measure the beat of the unshifted spectroscopy laser with the first order of diffraction of the AOM has also a frequency dependent response. This is measured using two frequency-doubled neodymium-doped yttrium aluminum garnet (Nd:YAG) lasers. Consider two CW lasers with constant power. The strength of the beat signal depends on the power, polarization and wavelength of the two lasers, and the response

function of the photodiode. Keeping all the laser parameters fixed, the strength of the beat signal is proportional to the response function of the RF detection chain at the frequency of the beat. In the calibration process, we lock one of the two lasers to an iodine absorption line. The frequency difference of the two lasers is swept continuously and the maximum value of the beat signal during the sweeps are recorded (Fig. 6.17a). An independent power measurement indicates that the power of the two lasers is not changing during the sweep, so that the recorded maximum of the beat signal reflects the frequency response function of the detection chain (*black dots* in Fig. 6.17b). The response function of the photodiode to RF frequency is determined with lasers at 532 nm, we have to assume that the RF response of the photodiode is independent of wavelength and apply it to derive a detection-chain induced shift for the spectroscopy laser at

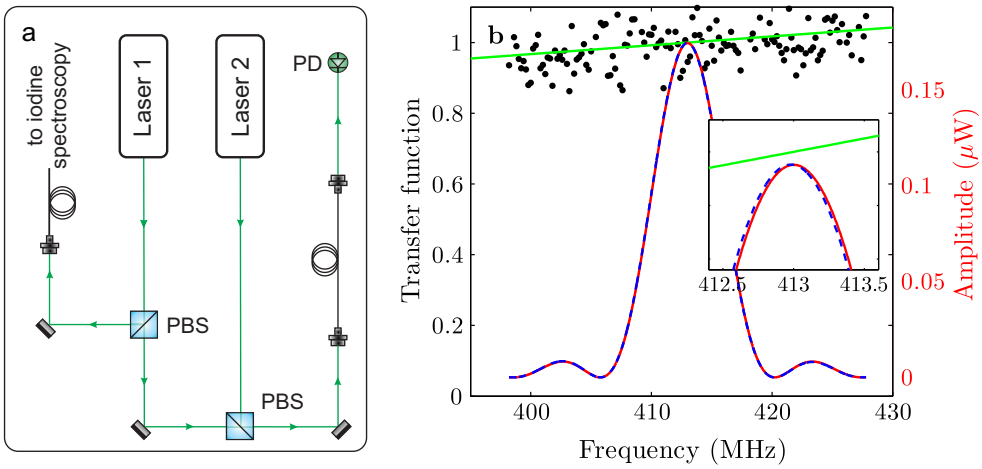

Figure 6.17: **Calibration of photodiode.** (**a**) Optical setup for calibrating the photodiode used for the beat measurement. The maximum value of the beat signal of the two lasers is recorded with a spectrum analyzer while sweeping their frequency difference. (**b**) The RF spectrum imprinted onto the spectroscopy laser (*blue dashed line*) is measured with a photodiode. The photodiode itself has a slightly frequency-dependent response (*green solid line*) corresponding to a positive slope here and therefore shifts the center of the beat signal to higher frequency (*solid red line*). The inset shows a zoom in into a smaller frequency range indicating a shift of the maximum of the spectrum to higher frequency.

397 nm.

In a small frequency range, the response function is approximated with a linear fit and the induced shift is modelled by multiplying a squared sinc function with the linearized response function. The new maximum of the resulting spectrum is interpreted as the new center and the shift against the original sinc-function is determined to be 22.0(3) kHz.

6.6.5 Doppler shift induced damping and anti-damping

The spectrum of the investigated transition is generated via detection of motional excitations. This results in a line-distortion if the motional excitation is not symmetric with respect to the detuning of the spectroscopy laser as in the case for photon recoil spectroscopy. A blue detuned laser excites the motion with higher probability than a red detuned laser with the same magnitude of detuning $|\Delta|$ because of Doppler shift induced damping and anti-damping. The measured center frequency shifts to the blue side. The shift is explained in the following with a simple model derived by K. Hammerer (Wan et al., 2014).

Under the effect of synchronous spectroscopy laser pulses, the momentum of the ion increases from pulse to pulse. The drift moment for the momentum

$$d_p(\Delta) = \langle p_n \rangle - \langle p_{n-1} \rangle \tag{6.58}$$

describing the change of the mean momentum in a single cycle is a function of the detuning of the laser from the atomic transition. Ignoring the Doppler shift, the drift moment of the momentum is an even function of the detuning and it transfers the atomic spectrum to the ions' motion without shifting the center. When including the Doppler shift, every variable that depends on the detuning of the laser now carries an implicit dependence on the momentum. This can be considered by replacing the detuning of the laser with a Doppler shifted detuning

$$\Delta \to \Delta_{\mathrm{dop}} = \Delta - \sqrt{2}\eta\omega_{\mathrm{T}} \cdot p\,. \tag{6.59}$$

The momentum p here is given in units of $\sqrt{\hbar m \omega_{\mathrm{T}}}$. The drift moment of the

momentum including the Doppler shift becomes

$$\begin{aligned} d_p(p,\Delta) &= \overline{d}_p(\Delta - \sqrt{2}\eta\omega_{\mathrm{T}} \cdot p) \\ &\approx \overline{d}_p(\Delta) - g \cdot p\,, \end{aligned} \tag{6.60}$$

with $\overline{d}_p(\Delta)$ denoting the drift moment of the momentum ignoring the Doppler effect and the function

$$g(\Delta) = \sqrt{2}\eta\omega_{\mathrm{T}}\frac{\partial \overline{d}_p}{\partial \Delta} \tag{6.61}$$

describing a Doppler shift induced damping and anti-damping rate at the detuning Δ. It takes a positive value for a red detuned laser and a negative value for a blue detuned laser in accordance with Doppler cooling and heating. Eq. (6.60) indicates that depending on the sign of the detuning the drift in momentum per cycle gets accelerated or decelerated compared to the value ignoring the Doppler effect. Eqs. (6.58) and (6.60) set up an implicit equation for the momentum, so that the mean momentum of the ion after a spectroscopy time s is given by

$$\langle p(s)\rangle = \frac{1-e^{-gs}}{g}\overline{d}_p \simeq \overline{d}_p s - \frac{\overline{d}_p s^2}{2} g\,, \tag{6.62}$$

where $s = t/T$ is the spectroscopy time given in units of the period of the spectroscopy mode. Eq. (6.62) shows that the mean momentum of the ion consists of two terms: the momentum kicks proportional to the spectroscopy time s and a Doppler shift induced correction. Since the correction of the drift moment in momentum is proportional to the mean momentum of the ion, for a positive g (red detuned laser), the fast moving part of the wave packet gets more decelerated than the slow moving part indicating a narrowing of the wave packet in momentum space. Similarly the wave packet becomes spread for a blue detuned laser. It can be shown using a Focker-Planck equation (Wan et al., 2014), that the variance of the momentum evolves according to

$$v_p(s) = e^{-2gs} + \frac{1-e^{-2gs}}{g} D_{pp} \simeq 1 + 2(D_{pp} - g)s\,, \tag{6.63}$$

where D_{pp} is the diffusion coefficient in momentum. The Doppler shift contributes to the mean momentum quadratically and to the variance of momentum linearly in time s. In the parameter regime considered here, the contribution from the diffusion D_{pp} is negligible compared to g and we set in the following $D_{pp} = 0$.

In the experiment, the spectroscopy signal is based on a STIRAP detection pulse, that separates the population in the motional ground state from the population in the motional excited states. The excitation probability including the diffusion of the wave packet becomes

$$\begin{aligned} P_{\mathrm{exc}}(s) &= 1 - \left[\frac{2}{1+v_p(s)}\right]^{1/2} \exp\left[-\frac{\langle p(s)\rangle^2}{1+v_p(s)}\right] \\ &\simeq \overline{P}_{\mathrm{exc}}(s) + \delta P_{\mathrm{exc}}(s)\,, \end{aligned} \tag{6.64}$$

where

$$\overline{P}_{\mathrm{exc}}(s) = 1 - \exp\left[-\frac{\overline{d}_p^2 s^2}{2}\right] \tag{6.65}$$

$$\delta P_{\mathrm{exc}}(s) = -\exp\left[-\frac{\overline{d}_p^2 s^2}{2}\right]\frac{gs}{2} \tag{6.66}$$

correspond to the excitation probability ignoring the Doppler effect and the first order correction in g, respectively. The final excitation of motion has two contributions: one corresponds to the momentum kicks during the AECs and the second term describing the effect of Doppler shift induced damping and anti-damping. The correction term is negative for a red detuned laser and positive for a blue detuned laser. For short spectroscopy times, the correction term scales linearly with s, while the drift term scales quadratically with time. At the starting stage of the cycle, the Doppler-induced heating is the dominant source contributing to the signal, while with more and more pulses, the drift in momentum becomes more dominant.

The shift of the center of the spectrum P_{exc} from the unperturbed one $\overline{P}_{\mathrm{exc}}$ is given by

$$\Delta\nu = -\frac{\delta P_{\mathrm{exc}}}{\dfrac{\partial \overline{P}_{\mathrm{exc}}}{\partial \Delta}} = \frac{\eta\omega_{\mathrm{T}}}{\sqrt{2}\,\overline{d}_p s} \tag{6.67}$$

With the two point sampling technique, the frequencies on the left and right side of the spectrum reaching a certain signal level $p_{\mathrm{l,r}}$ are determined. The necessary spectroscopy time to reach this signal level is to zeroth order in g determined by $p_{\mathrm{l,r}} = \overline{P}_{\mathrm{exc}}(s)$ or, equivalently, $\overline{d}_p = \sqrt{-2\log(1-p_{\mathrm{l,r}})}$. We can rewrite the

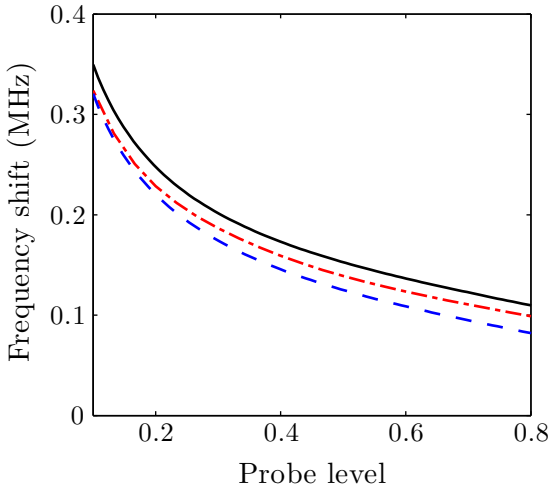

Figure 6.18: **Doppler shift induced damping and anti-damping.** A Doppler induced damping and anti-damping for red and blue detuned laser leads to an unsymmetric excitation of motion and therefore a distortion of the line profile. The systematic shift caused by the effect is modelled using a full numerical simulation of the eight level system using the experimental parameters (*black line*). In comparison, the predicted shift using the simple model according to Eq. (6.68) is plotted as *blue dashed line* and the result of from a full analytical model is plotted as in *red dash-dot line*.

Doppler induced shift measured with the two point sampling technique at the signal level $p_{\mathrm{l,r}}$ as

$$\Delta\nu = \frac{\eta\omega_{\mathrm{T}}}{2}\left[\log\left(\frac{1}{1-p_{\mathrm{l,r}}}\right)\right]^{-1/2} \tag{6.68}$$

The shift induced by the Doppler effect is also derived using an analytical model using Fokker-Planck equation including all the drift and diffusion coefficients (Wan et al., 2014) and from the density matrix simulation of the eight level system (Fig. 6.18). The Doppler induced shift from the simple model according to Eq. (6.68) and from the density matrix simulation is plotted in Fig. 6.18 as a function of the probe level. The result from the simple model is in agreement with the numerical models for excitation level between 0.1 and 0.9. For the typical signal level of $p_{\mathrm{l,r}} = 0.5$, the shift induced by the Doppler effect is extracted from the numerical simulation to be 151 kHz. With a conservatively estimated

fluctuation of motional excitation of ± 0.1, we attribute an uncertainty of $\pm 20\,\mathrm{kHz}$ to this shift.

6.6.6 Other shifts

Although the ion trap provides an ideal environment for precision spectroscopy, the presence of excess micromotion can lead to 2^{nd} order Doppler shifts and a distortion of the line profile. In case of a large crystal, an uncertainty as large as 1.2 MHz for the investigated transition has been determined experimentally in a different setup (Wolf et al., 2008). In our case, the effect of excess micromotion can be minimized through micromotion compensation using different techniques. We compensate the micromotion for a single $^{25}Mg^{+}$ ion using the sideband modulation technique as described in (Ibaraki et al., 2011). A modulation index $\beta = 0.005$ for the residual excess micromotion is determined from the ratio of the Rabi frequencies of the first micromotion sideband and the carrier transition (Hemmerling, 2011), driven between $|\uparrow\rangle \leftrightarrow |\downarrow\rangle$ states of the $^{25}Mg^{+}$ ion. The residual modulation index corresponds to an amplitude of the micromotion of $u'_z = \beta/k_{\mathrm{eff}} \approx 0.16\,\mathrm{nm}$ (Hemmerling, 2011) and a displacement of the ion's position from the optimal point by $u_{0z} = 2u'_z/q_z \approx 50\,\mathrm{nm}$ along the axial direction (Berkeland et al., 1998), where k_{eff} is the effective vector of the Raman lasers and q_z is the trap parameter given in Appendix A.2. In case of two ions, both ions are shifted away from the position with minimum micromotion. For the two ion crystal of $^{25}Mg^{+}$ and $^{40}Ca^{+}$ in the same potential as a single $^{25}Mg^{+}$, both ions are shifted aside by approximately $1.93\,\mu\mathrm{m}$. The modulation index for both ions is increased by a factor of around 40 to $\beta \approx 0.2$.

The second-order Doppler shift and the Stark shift induced by the residual excess micromotion are given by

$$\frac{\Delta\nu_{D2}}{\nu} \simeq -\left(\frac{\Omega_{\mathrm{rf}}}{ck\cos\theta_{\mu k}}\right)^2\left(\frac{\beta}{2}\right)^2, \tag{6.69}$$

$$\nu_{\mathrm{S}} \simeq 2\sigma_{\mathrm{S}}\left(\frac{m\Omega_{\mathrm{rf}}^2}{ek\cos\theta_{\mu k}}\right)^2\left(\frac{\beta}{2}\right)^2, \tag{6.70}$$

where Ω_{rf} is the trap driving frequency and k is the wave number of the spectroscopy laser, $\theta_{\mu k}$ is the angle between the laser and the direction of the micro-

Table 6.2: **Evaluation of systematic shifts and uncertainties.** The given uncertainties correspond to 1σ errors. The envelope shift of the spectroscopy pulses is measured on a daily basis and included in the individual measurement, while the uncertainty for the envelope shift contains the contributions from the envelope shift and the photodiode chain calibration.

effect	shift (kHz)
Zeeman	-8 ± 59
AC-Stark spectroscopy laser	60 ± 44
AC-Stark repumper	0 ± 0
spectroscopy pulse envelope shift	0 ± 16
lineshape	151 ± 20
second-order Doppler shift	0 ± 0
RF Stark effect	0 ± 0
statistics	0 ± 42
total	203 ± 88

motion and σ_S is the static Stark shift constant (Arora et al., 2007). With the modulation index for the two-ion crystal, the second-order Doppler shift and the Stark shift are estimated to be smaller than 1 Hz.

A summary of all the systematic effects with their corresponding uncertainties is shown in Tab. 6.2. Considering all the contributions as independent from each other, uncertainties from different effects add up according to

$$\sigma = \sqrt{\sum_k \sigma_k^2}\,, \tag{6.71}$$

which results in a total uncertainty of 88 kHz containing 78 kHz from systematic effects and 42 kHz from statistics. Compared with the previous measurement of the same transition using laser induced fluorescence on a cloud of ions (Wolf et al., 2008), an improvement of almost a factor of 20 in uncertainty is achieved, rendering our measurements one of the most accurate measurements of a broad transition.

6.7 Discussion

The high photon sensitivity and the absolute accuracy of photon recoil spectroscopy promise applications in a broad range of atomic and molecular species. Its high photon sensitivity enables spectroscopy of transitions that are not closed or have intrinsically low scattering rates. Such transitions appear in molecular ions (Lien et al., 2011; Nguyen et al., 2011b; Nguyen et al., 2011a), astrophysically relevant metal-ions (Webb et al., 2011; Rahmani et al., 2012; Berengut et al., 2011b) and highly-charged ions (Nörtershäuser, 2011). For the first two cases, the complicated level structure opens up multiple-decay paths and therefore limits the number of scattered photons, while for highly-charged ions the intrinsically narrow linewidth on the order of several kHz demands a sensitive spectroscopy technique. The sensitivity of the technique could be further improved by employing other non-classical states of motion, like higher Fock-state, squeezed state or Schrödinger cat states (Hempel et al., 2013). These non-classical states of motion have a larger spatial extent compared to the motional ground state, which leads to an increased effective Lamb-Dicke parameter and a higher photon sensitivity. For a squeezed vacuum state of motion $|\xi\rangle = \hat{S}(\xi)\,|0\rangle$ with $\hat{S}(\xi)$ as the squeeze operator and $\xi = r\,e^{i\theta}$ as the squeeze parameter, the ratio of the uncertainties of the two quadratures is given by $\beta = e^{2r}$ (Gerry et al., 2004). For $\theta = \pi$, the spatial extent of the ion is increased by a factor of $\sqrt{\beta}$

$$\Delta x = \sqrt{\langle(\Delta\hat{x})^2\rangle} = x_0\sqrt{\beta} \tag{6.72}$$

compared to the motional ground state with a spatial extension of x_0 (Gerry et al., 2004). Such a squeezed motional state with $\beta = 40(10)$ has been created using a periodically oscillating dipole force at twice the trap frequency (Meekhof et al., 1996a). An increase of effective Lamb-Dicke parameter and photon sensitivity by a factor of ~ 6.3 could potentially be achieved.

Besides the high photon sensitivity, PRS provides a background-free detection by separating the spectroscopy sequence with the detection period. This increases the SNR in direct frequency comb spectroscopy (Marian et al., 2004; Diddams et al., 2007), XUV (Jones et al., 2005; Gohle et al., 2005) and x-ray spectroscopy (Epp et al., 2007; Bernitt et al., 2012), where the number of photons per spectral bandwidth is limited.

Chapter 7

State preparation of molecular ions

In this chapter, we describe the proposed scheme for state preparation of molecular ions using the quantum logic technique. After a short introduction of previous experiments aimed at production of rotationally cold molecular ions in Sec. 7.1, the basic properties of our molecular ion $^{24}MgH^+$ are discussed in Sec. 7.2. In Sec. 7.3, we introduce the principle of rotational state preparation, where we use an optical lattice to distinguish different rotational states of the molecular ion. The coupling of an optical lattice to an ion is discussed in Sec. 7.4. Here we investigate the influence of a moving optical lattice on the $^{25}Mg^+$ ion and on the molecular ion. In Sec. 7.5, the optical lattice is employed to produce a coherent state on a two-ion crystal of $^{25}Mg^+$ and $^{24}MgH^+$. In the last section, an outlook for the current experiments is presented.

7.1 Introduction

Cold and ultracold molecules provide the ideal test fields from fundamental physics to ultracold chemistry (Carr et al., 2009). A comparison of astrophysical and laboratory spectroscopy of rovibrational transitions of molecular ions allows the test of a possible variation of fundamental constants (Murphy et al., 2008). The large effective electric field within a molecule (Sandars, 1965) allows to probe the existence of an electron electric dipole moment (Meyer et al., 2006). Studies of molecular collisions at low temperature allow detailed investigation of quantum mechanical description of chemical reactions (Willitsch et al., 2008b; Willitsch et

al., 2008a; Staanum et al., 2008). All these intriguing applications raise interests in the study of cold neutral molecules and molecular ions.

Molecular systems have a much richer level structure compared to atomic systems. Besides the electronic levels, the relative motion between the atoms composing the molecule leads to vibrational and rotational bands lying on top of the electronic structure. This complexity in the internal level structure forms the challenge of coherent control of molecules. In recent years, various approaches have been pursued for generating cold molecular ions. One of the general methods to cool the external degrees of freedom of charged particles is sympathetic cooling. For this, molecular ions are trapped together with laser-cooled atomic ions. Through the Coulomb interaction between the atomic and molecular species, the translational degrees of freedom of the molecular ion is sympathetically cooled to a temperature of below 100 mK (Bowe et al., 1999; Mølhave et al., 2000). Because of the large energy separation between the rovibrational energy and the motional energy, the internal degrees of freedom of the molecular ion are decoupled from the external motion (Vogelius et al., 2002; Bertelsen et al., 2006). The distribution over the internal states are strongly influenced by blackbody radiation (BBR) from the environment. The cooling of internal degrees of freedom of translationally cold ions has been demonstrated on polar molecular ions like $^{24}MgH^+$ (Staanum et al., 2010) and HD^+ ion (Schneider et al., 2010b) using optical pumping on dipole-allowed transitions, resulting in a fractional population of 36.7% and 78% in the rotational ground state, respectively. On apolar molecular ions, state-selective threshold photoionization has been applied to produce an accumulation of N_2^+ molecules in selected rotational states (Tong et al., 2010). As an alternative method, buffer-gas cooling has been demonstrated on various systems as an efficient method of cooling both internal and external degrees of freedom of molecular ions using cryogenic He buffer gas (Gerlich, 1995; Kreckel et al., 2005; Trippel et al., 2006). Very recently, using a combination of sympathetic cooling and He buffer-gas, a rotational temperature of $\sim$7.5 K has been demonstrated on $^{24}MgH^+$ ions (Hansen et al., 2014).

In these experiments, the cooling of molecular ions has been demonstrated on a cloud of molecular ions. The state detection of different internal states is performed via destructive methods, such as resonance-enhanced multi-photon disso-

ciation (Bertelsen et al., 2006; Roth et al., 2006; Koelemeij et al., 2007a; Staanum et al., 2010; Schneider et al., 2010b; Hansen et al., 2014) or laser-induced charge transfer with Ar atoms (Schlemmer et al., 1999; Tong et al., 2010), which lead to dissociation of the molecular ions. We propose in this chapter an alternative method to prepare a single molecular ion in a pure quantum mechanical state. The method is based on the non-destructive detection of the rotational state of the molecular ion $^{24}MgH^+$ using the quantum logic technique.

7.2 Properties of Magnesium Hydride

7.2.1 Level scheme

Fig. 7.1a shows the potential energy curves for the lowest two electronic levels $X\,^1\Sigma^+$ and $A\,^1\Sigma^+$ of the $^{24}MgH^+$ molecule (Jørgensen et al., 2005). The transition frequencies between the two lowest vibrational bands of these electronic states lie at around 281 nm (Balfour, 1972). The electronic ground state $X\,^1\Sigma^+$ has a

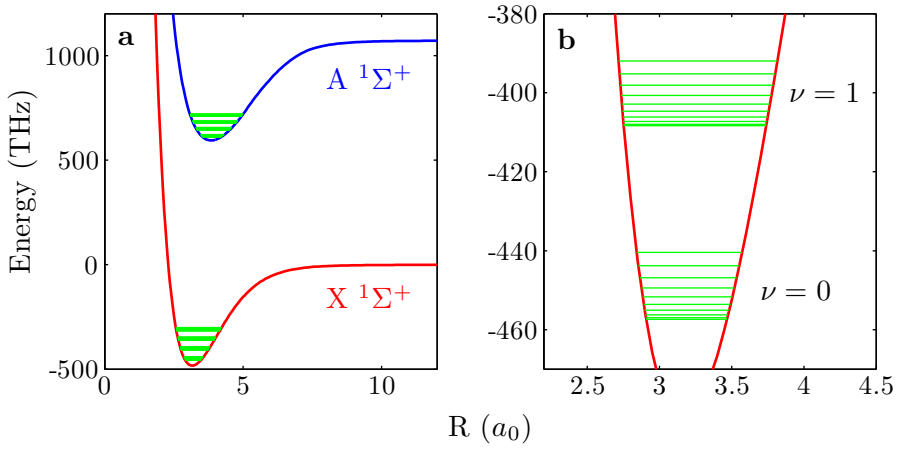

Figure 7.1: **Potential energy curves of magnesium hydride.** (**a**) Potential energy curves for the lowest two electronic levels of $^{24}MgH^+$. In each electronic level, there is a series of rovibrational bands indicated with *green lines*. (**b**) The lowest two vibrational bands in the electronic ground state. At room temperature, more than 99% of the population stay in the vibrational ground state, but more than ten rotational levels are filled with a population of more than 1%.

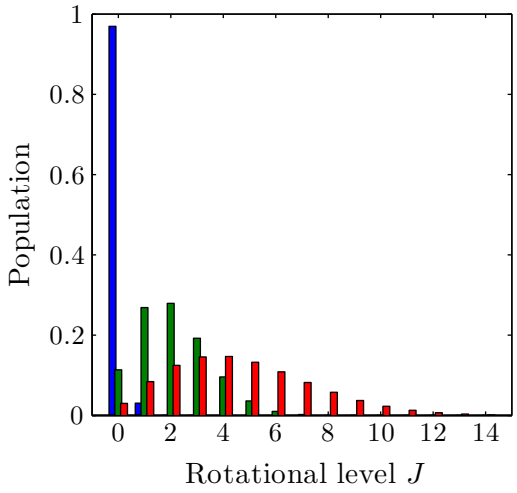

Figure 7.2: **Equilibrium distribution of rotational levels.** The equilibrium distribution of $^{24}MgH^+$ in different rotational states of the electronic and vibrational ground state at $T = 4\,\mathrm{K}$ (*blue*), $77\,\mathrm{K}$ (*green*) and $300\,\mathrm{K}$ (*red*).

vibrational constant of $1699\,\mathrm{cm}^{-1}$ (Balfour, 1972; Aymar et al., 2009). At room temperature ($T = 300\,\mathrm{K}$), the splitting in the vibrational states is much larger than the thermal energy ($k_\mathrm{B}T \mathrel{\widehat{=}} 6.25\,\mathrm{THz} \mathrel{\widehat{=}} 208\,\mathrm{cm}^{-1}$), so that more than 99% of the population is in the electronic and vibrational ground state.

Through incoherent coupling to the BBR, the rotational levels in the electronic and vibrational ground state reach a thermal equilibrium on a typical timescale of $10 - 100\,\mathrm{s}$ with a population

$$\mathcal{P}(J) = \frac{1}{Z} \cdot g_J \, e^{-E_J/k_\mathrm{B}T} \tag{7.1}$$

in the rotational state $|\mathrm{X}\,^1\Sigma^+, \nu'' = 0, J''\rangle \equiv |J\rangle_\mathrm{X}$, where $Z = \sum_J g_J \, e^{-E_J/k_\mathrm{B}T}$ is the canonical partition function, k_B is the Boltzmann constant and E_J, $g_J = 2J+1$ are the energy and degeneracy of the rotational level $|J\rangle_\mathrm{X}$ in the electronic and vibrational ground state of the molecule. Fig. 7.2 shows the equilibrium distributions of rotational levels in the electronic and vibrational ground state for three different temperatures. At room temperature $T = 300\,\mathrm{K}$, rotational levels up to $J = 12$ have a population of more than 1%, while at liquid helium temperature of $T = 4\,\mathrm{K}$, more than 95% of the population are in the rotational ground state.

7.2.2 Transition frequencies between electronic states

Consider that we drive a direct transition between the two electronic states $|\mathrm{X}\,^1\Sigma^+, \nu'' = 0, J''\rangle \equiv |J''\rangle_\mathrm{X}$ and $|\mathrm{A}\,^1\Sigma^+, \nu' = 0, J'\rangle \equiv |J'\rangle_\mathrm{A}$ of the molecular ion. Note that we use a double-prime (ν'', J'') to indicate the quantum number of the electronic ground state and a single prime (ν', J') for the electronically excited state. The possible transitions are limited by the selection rule $\Delta J = J' - J'' = \pm 1$ for a transition between two Σ-states (Ellis et al., 2011, Chap. 7). The transition frequencies for the P- and R-branch, with $J' = J'' \mp 1$ respectively (Fig. 7.3b), are given by

$$\begin{aligned}\overline{\nu}_{\mathrm{P,R}}(J'') &= \overline{\nu}_{(\nu',\nu'')} + B'J'(J'+1) - B''J''(J''+1) \\ &= \begin{cases} \overline{\nu}_{(\nu',\nu'')} - (B'+B'')J'' + (B'-B'')J''^2 & \text{for P-branch} \\ \overline{\nu}_{(\nu',\nu'')} + (B'+B'')J' + (B'-B'')J'^2 & \text{for R-branch}\,, \end{cases}\end{aligned} \tag{7.2}$$

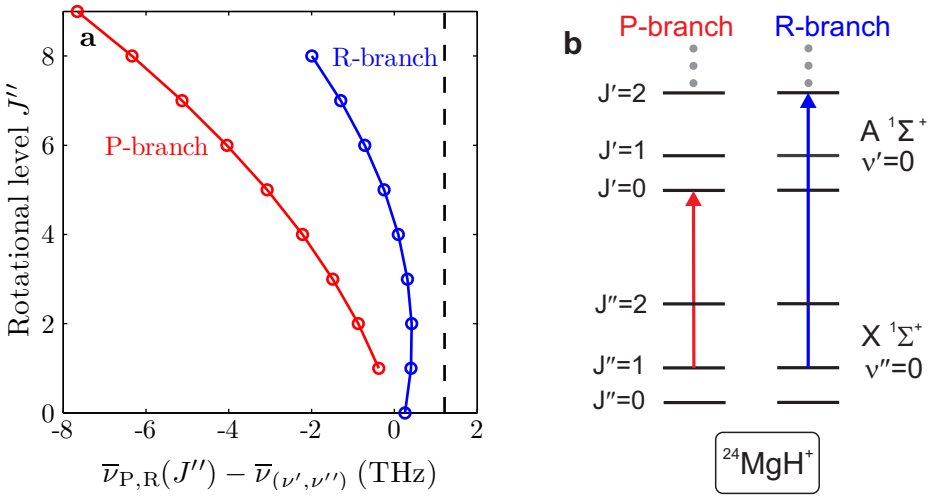

Figure 7.3: **Fortrat diagram.** (**a**) The transition frequencies between $|\mathrm{X}\,^1\Sigma^+, \nu'', J''\rangle$ and $|\mathrm{A}\,^1\Sigma^+, \nu', J'\rangle$ show typically a quadratic dependence on the rotational quantum number J''. For $^{24}\mathrm{MgH}^+$ with $B' < B''$, the R-branch bends towards lower frequencies with increasing rotational quantum number J''. (**b**) The possible transitions are limited by the selection rules $\Delta J = \pm 1$ for a $\Sigma \to \Sigma$ transition to P- and R-branches, while transitions in the Q-branch with $\Delta J = 0$ are not allowed.

where $\overline{\nu}_{(\nu',\nu'')}$ denotes the band origin corresponding to the transition frequency between $|J''=0\rangle_{\mathrm{X}}$ and $|J'=0\rangle_{\mathrm{A}}$ and $B'' \approx 6.4\,\mathrm{cm}^{-1}$, $B' \approx 4.4\,\mathrm{cm}^{-1}$ are the rotational constants for the electronic ground and excited states, respectively. The transition frequencies between the two rotational states $|J''\rangle_{\mathrm{X}}$ and $|J'\rangle_{\mathrm{A}}$ show in general ($B'' \neq B'$) a quadratic dependence on the rotational quantum number. This is illustrated in a Fortrat diagram (Fig. 7.3a), where the rotational quantum number J'' is plotted against the transition frequency $\overline{\nu}_{\mathrm{P,R}}(J'')$ referenced to the band origin $\overline{\nu}_{\nu',\nu''}$. For $^{24}\mathrm{MgH}^+$ ions, the equilibrium distance between the two nuclei in the excited state R'_{e} is larger than in the electronic ground state R''_{e}, leading to a smaller rotational constant for the electronically excited state $B' < B''$. The R-branch bends in this case towards lower frequencies with increasing rotational quantum number J'', corresponding to a non-monotonic change of the transition frequency as a function the rotational quantum number J''.

7.2.3 Dynamics of rotational degrees of freedom

With a cloud of the molecular ions in the trap, the incoherent coupling to the BBR leads to a statistical distribution of the ions in different rotational states of the electronic and vibrational ground state. With a single molecular ion in the trap, the coupling to the BBR results in incoherent jumps between different rotational states. We model in this section the dynamics between the rotational states using Master equation simulation and the Monte Carlo wave-function (MCWF) method.

7.2.3.1 Master equation model

The free evolution of the rotational degrees of freedom coupling to a thermal reservoir at a temperature T is described by the master equation (Meystre et al., 1999; Lambropoulos et al., 2007)

$$\begin{aligned}\dot{\rho} = \sum_J \Bigg[& \frac{A_J}{2}(\bar{n}_J + 1)\left(2\,\hat{\sigma}_J \rho \hat{\sigma}_J^\dagger - \hat{\sigma}_J^\dagger \hat{\sigma}_J \rho - \rho \hat{\sigma}_J^\dagger \hat{\sigma}_J\right) \\ & + \frac{A_J}{2}\frac{g_{J+1}}{g_J}\bar{n}_J\left(2\,\hat{\sigma}_J^\dagger \rho \hat{\sigma}_J - \hat{\sigma}_J \hat{\sigma}_J^\dagger \rho - \rho \hat{\sigma}_J \hat{\sigma}_J^\dagger\right)\Bigg],\end{aligned} \tag{7.3}$$

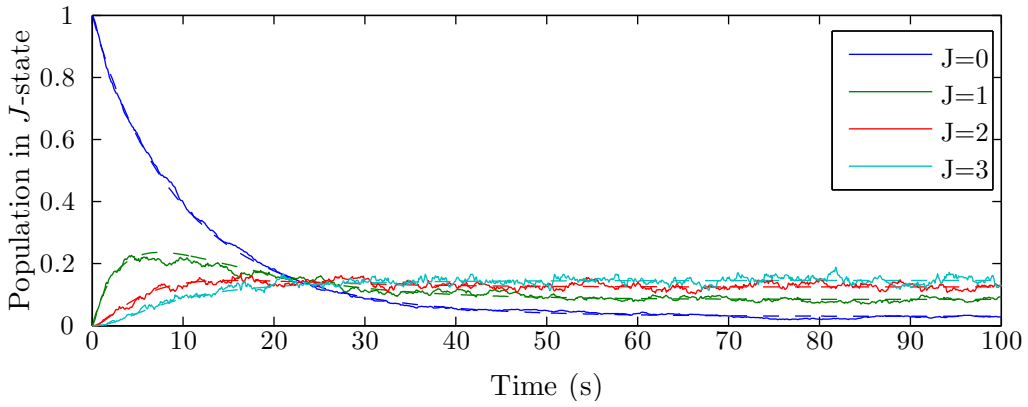

Figure 7.4: **Thermalization of rotational states.** Starting from a pure rotational state $|J=0\rangle_{\mathrm{X}}$, the incoherent coupling to the BBR at T = 300 K redistributes the molecular ion(s) between different rotational states towards a thermal equilibrium within 100 s. The population of the lowest four rotational states are plotted as a function of time. Density matrix simulation: *dashed lines*. Monte Carlo simulation with 1000 trajectories: *solid lines*.

where $\hat{\sigma}_J$ is the spin-flip operator

$$\hat{\sigma}_J = |J\rangle_{\mathrm{XX}}\langle J+1|\,, \tag{7.4}$$

A_J is the Einstein coefficient and

$$\bar{n}_J = \frac{1}{\exp\left(\frac{\hbar\bar{\nu}_J}{k_{\mathrm{B}}T}\right)-1} \tag{7.5}$$

is the mean number of quanta of BBR in the mode of the transition frequency $\bar{\nu}_J$ between the two states $|J\rangle_{\mathrm{X}}$ and $|J+1\rangle_{\mathrm{X}}$. The double primes are omitted here, since only the electronic ground state is relevant. We introduce the collapse operators

$$\hat{c}_{J,k} = \begin{cases} \sqrt{A_J(\bar{n}_J+1)}\hat{\sigma}_J & \text{for } k=-\\ \sqrt{A_J\frac{g_{J+1}}{g_J}\bar{n}_J}\hat{\sigma}_J^\dagger & \text{for } k=+\,, \end{cases} \tag{7.6}$$

describing the quantum jump for the transition $|J+1\rangle_{\mathrm{X}} \to |J\rangle_{\mathrm{X}}$ and the inversed transition, respectively. The master equation is rewritten in Lindblad form to

$$\dot{\rho} = \sum_J \sum_k \frac{1}{2}\left(2\,\hat{c}_{J,k}\rho\hat{c}_{J,k}^\dagger - \hat{c}_{J,k}^\dagger\hat{c}_{J,k}\rho - \rho\hat{c}_{J,k}^\dagger\hat{c}_{J,k}\right)\,. \tag{7.7}$$

Starting from the rotational ground state $|J=0\rangle_{\mathrm{X}}$, the equilibrium between different rotational states is reached within less than 100 s as shown with dashed lines in Fig. 7.4. The final distribution in thermal equilibrium is in agreement with Eq. (7.1). The Einstein coefficients and the transition frequencies used in the simulation are taken from Højbjerre, 2009 and Balfour, 1972, respectively.

7.2.3.2 MCWF method

In order to model the time evolution of the rotational degrees of freedom of a single molecular ion, we use the MCWF method (Molmer et al., 1993). We summarize the basic procedure for the MCWF method applied to the rotational evolution in a single molecular ion. The reader is referred to Molmer et al., 1993; Carmichael, 1993; Plenio et al., 1998; Carmichael, 2008 for further details.

From a certain initial state $|\phi(t)\rangle$, *e.g.* $|J=0\rangle$, the rotational states of a molecular ion evolves under the effective Hamiltonian

$$H_{\mathrm{eff}} = -\frac{i\hbar}{2}\sum_{J}\sum_{k}\hat{c}^{\dagger}_{J,k}\hat{c}_{J,k}\,, \tag{7.8}$$

for a short time δt to an un-normalized state $|\overline{\phi}(t+\delta t)\rangle$ with the square of the norm

$$\left\langle\overline{\phi}(t+\delta t)\,\middle|\,\overline{\phi}(t+\delta t)\right\rangle = 1-\delta p\,, \tag{7.9}$$

where

$$\delta p = \delta t\frac{i}{\hbar}\left\langle\phi(t)\,\middle|\,\hat{H}_{\mathrm{eff}}-\hat{H}^{\dagger}_{\mathrm{eff}}\,\middle|\,\phi(t)\right\rangle = \sum_{J,k}\delta p_{J,k} \tag{7.10}$$

$$\delta p_{J,k} = \delta t\left\langle\phi(t)\,\middle|\,\hat{c}^{\dagger}_{J,k}\hat{c}_{J,k}\,\middle|\,\phi(t)\,\middle|\,\right\rangle \tag{7.11}$$

are the total loss of population and the losses from each channel in the time interval δt, respectively. In the second step, a random number ϵ between 0 and 1 is chosen. If the random number ϵ is larger than δp, then no quantum jump between the states has occured and the normalized wave function becomes (Molmer et al., 1993; Leth et al., 2010)

$$|\phi(t+\delta t)\rangle = \frac{|\overline{\phi}(t+\delta t)\rangle}{(1-\delta p)^{1/2}} \qquad \text{if } \delta p<\epsilon\,. \tag{7.12}$$

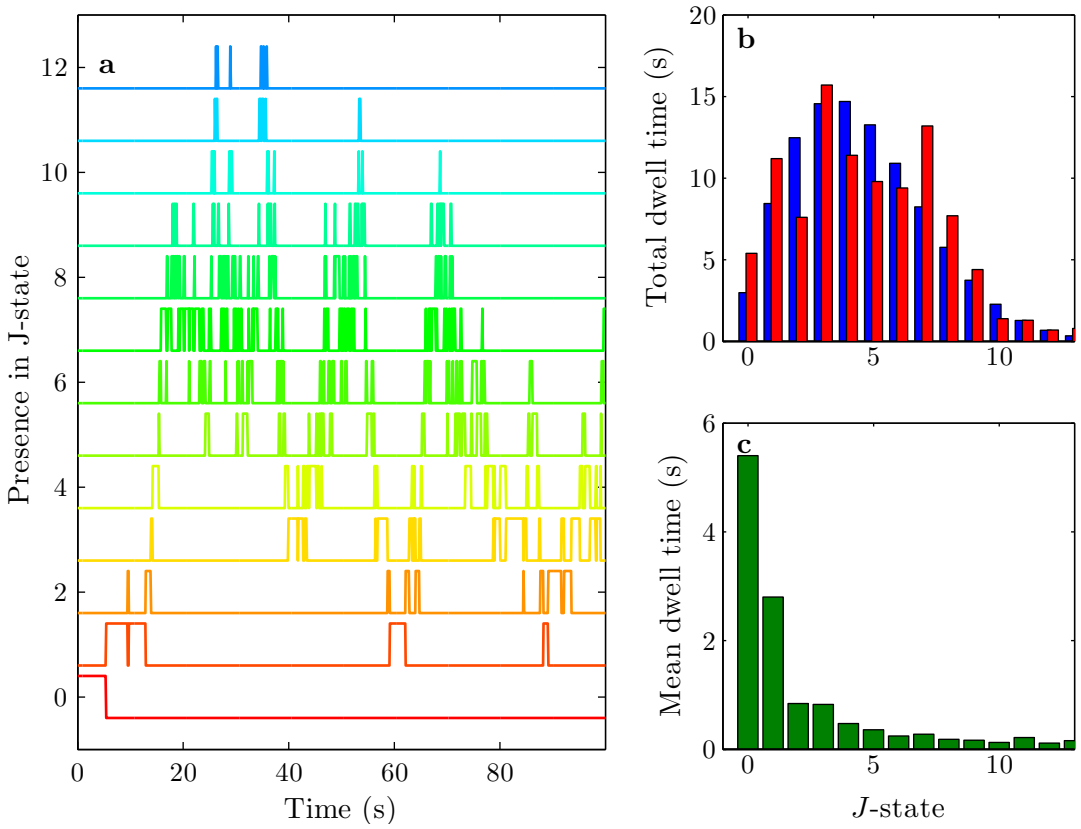

Figure 7.5: **Single trajectory for evolution between rotational states.** (**a**) Because of the incoherent coupling with BBR, the molecular ion jumps between different rotational states. The presence in certain rotational states is indicated as a square function in the figure. (**b**) The accumulated duration (*red bars*) that the ion has stayed in a certain rotational state follows the Boltzmann distribution (*blue bars*) at the temperature of BBR. The deviations are caused by the limited evolution time. (**c**) The mean dwell time for the ion to stay in a certain state is longer for a low rotational state than for a high rotational state (*green bars*).

If $\epsilon < \delta p$, the initial state $|\phi(t)\rangle$ is projected at random with a weight $\delta p_{J,m}/\delta p$ to

$$|\phi(t+\delta t)\rangle = \frac{\hat{c}_{J,k}\,|\phi(t)\rangle}{(\delta p_{J,k}/\delta t)^{1/2}} \qquad \text{if } \delta p > \epsilon\,. \tag{7.13}$$

It can be shown that the solution from MCWF method is equivalent with the result of the master equation (Molmer et al., 1993). In Fig. 7.4, the result of the

master equation (*dashed lines*) is compared with the result of the Monte Carlo (MC) simulation (*solid lines*) averaged over 1000 trajectories starting from the same initial condition $|\phi(t=0)\rangle = |J\rangle_{\mathrm{X}}$. They match within small fluctuations, which is limited only by the number of trajectories used in the MC simulations (Molmer et al., 1993).

Fig. 7.5a shows the evolution of rotational states in a single trajectory. The incoherent coupling to the BBR results in jumps of the ion between different rotational states. It can only be found in one of the rotational states at a time. Although the accumulated duration during which the molecular ion to stay in one of the rotational states in this single trajectory is proportional to the population predicted by the Boltzmann distribution given in Eq. (7.1) (Fig. 7.5b), the mean dwell time for the ion to stay in the low lying states is longer than in the higher rotational states (Fig. 7.5c).

7.3 Principle of rotational state preparation

The principle of rotational state preparation is illustrated in Fig. 7.6. The $^{25}Mg^{+}$ ion is initialized to the $|\downarrow\rangle$ state, while the molecular ion stays in the electronic and vibrational ground state $|\mathrm{X}\,^1\Sigma^+, \nu''=0\rangle$ with more than 99% probability, but jumps between different rotational states $|J''\rangle_{\mathrm{X}}$ as illustrated in Fig. 7.5. We cool the two-ion crystal of $^{25}Mg^{+}$ and $^{24}MgH^{+}$ ions to the motional ground state with resolved sideband cooling (SBC) as described in Sec. 4.3 (Fig. 7.6a). During the interrogation period, we apply a pulse of two counter-propagating laser beams forming a moving optical lattice for a duration t. The lattice beams at around 281 nm are produced using a frequency-doubled dye laser[1] and are aligned along the trap axis to provide the largest Lamb-Dicke parameter for the axial modes (Fig. 3.3). The frequency difference of the two lattice beams is detuned to the axial trap frequency of the in-phase (ip) mode, while the frequency of each lattice beam is tuned close to the resonance of a direct electronic transition $\overline{\nu}_{\mathrm{P,R}}(J'')$ between $|\mathrm{X}\,^1\Sigma^+, \nu''=0, J''\rangle$ and $|\mathrm{A}\,^1\Sigma^+, \nu'=0, J''\mp 1\rangle$. If the molecular ion is in the target rotational state $|J''\rangle_{\mathrm{X}}$, the moving optical lattice excites the ions'

[1] Radiant Dyes Laser & Accessories GmbH Active stabilized CW dye ring laser

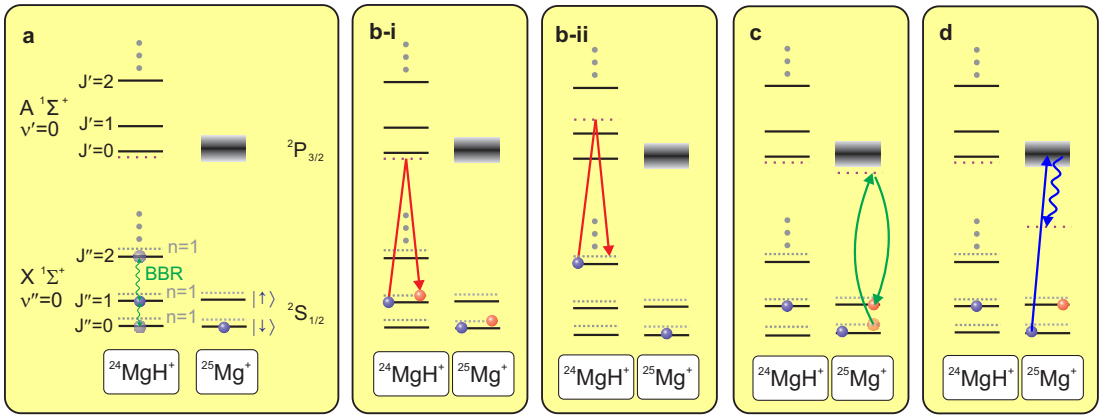

Figure 7.6: **Principle of rotational state preparation.** (**a**) At the beginning of the sequence, the logic ion $^{25}Mg^+$ is initialized in the $|\downarrow\rangle$ state via optical pumping and the molecular ion $^{24}MgH^+$ decays to the electronic and vibrational ground state, but jumps between different rotational states via incoherent coupling to the BBR at room temperature. Using resolved SBC, the two-ion crystal is cooled to the motional ground state of both axial modes. (**b-i**) A moving optical lattice is used to excite the motion of the two-ion crystal with the frequency of the lattice beams tuned close to resonance of the electronic transition $|X\,^1\Sigma^+, \nu'' = 0, J''\rangle \leftrightarrow |A\,^1\Sigma^+, \nu', J'' \mp 1\rangle$. If the molecular ion is in the target rotational state $|J''\rangle_X$, the moving optical lattice excites the motion of the ion crystal. (**b-ii**) If the molecular ion is in another rotational state, the lattice beams are far-detuned from the closest electronic transition and the ions' motion will not be influenced. (**c**) The potentially generated motional excitation is shared by both ions and is converted into an internal state excitation of $^{25}Mg^+$ via a STIRAP pulse on the RSB. (**d**) The two internal states of $^{25}Mg^+$ are distinguished using a resonant detection pulse. A molecular ion in the target rotational state $|J''\rangle_X$ is identified by a $^{25}Mg^+$ ion in the $|\uparrow\rangle$ state.

motion into a coherent state through an optical dipole force oscillating at the trap frequency (Fig. 7.6b-i). If the molecular ion is not in the target rotational state $|J''\rangle_X$, the lattice beams are far-detuned from the closest electronic transitions (Fig. 7.6b-ii) and no motional excitation is generated. The motional excitation is shared by both ions because of the strong Coulomb interaction and is converted into an electronic excitation on the $^{25}Mg^+$ ion via a stimulated Raman adiabatic

passage (STIRAP) pulse on the red sideband (RSB) (Fig. 7.6c). A detection pulse coupling $|\downarrow\rangle$ with the $^2P_{3/2}$ state of the $^{25}Mg^+$ ion distinguishes the $|\downarrow\rangle$ and $|\uparrow\rangle$ states and provides information about the rotational state of the molecular ion $^{24}MgH^+$ (Fig. 7.6d).

7.4 Interaction of an ion with an optical lattice

7.4.1 Light shift

Consider a two-level system with transition frequency ω_0 in the field of a far-detuned laser with frequency ω_L. The full Hamiltonian of the system in the frame of the laser reads

$$\hat{H} = \frac{\hbar}{2}\begin{pmatrix} \Delta_R & \Omega_R \\ \Omega_R & -\Delta_R \end{pmatrix} \tag{7.14}$$

where

$$\Omega_R = \frac{|\boldsymbol{d}\cdot\boldsymbol{E}_0|}{\hbar} \tag{7.15}$$

is the resonant Rabi frequency, $\Delta_R = \omega_L - \omega_0$ is the detuning of the laser from the investigated transition, $\boldsymbol{d}$ is the electric dipole moment and $\boldsymbol{E}_0$ is the amplitude of the oscillating electric field $\boldsymbol{E} = \boldsymbol{E}_0\cos(\omega_L t)$ at the position of the ion. The presence of the far-detuned laser perturbs the energy levels of the ion. The eigenvalues of the Hamiltonian read

$$\lambda_\pm = \pm\frac{\hbar}{2}\sqrt{\Omega_R^2 + \Delta_R^2} \approx \pm\hbar\left(\frac{\Delta_R}{2} + \frac{\Omega_R^2}{4\Delta_R}\right), \tag{7.16}$$

where the second step the detuning is valid for large detuning ($\Omega_R \ll \Delta_R$). The first term corresponds to the eigenvalue of the unperturbed system in the rotating frame of the laser and the second term gives the light shift induced by the far-detuned laser. The ground and the excited state are shifted by the same amount but towards different directions. For an ion located in the ground state, this shift reads

$$V_{ls} = \frac{\hbar\Omega_R^2}{4\Delta_R}, \tag{7.17}$$

which takes a positive value for a blue detuned laser and a negative value for a red detuned laser. Making use of the relation between the electric dipole moment

$\boldsymbol{d}$ and the spontaneous emission rate Γ_0 of the excited state (Hilborn, 1982)

$$\Gamma_0 = \frac{\omega_0^3}{3\pi\epsilon_0\hbar c^3}|\boldsymbol{d}|^2 \tag{7.18}$$

and the relation between the electric field amplitude $\boldsymbol{E}_0$ of the oscillating field $\boldsymbol{E} = \boldsymbol{E}_0\cos(\omega_L t)$ and the time-averaged intensity I

$$I = \frac{\epsilon_0 c}{2}|\boldsymbol{E}_0|^2 = \frac{\hbar\omega_0^3}{6\pi c^2}\frac{\Omega_R^2}{\Gamma_0}\,, \tag{7.19}$$

we rewrite Eq. (7.17) as

$$V_{ls}(\boldsymbol{r}) = \frac{3\pi c^2}{2\omega_0^3}\frac{\Gamma_0}{\Delta_R}I(\boldsymbol{r}). \tag{7.20}$$

The dipole potential possesses a spatial dependency caused e.g. by the intensity profile of the far-detuned laser. A red-detuned laser shifts the energy level downwards and therefore exerts an attracting force on the ion towards the regime with high laser intensity. A blue-detuned laser lifts the energy level up and exerts a repelling force pushing the ion out of the laser field.

The scattering rate of the ion from the excited state $|e\rangle$ at the detuning Δ_R is given by the product of the population ρ_{ee} in the excited state and the spontaneous emission rate Γ_0

$$\Gamma_{sc} = \Gamma_0\rho_{ee} = \frac{\Gamma_0}{2}\frac{\Omega_R^2/2}{\Delta_R^2 + \Omega_R^2/2 + \Gamma_0^2/4}\,, \tag{7.21}$$

where in the second step the steady state solution for ρ_{ee} is used (Foot, 2005). In case of large frqeuency detuning ($\Delta_R \gg \Gamma_0, \Omega_R$) the expression simplifies to

$$\Gamma_{sc} \approx \frac{\Gamma_0}{4}\frac{\Omega_R^2}{\Delta_R^2} = \frac{3\pi c^2}{2\hbar\omega_0^3}\frac{\Gamma_0^2}{\Delta_R^2}I(\boldsymbol{r})\,. \tag{7.22}$$

Both the light shift and the scattering rate scale linearly with the laser intensity, but they have different scaling with the laser detuning. The scattering rate drops faster with $1/\Delta_R^2$ at large detuning, while the dipole potential decreases according to $1/\Delta_R$.

The light shift can also be derived from second-order perturbation theory Grimm et al., 2000. Consider the atom in the ground state and with n photons

in the light field. The total energy of the system consisting of the atom and the light field equals $E_\mathrm{i} = n\hbar\omega_L$. The atom gets excited after absorbing a photon under the interaction Hamiltonian $\hat{H}_\mathrm{int} = -\boldsymbol{d}\cdot\boldsymbol{E}_0/2$ in the rotating frame of the laser, so that the final state has the total energy of $E_\mathrm{f} = \hbar\omega_0 + (n-1)\hbar\omega_\mathrm{L}$. The energy level of the atomic ground state is shifted according to the second-order perturbation theory by

$$\Delta E_i = \frac{|\langle \mathrm{e}|\,\hat{H}_\mathrm{int}\,|\mathrm{g}\rangle|^2}{E_\mathrm{i} - E_\mathrm{f}} = \frac{|\langle \mathrm{e}|\,\boldsymbol{d}\,|\mathrm{g}\rangle|^2}{\hbar\Delta_\mathrm{R}}\frac{|\boldsymbol{E}_0|^2}{4} = \frac{3\pi c^2}{2\omega_0^3}\frac{\Gamma_0}{\Delta_\mathrm{R}}I(\boldsymbol{r}), \tag{7.23}$$

where we used Eqs. (7.18) and (7.19) in the last step.

For a multi-level atom with sub-levels, the energy shift of a specific ground state $|\mathrm{g}_i\rangle$ is calculated by summing up the contributions from all the excited states $|\mathrm{e}_j\rangle$ (Griesmaier, 2007)

$$\Delta E_i = \frac{1}{2\epsilon_0\hbar c}\sum_j\sum_q \frac{|\langle e_j|\,\epsilon^q d_q\,|\mathrm{g}_i\rangle|^2}{\omega_\mathrm{L} - \omega_{ij}} I(\boldsymbol{r})\,, \tag{7.24}$$

where ϵ^q are the components of the polarization vector and d_q are the components of the dipole-moment vector in the spherical basis (Auzinsh et al., 2010) and ω_{ij} are the transition frequencies between $|\mathrm{g}_i\rangle$ and $|\mathrm{e}_j\rangle$.

7.4.2 Interference of counter-propagating fields

Consider a pair of laser beams counter-propagating along the z-axis $\boldsymbol{e}_\mathrm{z}$ with the frequencies ω_1, ω_2 and the wave vectors $\boldsymbol{k}_1$, $\boldsymbol{k}_2$. The two laser beams are linearly polarized along the x-axis $\boldsymbol{e}_\mathrm{x}$. The electric fields of the two laser beams are

$$\boldsymbol{E}_1 = \boldsymbol{e}_\mathrm{x} E_1 \cos(k_1 z - \omega_1 t) \tag{7.25}$$

$$\boldsymbol{E}_2 = \boldsymbol{e}_\mathrm{x} E_2 \cos(k_2 z - \omega_2 t) \tag{7.26}$$

The total electric field generated by the two laser beams is

$$\begin{aligned}\boldsymbol{E} &= \boldsymbol{E}_1 + \boldsymbol{E}_2 \\ &= \boldsymbol{e}_\mathrm{x}\left[E_1\cos(k_1 z - \omega_1 t) + E_2\cos(k_2 z - \omega_2 t)\right].\end{aligned} \tag{7.27}$$

The time-averaged intensity (averaged over the fast oscillations at frequency ω_1 and ω_2) with the presence of both lasers is given by

$$\begin{aligned} I(z,t) &= \epsilon_0 c \left\langle |\boldsymbol{E}|^2 \right\rangle \\ &= \epsilon_0 c \left[\left\langle |\boldsymbol{E}_1|^2 \right\rangle + \left\langle |\boldsymbol{E}_2|^2 \right\rangle + 2 \left\langle \boldsymbol{E}_1 \cdot \boldsymbol{E}_2 \right\rangle \right] \\ &= I_1 + I_2 + 2\sqrt{I_1 I_2} \cos(\delta k_\mathrm{L} z - \delta\omega_\mathrm{L} t), \end{aligned} \tag{7.28}$$

where I_1 and I_2 are the intensities of every single laser beams, $\delta\omega_\mathrm{L} = \omega_1 - \omega_2$ is the frequency difference of the two lasers and $\delta k_\mathrm{L} = |\boldsymbol{k}_1 - \boldsymbol{k}_2|$ is the difference of the two wave vectors. The two counter-propagating laser beams generate a moving optical lattice that moves with the speed $v_\mathrm{L} = \delta k_\mathrm{L}/\delta\omega_\mathrm{L}$.

7.4.3 Displacement and off-resonant excitation from optical lattice

The optical lattice generated by two counter-propagating laser beams possesses besides the spatial dependence from the intensity profile of the laser also a spatial dependence along the direction of the laser beam caused by the interference of the two laser beams. In addition it introduces a time-dependence caused by the frequency difference of the two lasers. After inserting Eq. (7.28) in Eq. (7.20), we see that the optical lattice produces an additional potential at the position of the ion

$$V'_\mathrm{lattice} = \frac{3\pi c^2}{2\omega_0^3} \frac{\Gamma_0}{\Delta_\mathrm{R}} \left[I_1 + I_2 + 2\sqrt{I_1 I_2} \cos(\delta k_\mathrm{L} z - \delta\omega_\mathrm{L} t) \right]. \tag{7.29}$$

The first two terms in the square brackets produce a constant shift of the potential and can be merged into the definition of the ground state energy, while the last term introduces a periodic modulation on the ion. After replacing $z = z_0 (\hat{a} + \hat{a}^\dagger)$ and defining the Lamb-Dicke parameter for the lattice $\eta_\mathrm{L} = \delta k_\mathrm{L} z_0$, we express the potential as

$$V''_\mathrm{lattice} = \frac{3\pi c^2}{2\omega_0^3} \frac{\Gamma_0}{\Delta_\mathrm{R}} \sqrt{I_1 I_2} \left[e^{i\eta_\mathrm{L}(\hat{a}+\hat{a}^\dagger)} e^{-i\delta\omega_\mathrm{L} t} + \mathrm{h.c.} \right]. \tag{7.30}$$

After an unitary transformation into the frame of the trap frequency, we write this potential as

$$\begin{aligned} V_{\text{lattice}} &= \frac{3\pi c^2}{2\omega_0^3}\frac{\Gamma_0}{\Delta_{\text{R}}}\sqrt{I_1 I_2}\left[e^{i\eta_{\text{L}}(\hat{a}e^{-i\omega_{\text{T}}t}+\hat{a}^\dagger e^{i\omega_{\text{T}}t})}e^{-i\delta\omega_{\text{L}}t}+\text{h.c.}\right] \\ &\approx \frac{3\pi c^2}{2\omega_0^3}\frac{\Gamma_0}{\Delta_{\text{R}}}\sqrt{I_1 I_2}\left[i\eta_{\text{L}}\left(\hat{a}e^{-i\omega_{\text{T}}t}+\hat{a}^\dagger e^{i\omega_{\text{T}}t}\right)e^{-i\delta\omega_{\text{L}}t}+\text{h.c.}\right] \\ &\approx \frac{3\pi c^2}{2\omega_0^3}\frac{\Gamma_0}{\Delta_{\text{R}}}\sqrt{I_1 I_2}\left[i\eta_{\text{L}}\hat{a}^\dagger e^{-i\delta\omega t}+\text{h.c.}\right] \\ &= \hbar\frac{\Omega_1\Omega_2}{4\Delta_{\text{R}}}\left[i\eta_{\text{L}}\hat{a}^\dagger e^{-i\delta\omega t}+\text{h.c.}\right], \end{aligned} \tag{7.31}$$

where in the first step Lamb-Dicke approximation is made and in the second step rotating wave approximation is made. In the last step we replace the intensity of the two laser beams with the corresponding Rabi frequencies using Eq. (7.19). The detuning $\delta\omega = \delta\omega_{\text{L}} - \omega_{\text{T}}$ gives the deviation of the frequency difference of the two lattice lasers from the trap frequency ω_{T}. The optical lattice causes an interaction Hamiltonian of the same form as in Eq. (5.2) for the classical driving field and therefore has the same effect as the classical driving field and displaces the ion's motion. A simple comparison with Eq. (5.2) reveals the displacement strength for the optical lattice

$$\Omega_{\text{d}} = \eta\frac{\Omega_1\Omega_2}{4\Delta_{\text{R}}}. \tag{7.32}$$

With $\delta\omega = 0$, the ion is displaced to a coherent state $|\alpha = \Omega_{\text{d}}t\rangle$ after an interaction time t and the population in the motional excited states is given by

$$P_0 = 1 - \exp\left(-|\Omega_{\text{d}}t|^2\right). \tag{7.33}$$

With an excitation to the coherent state $|\alpha = 3\rangle$, the population left in the motional ground state is less than 0.01%.

The optical lattice induces at the same time an off-resonant excitation. Inserting Eq. (7.28) into Eq. (7.22) we derive the scattering rate from the two lattice lasers

$$\Gamma'_{\text{sc}}(z,t) = \frac{3\pi c^2}{2\hbar\omega_0^3}\frac{\Gamma_0^2}{\Delta_{\text{R}}^2}\left[I_1 + I_2 + 2\sqrt{I_1 I_2}\cos(\delta k_{\text{L}} z - \delta\omega_{\text{L}}t)\right], \tag{7.34}$$

which has a spatial and time-dependence. At the position of the ion ($z = 0$), the time-averaged scattering rate over the period of $2\pi/\delta\omega_{\mathrm{L}}$ is given by

$$\Gamma_{\mathrm{sc}} = \overline{\Gamma'_{\mathrm{sc}}(0,t)} = \frac{3\pi c^2}{2\hbar\omega_0^3}\frac{\Gamma_0^2}{\Delta_{\mathrm{R}}^2}\left[I_1 + I_2\right] = \frac{\Gamma_0}{4}\left[\frac{\Omega_1^2}{\Delta_{\mathrm{R}}^2} + \frac{\Omega_2^2}{\Delta_{\mathrm{R}}^2}\right] . \tag{7.35}$$

As can been seen here, the total scattering rate corresponds to the sum of the off-resonant excitation rates of the two individual lattice lasers.

The ratio between off-resonant excitation and coherent excitation by the optical lattice is given by

$$\frac{\Gamma_{\mathrm{sc}}}{\Omega_{\mathrm{d}}} = \frac{\Gamma_0}{\eta\Delta_{\mathrm{R}}}\frac{\Omega_1^2 + \Omega_2^2}{\Omega_1\Omega_2} \approx \frac{2\Gamma_0}{\eta\Delta_{\mathrm{R}}}, \tag{7.36}$$

where we assumed that the two lattice lasers have about equal amount of intensities on the ion ($\Omega_1 \approx \Omega_2$).

7.4.4 Coupling strength for magnesium ion

The lattice laser used to generate a state-dependent force on the molecular ion is at around 281 nm, which is not far away from the

$$\begin{aligned}
&\mathrm{D1}: \ |^2\mathrm{S}_{1/2}, J'' = 1/2\rangle \rightarrow |^2\mathrm{P}_{1/2}, J' = 1/2\rangle \\
&\mathrm{D2}: \ |^2\mathrm{S}_{1/2}, J'' = 1/2\rangle \rightarrow |^2\mathrm{P}_{3/2}, J' = 3/2\rangle
\end{aligned}$$

transitions of the $^{25}\mathrm{Mg}^+$ ion at around 280 nm. In this section, We calculate the displacement strength Ω_{d} exerted on the $^{25}\mathrm{Mg}^+$ ion. For this, we consider first the transition strength for a direct dipole transition. Using the Wigner-Eckart-Theorem, the transition dipole matrix element for a $^{25}\mathrm{Mg}^+$ ion between the two states $|\xi'' L'' J'' F'' m''_F\rangle$ and $|\xi' L' J' F' m'_F\rangle$ can be expressed as (Auzinsh et al., 2010)

$$\begin{aligned}
&\langle \xi' J' F' m'_F |\, d_q \,| \xi'' J'' F'' m''_{\mathrm{F}} \rangle \\
&= (-1)^{F'-m'_F} \begin{Bmatrix} F' & 1 & F'' \\ -m'_F & q & m''_F \end{Bmatrix}_{3j} \\
&\quad \times (-1)^{J'+I+F''+1} \sqrt{(2F''+1)(2F'+1)} \begin{Bmatrix} J' & F' & I \\ F'' & J'' & 1 \end{Bmatrix}_{6j} \\
&\quad \times \langle \xi' J' \,\|\, d \,\|\, \xi'' J'' \rangle \ ,
\end{aligned} \tag{7.37}$$

where ξ stands for the atomic quantum numbers other than J, I, F and m_F. Similarly as for the molecular ions, we use double primes to denote the quantum numbers of the electronic ground state and single primes to denote the quantum numbers of the electronic excited state. The factor in the first line gives a correction due to the coupling to different Zeeman sub-levels and the factor in the second line gives the correction due to the hyperfine structure. The absolute-value-squared reduced dipole matrix element $|\langle \xi' J' \,\|\, d \,\|\, \xi'' J'' \rangle|^2$ in the J-basis is related with the linewidth of the upper state according to (Corney, 2006; Auzinsh et al., 2010)

$$\Gamma_0 = \frac{\omega_0^3}{3\pi\epsilon_0\hbar c^3} \cdot \frac{1}{2J'+1} |\, \langle \xi' J' \,\|\, d \,\|\, \xi'' J'' \rangle \,|^2. \tag{7.38}$$

This allows us to calculate the reduced dipole matrix elements of the D1 and D2 lines in the $^{25}Mg^+$ ion from the experimental values of the spontaneous emission rate:

$$\mu_{J'=1/2} = \left| \left\langle \xi', J' = \frac{1}{2} \middle\| d \middle\| \xi'', J'' = \frac{1}{2} \right\rangle \right| = 2.36\, e a_0 \tag{7.39}$$

$$\mu_{J'=3/2} = \left| \left\langle \xi', J' = \frac{3}{2} \middle\| d \middle\| \xi'', J'' = \frac{1}{2} \right\rangle \right| = 3.35\, e a_0 \tag{7.40}$$

Including all the contributions from the two closest electronic states $|^2P_{1/2}\rangle$ and $|^2P_{3/2}\rangle$, the displacement strength of the optical lattice exerted on the $^{25}Mg^+$ ion in Eq. (7.32) becomes

$$\begin{aligned} \Omega_{\mathrm{d}}^{\mathrm{mg}} &= \eta \frac{E_1 E_2}{4\hbar^2} \sum_{J'} \sum_{F'} \sum_{m'_F q} \frac{|\epsilon^q \langle \xi' J' F' m'_F |\, d_q \,| \xi'' J'' F'' m''_F \rangle|^2}{\Delta_{J'}} \\ &= \eta \frac{E_1 E_2}{4\hbar^2} \sum_{J'} \left(\frac{\mu_{J'}^2}{\Delta_{J'}} \sum_{F'} \sum_{m'_F q} S^{\mathrm{MQ}}_{F' m'_F q} S^{\mathrm{JI}}_{F'} \right) \\ &= \eta \frac{E_1 E_2}{4\hbar^2} \sum_{J'} \left(\frac{\mu_{J'}^2}{\Delta_{J'}} S_{J'} \right), \end{aligned} \tag{7.41}$$

where we considered the detuning of the lattice lasers $\Delta_{J'}$ to be large compared to the hyperfine and Zeeman splitting and therefore to be only dependent on the

Table 7.1: **Geometric factor for magnesium ion.** The geometric factors for the D1 and D2 transitions in $^{25}Mg^+$ ion including the effect of polarization.

	J'	1/2	3/2
$S_{J'}$	unpolarized	1/6	1/6
	σ^+-polarized	0	1/4
	$\epsilon^1 = -\frac{1}{2}, \epsilon^0 = -\frac{1}{\sqrt{2}}, \epsilon^{-1} = \frac{1}{2}$	1/6	1/6

quantum number J'. We introduced coefficients to simplify the notation

$$S^{\mathrm{MQ}}_{F'm'_F q} = \left| \epsilon^q \begin{Bmatrix} F' & 1 & F'' \\ -m'_F & q & m''_F \end{Bmatrix}_{3j} \right|^2 \tag{7.42}$$

$$S^{\mathrm{JI}}_{F'} = (2F''+1)(2F'+1) \left| \begin{Bmatrix} J' & F' & I \\ F'' & J'' & 1 \end{Bmatrix}_{6j} \right|^2 . \tag{7.43}$$

With a $^{25}Mg^+$ ion initialized in the $|\downarrow\rangle = |^2\mathrm{S}_{1/2}, F''=3, m''_F=3\rangle$ state, the displacement strength exerted on the $^{25}Mg^+$ ion depends on the detuning of the lattice laser $\Delta_{J'}$ and the geometric factor $S_{J'}$. For unpolarized light with

$$\left(\epsilon^1\right)^2 = \frac{1}{3}, \left(\epsilon^0\right)^2 = \frac{1}{3}, \left(\epsilon^{-1}\right)^2 = \frac{1}{3}, \tag{7.44}$$

the geometric factor simplifies to

$$S_{J'} = \sum_{F'} \sum_{m'_F q} S^{\mathrm{MQ}}_{F'm'_F q} S^{\mathrm{JI}}_{F'} = \frac{1}{3} \frac{1}{2J''+1} \tag{7.45}$$

using the sum rules of the Wigner coefficients resulting a geometric factor of 1/6 for both states $|^2\mathrm{P}_{1/2}\rangle$ and $|^2\mathrm{P}_{3/2}\rangle$. With the optical lattice entering the chamber along the axial direction and linearly polarized in the plane defined by the $\boldsymbol{k}$-vector and the quantization axis, the polarization vector has the components

$$\epsilon^1 = -\frac{1}{2}, \epsilon^0 = -\frac{1}{\sqrt{2}}, \epsilon^{-1} = \frac{1}{2} . \tag{7.46}$$

The geometric factors for the two states $|^2\mathrm{P}_{1/2}\rangle$ and $|^2\mathrm{P}_{3/2}\rangle$ are listed in Tab. 7.1.

7.4.5 Coupling strength for molecular ion

In order to calculate the displacement strength exerted on the molecular ion, we investigate first the transition strength for a direct electronic transition between the two states $|\xi''\nu''J''m_J''\Lambda''\rangle$ and $|\xi'\nu'J'm_J'\Lambda'\rangle$ with Λ as the projection of the angular momentum on the molecular axis. We explicitly include the quantum number Λ here, since it is necessary in the following calculation. In case of a $\Sigma \to \Sigma$ transition, we have $\Lambda' = \Lambda'' = 0$. The transition dipole moment of such a transition in a molecule is given by (Dai et al., 1995)

$$\begin{aligned} &\langle \xi'\nu'J'm_J'\Lambda'|\, d_q \,|\xi''\nu''J''m_J''\Lambda''\rangle \\ &= \mu_{\mathrm{XA}} \sqrt{S^{\mathrm{FC}}(\nu',\nu'')S^{\mathrm{HL}}(J',\Lambda';J'',\Lambda'')S^{\mathrm{geom}}(J',m_J';J'',m_J'')}\,. \end{aligned} \tag{7.47}$$

The transition dipole matrix moment $\mu_{\mathrm{XA}} \approx 1.7\, ea_0$ at the equilibrium distance of the $X\,{}^1\Sigma^+$ state is extracted from Aymar et al., 2009. The Franck-Condon factor describing the overlap of the wave functions of the two vibrational ground states

$$S^{\mathrm{FC}}(\nu'=0,\nu''=0) = \left[\int \psi^*_{\nu'=0}\psi_{\nu''=0}\,\mathrm{d}r\right]^2 \approx 0.091 \tag{7.48}$$

is listed in Balfour, 1972. The Hönl-London factor describing the dependence of the transition strength on the rotational quantum numbers is given by (Hansson et al., 2005)

$$S^{\mathrm{HL}}(J',\Lambda'=0;J'',\Lambda''=0) = \max(J',J''). \tag{7.49}$$

The geometric factor describing the addition of total angular momentum of the molecule and the angular momentum of the photon is given by

$$S^{\mathrm{geom}}_{m_J'q}(J'm_J';J''m_J'') = \left|\epsilon^q \begin{Bmatrix} J' & 1 & J'' \\ -m_J' & q & m_J'' \end{Bmatrix}_{3j}\right|^2 \tag{7.50}$$

The displacement strength exerted from the optical lattice on the molecular

Table 7.2: **Geometric factor for the molecular ion.** For the molecular ion initialized in the state $|\mathrm{X}\,^1\Sigma^+, \nu''=0, J''=1, m_J''\rangle$, the geometric factors in the displacement strength of the optical lattice coupling via the state $|\mathrm{A}\,^1\Sigma^+, \nu', J'=0, m_J'\rangle$ are listed as an example here for different polarizations.

	m_J''	-1	0	1
S^{geom}	unpolarized	1/9	1/9	1/9
	σ^+-polarized	1/3	0	0
	$\epsilon^1=-\frac{1}{2}, \epsilon^0=-\frac{1}{\sqrt{2}}, \epsilon^{-1}=\frac{1}{2}$	1/12	1/6	1/12

ion starting from a specific rotational state $|\xi''\nu''J''m_J''\rangle$ is given by

$$\begin{aligned}\Omega_{\mathrm{d}}^{\mathrm{mol}} &= \eta\frac{E_1E_2}{4\hbar^2}\sum_{m_J'}\sum_{q}\frac{|\epsilon^q\,\langle\xi'\nu'J'm_J'|\,d_q\,|\xi''\nu''J''m_J''\rangle\,|^2}{\Delta}\\ &= \eta\frac{E_1E_2}{4\hbar^2}\frac{\mu_{\mathrm{XA}}^2}{\Delta}S^{\mathrm{FC}}S^{\mathrm{HL}}\sum_{m_J'}\sum_{q}S_{m_J'q}^{\mathrm{geom}}\\ &= \eta\frac{E_1E_2}{4\hbar^2}\frac{\mu_{\mathrm{XA}}^2}{\Delta}S^{\mathrm{FC}}S^{\mathrm{HL}}S^{\mathrm{geom}}\end{aligned} \tag{7.51}$$

For unpolarized light, the geometric factor simplifies to

$$S^{\mathrm{geom}} = \sum_{m_J',q}\left|\epsilon^q\begin{Bmatrix}J' & 1 & J''\\ -m_J' & q & m_J''\end{Bmatrix}_{3j}\right|^2 = \frac{1}{3}\cdot\frac{1}{2J''+1}\,. \tag{7.52}$$

For the molecular ion in the state $|\mathrm{X}\,^1\Sigma^+, \nu'', J''=1, m_J''\rangle$, the geometric factor in the displacement strength of the optical lattice coupling via the state $|\mathrm{A}\,^1\Sigma^+, \nu', J'=0, m_J'\rangle$ are listed as an example for different polarizations in Tab. 7.2.

The scattering rate of the molecular ions via a direct excitation by the lattice lasers can be calculated from Eq. (7.36)

$$\Gamma_{\mathrm{sc}} = \frac{2\Gamma_0}{\eta\Delta_{\mathrm{R}}}\Omega_{\mathrm{d}}, \tag{7.53}$$

where for Γ_0 the scattering rate for the upper electronic state

$$\Gamma_0 = \frac{\omega_0^3}{3\pi\epsilon_0\hbar c^3}\mu_{\mathrm{XA}}^2 \tag{7.54}$$

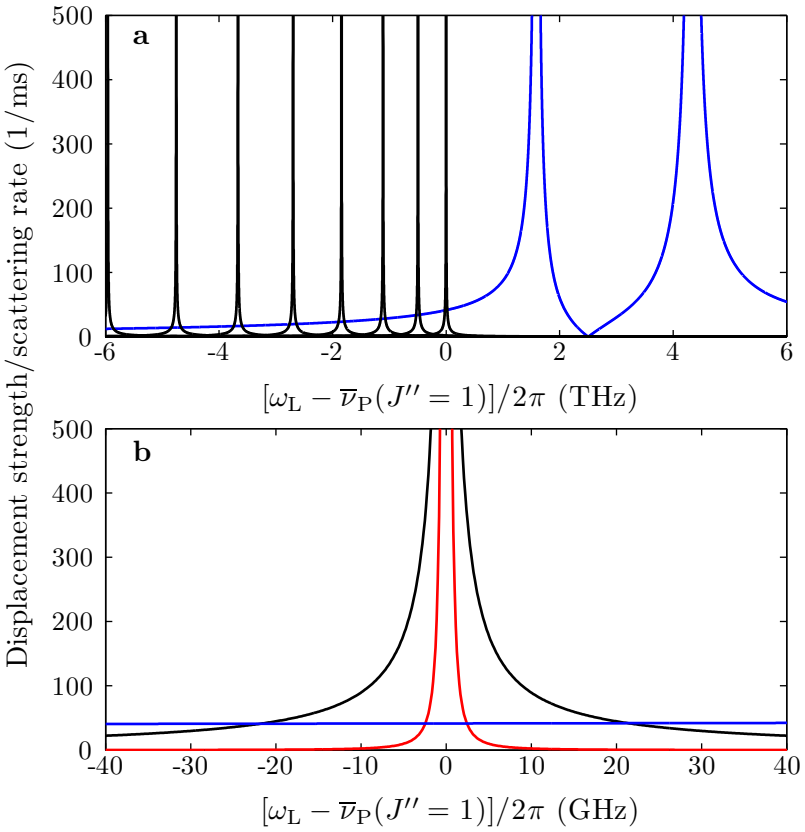

Figure 7.7: **Displacement strength of Magnesium and Magnesium hydride.** (**a**) Because of the additional factors in the transition matrix for a molecular transition, the displacement strength of the Magnesium ion (*blue lines*) overtakes the displacement strength of the molecular ion (*black lines*) as soon as the lattice lasers are detuned by tens of gigahertz from the molecular transition. In the calculation, the molecular ion is considered to be in the magnetic sublevel $|m_J'' = J''\rangle$ and the resonances from the R-branch are omitted for clarity. (**b**) Close to a molecular resonance, the displacement strength from the molecular ion becomes dominant but the scattering rate (*red lines*) via a direct excitation becomes comparable with the displacement rate. Intensities of $I_1 = I_2 = 7 \times 10^5\,\mathrm{W/m^2}$ corresponding to a power of $350\,\mu\mathrm{W}$ in each beam focused to a waist of $18\,\mu\mathrm{m}$ are used for the two lattice lasers.

is used. This corresponds to a linewidth of 39.5 MHz or a lifetime 4.0 ns for the electronic excited state $\mathrm{A}\,^1\Sigma^+$ (Højbjerre, 2009).

The calculated displacement strengths exerted on the $^{25}Mg^+$ ion (*blue lines*) and the molecular ion (*black lines*) are plotted in Fig. 7.7 as a function of the detuning of the lattice lasers from a chosen resonance of the molecular transition. The two resonances resulting from the Magnesium ions correspond to coupling via the $^2S_{1/2} \leftrightarrow {}^2P_{1/2}$ and the $^2S_{1/2} \leftrightarrow {}^2P_{3/2}$ transitions. The resonances from the molecular ions correspond to coupling via transitions between the two states $|X\,^1\Sigma^+, \nu'' = 0, J'', m_J'' = -J''\rangle$ and $|A\,^1\Sigma^+, \nu' = 0, J' = J'' - 1\rangle$, while the resonances from the R-branch are omitted here for clarity. Here a specific magnetic sublevel $|m_J'' = -J''\rangle_X$ of the electronic ground state is taken as an example, while all the contributions from different magnetic sublevels of the electronic excited state are summed up. Because of the additional factors which reduce the strength of a molecular transition, the displacement strength from the $^{25}Mg^+$ ion becomes dominant as soon as the laser is far-detuned from the molecular resonance. If the lattice laser is tuned too close to the molecular resonance, the off-resonant scattering rate (*red lines*) becomes strong compared to the displacement rate (Fig. 7.7b).

7.5 Experimental results

7.5.1 Loading of molecular ions

The preparation of a two-ion crystal consisting of a single $^{25}Mg^+$ and a single $^{24}MgH^+$ starts from loading a single $^{24}Mg^+$ in the trap. For this, the Doppler cooling laser is slightly red detuned from the $^2S_{1/2} \leftrightarrow {}^2P_{3/2}$ transition, while the photoionization laser is shifted on resonance with the $^1S_0 \leftrightarrow {}^1P_1$ transition of neutral ^{24}Mg atoms (Salumbides et al., 2006). For additionally loading a $^{25}Mg^+$ ion, we keep the frequency of the Doppler cooling laser unchanged, while shifting the frequency of the photoionization laser to be resonant with the neutral ^{25}Mg atoms. If the trap frequencies are lowered during loading of the $^{25}Mg^+$ ion, the presence of the $^{25}Mg^+$ ion in the trap is indicated by a sudden jump of the bright $^{24}Mg^+$ ion on the camera. In contrast to loading an additional $^{40}Ca^+$ ion into the trap as described in Sec. 6.4.3, we can actually check the presence of the $^{25}Mg^+$ ion by tuning the Doppler cooling laser on resonance with the $^{25}Mg^+$

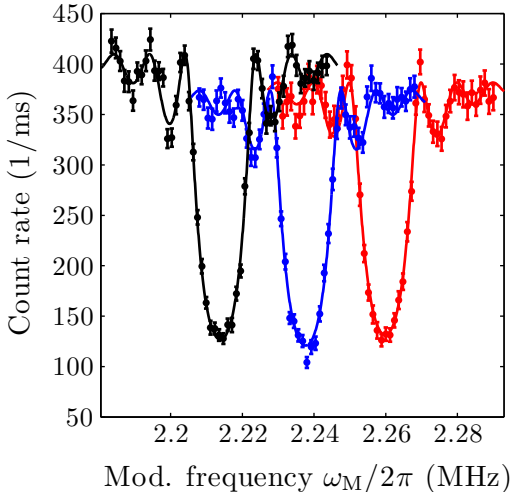

Figure 7.8: **Verification of molecular ions.** After each loading step, laser fluorescence mass spectroscopy is performed to check the components in the trap. The measured trap frequencies are in agreement with the predicted values for a single $^{24}Mg^+$ (*red*), a crystal of $^{24}Mg^+$ and $^{25}Mg^+$ (*blue*), and a crystal of $^{25}Mg^+$ and $^{24}MgH^+$ (*black*).

transition. For the production of molecular ions, we leave the Doppler cooling laser slightly red detuned with respect to the cooling transition of $^{24}Mg^+$ and leak in hydrogen gas through the leak valve, until the pressure of the vacuum chamber rises up typically from less than 1×10^{-11} mbar to 1×10^{-9} mbar. The hydrogen gas reacts with the electronically excited $^{24}Mg^+$ according to

$$^{24}Mg^+(3p) + H_2 \rightarrow {}^{24}MgH^+ + H\,, \tag{7.55}$$

while the $^{25}Mg^+$ ion in the electronic ground state cannot form a molecular ion with the hydrogen gas as shown in Mølhave et al., 2000. After the formation of the molecular ion, we shift the cooling laser to the cooling transition of $^{25}Mg^+$ and ramp up the trap potentials.

As an additional check of the species in the trap, laser fluorescence mass spectroscopy (see Sec. 5.4) is performed after each loading step with the trap parameters at the values of standard operation. The measured trap frequencies for a single $^{24}Mg^+$ ion (*red*), a crystal of $^{24}Mg^+$ and $^{25}Mg^+$ (*blue*), and a crystal

of $^{25}Mg^+$ and $^{24}MgH^+$ (*black*) are in agreement with the predicted values based on the axial trap frequency for a single $^{25}Mg^+$.

7.5.2 Displacement using a moving optical lattice

The technique for generating motional coherent states using an optical lattice is demonstrated on a two-ion crystal consisting of $^{25}Mg^+$ and $^{24}MgH^+$. The experimental sequence is illustrated in Fig. 7.9. Starting with Doppler cooling and SBC, we cool the two-ion crystal to the motional ground state of the axial mode. With the frequency difference of the two lattice beams $\delta\omega_L$ resonant with the axial trap frequency of the ip mode, a pulse of the moving optical lattice with a duration t displaces the ion to the coherent state $|\alpha = \Omega_D t\rangle$ with the corresponding motional excitation given in Eq. (7.33). In the experiment, the lattice lasers have a power of 290 μW and 430 μW respectively, and are about 1.2 GHz detuned from the $|J'' = 4\rangle_X \leftrightarrow |J' = 3\rangle_A$ transition of the molecular ion, corresponding to a detuning of −3.4 THz and −6.2 THz with respect to the D1 and D2 transitions of the $^{25}Mg^+$ ion, respectively. In order to detect the motional excitation generated by the optical lattice, we use a combination of radio frequency (RF) π-pulse and a STIRAP pulse on the BSB instead of a simple STIRAP pulse on the RSB because of technical limitations. The population in the $|\downarrow\rangle$ state of $^{25}Mg^+$ after the transfer pulses (RF and STIRAP) corresponds to the motional excitation generated by the optical lattice as described in Sec. 4.2.1. Fig. 7.10a shows the detected motional excitation using STIRAP as a function of the frequency difference of the two lattice lasers $\delta\omega_L$. The maximum excitation is reached at around the axial trap frequency ω_T^{ip}. With the relative detuning of the two lattice lasers

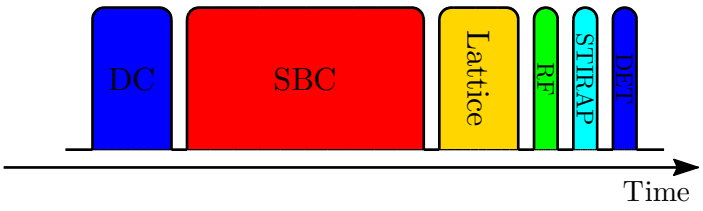

Figure 7.9: The experimental sequence for generating a coherent state of motion using a moving optical lattice.

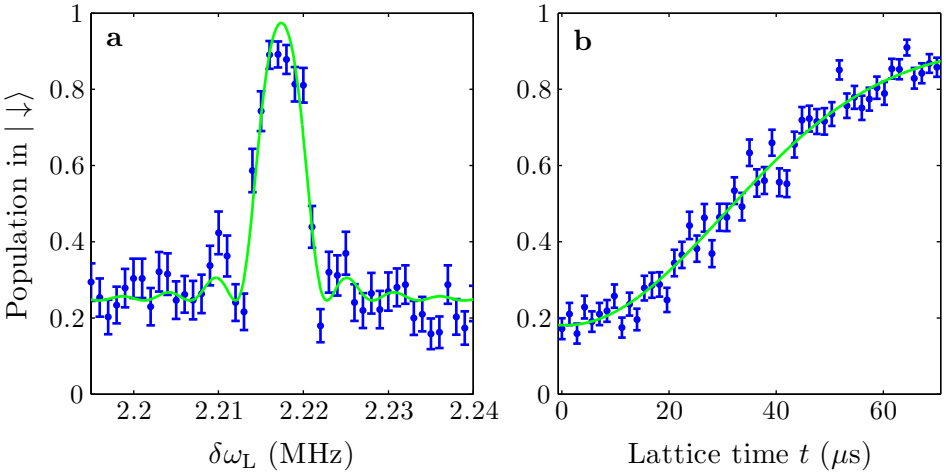

Figure 7.10: **Displacement using a moving optical lattice.** The motional excitation generated with a moving optical lattice is detected using a RF π-pulse followed by a STIRAP pulse on the blue sideband (BSB). The lattice lasers have a power of 290 μW and 430 μW respectively, and are about 1.2 GHz detuned from the $|J''=4\rangle_X \leftrightarrow |J'=3\rangle_X$ transition of the molecular ion. (**a**) The frequency difference $\delta\omega_L$ of the two Raman lasers is scanned over the axial trap frequency. The maximum motional excitation is achieved with $\delta\omega_L = \omega_T^{ip}$. (**b**) With the relative detuning of the two lattice beams on resonance, the motional excitation is probed as a function of the excitation time. A displacement strength of $\Omega_d = 24(1)\,\mathrm{ms}^{-1}$ is extracted from the fit dominated by the contribution from the $^{25}Mg^+$ ion.

on resonance, a displacement strength of $\Omega_d = 24(1)\,\mathrm{ms}^{-1}$ is extracted from a scan of the lattice time (Fig. 7.10b). We attribute this displacement strength to the background signal produced by the $^{25}Mg^+$ ion (*blue lines* in Fig. 7.7), since the excitation signal presents no stochastic character.

7.6 Discussion and outlook

In order to observe the quantum jumps between the rotational states, the detuning of the lattice laser from the electronic transition of the molecular ion needs to be controlled, so that the displacement strength from the molecular ion over-

whelms the displacement strength from the $^{25}Mg^+$ ion and the scattering rate via the electronic transition in the molecule. Alternative experimental sequences could be employed to reduce the effect from the $^{25}Mg^+$ ion.

The second factor is the delay time between the subsequent detections using the optical lattice. Each time the moving optical lattice is applied, the rotational state of the molecular ion is probed. The delay time between the subsequent probes is determined by the duration of a single experimental cycle, which is typically on the order of $5 - 10\,\mathrm{ms}$. The experimental cycles need to be repeated by typically $N_{\mathrm{cycles}} = 50 - 100$ times to reduce the quantum projection noise (QPN), so that it takes several hundred milliseconds to extract a distinguishable detection result. A longer dwell time in a specific rotational state would be advantageous for a significant detection. This would be e.g. the rotational states $|J = 0\rangle_{\mathrm{X}}$ and $|J = 1\rangle_{\mathrm{X}}$, which have a mean dwell time of longer than 2 s (Fig. 7.5).

With the molecular ion $^{24}MgH^+$ prepared in the electronic, vibrational, rotational, and motional ground state $|\mathrm{X}\,^1\Sigma^+, \nu = 0, J = 0, n = 0\rangle$, spectroscopy of the pure vibrational transition

$$|\mathrm{X}\,^1\Sigma^+, \nu = 0, J = 0\rangle \leftrightarrow |\mathrm{X}\,^1\Sigma^+, \nu = 1, J = 0\rangle$$

can be performed. Comparison of these spectroscopy data with atomic transitions would allow the test of variation of the proton-to-electron mass ratio (Kajita et al., 2011).

Chapter 8

Summary and outlook

In this thesis, we have demonstrated the universality of the quantum logic technique originally implemented on the narrow transition of an aluminum ion co-trapped with a laser-cooled beryllium ion (Schmidt et al., 2005) by extending its range of applicability to spectroscopy of broad transitions in atomic ions and towards state preparation of molecular ions.

A quasi-continuous sideband cooling (SBC) scheme has been implemented. The technique has been demonstrated on a single $^{25}Mg^+$ ion and on a two-ion crystal of $^{25}Mg^+$ and $^{24}MgH^+$, resulting in a final $\bar{n}$ of 0.01(2) for a single $^{25}Mg^+$ ion and 0.06(3) and 0.03(3) for the in-phase and out-of-phase mode of the two-ion crystal, respectively. The technique does not depend on the specific choice of individual pulse lengths and therefore provides a high stability against variation of experimental parameters, like intensity and pointing fluctuations of the laser. Employing a direct optical repumping scheme reduces the required time for SBC in comparison to the RF-assisted repumping scheme used in Hemmerling et al., 2011 from tens of milliseconds to the millisecond timescale. A short duration of single experimental cycles has been shown to be advantages for reducing the averaging time in absolute frequency measurements (Gebert et al., 2014a) or even inevitable for detection of physical effects happening in seconds or even shorter timescales as shown in Chapter 7.

SBC prepares an ion in the ground state of the harmonic potential. Starting from this state, coherent states of motion have been generated by applying an oscillating electric field at the axial trap frequency. This effect has been used to

determine the axial trap frequency of the ion and therefore allows us to infer the mass of the co-trapped ion. Using a single displacement pulse as demonstrated in laser fluorescence mass spectroscopy, we have determined the axial trap frequency with a fractional uncertainty of 3×10^{-6} from a single resonance curve containing only the statistical error, while this uncertainty has been further reduced to 3×10^{-7} using a Ramsey sequence.

A new spectroscopy technique, photon recoil spectroscopy (PRS), has been developed to perform precision spectroscopy on broad transitions of metal ions. High precision laboratory spectroscopy data of metal ions and their isotopes would allow to probe for a possible variation of the fine structure constant α through comparison with astrophysical data (Berengut et al., 2011a). But the accuracy of the analysis relies on high precision laboratory data of selected metal ions such as Ti^+ and Fe^+ which are either missing or not accurate enough (Berengut et al., 2011b; Murphy et al., 2014). Conventional spectroscopy methods for trapped ions like laser induced fluorescence and laser absorption spectroscopy, which are based on the detection of scattered or absorbed photons, the signal-to-noise ratio (SNR) is limited by the low photon collection efficiency or the small atom-light-coupling efficiency, respectively. PRS circumvents these problems by transferring the spectroscopy information from the spectroscopy ion through the common motion of the two-ion crystal to the internal state of the logic ion. The SNR is in this case limited by the quantum projection noise (QPN) appearing during state detection of a two-level system. We have demonstrated PRS on the $^2S_{1/2} \leftrightarrow {}^2P_{1/2}$ transition of the $^{40}Ca^+$ ion. The high sensitivity of ground state cooled ions achieved via resolved SBC on the logic ion $^{25}Mg^+$ is combined with synchronous spectroscopy pulses to enhance the sensitivity to photon absorption events. A motional excitation of 0.5 corresponding to a SNR of 1 has been achieved after absorption of 9.5(1.2) photons. Absolute frequency measurements of the investigated transition have been performed. From the consecutive measurements using the two-point sampling technique, an instability of 5.1×10^{-9} for an averaging time of 1 s was inferred in accordance with the predicted instability of $5.8(9) \times 10^{-9}$ derived from the QPN limit for the state detection. Including systematic effects, the center frequency for the $^2S_{1/2} \leftrightarrow {}^2P_{1/2}$ transition of $^{40}Ca^+$ ions has been determined to

$\nu = 755,222,765,896$ kHz with a total uncertainty of 88 kHz containing 78 kHz from systematic effects and 42 kHz from statistics.

PRS has recently been applied to measure the isotope shift of the $^2S_{1/2} \leftrightarrow {}^2P_{1/2}$ transition at 397 nm and the $^2D_{3/2} \leftrightarrow {}^2P_{1/2}$ transition at 866 nm of different isotopes of Ca^+ ions (Gebert et al., 2014a). High precision spectroscopy data of different isotopes could allows to investigate the influence of nuclear structure on the atomic transitions (Nörtershäuser et al., 1998a; Palmer et al., 1984; Batteiger et al., 2009; Lee et al., 2013), while calcium isotopes containing two "double-magic" nuclei raised huge interest in the study of nuclear charge distribution both in neutral atoms (Brandt et al., 1978; Träger, 1981; Andl et al., 1982; Palmer et al., 1984; Nörtershäuser et al., 1998b) and singly charged ions (Maleki et al., 1992; Kurth et al., 1995; Alt et al., 1997; Mortensen et al., 2004).

The sensitivity of PRS could be increased using quantum mechanical states of motion, like Schrödinger cat states (Hempel et al., 2013) or squeezed states. Using the optical lattice described in Chapter 7, a squeezed state of motion with an increased spatial extension could be produced and single photon sensitivity would be attainable.

We have proposed to use the quantum logic technique for rotational state preparation of molecular ions based on rotational state dependent dipole forces oscillating at one of the motional frequencies. The dipole force is implemented through an optical lattice. Blackbody radiation induced quantum jumps between different rotational states have been modelled using the Monte Carlo wavefunction method, which indicates that the total dwell time of the molecular ion in different rotational states follows a Boltzmann distribution. The mean dwell time is longer for molecules in a low rotational state than for those in a high rotational state. Through the comparison of the coupling strengths of the optical lattice with the atomic ion $^{25}Mg^+$ and the molecular ion $^{24}MgH^+$, it has been shown that careful control of the detuning of the optical lattice from the electronic transition of the molecular ion is crucial for the detection of quantum jumps between the rotational states.

As an alternative way to produce a ground state molecule, rotational cooling using a frequency comb could be implemented (Leibfried, 2012; Ding et al., 2012). Frequency combs which span about 30 THz are able to address all rotational states

populated at room temperature. This allows efficient pumping of population from the rotational state $|J\rangle_{\mathrm{X}}$ to $|J-2\rangle_{\mathrm{X}}$ via a Raman transition, while SBC on the co-trapped atomic ion provides the necessary dissipation for the cooling process.

After successful implementation of the rotational state preparation of molecular ions, spectroscopy of the pure vibrational transition $|\mathrm{X}\,^1\Sigma^+, \nu = 0, J = 0\rangle \leftrightarrow |\mathrm{X}\,^1\Sigma^+, \nu = 1, J = 0\rangle$ could be performed. It has been predicted that the frequency uncertainty could be reduced down to the order of 1×10^{-16} (Kajita et al., 2011). Comparison of the vibrational transition frequency with atomic transitions would allow to probe for a possible variation of the proton-to-electron mass ratio.

Appendix A

Stability parameters of the trap

Here we give a summary of the trap used in the experiment. From the experimentally determined axial and radial trap frequencies, the stability parameters of the trap are derived. The reader is referred to (Hemmerling, 2011) for further details.

A.1 Axial trap frequencies

The axial trap frequencies are measured with the modulation techniques as described in Sec. 5.4. Fig. A.1 shows the axial trap frequency as a function of the endcap voltage. As expected we observe a square root scaling of the axial trap frequency with the applied endcap voltage plus a shift to the negative side of the voltage axis (*blue curve*)

$$\omega_{\mathrm{T}}(U) = 2\pi\zeta\sqrt{U + U_0} \tag{A.1}$$

with $\zeta = 0.0487\,\mathrm{MHz}/\sqrt{\mathrm{V}}$ as a scaling factor and $U_0 = 67\,\mathrm{V}$ as the offset along the voltage axis. The shift here is caused by an additional $\sim$6 V and $\sim$126 V on the two endcap electrodes used for micromotion compensation. With the additional compensation voltage switched off, the residual offset approaches $U_0 = 0\,\mathrm{V}$ shown as *red curve* in Fig. A.1. Comparing Eq. (A.1) with Eq. (3.8) for the axial trap frequency, one can relate the scaling factor ζ with the geometric factor κ

$$2\pi\zeta = \sqrt{\frac{2e\kappa}{mz_0^2}}\,, \tag{A.2}$$

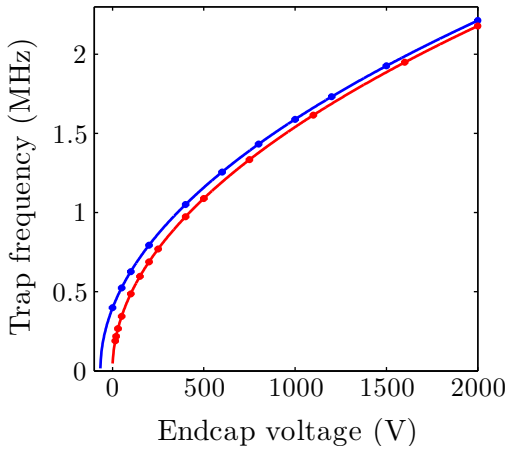

Figure A.1: **Axial trap frequencies.** Axial trap frequency determined by the modulation technique as a function of the endcap voltage. *blue*: The axial trap frequency is measured with an additional 120 V on one endcap for micromotion compensation. *red*: The axial trap frequency is measured with the compensation voltage off.

and derive a geometric factor of $\kappa = 0.076$ using the distance between the two endcaps $2z_0 = 5\,\mathrm{mm}$.

A.2 Radial trap frequencies

The radial trap frequencies are measured by modulating the amplitude of the trap drive at the frequency ω_M (Ibaraki et al., 2011). The fluorescence rate detected by the photomultiplier tube (PMT) decreases if the modulation frequency is around the radial trap frequency as shown in Fig. A.2. A splitting of the radial modes by ~60 kHz is observed at a RF power of ~5 W. The splitting can be explained by the extinction of the radial electric fields into the axial direction, which causes a symmetry breaking for the two radial directions. Due to the finite length of the radial electrodes, the electric potential due to the radial electrodes is modified to

$$\Phi_\mathrm{R}(x,y,z,t) = \frac{V_0}{2}\left[1 + \frac{x^2 - (1-\beta)y^2 - \beta z^2}{r_0^2}\right]\cos(\Omega_\mathrm{rf} t)\,, \tag{A.3}$$

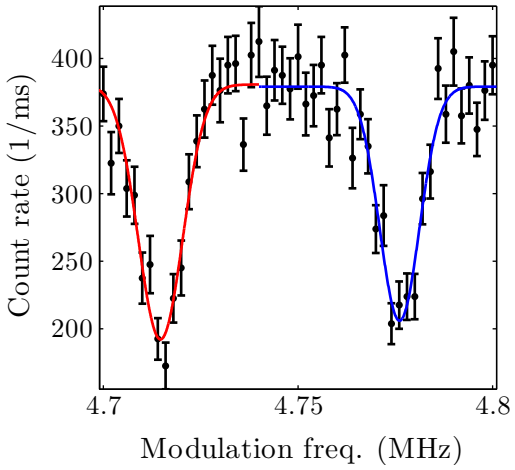

Figure A.2: **Radial trap frequencies.** Radial trap frequencies measured with the modulation technique at the RF power of $\sim 5\,\mathrm{W}$ with a single $^{25}Mg^{+}$ in the trap. The two radial modes are split by $\sim 60\,\mathrm{kHz}$ caused by the extinction of the radial field into the axial direction.

where r_0 is the perpendicular distance from the trap axis to the radial electrodes and Ω_{rf} is the radio frequency (RF) frequency generating the trap (Berkeland et al., 1998). This leads to a modified stability parameters of the trap

$$a_x = a_y = -\frac{1}{2}a_z = -\frac{4e\kappa U}{mz_0^2\Omega_{\mathrm{rf}}^2}\,, \tag{A.4}$$

$$q_x = \frac{2eV_0}{mr_0^2\Omega_{\mathrm{rf}}^2}\,,\ q_y = -(1-\beta)q_x\,,\ q_z = -\beta q_x\,, \tag{A.5}$$

which are related to the secular frequencies by Eq. (3.8). From the experimentally determined secular frequencies, we can derive the parameters a_i and q_i using a least-square approach. Consider a_x, q_x and β as free parameters, we can minimize the squared difference

$$y = \sum_i \left[\omega_i^{\mathrm{exp}} - \omega_i(a_x, q_x, \beta)\right]^2 \tag{A.6}$$

between the measured trap frequencies and the predicted trap frequencies, where $\omega_i(a_x, q_x, \beta)$ is the predicted trap frequencies using Eq. (A.4), (A.5) and (3.8). This results in the trap parameters at the endcap voltage of 2000 V and the RF

power of $\sim$5 W

$$a_x = -0.0159\,,\ a_y = -0.0159\,,\ a_z = 0.0318\,, \tag{A.7}$$

$$q_x = 0.572\,,\ q_y = -0.566\,,\ q_z = -0.00626\,. \tag{A.8}$$

and the extinction

$$\beta = 0.0109\,. \tag{A.9}$$

Appendix B

Coupled harmonic oscillators

Consider two harmonic oscillators with masses m_1, m_2, spring contants k_1, k_2 and a coupling constant κ. The dynamics of the system is given by

$$m_1 \frac{\mathrm{d}^2 x_1}{\mathrm{d}t^2} + k_1 x_1 + \kappa(x_1 - x_2) = 0 \tag{B.1}$$

$$m_2 \frac{\mathrm{d}^2 x_2}{\mathrm{d}t^2} + k_2 x_2 + \kappa(x_2 - x_1) = 0. \tag{B.2}$$

The system of linear equations can be written in matrix form

$$\boldsymbol{T}\ddot{\boldsymbol{x}} + \boldsymbol{V}\boldsymbol{x} = \boldsymbol{0} \tag{B.3}$$

with

$$\boldsymbol{T} = \begin{pmatrix} m_1 & 0 \\ 0 & m_2 \end{pmatrix}, \boldsymbol{V} = \begin{pmatrix} k_1 + \kappa & -\kappa \\ -\kappa & k_2 + \kappa \end{pmatrix}, \boldsymbol{x} = \begin{pmatrix} x_1 \\ x_2 \end{pmatrix}. \tag{B.4}$$

The linear equations are solved by tranforming into the normal mode basis according to

$$\boldsymbol{x} = \boldsymbol{\beta}\boldsymbol{q} \tag{B.5}$$

with

$$\boldsymbol{\beta} = \begin{pmatrix} \boldsymbol{\beta}^1 & \boldsymbol{\beta}^2 \end{pmatrix} \tag{B.6}$$

and $\boldsymbol{\beta}^1$, $\boldsymbol{\beta}^2$ as the non-trivial solutions of the equation system

$$(\boldsymbol{V} - \lambda_\gamma \boldsymbol{T})\,\boldsymbol{\beta}^\gamma = \boldsymbol{0}. \tag{B.7}$$

The amplitude of the vectors $\boldsymbol{\beta}^{\gamma}$ are chosen that they fulfil the orthogonality relations

$$(\boldsymbol{\beta}^{\gamma'})^{\mathsf{T}} \cdot \boldsymbol{T} \cdot \boldsymbol{\beta}^{\gamma} = \begin{cases} 0 & \text{if } \gamma' \neq \gamma\,, \\ m & \text{if } \gamma' = \gamma\,, \end{cases} \tag{B.8}$$

where $m = \sum_i m_i$ is the sum of all the masses[1]. This normalization indicates that the transformation matrix $\boldsymbol{\beta}$ is proportional to $\sqrt{m}$. The transformation matrix $\boldsymbol{\beta}$ fulfils the matrix equations

$$\boldsymbol{\beta}^{\mathsf{T}}\boldsymbol{T}\boldsymbol{\beta} = m\boldsymbol{E}\,, \tag{B.9}$$

$$\boldsymbol{\beta}^{\mathsf{T}}\boldsymbol{V}\boldsymbol{\beta} = m\boldsymbol{\Lambda}\,, \tag{B.10}$$

with $\boldsymbol{E}$ as the identity matrix and $\boldsymbol{\Lambda}$ as a diagonal matrix

$$\boldsymbol{\Lambda} = \begin{pmatrix} \lambda_1 & 0 \\ 0 & \lambda_2 \end{pmatrix}. \tag{B.11}$$

Note that Eq. (B.9) results in the relations

$$\boldsymbol{T}\boldsymbol{\beta}\boldsymbol{\beta}^{\mathsf{T}} = m\boldsymbol{E}\,, \tag{B.12}$$

$$\boldsymbol{\beta}\boldsymbol{\beta}^{\mathsf{T}}\boldsymbol{T} = m\boldsymbol{E}\,, \tag{B.13}$$

which are useful for transforming the coordinates from normal modes back into the laboratory frame. Transformation into the normal modes leads to the new equation system

$$\boldsymbol{T}\boldsymbol{\beta}\ddot{\boldsymbol{q}} + \boldsymbol{V}\boldsymbol{\beta}\boldsymbol{q} = \boldsymbol{0}. \tag{B.14}$$

Multiplying Eq. (B.14) from left side with $\boldsymbol{\beta}^{\mathsf{T}}$ results in a simple equation system for the new variables $\boldsymbol{q}$

$$m\ddot{\boldsymbol{q}} + m\boldsymbol{\Lambda}\boldsymbol{q} = \boldsymbol{0}. \tag{B.15}$$

Eq. (B.15) shows that the dynamics of the system evolves under the equations

$$\ddot{q}_{\gamma} + \lambda_{\gamma} q_{\gamma} = 0\,, \tag{B.16}$$

[1] In principle, the choice of this normalization factor is arbitrary. Choosing the normalization factor to be m makes the definition of the transformation matrix $\boldsymbol{\beta}$ identical to the definition in Morigi et al., 2001.

so that that the transformation into the normal modes leads to 2 uncoupled harmonic oscillators with the frequencies $\Omega_\gamma = \sqrt{\lambda_\gamma}$. Using Eq. (B.9), a transformation back to the laboratory coordinate is given by

$$\boldsymbol{q} = \frac{1}{m}\boldsymbol{\beta}^{\mathsf{T}}\boldsymbol{T}\boldsymbol{x}\,. \tag{B.17}$$

Consider that we apply an additional force $\boldsymbol{F}(t)$ on the two oscillators. The system of linear equations describing the dynamics (Eq. (B.3)) is modified to

$$\boldsymbol{T}\ddot{\boldsymbol{x}} + \boldsymbol{V}\boldsymbol{x} = \boldsymbol{F} \tag{B.18}$$

The transformation into the normal modes as performed above gives the new equation system

$$m\ddot{\boldsymbol{q}} + m\boldsymbol{\Lambda}\boldsymbol{q} = \boldsymbol{\beta}^{\mathsf{T}}\boldsymbol{F}(t), \tag{B.19}$$

which indicates that each of the normal modes can also be considered as an independent harmonic oscillator with a virtual mass m and the effective force on each normal modes is given by

$$\widetilde{F}_\gamma(t) = \sum_i \beta_i^\gamma F_i(t). \tag{B.20}$$

If we apply the force on only one of the oscillators $\boldsymbol{F}(t) = \begin{pmatrix} F_1(t) & 0 \end{pmatrix}^{\mathsf{T}}$, Eq. (B.19) indicates that this force acts simultaneously on both of the normal modes with corresponding amplitudes

$$\widetilde{F}_\gamma(t) = \beta_1^\gamma F_1(t) \tag{B.21}$$

These relations are used in Sec. 5.2.3 to derive the excitation strength for a two-ion crystal using electric modulation and in Sec. 6.3.2 for the discussion of the momentum transfer in photon recoil spectroscopy. It is worth mentioning here, that although the normalization factor in Eq. (B.8) changes the scaling between the normal modes and the laboratory frame, the parameters determining the dynamics of the systems like the excitation strength in Eq. (5.14) or the Lamb-Dicke parameter in Eq. (6.12) do not depends on this normalization, since the mass dependence in the transformation matrix $\boldsymbol{\beta}$ and in the ground state extension $z_0 = \sqrt{\hbar/2m\omega_{\mathrm{T}}}$ of the harmonic oscillator cancel out.

Appendix C

Numerical simulation for SBC

The dynamics of the system during quasi-continuous sideband cooling (SBC) is modelled using the optical Bloch equations, where two electronic states $|\uparrow\rangle$ and $|\downarrow\rangle$ and 80 trap levels (Fig. C.1) are considered. The Raman RSB pulses are included as a resonant coupling between $|\downarrow, n\rangle$ and $|\uparrow, n-\beta\rangle$ with β indicating

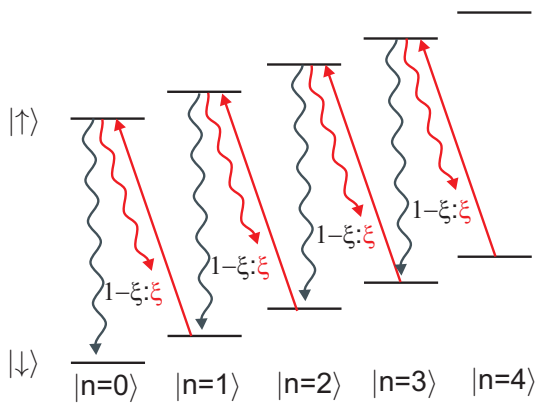

Figure C.1: **Relevant levels for numerical simulation of the dynamics during the Raman SBC cycles.** The Raman lasers are tuned to be resonant with the β^{th} order red sideband (RSB) ($\beta = 1$ in graph). Through the dissipative channels either from off-resonant excitation or via a repumping process followed by spontaneous emission, the ion falls down to the $|\downarrow\rangle$ with a decay rate of $0.006\,\text{s}^{-1}$ and $0.07\,\text{s}^{-1}$ respectively. The spontaneous emission happens on the carrier transition with a probability $1-\xi$ and the remaining small fraction ξ happens on the RSB transitions.

the sideband order used. The spontaneous decay during the Raman cooling cycle via the auxiliary states[1] is implemented with an effective decay rate determined experimentally. Outside of the Raman cooling cycle, the repumping is assumed to be complete and a simple projection of the population is performed. Within the Lamb-Dicke approximation, a branching ratio of $1-\xi:\xi$ for the spontaneous decay is assumed to include the heating process during repumping and spontaneous emission. Here ξ is on the order of $2\cdot\widetilde{\eta}^2\approx 0.1$. In this way the ion in the state $|\uparrow,n\rangle$ decays into the state $|\downarrow,n\rangle$ with probability $1-\xi$ and into the state $|\downarrow,n+1\rangle$ with probability ξ. Combining all the ingredients above, we end up with the following optical Bloch equations

$$\begin{aligned}\dot{\rho}_{\mathrm{gn,gn}} = i\frac{\Omega_{\mathrm{n-\beta,n}}}{2}\left[\rho_{\mathrm{gn,e(n-\beta)}}-\rho_{\mathrm{e(n-\beta),gn}}\right] &+ (1-\xi)\cdot\Gamma\rho_{\mathrm{en,en}} \\ &+ \xi\cdot\Gamma\rho_{\mathrm{e(n-1),e(n-1)}} \qquad \text{(C.1)}\\ \dot{\rho}_{\mathrm{gn,e(n-\beta)}} = i\frac{\Omega_{\mathrm{n-\beta,n}}}{2}\left[\rho_{\mathrm{gn,gn}}-\rho_{\mathrm{e(n-\beta),e(n-\beta)}}\right] &- \frac{\Gamma}{2}\rho_{\mathrm{gn,e(n-\beta)}} \qquad \text{(C.2)}\\ \dot{\rho}_{\mathrm{e(n-\beta),gn}} = i\frac{\Omega_{\mathrm{n-\beta,n}}}{2}\left[\rho_{\mathrm{e(n-\beta),e(n-\beta)}}-\rho_{\mathrm{gn,gn}}\right] &- \frac{\Gamma}{2}\rho_{\mathrm{e(n-\beta),gn}} \qquad \text{(C.3)}\\ \dot{\rho}_{\mathrm{e(n-\beta),e(n-\beta)}} = i\frac{\Omega_{\mathrm{n-\beta,n}}}{2}\left[\rho_{\mathrm{e(n-\beta),gn}}-\rho_{\mathrm{gn,e(n-\beta)}}\right] &- \Gamma\rho_{\mathrm{e(n-\beta),e(n-\beta)}} \qquad \text{(C.4)}\end{aligned}$$

with the density matrix elements defined as

$$\begin{aligned}\rho_{\mathrm{gn,gn}} &= \langle g,n|\,\rho\,|g,n\rangle \qquad \text{(C.5)}\\ \rho_{\mathrm{gn,e(n-\beta)}} &= \langle g,n|\,\rho\,|e,(n-\beta)\rangle \qquad \text{(C.6)}\\ \rho_{\mathrm{e(n-\beta),gn}} &= \langle e,(n-\beta)|\,\rho\,|g,n\rangle \qquad \text{(C.7)}\\ \rho_{\mathrm{e(n-\beta),e(n-\beta)}} &= \langle e,(n-\beta)|\,\rho\,|e,(n-\beta)\rangle \qquad \text{(C.8)}\end{aligned}$$

and $\Omega_{\mathrm{n,n-\beta}}$ as the effective Rabi frequency coupling the two states $|\downarrow,n\rangle$ and $|\uparrow,n-\beta\rangle$. Introducing the new variables

$$\begin{aligned}u_{\mathrm{n}} &= \rho_{\mathrm{gn,e(n-\beta)}}+\rho_{\mathrm{e(n-\beta),gn}} \qquad \text{(C.9)}\\ v_{\mathrm{n}} &= i(\rho_{\mathrm{e(n-\beta),gn}}-\rho_{\mathrm{gn,e(n-\beta)}}) \qquad \text{(C.10)}\\ w_{\mathrm{n}} &= \rho_{\mathrm{gn,gn}}-\rho_{\mathrm{e(n-\beta),e(n-\beta)}} \qquad \text{(C.11)}\\ p_{\mathrm{n}} &= \rho_{\mathrm{gn,gn}}+\rho_{\mathrm{e(n-\beta),e(n-\beta)}}. \qquad \text{(C.12)}\end{aligned}$$

[1] The spontaneous decay during the Raman cooling cycle is either caused by the off-resonant excitation from the Raman lasers or via the RF coupling and the $^2\mathrm{P}_{1/2}$ laser.

allows us to tranform the differential equations above to

$$\dot{u}_{\mathrm{n}} = -\frac{\Gamma}{2}u_{\mathrm{n}} \tag{C.13}$$

$$\dot{v}_{\mathrm{n}} = \Omega_{\mathrm{n,n}-\beta}w_{\mathrm{n}} - \frac{\Gamma}{2}v_{\mathrm{n}} \tag{C.14}$$

$$\begin{aligned}\dot{w}_{\mathrm{n}} = & -\Omega_{\mathrm{n,n}-\beta}v_{\mathrm{n}} + (1-\xi)\Gamma\left(\frac{p_{\mathrm{n}+\beta}-w_{\mathrm{n}+\beta}}{2}+\frac{p_{\mathrm{n}}-w_{\mathrm{n}}}{2}\right)\\ & +\xi\Gamma\left(\frac{p_{\mathrm{n}+\beta-1}-w_{\mathrm{n}+\beta-1}}{2}+\frac{p_{\mathrm{n}}-w_{\mathrm{n}}}{2}\right)\end{aligned} \tag{C.15}$$

$$\begin{aligned}\dot{p}_{\mathrm{n}} = & (1-\xi)\Gamma\left(\frac{p_{\mathrm{n}+\beta}-w_{\mathrm{n}+\beta}}{2}-\frac{p_{\mathrm{n}}-w_{\mathrm{n}}}{2}\right)\\ & +\xi\Gamma\left(\frac{p_{\mathrm{n}+\beta-1}-w_{\mathrm{n}+\beta-1}}{2}-\frac{p_{\mathrm{n}}-w_{\mathrm{n}}}{2}\right).\end{aligned} \tag{C.16}$$

These differential equation systems are solved numerically to produce the evolution during a single Raman cooling pulse.

For every set of parameters (T_{c}, α, t_{R1} and t_{R2}), the evolution during the pulse sequence as in Fig. 4.4 is computed by repeatedly solving the equations above. The actual evolution time for the atomic system during each pulse is reduced by $1\,\mu$s from the chosen pulse lengths to include the switching delay of the direct digital synthesizer (DDS) boards and the acousto-optical modulators (AOMs). The final population in the motional ground state is considered as the signal detected by the stimulated Raman adiabatic passage (STIRAP) pulse and corrected by an amplitude $a = 0.7$ and an offset $b = 0.23$ reduction due to experimental imperfections according to

$$y = a \times (y_{\mathrm{theory}} - b). \tag{C.17}$$

A scan over the SBC cooling time T_{c} reproduces the experimental data, which are processed in a similar way as described in Sec. 4.2.2.

References

[1] W. Alt, M. Block, V. Schmidt, T. Nakamura, P. Seibert, X. Chu, and G. Werth. "Shifts of the 3D - 4P transitions in different isotopes of positive calcium ions". *Journal of Physics B: Atomic, Molecular and Optical Physics* **30**, L677 (1997) (Cited on page 139).

[2] L. An der Lan. "Aufbau eines frequenzvervierfachten Lasersystems zum Coulomb-Kühlen von Magnesium Ionen". Master thesis. University of Innsbruck, 2008 (Cited on page 13).

[3] M. H. Anderson, J. R. Ensher, M. R. Matthews, C. E. Wieman, and E. A. Cornell. "Observation of Bose-Einstein condensation in a dilute atomic vapor". *Science* **269**, 198–201 (1995) (Cited on page 2).

[4] A. Andl, K. Bekk, S. Göring, A. Hanser, G. Nowicki, H. Rebel, G. Schatz, and R. C. Thompson. "Isotope shifts and hyperfine structure of the $4s^2\,{}^1\mathrm{S}_0$-$4s4p\,{}^1\mathrm{P}_1$ transition in calcium isotopes". *Physical Review C* **26**, 2194–2202 (1982) (Cited on page 139).

[5] A. Antognini, F. Nez, K. Schuhmann, F. D. Amaro, F. Biraben, J. M. R. Cardoso, D. S. Covita, A. Dax, S. Dhawan, M. Diepold, L. M. P. Fernandes, A. Giesen, A. L. Gouvea, T. Graf, T. W. Hänsch, P. Indelicato, L. Julien, C.-Y. Kao, P. Knowles, F. Kottmann, E.-O. L. Bigot, Y.-W. Liu, J. A. M. Lopes, L. Ludhova, C. M. B. Monteiro, F. Mulhauser, T. Nebel, P. Rabinowitz, J. M. F. d. Santos, L. A. Schaller, C. Schwob, D. Taqqu, J. F. C. A. Veloso, J. Vogelsang, and R. Pohl. "Proton structure from the measurement of 2S-2P transition frequencies of muonic hydrogen". *Science* **339**, 417–420 (2013) (Cited on page 1).

[6] H. F. Arnoldus and R. A. Riehle. "Waiting times, probabilities and the Q factor of fluorescent photons". *Journal of Modern Optics* **59**, 1002–1015 (2012) (Cited on page 71).

[7] B. Arora, M. Safronova, and C. Clark. "Blackbody-radiation shift in a $^{43}Ca^{+}$ ion optical frequency standard". *Physical Review A* **76** (2007) (Cited on page 107).

[8] A. Aspect, E. Arimondo, R. Kaiser, N. Vansteenkiste, and C. Cohen-Tannoudji. "Laser cooling below the one-photon recoil energy by velocity-selective coherent population trapping". *Physical Review Letters* **61**, 826–829 (1988) (Cited on page 1).

[9] M. Auzinsh, D. Budker, and S. Rochester. *Optically Polarized Atoms: Understanding Light-Atom Interactions*. Oxford University Press, 2010 (Cited on pages 78, 122, 125, 126).

[10] M. Aymar, R. Guérout, M. Sahlaoui, and O. Dulieu. "Electronic structure of the magnesium hydride molecular ion". *Journal of Physics B: Atomic, Molecular and Optical Physics* **42**, 154025 (2009) (Cited on pages 60, 112, 128).

[11] T. Baba and I. Waki. "Cooling and mass-analysis of molecules using laser-cooled atoms". *Japanese Journal of Applied Physics* **35**, L1134–L1137 (1996) (Cited on page 53).

[12] W. J. Balfour. "Rotational analysis of the $A^1\Sigma^+ \rightarrow X^1\Sigma^+$ and $B^1\Pi \rightarrow X^1\Sigma^+$ systems of $^{24}MgH^+$, $^{25}MgH^+$, and $^{26}MgH^+$". *Canadian Journal of Physics* **50**, 1082–1091 (1972) (Cited on pages 111, 112, 116, 128).

[13] V. Batteiger, S. Knünz, M. Herrmann, G. Saathoff, H. A. Schüssler, B. Bernhardt, T. Wilken, R. Holzwarth, T. W. Hänsch, and T. Udem. "Precision spectroscopy of the $3s$–$3p$ fine-structure doublet in Mg^+". *Physical Review A* **80**, 022503 (2009) (Cited on pages 1, 3, 62, 139).

[14] J. C. Berengut and V. V. Flambaum. "Astronomical and laboratory searches for space-time variation of fundamental constants". *Journal of Physics: Conference Series* **264**, 012010 (2011) (Cited on page 138).

[15] J. C. Berengut, V. A. Dzuba, V. V. Flambaum, J. A. King, M. G. Kozlov, M. T. Murphy, and J. K. Webb. "Atomic transition frequencies, isotope shifts, and sensitivity to variation of the fine structure constant for studies of quasar absorption spectra". *From Varying Couplings to Fundamental Physics*. Springer-Verlag, 2011, 9–16 (Cited on pages 3, 108, 138).

[16] D. J. Berkeland, J. D. Miller, J. C. Bergquist, W. M. Itano, and D. J. Wineland. "Minimization of ion micromotion in a Paul trap". *Journal of Applied Physics* **83**, 5025–5033 (1998) (Cited on pages 13, 15, 44, 106, 143).

[17] S. Bernitt, G. V. Brown, J. K. Rudolph, R. Steinbrügge, A. Graf, M. Leutenegger, S. W. Epp, S. Eberle, K. Kubiček, V. Mäckel, M. C. Simon, E. Träbert, E. W. Magee, C. Beilmann, N. Hell, S. Schippers, A. Müller, S. M. Kahn, A. Surzhykov, Z. Harman, C. H. Keitel, J. Clementson, F. S. Porter, W. Schlotter, J. J. Turner, J. Ullrich, P. Beiersdorfer, and J. R. C. López-Urrutia. "An unexpectedly low oscillator strength as the origin of the Fe XVII emission problem". *Nature* **492**, 225–228 (2012) (Cited on page 108).

[18] A. Bertelsen, S. Jørgensen, and M. Drewsen. "The rotational temperature of polar molecular ions in Coulomb crystals". *Journal of Physics B: Atomic, Molecular and Optical Physics* **39**, L83 (2006) (Cited on pages 110, 111).

[19] M. J. Biercuk, H. Uys, J. W. Britton, A. P. VanDevender, and J. J. Bollinger. "Ultrasensitive detection of force and displacement using trapped ions". *Nature Nanotechnology* **5**, 646–650 (2010) (Cited on page 63).

[20] S. K. Blau. "Highly charged ions challenge QED". *Physics Today* **65**, 22–22 (2012) (Cited on page 3).

[21] K. Blaum, J. Dilling, and W. Nörtershäuser. "Precision atomic physics techniques for nuclear physics with radioactive beams". *Physica Scripta* **2013**, 014017 (2013) (Cited on page 62).

[22] K.-J. Boller, A. Imamolu, and S. E. Harris. "Observation of electromagnetically induced transparency". *Physical Review Letters* **66**, 2593–2596 (1991) (Cited on page 2).

[23] P. Bowe, L. Hornekær, C. Brodersen, M. Drewsen, J. S. Hangst, and J. P. Schiffer. "Sympathetic crystallization of trapped ions". *Physical Review Letters* **82**, 2071 (1999) (Cited on pages 4, 110).

[24] H.-W. Brandt, K. Heilig, H. Knöckel, and A. Steudel. "Isotope shift in the Ca I resonance line and changes in mean-square nuclear charge radii of the stable Ca isotopes". *Zeitschrift für Physik A Atoms and Nuclei* **288**, 241–246 (1978) (Cited on page 139).

[25] K. R. Brown, A. C. Wilson, Y. Colombe, C. Ospelkaus, A. M. Meier, E. Knill, D. Leibfried, and D. J. Wineland. "Single-qubit-gate error below 10^{-4} in a trapped ion". *Physical Review A* **84**, 030303 (2011) (Cited on page 19).

[26] K. E. Cahill and R. J. Glauber. "Ordered expansions in boson amplitude operators". *Physical Review* **177**, 1857–1881 (1969) (Cited on page 10).

[27] H. J. Carmichael. "Quantum trajectory theory for cascaded open systems". *Physical Review Letters* **70**, 2273–2276 (1993) (Cited on page 116).

[28] H. J. Carmichael. *Statistical Methods in Quantum Optics 2: Non-Classical Fields*. Springer-Verlag, 2008 (Cited on page 116).

[29] L. D. Carr, D. DeMille, R. V. Krems, and J. Ye. "Cold and ultracold molecules: science, technology and applications". *New Journal of Physics* **11**, 055049 (2009) (Cited on page 109).

[30] C. W. Chou, D. B. Hume, J. C. J. Koelemeij, D. J. Wineland, and T. Rosenband. "Frequency comparison of two high-accuracy Al^+ optical clocks". *Physical Review Letters* **104**, 070802 (2010) (Cited on pages 2, 62).

[31] S. Chu, L. Hollberg, J. E. Bjorkholm, A. Cable, and A. Ashkin. "Three-dimensional viscous confinement and cooling of atoms by resonance radiation pressure". *Physical Review Letters* **55**, 48–51 (1985) (Cited on page 1).

[32] J. I. Cirac, R. Blatt, P. Zoller, and W. D. Phillips. "Laser cooling of trapped ions in a standing wave". *Physical Review A* **46**, 2668–2681 (1992) (Cited on page 26).

[33] C. R. Clark, J. E. Goeders, Y. K. Dodia, C. R. Viteri, and K. R. Brown. "Detection of single-ion spectra by Coulomb-crystal heating". *Physical Review A* **81** (2010) (Cited on pages 3, 62).

[34] G. Clos, M. Enderlein, U. Warring, T. Schaetz, and D. Leibfried. "Decoherence-assisted spectroscopy of a single Mg^+ ion". *Physical Review Letters* **112**, 113003 (2014) (Cited on page 19).

[35] C. Cohen-Tannoudji, J. Dupont-Roc, and G. Grynberg. *Atom-Photon Interactions: Basic Processes and Applications*. J. Wiley, 1992 (Cited on page 7).

[36] A. Corney. *Atomic and Laser Spectroscopy*. Oxford University Press, 2006 (Cited on page 126).

[37] H.-L. Dai and R. W. Field. *Molecular Dynamics and Spectroscopy by Stimulated Emission Pumping*. World Scientific, 1995 (Cited on page 128).

[38] J. Dalibard and C. Cohen-Tannoudji. "Laser cooling below the Doppler limit by polarization gradients: simple theoretical models". *Journal of the Optical Society of America B* **6**, 2023–2045 (1989) (Cited on page 1).

[39] H. G. Dehmelt. "Radiofrequency spectroscopy of stored ions I: storage". *Advances in Atomic and Molecular Physics* **3**, 53–72 (1968) (Cited on page 15).

[40] H. Dehmelt. "Monoion oscillator as potential ultimate laser frequency standard". *IEEE Transactions on Instrumentation and Measurement* **IM-31**, 83–87 (1982) (Cited on page 1).

[41] L. Deslauriers, S. Olmschenk, D. Stick, W. K. Hensinger, J. Sterk, and C. Monroe. "Scaling and suppression of anomalous heating in ion traps". *Physical Review Letters* **97**, 103007 (2006) (Cited on page 39).

[42] S. A. Diddams, D. J. Jones, J. Ye, S. T. Cundiff, J. L. Hall, J. K. Ranka, R. S. Windeler, R. Holzwarth, T. Udem, and T. W. Hänsch. "Direct Link between Microwave and Optical Frequencies with a 300 THz Femtosecond Laser Comb". *Physical Review Letters* **84**, 5102–5105 (2000) (Cited on page 81).

[43] S. A. Diddams, L. Hollberg, and V. Mbele. "Molecular fingerprinting with the resolved modes of a femtosecond laser frequency comb". *Nature* **445**, 627–630 (2007) (Cited on page 108).

[44] F. Diedrich, J. C. Bergquist, W. M. Itano, and D. J. Wineland. "Laser cooling to the zero-point energy of motion". *Physical Review Letters* **62**, 403–406 (1989) (Cited on pages 2, 24–26).

[45] F. Diedrich and H. Walther. "Nonclassical radiation of a single stored ion". *Physical Review Letters* **58**, 203–206 (1987) (Cited on page 71).

[46] S. Ding and D. N. Matsukevich. "Quantum logic for the control and manipulation of molecular ions using a frequency comb". *New Journal of Physics* **14**, 023028 (2012) (Cited on page 139).

[47] M. Drewsen, A. Mortensen, R. Martinussen, P. Staanum, and J. L. Sørensen. "Nondestructive identification of cold and extremely localized single molecular ions". *Physical Review Letters* **93**, 243201 (2004) (Cited on pages 53, 56, 63).

[48] R. E. Drullinger, D. J. Wineland, and J. C. Bergquist. "High-resolution optical spectra of laser cooled ions". *Applied Physics* **22**, 365–368 (1980) (Cited on pages 1, 3, 62).

[49] J. L. Dunham. "The energy levels of a rotating vibrator". *Physical Review* **41**, 721–731 (1932) (Cited on page 3).

[50] V. A. Dzuba, V. V. Flambaum, and J. K. Webb. "Space-time variation of physical constants and relativistic corrections in atoms". *Physical Review Letters* **82**, 888–891 (1999) (Cited on page 3).

[51] A. M. Ellis, M. Feher, and T. G. Wright. *Electronic and Photoelectron Spectroscopy: Fundamentals and Case Studies*. Cambridge University Press, 2011 (Cited on page 113).

[52] S. W. Epp, J. R. C. López-Urrutia, G. Brenner, V. Mäckel, P. H. Mokler, R. Treusch, M. Kuhlmann, M. V. Yurkov, J. Feldhaus, J. R. Schneider, M. Wellhöfer, M. Martins, W. Wurth, and J. Ullrich. "Soft X-ray laser spectroscopy on trapped highly charged ions at FLASH". *Physical Review Letters* **98**, 183001 (2007) (Cited on pages 3, 108).

[53] J. Eschner, G. Morigi, F. Schmidt-Kaler, and R. Blatt. "Laser cooling of trapped ions". *Journal of the Optical Society of America B* **20**, 1003–1015 (2003) (Cited on page 24).

[54] J. E. Field, K. H. Hahn, and S. E. Harris. "Observation of electromagnetically induced transparency in collisionally broadened lead vapor". *Physical Review Letters* **67**, 3062–3065 (1991) (Cited on page 2).

[55] V. V. Flambaum and M. G. Kozlov. "Limit on the cosmological variation of m_p/m_e from the inversion spectrum of ammonia". *Physical Review Letters* **98**, 240801 (2007) (Cited on page 61).

[56] M. Fleischhauer, A. Imamoglu, and J. P. Marangos. "Electromagnetically induced transparency: Optics in coherent media". *Reviews of Modern Physics* **77**, 633–673 (2005) (Cited on page 2).

[57] C. J. Foot. *Atomic Physics*. Oxford University Press, 2005 (Cited on pages 7, 121).

[58] T. R. Geballe and T. Oka. "A key molecular ion in the universe and in the laboratory". *Science* **312**, 1610–1612 (2006) (Cited on page 1).

[59] F. Gebert. "Precision measurement of the isotopic shift in calcium ions using photon recoil spectroscopy". PhD thesis. University of Hannover, 2015 (Cited on page 20).

[60] F. Gebert, Y. Wan, F. Wolf, and P. O. Schmidt. "Isotope shift of calcium ions using photon recoil spectroscopy". *in preparation* (2014) (Cited on pages 59, 137, 139).

[61] F. Gebert, Y. Wan, F. Wolf, and O. P. Schmidt. "Stimulated Raman adiabatic passage for state manipulation of trapped ions". *in preparation* (2014) (Cited on pages 29, 66).

[62] D. Gerlich. "Ion-neutral collisions in a 22-pole trap at very low energies". *Physica Scripta* **1995**, 256 (1995) (Cited on pages 4, 110).

[63] C. Gerry and P. Knight. *Introductory Quantum Optics*. Cambridge University Press, 2004 (Cited on pages 49, 54, 108).

[64] P. K. Ghosh. *Ion Traps*. Oxford University Press, 1995 (Cited on pages 13, 14).

[65] R. J. Glauber. "Photon correlations". *Physical Review Letters* **10**, 84–86 (1963) (Cited on page 45).

[66] C. Gohle, T. Udem, M. Herrmann, J. Rauschenberger, R. Holzwarth, H. A. Schuessler, F. Krausz, and T. W. Hänsch. "A frequency comb in the extreme ultraviolet". *Nature* **436**, 234–237 (2005) (Cited on page 108).

[67] R. N. Gosselin, E. H. Pinnington, and W. Ansbacher. "Measurement of the lifetimes of the 4*p* levels in Ca II using laser excitation of a fast beam". *Physical Review A* **38**, 4887–4890 (1988) (Cited on page 65).

[68] A. Griesmaier. "Dipole-dipole interaction in a degenerate quantum gas Bose-Einstein condensation of chromium atoms". PhD thesis. University of Stuttgart, 2007 (Cited on page 122).

[69] R. Grimm, M. Weidemüller, and Y. B. Ovchinnikov. "Optical dipole traps for neutral atoms". *Advances In Atomic, Molecular, and Optical Physics*. Vol. 42. Academic Press, 2000, 95–170 (Cited on page 121).

[70] S. E. Hamann, D. L. Haycock, G. Klose, P. H. Pax, I. H. Deutsch, and P. S. Jessen. "Resolved-sideband Raman cooling to the ground state of an optical lattice". *Physical Review Letters* **80**, 4149–4152 (1998) (Cited on page 24).

[71] T. Hänsch. "Nobel Lecture: Passion for precision". *Reviews of Modern Physics* **78**, 1297–1309 (2006) (Cited on page 1).

[72] A. K. Hansen, O. O. Versolato, Ł Kłosowski, S. B. Kristensen, A. Gingell, M. Schwarz, A. Windberger, J. Ullrich, J. R. C. López-Urrutia, and M. Drewsen. "Efficient rotational cooling of Coulomb-crystallized molecular ions by a helium buffer gas". *Nature* **508**, 76–79 (2014) (Cited on pages 4, 110, 111).

[73] A. Hansson and J. K. G. Watson. "A comment on Hönl-London factors". *Journal of Molecular Spectroscopy* **233**, 169–173 (2005) (Cited on page 128).

[74] S. E. Harris, J. E. Field, and A. Imamoğlu. "Nonlinear optical processes using electromagnetically induced transparency". *Physical Review Letters* **64**, 1107–1110 (1990) (Cited on page 2).

[75] D. J. Heinzen and D. J. Wineland. "Quantum-limited cooling and detection of radio-frequency oscillations by laser-cooled ions". *Physical Review A* **42**, 2977–2994 (1990) (Cited on page 45).

[76] B. Hemmerling, F. Gebert, Y. Wan, and P. O. Schmidt. "A novel, robust quantum detection scheme". *New Journal of Physics* **14**, 023043 (2012) (Cited on pages 13, 19, 21, 66, 89).

[77] B. Hemmerling. "Towards Direct Frequency Comb Spectroscopy using Quantum Logic". PhD thesis. Hannover, 2011 (Cited on pages 13, 18, 29, 55, 106, 141).

[78] B. Hemmerling, F. Gebert, Y. Wan, D. Nigg, I. V. Sherstov, and P. O. Schmidt. "A single laser system for ground state cooling of $^{25}Mg^{+}$". *Applied Physics B: Lasers and Optics* **104**, 583–590 (2011) (Cited on pages 13, 16, 26–29, 38, 46, 65, 137).

[79] C. Hempel, B. P. Lanyon, P. Jurcevic, R. Gerritsma, R. Blatt, and C. F. Roos. "Entanglement-enhanced detection of single-photon scattering events". *Nature Photonics* **7**, 630–633 (2013) (Cited on pages 4, 63, 108, 139).

[80] M. Herrmann, V. Batteiger, S. Knünz, G. Saathoff, T. Udem, and T. Hänsch. "Frequency metrology on single trapped ions in the weak binding limit: the $3s_{1/2} - 3p_{3/2}$ transition in $^{24}Mg^{+}$". *Physical Review Letters* **102** (2009) (Cited on pages 3, 62).

[81] R. C. Hilborn. "Einstein coefficients, cross sections, f values, dipole moments, and all that". *American Journal of Physics* **50**, 982–986 (1982) (Cited on page 121).

[82] K. Højbjerre. "Experiments with cold trapped molecular ions". PhD thesis. University of Aarhus, 2009 (Cited on pages 116, 130).

[83] N. Huntemann, M. Okhapkin, B. Lipphardt, S. Weyers, C. Tamm, and E. Peik. "High-accuracy optical clock based on the octupole transition in $^{171}Yb^{+}$". *Physical Review Letters* **108**, 090801 (2012) (Cited on page 62).

[84] Y. Ibaraki, U. Tanaka, and S. Urabe. "Detection of parametric resonance of trapped ions for micromotion compensation". *Applied Physics B* **105**, 219–223 (2011) (Cited on pages 106, 142).

[85] W. M. Itano, J. C. Bergquist, J. J. Bollinger, J. M. Gilligan, D. J. Heinzen, F. L. Moore, M. G. Raizen, and D. J. Wineland. "Quantum projection noise: Population fluctuations in two-level systems". *Physical Review A* **47**, 3554–3570 (1993) (Cited on page 35).

[86] W. M. Itano and D. J. Wineland. "Precision measurement of the ground-state hyperfine constant of $^{25}Mg^{+}$". *Physical Review A* **24**, 1364 (1981) (Cited on page 16).

[87] W. M. Itano, D. J. Heinzen, J. J. Bollinger, and D. J. Wineland. "Quantum Zeno effect". *Physical Review A* **41**, 2295–2300 (1990) (Cited on page 77).

[88] E. Jaynes and F. W. Cummings. "Comparison of quantum and semiclassical radiation theories with application to the beam maser". *Proceedings of the IEEE* **51**, 89–109 (1963) (Cited on page 9).

[89] S. Jefferts, C. Monroe, A. S. Barton, and D. Wineland. "Paul trap for optical frequency standards". *IEEE Transactions on Instrumentation and Measurement* **44**, 148–150 (1995) (Cited on page 54).

[90] J. Jin and D. A. Church. "Precision lifetimes for the Ca^{+} $4p\,^2P$ levels: experiment challenges theory at the 1% level". *Physical Review Letters* **70**, 3213 (1993) (Cited on page 65).

[91] J. R. Johansson, P. D. Nation, and F. Nori. "QuTiP 2: a Python framework for the dynamics of open quantum systems". *Computer Physics Communications* **184**, 1234–1240 (2013) (Cited on page 78).

[92] R. Jones, K. Moll, M. Thorpe, and J. Ye. "Phase-coherent frequency combs in the vacuum ultraviolet via high-harmonic generation inside a femtosecond enhancement cavity". *Physical Review Letters* **94** (2005) (Cited on page 108).

[93] S. Jørgensen, M. Drewsen, and R. Kosloff. "Intensity and wavelength control of a single molecule reaction: Simulation of photodissociation of cold-trapped MgH^{+}". *The Journal of Chemical Physics* **123**, 094302 (2005) (Cited on page 111).

[94] M. Kajita, M. Abe, M. Hada, and Y. Moriwaki. "Estimated accuracies of pure XH^{+} (X: even isotopes of group II atoms) vibrational transition frequencies: towards the test of the variance in m_p/m_e". *Journal of Physics*

B: Atomic, Molecular and Optical Physics **44**, 025402 (2011) (Cited on pages 135, 140).

[95] M. Kasevich and S. Chu. "Laser cooling below a photon recoil with three-level atoms". *Physical Review Letters* **69**, 1741 (1992) (Cited on page 1).

[96] B. E. King, C. S. Wood, C. J. Myatt, Q. A. Turchette, D. Leibfried, W. M. Itano, C. Monroe, and D. J. Wineland. "Cooling the collective motion of trapped ions to initialize a quantum register". *Physical Review Letters* **81**, 1525–1528 (1998) (Cited on page 2).

[97] N. Kjaergaard, L. Hornekaer, A. M. Thommesen, Z. Videsen, and M. Drewsen. "Isotope selective loading of an ion trap using resonance-enhanced two-photon ionization". *Applied Physics B* **71**, 207–210 (2000) (Cited on page 85).

[98] J. C. J. Koelemeij, B. Roth, and S. Schiller. "Blackbody thermometry with cold molecular ions and application to ion-based frequency standards". *Physical Review A* **76**, 023413 (2007) (Cited on page 111).

[99] J. C. J. Koelemeij, B. Roth, A. Wicht, I. Ernsting, and S. Schiller. "Vibrational spectroscopy of HD^+ with 2-ppb accuracy". *Physical Review Letters* **98**, 173002 (2007) (Cited on page 1).

[100] H. Kreckel, M. Motsch, J. Mikosch, J. Glosík, R. Plašil, S. Altevogt, V. Andrianarijaona, H. Buhr, J. Hoffmann, L. Lammich, M. Lestinsky, I. Nevo, S. Novotny, D. A. Orlov, H. B. Pedersen, F. Sprenger, A. S. Terekhov, J. Toker, R. Wester, D. Gerlich, D. Schwalm, A. Wolf, and D. Zajfman. "High-resolution dissociative recombination of cold H_3^+ and first evidence for nuclear spin effects". *Physical Review Letters* **95**, 263201 (2005) (Cited on pages 4, 110).

[101] F. Kurth, T. Gudjons, B. Hilbert, T. Reisinger, G. Werth, and A.-M. Mårtensson-Pendrill. "Doppler free "dark resonances" for hyperfine measurements and isotope shifts in Ca^+ isotopes in a Paul trap". *Zeitschrift für Physik D Atoms, Molecules and Clusters* **34**, 227–232 (1995) (Cited on page 139).

[102] P. Lambropoulos and D. Petrosyan. *Fundamentals of Quantum Optics and Quantum Information*. Springer-Verlag, 2007 (Cited on page 114).

[103] C. Langer, R. Ozeri, J. Jost, J. Chiaverini, B. DeMarco, A. Ben-Kish, R. Blakestad, J. Britton, D. Hume, W. Itano, D. Leibfried, R. Reichle, T. Rosenband, T. Schaetz, P. Schmidt, and D. Wineland. "Long-lived qubit memory using atomic ions". *Physical Review Letters* **95** (2005) (Cited on page 19).

[104] D. J. Larson, J. C. Bergquist, J. J. Bollinger, W. M. Itano, and D. J. Wineland. "Sympathetic cooling of trapped ions: A laser-cooled two-species nonneutral ion plasma". *Physical Review Letters* **57**, 70 (1986) (Cited on page 2).

[105] J. Lee, J. Chen, and A. E. Leanhardt. "High resolution isotope shifts and hyperfine structure measurements of tungsten by laser-induced fluorescence spectroscopy". *Journal of Physics B: Atomic, Molecular and Optical Physics* **46**, 075003 (2013) (Cited on pages 1, 62, 139).

[106] E. L. Lehmann and J. P. Romano. *Testing Statistical Hypotheses*. Springer, 2005 (Cited on page 91).

[107] D. Leibfried. "Quantum state preparation and control of single molecular ions". *New Journal of Physics* **14**, 023029 (2012) (Cited on page 139).

[108] D. Leibfried, B. DeMarco, V. Meyer, D. Lucas, M. Barrett, J. Britton, W. M. Itano, B. Jelenković, C. Langer, T. Rosenband, and D. J. Wineland. "Experimental demonstration of a robust, high-fidelity geometric two ion-qubit phase gate". *Nature* **422**, 412–415 (2003) (Cited on pages 23, 49, 51).

[109] D. Leibfried, D. M. Meekhof, B. E. King, C. Monroe, W. M. Itano, and D. J. Wineland. "Experimental determination of the motional quantum state of a trapped atom". *Physical Review Letters* **77**, 4281–4285 (1996) (Cited on page 20).

[110] D. Leibfried, R. Blatt, C. Monroe, and D. Wineland. "Quantum dynamics of single trapped ions". *Reviews of Modern Physics* **75**, 281–324 (2003) (Cited on pages 7, 8).

[111] H. A. Leth, L. B. Madsen, and K. Mølmer. "Monte Carlo wave packet approach to dissociative multiple ionization in diatomic molecules". *Physical Review A* **81**, 053409 (2010) (Cited on page 116).

[112] P. D. Lett, R. N. Watts, C. I. Westbrook, W. D. Phillips, P. L. Gould, and H. J. Metcalf. "Observation of atoms laser cooled below the Doppler limit". *Physical Review Letters* **61**, 169–172 (1988) (Cited on page 1).

[113] C.-Y. Lien, S. R. Williams, and B. Odom. "Optical pulse-shaping for internal cooling of molecules". *Phys. Chem. Chem. Phys.* **13**, 18825–18829 (2011) (Cited on page 108).

[114] Y. Lin, J. P. Gaebler, T. R. Tan, R. Bowler, J. D. Jost, D. Leibfried, and D. J. Wineland. "Sympathetic electromagnetically-induced-transparency laser cooling of motional modes in an ion chain". *Physical Review Letters* **110**, 153002 (2013) (Cited on page 2).

[115] Y.-W. Lin, S. Williams, and B. C. Odom. "Resonant few-photon excitation of a single-ion oscillator". *Physical Review A* **87**, 011402 (2013) (Cited on pages 3, 63).

[116] D. Lucas, A. Ramos, J. Home, M. McDonnell, S. Nakayama, J.-P. Stacey, S. Webster, D. Stacey, and A. Steane. "Isotope-selective photoionization for calcium ion trapping". *Physical Review A* **69** (2004) (Cited on page 85).

[117] S. Machnes, M. B. Plenio, B. Reznik, A. M. Steane, and A. Retzker. "Superfast Cooling". *arXiv:1001.2714 [quant-ph]* (2010) (Cited on page 2).

[118] A. A. Madej, P. Dubé, Z. Zhou, J. E. Bernard, and M. Gertsvolf. "$^{88}Sr^{+}$ 445-THz single-ion reference at the 10^{-17} level via control and cancellation of systematic uncertainties and its measurement against the SI second". *Physical Review Letters* **109**, 203002 (2012) (Cited on page 62).

[119] F. G. Major. *Charged Particle Traps: Physics and Techniques of Charged Particle Field Confinement*. Springer-Verlag, 2005 (Cited on pages 13, 15).

[120] S. Maleki and A. T. Goble. "Isotope-shift measurements in Ca^+". *Physical Review A* **45**, 524–526 (1992) (Cited on page 139).

[121] A. Marian, M. C. Stowe, J. R. Lawall, D. Felinto, and J. Ye. "United time-frequency spectroscopy for dynamics and global structure". *Science* **306**, 2063 –2068 (2004) (Cited on page 108).

[122] I. Marzoli, J. I. Cirac, R. Blatt, and P. Zoller. "Laser cooling of trapped three-level ions: Designing two-level systems for sideband cooling". *Physical Review A* **49**, 2771–2779 (1994) (Cited on page 26).

[123] D. M. Meekhof, C. Monroe, B. E. King, W. M. Itano, and D. J. Wineland. "Generation of nonclassical motional states of a trapped atom". *Physical Review Letters* **76**, 1796–1799 (1996) (Cited on pages 2, 20, 44–47, 108).

[124] D. M. Meekhof, C. Monroe, B. E. King, W. M. Itano, and D. J. Wineland. "Generation of nonclassical motional states of a trapped atom". *Physical Review Letters* **77**, 2346–2346 (1996) (Cited on page 47).

[125] E. R. Meyer, J. L. Bohn, and M. P. Deskevich. "Candidate molecular ions for an electron electric dipole moment experiment". *Physical Review A* **73**, 062108 (2006) (Cited on page 109).

[126] P. Meystre and M. Sargent. *Elements of Quantum Optics*. Springer-Verlag, 1999 (Cited on page 114).

[127] K. Mølhave and M. Drewsen. "Formation of translationally cold MgH^+ and MgD^+ molecules in an ion trap". *Physical Review A* **62**, 011401 (2000) (Cited on pages 4, 110, 132).

[128] K. Molmer, Y. Castin, and J. Dalibard. "Monte Carlo wave-function method in quantum optics". *Journal of the Optical Society of America B* **10**, 524–538 (1993) (Cited on pages 116–118).

[129] C. Monroe, D. M. Meekhof, B. E. King, and D. J. Wineland. "A "Schrödinger cat" superposition state of an atom". *Science* **272**, 1131–1136 (1996) (Cited on pages 2, 44).

[130] C. Monroe, D. M. Meekhof, B. E. King, W. M. Itano, and D. J. Wineland. "Demonstration of a fundamental quantum logic gate". *Physical Review Letters* **75**, 4714 (1995) (Cited on pages 2, 23).

[131] C. Monroe, D. M. Meekhof, B. E. King, S. R. Jefferts, W. M. Itano, D. J. Wineland, and P. Gould. "Resolved-sideband Raman cooling of a bound atom to the 3D zero-point energy". *Physical Review Letters* **75**, 4011–4014 (1995) (Cited on pages 2, 24, 27).

[132] G. Morigi, J. Eschner, J. I. Cirac, and P. Zoller. "Laser cooling of two trapped ions: sideband cooling beyond the Lamb-Dicke limit". *Physical Review A* **59**, 3797–3808 (1999) (Cited on page 25).

[133] G. Morigi and H. Walther. "Two-species Coulomb chains for quantum information". *The European Physical Journal D - Atomic, Molecular, Optical and Plasma Physics* **13**, 261–269 (2001) (Cited on pages 44, 60, 146).

[134] G. Morigi, J. Eschner, and C. H. Keitel. "Ground State Laser Cooling Using Electromagnetically Induced Transparency". *Physical Review Letters* **85**, 4458–4461 (2000) (Cited on page 2).

[135] A. Mortensen, J. Lindballe, I. Jensen, P. Staanum, D. Voigt, and M. Drewsen. "Isotope shifts of the $4s^2\,{}^1\mathrm{S}_0 \rightarrow 4s5p\,{}^1\mathrm{P}_1$ transition and hyperfine splitting of the $4s5p\,{}^1\mathrm{P}_1$ state in calcium". *Physical Review A* **69** (2004) (Cited on page 139).

[136] M. T. Murphy, V. V. Flambaum, S. Muller, and C. Henkel. "Strong limit on a variable proton-to-electron mass ratio from molecules in the distant universe". *Science* **320**, 1611–1613 (2008) (Cited on pages 3, 61, 109).

[137] M. T. Murphy and J. C. Berengut. "Laboratory atomic transition data for precise optical quasar absorption spectroscopy". *Monthly Notices of the Royal Astronomical Society* **438**, 388–411 (2014) (Cited on pages 3, 138).

[138] T. Nakamura, M. WADA, K. Okada, A. Takamine, Y. Ishida, Y. Yamazaki, T. Kambara, Y. Kanai, T. M. Kojima, Y. Nakai, N. Oshima, A. Yoshida, T. Kubo, S. Ohtani, K. Noda, I. Katayama, V. Lioubimov, H. Wollnik, V. Varentsov, and H. A. Schuessler. "Laser spectroscopy of $^{7,10}Be^{+}$ in an online ion trap". *Physical Review A* **74**, 052503 (2006) (Cited on page 62).

[139] W. Neuhauser, M. Hohenstatt, P. Toschek, and H. Dehmelt. "Optical-sideband cooling of visible atom cloud confined in parabolic well". *Physical Review Letters* **41**, 233–236 (1978) (Cited on page 1).

[140] J. H. V. Nguyen and B. Odom. "Prospects for Doppler cooling of three-electronic-level molecules". *Physical Review A* **83**, 053404 (2011) (Cited on page 108).

[141] J. H. V. Nguyen, C. R. Viteri, E. G. Hohenstein, C. D. Sherrill, K. R. Brown, and B. Odom. "Challenges of laser-cooling molecular ions". *New Journal of Physics* **13**, 063023 (2011) (Cited on page 108).

[142] D. Nigg. "Aufbau eines Frequenz-vervierfachten Diodenlasers für die Photoionisation von Magnesium". Diploma thesis. University of Innsbruck, 2009 (Cited on page 13).

[143] W. Nörtershäuser, K. Blaum, K. Icker, P. Müller, A. Schmitt, K. Wendt, and B. Wiche. "Isotope shifts and hyperfine structure in the $3d\,^2D_J \rightarrow 4p\,^2P_J$ transitions in calcium II". *The European Physical Journal D - Atomic, Molecular, Optical and Plasma Physics* **2**, 33–39 (1998) (Cited on pages 1, 62, 139).

[144] W. Nörtershäuser, N. Trautmann, K. Wendt, and B. A. Bushaw. "Isotope shifts and hyperfine structure in the $4s^2\ ^1S_0 \rightarrow 4s4p\ ^1P_1 \rightarrow 4s4d\ ^1D_2$ transitions of stable calcium isotopes and calcium-41". *Spectrochimica Acta Part B: Atomic Spectroscopy* **53**, 709–721 (1998) (Cited on page 139).

[145] W. Nörtershäuser. "Laser spectroscopy for QED tests in highly charged ions". *Hyperfine Interactions* **199**, 131–140 (2011) (Cited on pages 3, 108).

[146] C. Ospelkaus, U. Warring, Y. Colombe, K. R. Brown, J. M. Amini, D. Leibfried, and D. J. Wineland. "Microwave quantum logic gates for trapped ions". *Nature* **476**, 181–184 (2011) (Cited on page 19).

[147] C. W. P. Palmer, P. E. G. Baird, S. A. Blundell, J. R. Brandenberger, C. J. Foot, D. N. Stacey, and G. K. Woodgate. "Laser spectroscopy of calcium isotopes". *Journal of Physics B: Atomic and Molecular Physics* **17**, 2197–2211 (1984) (Cited on page 139).

[148] Y.-S. Park and H. Wang. "Resolved-sideband and cryogenic cooling of an optomechanical resonator". *Nature Physics* **5**, 489–493 (2009) (Cited on page 24).

[149] W. Paul. "Electromagnetic traps for charged and neutral particles". *Reviews of Modern Physics* **62**, 531–540 (1990) (Cited on page 13).

[150] W. D. Phillips and H. Metcalf. "Laser Deceleration of an Atomic Beam". *Physical Review Letters* **48**, 596–599 (1982) (Cited on page 1).

[151] M. B. Plenio and P. L. Knight. "The quantum-jump approach to dissipative dynamics in quantum optics". *Reviews of Modern Physics* **70**, 101–144 (1998) (Cited on page 116).

[152] H. Rahmani, R. Srianand, N. Gupta, P. Petitjean, P. Noterdaeme, and D. A. Vásquez. "Constraining the variation of fundamental constants at $z \sim 1.3$ using 21-cm absorbers". *Monthly Notices of the Royal Astronomical Society* **425**, 556–576 (2012) (Cited on page 108).

[153] M. Ramm, T. Pruttivarasin, M. Kokish, I. Talukdar, and H. Häffner. "Precision measurement method for branching fractions of excited $P_{1/2}$ states applied to $^{40}Ca^{+}$". *Physical Review Letters* **111**, 023004 (2013) (Cited on pages 65, 88).

[154] E. Reinhold, R. Buning, U. Hollenstein, A. Ivanchik, P. Petitjean, and W. Ubachs. "Indication of a cosmological variation of the proton-electron mass ratio based on laboratory measurement and reanalysis of H_2 spectra". *Physical Review Letters* **96** (2006) (Cited on page 61).

[155] A Retzker and M. B. Plenio. "Fast cooling of trapped ions using the dynamical Stark shift". *New Journal of Physics* **9**, 279–279 (2007) (Cited on page 2).

[156] H. Rohde, S. T. Gulde, C. F. Roos, P. A. Barton, D. Leibfried, J. Eschner, F. Schmidt-Kaler, and R. Blatt. "Sympathetic ground-state cooling and coherent manipulation with two-ion crystals". *Journal of Optics B: Quantum and Semiclassical Optics* **3**, S34 (2001) (Cited on page 2).

[157] C. Roos. "Controlling the quantum state of trapped ions". PhD thesis. University of Innsbruck, 2000 (Cited on pages 24, 25).

[158] C. F. Roos, D. Leibfried, A. Mundt, F. Schmidt-Kaler, J. Eschner, and R. Blatt. "Experimental demonstration of ground state laser cooling with electromagnetically induced transparency". *Physical Review Letters* **85**, 5547–5550 (2000) (Cited on page 2).

[159] C. Roos, T. Zeiger, H. Rohde, H. C. Nägerl, J. Eschner, D. Leibfried, F. Schmidt-Kaler, and R. Blatt. "Quantum state engineering on an optical transition and decoherence in a Paul trap". *Physical Review Letters* **83**, 4713–4716 (1999) (Cited on page 26).

[160] T. Rosenband, D. B. Hume, P. O. Schmidt, C. W. Chou, A. Brusch, L. Lorini, W. H. Oskay, R. E. Drullinger, T. M. Fortier, J. E. Stalnaker, S. A. Diddams, W. C. Swann, N. R. Newbury, W. M. Itano, D. J. Wineland, and J. C. Bergquist. "Frequency ratio of Al^+ and Hg^+ single-ion optical clocks; metrology at the 17^{th} decimal place". *Science* **319**, 1808–1812 (2008) (Cited on pages 2, 23, 62).

[161] T. Rosenband, P. O. Schmidt, D. B. Hume, W. M. Itano, T. M. Fortier, J. E. Stalnaker, K. Kim, S. A. Diddams, J. C. J. Koelemeij, J. C. Bergquist, and D. J. Wineland. "Observation of the $^1S_0 \rightarrow {}^3P_0$ clock transition in $^{27}Al^+$". *Physical Review Letters* **98**, 220801 (2007) (Cited on page 2).

[162] B. Roth, J. C. J. Koelemeij, H. Daerr, and S. Schiller. "Rovibrational spectroscopy of trapped molecular hydrogen ions at millikelvin temperatures". *Physical Review A* **74**, 040501 (2006) (Cited on page 111).

[163] E. J. Salumbides, S. Hannemann, K. S. E. Eikema, and W. Ubachs. "Isotopically resolved calibration of the 285-nm Mg I resonance line for comparison with quasar absorptions". *Monthly Notices of the Royal Astronomical Society: Letters* **373**, L41–L44 (2006) (Cited on page 131).

[164] P. G. H. Sandars. "The electric dipole moment of an atom". *Physics Letters* **14**, 194–196 (1965) (Cited on page 109).

[165] M. P. Savedoff. "Physical constants in extra-galactic nebulæ". *Nature* **178**, 688–689 (1956) (Cited on page 3).

[166] S. Schlemmer, T. Kuhn, E. Lescop, and D. Gerlich. "Laser excited N_2^+ in a 22-pole ion trap:: experimental studies of rotational relaxation processes". *International Journal of Mass Spectrometry* **185–187**, 589–602 (1999) (Cited on page 111).

[167] A. Schliesser, R. Rivière, G. Anetsberger, O. Arcizet, and T. J. Kippenberg. "Resolved-sideband cooling of a micromechanical oscillator". *Nature Physics* **4**, 415–419 (2008) (Cited on page 24).

[168] P. O. Schmidt, T. Rosenband, C. Langer, W. M. Itano, J. C. Bergquist, and D. J. Wineland. "Spectroscopy using quantum logic". *Science* **309**, 749–752 (2005) (Cited on pages 2, 23, 62, 137).

[169] F. Schmidt-Kaler, J. Eschner, G. Morigi, C. Roos, D. Leibfried, A. Mundt, and R. Blatt. "Laser cooling with electromagnetically induced transparency: application to trapped samples of ions or neutral atoms". *Applied Physics B: Lasers and Optics* **73**, 807–814 (2001) (Cited on page 2).

[170] C. Schneider, M. Enderlein, T. Huber, and T. Schaetz. "Optical trapping of an ion". *Nature Photonics* **4**, 772–775 (2010) (Cited on page 4).

[171] T. Schneider, B. Roth, H. Duncker, I. Ernsting, and S. Schiller. "All-optical preparation of molecular ions in the rovibrational ground state". *Nature Physics* **6**, 275–278 (2010) (Cited on pages 110, 111).

[172] S. A. Schulz, U. Poschinger, F. Ziesel, and F. Schmidt-Kaler. "Sideband cooling and coherent dynamics in a microchip multi-segmented ion trap". *New Journal of Physics* **10**, 045007 (2008) (Cited on page 25).

[173] E. S. Shuman, J. F. Barry, and D. DeMille. "Laser cooling of a diatomic molecule". *Nature* **467**, 820–823 (2010) (Cited on page 4).

[174] J. L. Sørensen, D. Møller, T. Iversen, J. B. Thomsen, F. Jensen, P. Staanum, D. Voigt, and M. Drewsen. "Efficient coherent internal state transfer in trapped ions using stimulated Raman adiabatic passage". *New Journal of Physics* **8**, 261–261 (2006) (Cited on page 20).

[175] P. F. Staanum, K. Højbjerre, R. Wester, and M. Drewsen. "Probing Isotope Effects in Chemical Reactions Using Single Ions". *Physical Review Letters* **100**, 243003 (2008) (Cited on pages 23, 110).

[176] P. F. Staanum, K. Højbjerre, P. S. Skyt, A. K. Hansen, and M. Drewsen. "Rotational laser cooling of vibrationally and translationally cold molecular ions". *Nature Physics* **6**, 271–274 (2010) (Cited on pages 4, 110, 111).

[177] S. Stenholm. "Dynamics of trapped particle cooling in the Lamb-Dicke limit". *Journal of the Optical Society of America B* **2**, 1743–1750 (1985) (Cited on page 31).

[178] S. Stenholm. "The semiclassical theory of laser cooling". *Reviews of Modern Physics* **58**, 699–739 (1986) (Cited on page 26).

[179] S. Sturm, F. Köhler, J. Zatorski, A. Wagner, Z. Harman, G. Werth, W. Quint, C. H. Keitel, and K. Blaum. "High-precision measurement of the atomic mass of the electron". *Nature* **506**, 467–470 (2014) (Cited on page 59).

[180] A. Takamine, M. Wada, K. Okada, T. Nakamura, P. Schury, T. Sonoda, V. Lioubimov, H. Iimura, Y. Yamazaki, Y. Kanai, T. M. Kojima, A. Yoshida, T. Kubo, I. Katayama, S. Ohtani, H. Wollnik, and H. A. Schuessler. "Isotope shift measurements of $^{11,\,9,\,7}Be^{+}$". *The European Physical Journal A* **42**, 369–373 (2009) (Cited on page 62).

[181] S. M. Tan. "A computational toolbox for quantum and atomic optics". *Journal of Optics B: Quantum and Semiclassical Optics* **1**, 424 (1999) (Cited on page 74).

[182] J. D. Thompson, T. G. Tiecke, A. S. Zibrov, V. Vuletić, and M. D. Lukin. "Coherence and Raman sideband cooling of a single atom in an optical tweezer". *Physical Review Letters* **110**, 133001 (2013) (Cited on page 24).

[183] R. I. Thompson. "The determination of the electron to proton inertial mass ratio via molecular transitions". *Astrophysical Letters* **16**, 3 (1975) (Cited on page 3).

[184] X. Tong, A. H. Winney, and S. Willitsch. "Sympathetic Cooling of Molecular Ions in Selected Rotational and Vibrational States Produced by Threshold Photoionization". *Physical Review Letters* **105**, 143001 (2010) (Cited on pages 4, 110, 111).

[185] F. Träger. "On the charge distribution of calcium nuclei". *Zeitschrift für Physik A Atoms and Nuclei* **299**, 33–39 (1981) (Cited on page 139).

[186] S. Trippel, J. Mikosch, R. Berhane, R. Otto, M. Weidemüller, and R. Wester. "Photodetachment of cold OH^- in a multipole ion trap". *Physical Review Letters* **97** (2006) (Cited on pages 4, 110).

[187] Q. A. Turchette, C. J. Myatt, B. E. King, C. A. Sackett, D. Kielpinski, W. M. Itano, C. Monroe, and D. J. Wineland. "Decoherence and decay of motional quantum states of a trapped atom coupled to engineered reservoirs". *Physical Review A* **62**, 053807 (2000) (Cited on page 47).

[188] Q. A. Turchette, D. Kielpinski, B. E. King, D. Leibfried, D. M. Meekhof, C. J. Myatt, M. A. Rowe, C. A. Sackett, C. S. Wood, W. M. Itano, C. Monroe, and D. J. Wineland. "Heating of trapped ions from the quantum ground state". *Physical Review A* **61**, 063418 (2000) (Cited on page 35).

[189] I. S. Vogelius, L. B. Madsen, and M. Drewsen. "Blackbody-radiation-assisted laser cooling of molecular ions". *Physical Review Letters* **89**, 173003 (2002) (Cited on page 110).

[190] V. Vuletić, C. Chin, A. J. Kerman, and S. Chu. "Degenerate Raman Sideband Cooling of Trapped Cesium Atoms at Very High Atomic Densities". *Phys. Rev. Lett.* **81**, 5768–5771 (1998) (Cited on page 24).

[191] D. F. Walls and G. J. Milburn. *Quantum Optics*. Springer-Verlag, 1995 (Cited on page 71).

[192] Y. Wan, F. Gebert, F. Wolf, and P. O. Schmidt. "Efficient sympathetic motional ground-state cooling of a molecular ion". *arXiv:1501.06987 [physics, physics:quant-ph]* (2015) (Cited on page 23).

[193] Y. Wan, F. Gebert, J. B. Wübbena, N. Scharnhorst, S. Amairi, I. D. Leroux, B. Hemmerling, N. Lörch, K. Hammerer, and P. O. Schmidt. "Precision spectroscopy by photon-recoil signal amplification". *Nature Communications* **5**, 3096 (2014) (Cited on pages 39, 61, 102, 103, 105).

[194] J. K. Webb, J. A. King, M. T. Murphy, V. V. Flambaum, R. F. Carswell, and M. B. Bainbridge. "Indications of a spatial variation of the fine structure constant". *Physical Review Letters* **107**, 191101 (2011) (Cited on pages 61, 108).

[195] S. Willitsch, M. T. Bell, A. D. Gingell, and T. P. Softley. "Chemical applications of laser- and sympathetically-cooled ions in ion traps". *Phys. Chem. Chem. Phys.* **10**, 7200–7210 (2008) (Cited on pages 23, 109).

[196] S. Willitsch, M. T. Bell, A. D. Gingell, S. R. Procter, and T. P. Softley. "Cold Reactive Collisions between Laser-Cooled Ions and Velocity-Selected Neutral Molecules". *Physical Review Letters* **100**, 043203 (2008) (Cited on pages 23, 109).

[197] D. J. Wineland, W. M. Itano, and J. C. Bergquist. "Absorption spectroscopy at the limit: detection of a single atom". *Optics Letters* **12**, 389–391 (1987) (Cited on pages 3, 62).

[198] D. J. Wineland, C. Monroe, W. M. Itano, D. Leibfried, B. E. King, and D. M. Meekhof. "Experimental issues in coherent quantum-state manipulation of trapped atomic ions". *Journal of Research of the National Institute*

of Standards and Technology **103**, 259–328 (1998) (Cited on pages 7, 11, 20).

[199] D. J. Wineland, W. M. Itano, J. C. Bergquist, and R. G. Hulet. "Laser-cooling limits and single-ion spectroscopy". *Physical Review A* **36**, 2220–2232 (1987) (Cited on page 25).

[200] D. J. Wineland and W. M. Itano. "Laser cooling of atoms". *Physical Review A* **20**, 1521–1540 (1979) (Cited on page 10).

[201] D. J. Wineland, J. J. Bollinger, and W. M. Itano. "Laser-fluorescence mass spectroscopy". *Physical Review Letters* **50**, 628 (1983) (Cited on page 53).

[202] D. J. Wineland, R. E. Drullinger, and F. L. Walls. "Radiation-pressure cooling of bound resonant absorbers". *Physical Review Letters* **40**, 1639–1642 (1978) (Cited on page 1).

[203] D. J. Wineland. "Nobel lecture: superposition, entanglement, and raising schrödinger's cat". *Reviews of Modern Physics* **85**, 1103–1114 (2013) (Cited on page 2).

[204] A. Wolf, S. van den Berg, C. Gohle, E. Salumbides, W. Ubachs, and K. Eikema. "Frequency metrology on the $4s\,^2\mathrm{S}_{1/2}-4p\,^2\mathrm{P}_{1/2}$ transition in $^{40}\mathrm{Ca}^+$ for a comparison with quasar data". *Physical Review A* **78**, 032511 (2008) (Cited on pages 106, 107).

[205] J. B. Wübbena, S. Amairi, O. Mandel, and P. O. Schmidt. "Sympathetic cooling of mixed-species two-ion crystals for precision spectroscopy". *Physical Review A* **85**, 043412 (2012) (Cited on page 44).

[206] C. Wunderlich, T. Hannemann, T. Körber, H. Häffner, C. Roos, W. Hänsel, R. Blatt, and F. Schmidt-Kaler. "Robust state preparation of a single trapped ion by adiabatic passage". *Journal of Modern Optics* **54**, 1541–1549 (2007) (Cited on page 20).

Abbreviations

AEC absorption-emission cycle. 68–70, 72–74, 104

AOM acousto-optical modulator. 16, 32, 82–84, 86, 94, 98–100, 150

BBR blackbody radiation. 4, 110, 112, 114, 115, 117–119, 139

BSB blue sideband. 9, 24, 25, 29, 35–39, 43, 133, 134

CDF cumulative distribution function. 92, 93

DC Doppler cooling. 28, 29, 37, 39–41

DDS direct digital synthesizer. 81–83, 150

ECDL external cavity diode laser. 81

EIT electromagnetically induced transparency. 2

EOM electro-optical modulator. 16, 29

EST electron shelving technique. 17, 20, 62, 63

FWHM full width at half maximum. 86, 89

ip in-phase. 36–38, 44, 50, 51, 65, 66, 69, 70, 76, 85, 86, 118, 133, 137

LAS laser absorption spectroscopy. iii, iv, 3, 62, 138

LDA Lamb-Dicke approximation. 8, 9, 124

LFMS laser fluorescence mass spectroscopy. 53–57, 59, 132, 138

LIF laser induced fluorescence. iii, iv, 3, 62, 107, 138

MC Monte Carlo. 115, 118

MCWF Monte Carlo wave-function. 114, 116, 117, 139

Nd:YAG neodymium-doped yttrium aluminum garnet. 100

op out-of-phase. 37, 38, 44, 50, 51, 65, 69, 70, 86, 137

PBS polarizing beam splitter. 82, 84

PFC phase frequency comparator. 82, 83

PI proportional-integral. 81, 83, 91

PMT photomultiplier tube. 21, 85, 142

PPLN periodically-poled Lithium Niobate. 81

PRS photon recoil spectroscopy. iii, iv, 5, 10, 17, 18, 42, 61, 63–66, 70, 72, 74–77, 81, 86–88, 102, 108, 138, 139, 147

PTB Physikalisch-Technische Bundesanstalt. 81

QED quantum electrodynamics. 3

QLS quantum logic spectroscopy. iii, iv, 2, 56, 61

QLT quantum logic technique. iii, iv, 2–5, 109, 111, 137, 139

QPN quantum projection noise. iii, iv, 62, 63, 89, 91, 96, 135, 138

RF radio frequency. 13, 14, 19, 28, 32, 40, 83, 101, 133, 134, 143

RSB red sideband. 9, 10, 20, 24–30, 32–43, 52, 57, 63, 64, 66, 119, 120, 133, 148

RWA rotating wave approximation. 8, 45, 124

SBC sideband cooling. iii, iv, 2, 5, 10, 11, 17, 18, 23–32, 34–39, 41–43, 45, 46, 50, 52, 58, 63–65, 118, 119, 137, 138, 140, 148, 150

SNR signal-to-noise ratio. 3, 63, 89, 108, 138

STIRAP stimulated Raman adiabatic passage. 20, 29, 37, 52, 53, 57, 58, 63, 64, 66, 87, 104, 119, 133, 134, 150

TPS two-point sampling. 138

Acknowledgements

This thesis would not be possible without the help from many other people. I would like to thank all of you for lasting and sincere support.

Firstly, I would like to to thank my supervisor Prof. Piet Schmidt, who provided me support through out the whole thesis. I appreciate his willingness to explain his thinking and ideas and also his patience to listen to the feedbacks from the other sides. I am especially grateful for his support not only in my current activity at PTB, but also in the network building and the future career plan.

I would like to thank Prof. Christian Ospelkaus for agreeing to be the co-referee of my thesis and also for providing me his office during the time of writing.

I would like to thank Prof. Klemens Hammerer for agreeing to be the co-referee of my thesis and also for the joyful collaboration.

I thank all my colleagues in the difcos team. I would like to thank Börge Hemmerling for leaving such a beautiful setup for me and for giving me the first guide into the business of ion trapping. His previous work is a big treasure for me. Without those I would not have developed the work in this thesis. Special thanks go to my co-worker Florian Gebert. Constructive cooperation with him makes everything in this thesis possible. His special ability in adjusting optics has saved me weeks to months. I would like also to thank Fabian Wolf for all the efforts on the molecule project. I also thank Ivan Sherstov for all the help he provided as I arrived at Braunschweig and thank Jan-Wilke Henke for his support in the difcos project.

I would like to thank the iQLOC team. I appreciate the help that Olaf Mandel has provided. His knowledge on computer science helped me to solve different kinds of problems from programming to software and hardware issues. I thank Jannes Wübbena and Nils Scharnhost for providing us the lasers. I enjoyed the time we spent together in conferences and seminars in Dresden/Stuttgart/Denmark and so on. It was joyful time with them play kicker or ping-pong. I am fond of all the passion and laugh Sana Amairi has brought to my life. I thank Ian Leroux for all the interesting discussions from physics to tea.

I would like to thank the team of Tanja Mehlstäubler. I would like to thank Jonas Keller who has been so kindly organizing the sneak peek, Movie night and all the other events, that enriched my life in Braunschweig. I want to thank all the mocha hosts Jonas and Heather Partner for upgrading me to the mocha group and I enjoyed every single night having Pizzas with you together. I acknowledge all the help and support from Norbert Herschbach, Karsten Pyka and Tobian Burgermeister

I would like to thank the team of Prof. Christian Ospelkaus. I thank Matthias Kohnen for offering us the valuable oxygen bottles at our urgent time and I enjoy the discussion with Martina Carsjens about the trap design and the microwave gate.

I acknowledge all the help from our secretary Sadra Ludwig, who surely affords much more than her responsibility. She provided me since the first day I have been in BS. From document filing to dentist searching she has always points me to the shortest path. I would also like to thank all our electronic and mechanical engineers. I admire Peter-Christian Carstens' ability and creativity of designing any electronic devices I wished at that moment. He is the definition of "professional" to me. I thank Sven Klitzing and Alexander Pablocki for various of components they produced for me. I also acknowledge the help from Christopher Bleuel, Olga Lick, Julia Fenske and Rebecca Müller.

I thank Piet, Florian, Fabian and Heather who did the final reading of this thesis. I appreciate all your comments and suggestions and thank you for sacrificing your free time.

Last but not least, I thank my parents for supporting me over all these years.